

Study of Wire-shaped Ferromagnetic Materials

Thesis submitted to
WEST BENGAL UNIVERSITY OF TECHNOLOGY
in partial fulfillment of the Degree of
DOCTORATE OF PHILOSOPHY
YEAR, 2011



Bipul Das

Faculty of Science
West Bengal University of Technology
Salt Lake, Kolkata – 700064
West Bengal, India

Thesis Certificate

This is to certify that the thesis entitled “**Study of wire-shaped ferromagnetic materials**” submitted by Bipul Das to the West Bengal University of Technology for the award of the degree of Philosophy, is a bona fide record of the research work done by him under my supervision in the duration of six years from August 2005 to August 2011. He has completed the work truthfully and successfully to the best of my knowledge. The contents of this thesis, in full or in part, have not been submitted to any other Institute or University for the award of any degree or diploma.

Kalyan Mandal
(Supervisor)
Professor, Materials Science Department,
Satyendranath Bose National Centre for Basic Sciences,
JD Block, Sector III, Salt Lake City, Kolkata 700 098
India

To You...

ACKNOWLEDGMENTS

First, I would like to thank my thesis supervisor Dr. Kalyan Mandal for his valuable guidance throughout the course of thesis work. It was a great pleasure to conduct research under his supervision. His constant encouragement to accept the challenges of performing research in various fields of nanoscience has broadened my experimental skill in this area.

I would like to thank Dr. Pintu Sen of Variable Energy Cyclotron Center for his support in preparing metallic nanowires. He was the first who introduced me to the electrochemical deposition set-up. This work would not be possible without his constant involvement.

Next, I would like to thank Dr. D. Atkinson of Durham University for giving me an opportunity to work in his lab. I learned the E-beam lithography technique and magneto optical Kerr set-up in his lab.

I acknowledge Mr. S. K. Deb for his very kind support in submitting my thesis. I would like to thank all our lab technicians including Mr. Ratan Acharya for his support at the beginning of my thesis work. In addition, I am grateful to all other non teaching staff members with special thanks to the security men and the gardeners of our center.

I would like to express my sincere thanks to my lab mates Madhuri'di, Debu (Debabrata), Arka, Shyamsundar, Debasish, Rajashree, Ashu (Ashutosh) and Gogo (Gobinda), Suman'da and Subarna'di for their kind supports throughout my thesis work in various manner.

It is my pleasure to thank my friends and seniors - Arya, Oli (Arunima), Amartya, Arnab, Anirban (Samanta), Abhishek'da, Anuj'da, Anjan'da, Anindya'di, Ankush'da, Ashis, Chandu, Saikat, Santa (Santosh), Deba'da, Goutam'da, Kunal'da, Kartick'da, Monodeep'da, Nupur'di, Saurav'da, Santo'da, Sagar, Sayanti, Saptarshi, Subrata, Tamoghno, Oindrila and Debasish (De Munshi) who have tolerated me and helped me to figure out my confusions at various times in last eight years. Finally, no thanks would be enough for my family members, Baba (father), Maa (mother), Didi-Indra'da, Dada-Debarati and Mamuni-Partho'da for their never ending supports, encouragements, sufferings and sacrifices. My sweet niece Somi and nephew Raj also deserve mention for adding vital colors to my life.

Bipul Das

S.N.Bose National Centre for Basic Sciences,

Kolkata, India

Publications

1. S. Sinha, K. Mandal and **Bipul Das**, “Magnetization dynamics in wire-shaped amorphous magnetic materials as probed by Barkhausen noise measurement”, Journal of Physics D: Applied Physics, **40**, 2710-2715 (2007).
2. **Bipul Das**, K. Mandal, Pintu Sen, S. K. Bandopadhyay, “Effect of Aspect Ratio on the Magnetic Properties of Nickel Nanowires”, Journal of Applied Physics, **103**, 013908 (1-4), (2008).
3. **Bipul Das**, K. Mandal, and Pintu Sen, "Preparation And Characterization Of Cobalt Nanowires With High Aspect Ratio", AIP Conf. Proc. **1003**, 46 (2008)
4. Madhuri Mandal, Vikash Mishra, **Bipul Das** and Kalyan Mandal, "Synthesis And Characterization Of High Coercive CoPt Alloy Nanoparticles", AIP Conf. Proc. **1003**, pp. 79-81
5. M. Mandal, **Bipul Das** and K. Mandal “Synthesis of $\text{Co}_x\text{Pt}_{1-x}$ alloy nanoparticles of different phase by micellar technique and their properties study”, Journal of Colloid & Interface Science, **335**, 40-43 (2009).
6. S. Sinha, **Bipul Das**, K. Mandal, “Magnetoimpedance of a glass-coated amorphous microwire”, Journal of Applied Physics, **105**, 07A311 (2009).
7. D. Pal, M. Mandal, A. Choudhuri, **Bipul Das**, D. Sarkar and K. Mandal, “Micelles induced high coercivity in single domain cobalt-ferrite nanoparticles” Journal of Applied Physics, **108**, 124317 (2010).
8. S. Ghosh, G. G. Khan, **Bipul Das** and K. Mandal, “Defect-engineered enhanced d0 Ferromagnetism and Photoluminescence in K-Doped ZnO Nanowires” Journal of Applied Physics, **109**, 123927 (2011).
9. **Bipul Das**, Ashis Bakshi, Pintu Sen, Pradip das and K. Mandal, “Magnetic Behavior of Two Dimensional Arrays of Cobalt Nanowires” (communicated).
10. **Bipul Das**, M. Mandal, Pintu Sen and K. Mandal, “Effect of heat treatment on the structural and magnetic properties of CoPt alloy nanowires: role of stress” (communicated).

Contents

1	Introduction	1
1.1	Wire-shaped ferromagnetic materials.....	1
1.2	Magnetic Domains.....	3
1.3	Magnetically interacting nanowires.....	8
1.4	Objective of the work.....	9
1.5	Outline of the thesis.....	11
2	Experimental details	18
2.1	Preamble.....	18
2.2	Synthesis techniques.....	18
2.2.1	Electrochemical anodization.....	18
2.2.2	Electrodeposition of NWs and NTs.....	21
2.2.3	Thermal deposition.....	24
2.2.4	Sputtering deposition.....	25
2.2.5	Electron Beam (E-beam) Lithography.....	28
2.2.6	Miceller technique to synthesis NPS.....	33
2.3	Surface morphological structural characterization techniques.....	35
2.3.1	Electron Microscopes (EMs).....	35
2.3.2	X-Ray Powder Diffraction.....	43
2.4	Magnetic characterization techniques.....	46
2.4.1	Magnetic Force Microscopy (MFM).....	47
2.4.2	Vibrating Sample Magnetometer (VSM).....	49
2.4.3	Superconducting Quantum Interference	

	Vibrating Sample Magnetometer (S-VSM).....	52
	2.4.4 Ferromagnetic Resonance (FMR) Spectrometer.....	55
	2.4.5 Magneto Optical Kerr Effect (MOKE) magnetometer.....	58
3	Study of glass coated amorphous MWs	63
	3.1 Preamble.....	63
	3.2 Experimental.....	64
	3.3 Results and discussions.....	65
	3.3.1 Structural properties.....	65
	3.3.2 Magnetic properties and domain structure.....	66
	3.4 Conclusions.....	74
4	Synthesis and characterization of anodic alumina membrane	76
	4.1 Preamble.....	76
	4.2 Types of alumina oxide films.....	77
	4.3 Growth mechanism.....	79
	4.4 Synthesis and microstructures of porous oxide films.....	82
	4.5 Elemental and crystalline phase characterization.....	92
	4.6 Magnetic characterization.....	93
	4.7 Synthesis of Zinc-Oxide nanowires using the AAO membrane.....	94
	4.8 Conclusions.....	96
5	Structural and magnetic properties of 2-dimensional arrays of Ni NWs	101
	5.1 Preamble.....	101

5.2	Experimental.....	102
5.3	Results and discussions.....	103
5.3.1	Structural and elemental properties	103
5.3.2	Magnetic properties of arrays of Ni NWs.....	106
5.3.3	Magnetization measurement of three isolated Ni NWs.....	117
5.4	Conclusions.....	122
6	Magnetic behavior of 2-dimensional arrays of Co NWs:	
	Influence of aspect ratio	125
6.1	Preamble.....	125
6.2	Experimental.....	126
6.3	Results and discussions.....	127
6.3.1	Structural properties.....	127
6.3.2	Magnetic properties.....	137
6.4	Conclusions.....	164
7	In search of high coercive CoPt alloy NWs:	
	Influence of alumina membrane	169
7.1	Preamble.....	169
7.2	Experimental.....	170
7.3	Results and discussions.....	172
7.3.1	Structural characterizations.....	172
7.3.2	Magnetic characterizations.....	180
7.3.2.2	Magnetic properties of CoPt NPs.....	180
7.3.2.3	Magnetic properties of CoPt NWs.....	184

7.4	Conclusions.....	189
8	Electrochemical synthesis of NiFe alloy NWs and Ni NTs	193
8.1	Preamble.....	193
8.2	Synthesis of NiFe alloy NWs.....	194
8.3	Synthesis of Ni NTs.....	195
8.4	Results and discussions.....	197
8.4.1	Microstructural and elemental characterization of NiFe NWs.....	197
8.4.2	Microstructural characterization of Ni NTs.....	202
8.5	Conclusion.....	203

Chapter 1

Introduction

1.1 Wire-shaped ferromagnetic materials

Wire-shaped ferromagnetic materials, that have been researched since the last century and are also at the center of attraction of today's research in material science, can be categorized mainly in two; *microwires* (MWs) and *nanowires* (NWs). The MWs have diameters typically within the range of ~ 1 to $100\ \mu\text{m}$ whereas the NWs have the diameter less or of the order of $100\ \text{nm}$. The MWs can be several centimeters long whereas the NWs can have lengths of several micrometers.

MWs that have been fabricated for many years are made of alloys rich in ferromagnetic elements (Fe, Co, Ni etc.) depending on the interest in various sensing applications such as pulse generators, position and field sensors, rotational counters, magnetostrictive delay lines etc.^{1,2} The technological interests in amorphous MWs are related either to their characteristic single-domain wall propagation during magnetization reversal that determines their bistable magnetic behavior³ or their soft magnetic behavior important for GMI effect.⁴ Additionally, MWs with positive or vanishing magnetostriction show natural ferromagnetic resonance (NFMR) at microwave frequencies that make them suitable for high frequency applications such as radar technology.⁵ On the other hand, MWs are important for basic micromagnetic studies⁶ due to their simple magnetic domain structure. The amorphous MWs are fabricated by rapid solidification from the melt of the alloys.^{7, 8} The synthesis processes determines their cylindrical shape and the amorphous nature of the MWs. The amorphous MWs may be fabricated with or without a glass (Pyrex like) coating. The glass coat protects the metallic MWs from surface corrosion. Additionally, the glass coat reinforces the magnetoelastic anisotropy in contrast with amorphous MWs without the glass coat. First glass coated amorphous MWs were prepared in 1950s by

Ulitovsky⁷ employing a modified technique that was previously introduced by Taylor in 1924.⁹ Recently, attempts made to fabricate multilayered MWs consisting of several cylindrical microlayers with different magnetic behaviors and offering spin-wave-like or the asymmetric magnetoimpedance responses.¹⁰

The main interest in the research on ferromagnetic NWs is due to their potential applications in recording media¹¹⁻¹³ and spintronics systems.¹⁴⁻¹⁷ In case of magnetic storage media, the magnetization of a single NW treated as a single bit of data which is either '0' or '1' depending upon the direction of magnetization which may be 'up' or 'down' respectively. Propagation of DWs along the NWs by sending spin polarized current pulse current (where the spins of the conduction electrons are polarized) pulse or applying a magnetic field is the basic concept of spintronics. DW propagation through a NW opens up the possibility to store hundreds bits of data in a single NW.¹⁸ It is possible to transport information through the NWs by the use of DW motion within the NWs. Study of DW dynamics in NWs is one of the most exciting research areas today.¹⁴⁻¹⁷ In these regards, DW velocity, current density of the spin polarized current, precessional frequency of DW etc. are the important parameters to concern.¹⁴⁻¹⁸ Permalloy NWs show large anisotropic magnetoresistance (AMR) and hence easy to probe in the investigation of domain wall dynamics in the NWs make them important for spintronics applications.¹⁹ The two dimensional arrays of NWs show unique magnetic behavior depending upon NWs diameter, length, material of the NWs and on inter NW separation.²⁰ Highly ordered arrays of NWs can be used as data storage media in perpendicular magnetic recording systems. Multilayered NW, i.e. NWs that have different nanolayers made of different materials can show giant magneto resistance (GMR) effect.²¹ The unique resistive properties of multilayered NWs are potentially important for data read/write heads in magnetic storage systems. Investigation of NWs is also important for exploring the micromagnetism.⁶

The NWs are polycrystalline or single crystalline and made of ferromagnetic metals and their alloys. Magnetic nanowires can be prepared by various methods, such as E-beam lithography, chemical routes, electrochemical deposition etc.²² Among which, the electrochemical deposition is proved to be the modest, simplest and cost effective synthesis procedure. In this process, a porous diamagnetic membrane (few

microns thick) is used to deposit metallic NWs within the pores (diameter ~ few nanometers) of the membrane electrochemically. Membranes that are generally used for the purpose can be made of alumina or polycarbonate. The NWs have the same diameter as nano pores and are uniform in length throughout the membranes. The synthesis technique was first introduced by George E. Possin who reported the fabrication of tin, indium and zinc NWs by electrochemical deposition in 1969.²³ In 1975, magnetic properties of electrodeposited Co nanowires and Co-Ni alloy NWs within the pores of alumina membranes were investigated (Kawai & Ueda, 1975).²⁴ In 1986, as an application to perpendicular magnetic recording medium, alumina membranes containing Fe NWs were fabricated (Tsuya et al., 1986).²⁵ Magnetization curling process in perpendicular direction was studied by Huysmans et al.²⁶ using Fe NW arrays in alumina membrane in 1988. In 1990, influence of the packing density on the magnetic behavior was investigated using alumite media containing magnetic nanowires by Zhang et al.²⁷ At the same time, nanoporous polycarbonate membranes are also used to synthesize metallic NWs (including nickel, cobalt magnetic NWs).²⁸ Nano sized pores in the dielectric polycarbonate membranes are produced by the rapid passage of heavy ions (such as those emitted from a radioactive transuranium isotope) through the dielectric material that creates nuclear damage tracks or the parallel pores within the material.²⁹ In polycarbonate membranes, the pores are randomly distributed in the membranes. In 1995, Masuda and Fukuda in Japan developed³⁰ highly ordered nanoporous alumina membranes via electrochemical anodization of aluminum. Since the time, highly ordered porous alumina membranes have attracted many international groups as a template material for the synthesis of magnetic nanowires.³¹

1.2 Magnetic domains

Magnetic domains are the regions within a magnetic material that have distinct magnetization directions where all the magnetic spins are parallel to each other. The domains are separated by boundaries where the spins slowly rotate from one particular direction to other (i.e. the transition from one domain to other) and are called domain wall (DW). The dimension of a typical domain is of the order of 10 nm and the DWs,

that may be Neel or Bloch kind of walls, have the typical dimension of few atomic layers to several nanometers.³² In a ferromagnetic material, the domains are formed due to the ferromagnetic exchange interaction and the anisotropy energy of the materials. The positive exchange interaction, which is an inherent characteristic of all the ferromagnetic materials, tries to orient the neighboring spins parallel to each other within a domain. Whereas, the anisotropy energy, that may originate due to the peculiar shape, stress or crystalline structure of the material, try to orient the neighboring spins along the anisotropic direction within the domain. Shape anisotropy originates from the asymmetry in shape of a magnetic material. The demagnetizing field due to the free magnetic charges on the surface of the material is found to be different at different directions of the material. Whereas, different interaction of orbital and spin magnetic moment along different direction of a particular crystal lattice generates the magnetocrystalline anisotropy within a material. Thus, within a ferromagnetic material, the exchange interaction and the anisotropy field compete with each other and form a peculiar domain and DW distribution within a particular magnetic material.

The domain structures for MWs had been thoroughly investigated in various literatures.^{1, 33} In glass coated amorphous MWs, the domain distribution is mainly determined by the stresses that develop during synthesis processes and the cylindrical shape of the wires. The MWs are formed by rapid cooling of molten alloy coated with a glass coating on its surface. During the process, a gradient of stress is developed in the cylindrical alloy fibers. The outer surface of the alloy fiber cools faster than the inner core region of the alloy. The stress and the cylindrical shape of the MW promote a single domain inner core within the alloy MW.¹ Depending on the magnetostrictive nature of the MW, the rest portion of the MW i.e. the outer shell is subdivided in many small domains as depicted in Fig. 1.1 and Fig. 1.2. Fig.1.1 shows the schematic diagram of possible domain structure of a negative magnetostrictive MW. It shows an inner core single domain with magnetization parallel to the axis of the MW. Here, the outer shell is subdivided in many small domains with consecutively opposite circumferential magnetization. Fig. 1.2 shows the same for a positive magnetostrictive MW having outer shell domains with random magnetizations.

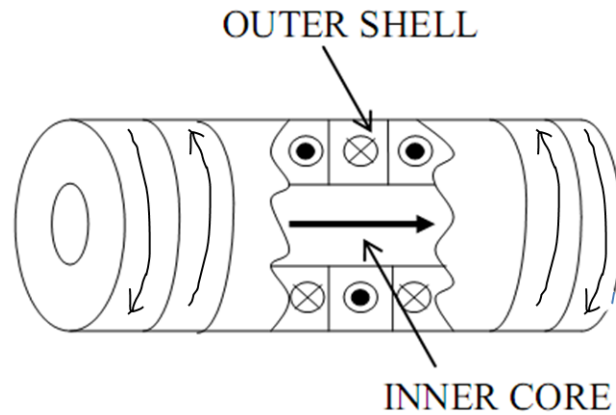


Figure 1.1. Possible domain structure of a negative magnetostrictive wire-shaped amorphous magnetic material.

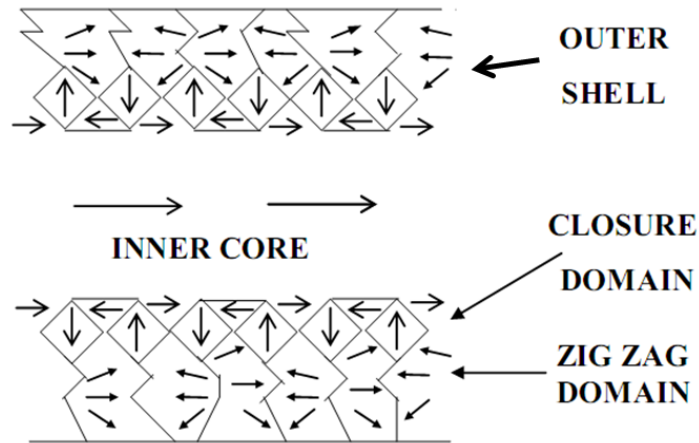


Figure 1.2. Possible domain structure of positive magnetostrictive wire-shaped amorphous magnetic material.

In bulk systems, one can observe multi-domain structure defined by Neel or Bloch domain walls³². But we know that, the domain structure in a cylindrical shaped MW is divided in to a cylindrical single domain inner core (IC) and a multidomain outer shell (OS). The diameter of inner core cylindrical single domain can occupy more than 50% of the diameter of MW.¹ Here the domain structure is determined by stress induced anisotropy in the MWs during synthesis, the cylindrical shape and composition of the MWs. Therefore in NWs, which have diameters of ~ 100 nm, single domain structure governed by shape anisotropy due to their cylindrical shape

may be possible. However in micromagnetic frame work, the NWs may take other complex remanent states.

Ideally, NWs have uniaxial anisotropy with a preferential magnetization direction along the axis of the NW. The anisotropy originates from the self demagnetizing field due to their cylindrical shaped structure and depends on the aspect ratio (length/diameter) of the NWs. Other anisotropies also present in the NWs. The magnetic spins near the surfaces of NWs realize less coordination numbers than the spins in the inner portions of the NWs. Thus due to the large surface to volume ratio in NWs compared to bulk systems (e.g. Wires and may even MWs), the anisotropy corresponds to surface energy has a significant contribution to the magnetic free energy of the NWs. The controlled synthesis of the NWs promotes crystallinity in the NWs and single crystal NWs can easily be obtained. Hence the magnetocrystalline anisotropy can have significant role depending on the crystal structure of the NWs. The domain sizes are comparable to the sizes of the NWs and the interplay among the exchange interaction and various anisotropies within the NWs gives unique spin distributions to them. Their remanent states have been calculated using micromagnetic framework by various researchers.³⁴⁻⁴⁰ Considering all these energy terms and assuming a classical ferromagnetic exchange interaction as written in Eq. 1.1, the total magnetic free energy for a ferromagnetic NW can be written as in Eq. 1.2 below,

$$E_{ex} = - \sum_{ij} J_{ij} \mathbf{S}_i \cdot \mathbf{S}_j = - J S^2 \sum_{neighbors} \cos \phi_{i,j} \quad [1.1]$$

$$E = \int [(cJS^2/a)\{(\nabla m_x)^2 + (\nabla m_y)^2 + (\nabla m_z)^2\} + w_a - 1/2 \mathbf{M} \cdot \mathbf{H}_d - \mathbf{M} \cdot \mathbf{H}_a] d\tau + \int w_a dS \quad [1.2]$$

By minimizing the free energy (Eq. 1.2) using micromagnetic simulations, researchers have shown two possible remanent state configurations for NWs. They found a critical diameter $D_c \sim 3.5 \lambda_{ex}$ that defines the transition point between the two states³⁸ where, λ_{ex} is the exchange length of the material. Exchange length is the

dimension of the region in which the exchange interaction of a particular spin exists. However, the simulations were carried out for NWs with aspect ratio (length/diameter) less than 3.5.³⁸ When the diameter of the NWs is less than D_c , the remanent state is flower state, where the spins are arranged parallel to each other with small radial tilts at both ends of the NWs. On the other hand, if the NWs have diameters greater than D_c , vortex remanent state is favorable within the NWs.^{36, 38} In vortex state, the spins are not parallel to each other and oriented in the circumferential direction. Schematic diagrams of the two states are shown in Fig.1.3. For cobalt, $D_c = 24.5$ nm and for nickel, $D_c = 70$ nm. In an infinite NW, the magnetostatic energy during the curling reversal reduces to a minimum compared to a finite cylinder. The energy barrier to the reversal is then entirely the exchange energy.³² As a result the value of the critical diameter decrease in infinite cylinder. In case of vortex NWs, surface energy term stabilizes the vortex state.⁴¹

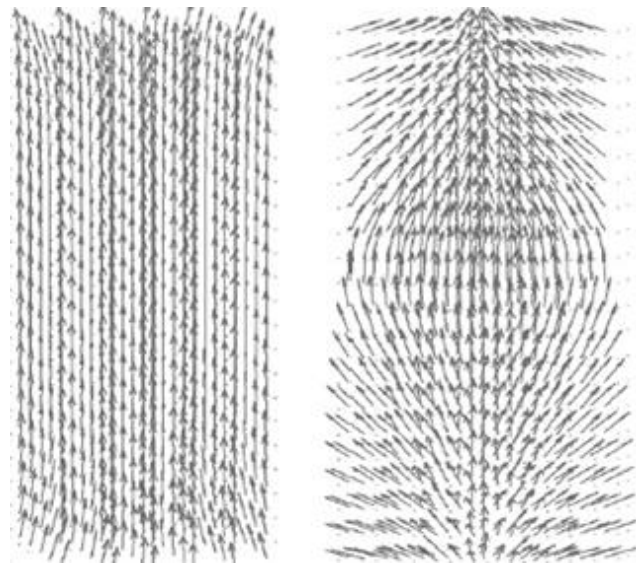


Figure 1.3. Schematic diagrams of flower (left) and vortex (right) remanent states of NW.

For an isolated NW, both the flower and vortex state develop an axial easy direction of magnetization which can be detected by MH loop measurements with the external applied field parallel and perpendicular to the NW. It can be seen that, the

NW is hardly magnetized when the external magnetic field is applied perpendicular to the NW axis whereas it saturate easily when the applied field is along the NW axis. Furthermore, the flower state has higher remanent magnetization than the vortex state as it is evident from the spin distribution in the two states. However, the flower state follows a coherent reversal and produces a square shaped magnetic hysteresis loop with a large coercivity. Whereas, NW with vortex state follow curling reversal mode and produces non-quadrilateral hysteresis loops with low remanence and low coercive field values compared to the flower state.

1.3 Magnetically interacting nanowires

Electrodeposition technique of synthesizing NWs in porous membranes produces a two dimensional arrays of NWs. That means, millions of NWs are arranged in a two dimensional hexagonal or squared mesh or randomly. Here it is obvious that, if the NWs are closely spaced, they should interact with each other magnetostatically. If one assumes each of the NW as a single magnetic dipole then the simplest form of the magnetostatic interaction is the dipolar interaction. In ideal case the dipoles should have low aspect ratios and should be infinitely far away from each other.⁴² The dipole assumption of individual NWs and dipolar approximation not necessarily hold when the length of the NWs are many orders of magnitude longer than their diameters and inter-wire spacings. Using the assumption, it was shown earlier in 1998 that the dipolar magnetostatic interaction between nanodots in a two dimensional (2D) array changes the magnetization process compared to the one of a single nanodot.⁴³ Later in 2000s, the dipolar approximation extensively used for explaining the magnetic properties of arrays of NWs even when their lengths are comparable to the NW diameter and interwire spacings.⁴⁴ The studies established that, the dipolar interaction among the NWs (considering each NW as single magnetic dipole) play the dominating role in determining the magnetic properties of arrays of NWs which are significantly different from the individual NWs. However at the same time, other approaches also made by other researchers. M. Vazquez et al. (2000) works on a model, which divides a NW into thousands of cubic cells each of which contains a point dipole parallel to each

other and then consider the dipolar interaction between the nearest neighbor inter-wire point dipoles.⁴⁵ This approach is more realistic compared to the consideration of each NW as single dipole as described earlier. The nature of magnetostatic interaction is difficult to simulate when the pores are randomly distributed in the membranes but possible⁴⁵ considering the average inter-wire distance. The other way to calculate the magnetostatic interaction field was introduced by Clime et al (2006) where they assumed each NW consisted of linear chain of tiny dipoles. They calculated the field produced by a single NW and then for the whole array on a particular test NW.⁴⁶ In this regard, the whole 2D array can be divided in two regions. One is the nearest neighbor discrete distribution of the NWs. For longer NWs, it was seen that the field produced by it and hence the interaction with other NWs is more concentrated at the ends of the NWs, breaking its dipolar approximation. Beyond the discrete region, the NWs can be considered as continuously distributed and their effect, the same as that of a thin film. This mean field approach is more realistic to calculate the interaction at saturation taking both dipolar and non-dipolar interaction among the NWs depending on its length. It shows an increase in axial saturation field of the NWs with the length dominated by the axial interaction between the NWs whereas, the transverse saturation field decreases upon increasing the length of NWs. The field acted on a particular NW by the others opposes (antiferromagnetic-“AFM” coupling) and supports (ferromagnetic-“FM” coupling) the magnetization along the axial and transverse direction respectively. The interaction field strength along the transverse direction is half of the axial direction. However, these models are valid throughout the hysteresis for the flower state (point dipoles are parallel to each other) of the NWs at remanence but not for vortex state.

1.4 Objective of the work

The magnetic properties of a single cylindrical shaped NW are difficult to investigate in detail unambiguously due to small dimension of the NWs which in turn limits the performance of the measuring instruments. However, attempts were made in

order to investigate the magnetic hysteresis loops of single cylindrical shaped NW using micro-SQUID instruments.⁴⁷ Study on template grown NWs is an alternate way to investigate the NWs as it is possible to tailor the NW diameter, inter-wire separation etc. by changing the template's geometrical parameters. If once the ceramic porous membranes can be synthesized successfully with high accuracy, then it is very easy and cost effective to make 2D arrays of NWs with various dimensions repeatedly using the membranes. The approximate results of single NW can be found by increasing the inter-pore separation of the membranes. Here in this work, we prepared and investigate several NWs of different materials using commercial membranes. Later we tried to synthesize alumina membranes by ourselves and got successive success. We also tried to synthesize cylindrical hollow nanotubes. But as beginner in the field of wire-shaped nanomaterials, we hoped at the start of our work that, study of wire-shaped microwires can make us comfortable and help us to understand the domain structures and magnetic properties of wire-shaped nanowires. Magnetic properties of MWs can change by inducing various anisotropies such as applying stress or annealing under different conditions. These studies can throw light on the domain structure of the MWs. Hence, we planned to study first the magnetic properties of amorphous MWs in presence of stress and after passing short duration current pulse through the MWs.

We started the study of NWs of ferromagnetic elements such as Ni, Co. The physical and structural properties are needed to investigate first to get a flavor of the system. With the change in aspect ratio at different NWs diameters and inter wire spacings, how the magnetization of the arrays of NWs changes that remained one of our goals. These studies are important for their use in high density storage media. Co rich alloy NWs are recently used for perpendicular storage materials. High coercive NWs are one of the prime needs to achieve the goal. In this regard extensive research is going on for alloy NWs, e.g. CoPt, FePt alloy NWs.⁴⁸⁻⁵⁰ Lithographically made single planar NWs (squared cross section) are studied by magneto optical Kerr signal measurements and electrical measurements to study the domain wall dynamics in NWs in the interest of spintronics systems.¹²⁻¹⁵ We tried to study the magnetization of isolated cylindrical Ni NWs as the similar study has been performed for planar NWs. Alumina membrane is the starting material of synthesizing NWs. Controlled

electrochemical anodization of aluminum leads to the formation of porous alumina oxide membrane. Within the scope of the thesis, we also tried to synthesize highly ordered porous alumina membranes. Permalloy NWs are found to be probed easily for DW dynamics study as it has significant anisotropic magneto-resistance.⁵¹ Hence, the preparation and study of permalloy NWs is the other goal of the work. Nanotubes are another interesting nanostructure as it has unique magnetic properties different from NWs and give the possibility to produce core shell nanowires. Nanotubes exhibit a core-free magnetic configuration leading to uniform switching fields, guaranteeing reproducibility^{52, 53} and due to their low density they can float in solutions making them suitable for applications in biotechnology.⁵⁴ Proper synthesis of NTs is critical what we have also tried in the thesis.

1.5 Outline of the thesis

In this thesis we report magnetization study of ferromagnetic amorphous alloy (cobalt rich) microwires (MWs) under different stressed and current pulse annealed conditions. Whereas, geometrical and crystal structure along with magnetization process of two dimensional (2D) arrays of cobalt, nickel, cobalt-platinum alloy nanowires (NWs) are investigated in detail. NWs are grown within the pores of commercially purchased alumina and polycarbonate membranes. However, it is possible to synthesize the alumina membranes in laboratory. An elaborate description of the synthesis technique and homemade alumina membranes are given at the beginning of the thesis. In addition, synthesis of nickel-iron alloy NWs and nickel nanotubes (NTs) are described briefly at the end of the thesis.

Glass coated alloy MWs with two different compositions are received from Instituto de Magnetismo Aplicado, Madrid, Spain. The compositions of the alloys are $\text{Co}_{83.2}\text{Mn}_{7.6}\text{Si}_{5.8}\text{B}_{3.3}$ and $(\text{Co}_{0.93}\text{Fe}_{0.07})_{63}\text{Ni}_{10}\text{Si}_{11}\text{B}_{16}$ and are amorphous in nature. Surface morphology of the MWs is studied by electron microscope and confirms the uniform diameter (~ 14 & 20 μm respectively) of the alloy cores with a glass coating (~ 5.5 μm) on the surface of the cores of MWs. The MWs are several centimeter long and

free of corrosion due to the glass coating. DC magnetic hysteresis loops of the MWs are recorded under different stressed conditions and after passing short current pulses through the MWs. Observed experimental results are in accordance with the inner single domain core surrounded by outer multi domain shell structure of the alloy cores of MWs.

Two dimensional arrays of ferromagnetic NWs of Co, Ni and CoPt are successfully synthesized within the pores of alumina and polycarbonate membranes by DC electrodeposition technique. NWs have diameters typically ranges from 50 to 275 nm and are several microns long. Surface morphological characterizations of the NWs indicate uniform length of the NWs throughout the membranes. Ni NWs show fcc crystalline phase. However, Co NWs have hcp phase and upon decreasing the wire diameter, Co NWs become more crystalline. Thermal annealing changes the crystalline phase of $\text{Co}_{0.5}\text{Pt}_{0.5}$ NWs from fcc to L1_0 fct phase. In order to better understand the annealing effect in arrays of CoPt NWs in a better way, a comparative study on CoPt nanoparticles (NPs) has been done. The NPs are prepared in micellar media synthesized by chemical process and have an average particle size of ~ 6 nm.

Magnetization study of the arrays of NWs are performed using vibrating sample magnetometer (VSM) and superconducting quantum interference device (SQUID) indicates strong magnetostatic interaction among the NWs which dominate over the other anisotropies (e.g. shape, magnetocrystalline) of the NWs. In most of the cases, the interaction makes the transverse direction of the NWs as easy direction of magnetization. Whereas in case of arrays of Co NWs with diameter 50 and 150 nm, we observe a directional change of magnetic easy axis of the NWs from axial to the transverse direction of the NWs upon increasing their length. The observed directional change of easy axis in 50 nm Co NWs is in accordance with the dipolar interaction model of interacting NWs. But, the 150 nm NWs does not follow the dipolar interaction model as observed in static hysteresis loop measurements and in their dynamic response measurements probed by ferromagnetic resonance (FMR) measurements. We conclude that, the magnetostatic interaction among the NWs is not dipolar in nature at all the circumstances which need a rigorous theoretical formulation.

Magnetic hysteresis loops of three isolated Ni NWs with diameter 300 nm are measured successfully by magneto optical Kerr signal measurement. Experimental observation indicates the easy axis of the NWs along their length i.e. opposite to the case of arrays of the NWs. Here, the shape of the hysteresis loop is determined by the shape anisotropy of the NWs.

Magnetization study of thermally annealed 2D arrays of $\text{Co}_{0.5}\text{Pt}_{0.5}$ NWs show enhanced coercivity of ~ 6.4 kOe compared to the as prepared NWs (~ 500 Oe). Comparatively, the thermally annealed $\text{Co}_{0.5}\text{Pt}_{0.5}$ NPs show an enhanced coercivity of ~ 4.4 kOe. Observed experimental facts indicate stress development on the NWs by alumina matrix during annealing and the enhanced coercivities are the consequence of large magnetocrystalline anisotropy of the nanostructures.

We synthesize highly ordered porous alumina membranes by two step anodization technique with an average pore diameter of ~ 50 and 70 nm. We anodize thin sheet of 99.99% pure aluminum in various acidic electrolyte solutions. The arrangements of the pores are highly ordered and upon proper post treatment of the porous oxide layers, the hexagonal cell structures are observed in the membranes. The removal of aluminum base using mercury chloride solution is critical to open the pores and obtain a smooth surface at the back side of oxide membranes which is ideal for electrodeposition of metal NWs. At our early stage of research on the membranes, ZnO NWs are successfully grown chemically within the pores of the membranes in order to investigate the magnetic properties of the NWs.

Arrays of FeNi alloy NWs with diameter 50 & 200 nm are prepared in porous alumina template by DC electrodeposition technique. The NWs are very uniform in length throughout the membranes whereas the compositions of the NWs are confirmed by energy dispersive X-ray analysis. X-ray diffraction pattern indicates fcc crystalline phase of the NWs. Ni NTs are prepared by slow deposition of Ni^{2+} ions within the pores (pore diameter ~ 200 nm) of alumina template. Surface morphological study of the NTs done by electron microscopes confirms the hollow cylindrical structures of the NTs.

Bibliography

- [1] Squire, P. T., Atkinson, D., Gibbs, M.R.J. and Atalay S., *J. Magn. Magn. Mater.* **132**, 10 (1994).
- [2] Vazquez, M. and Hernando, A., *Phys. D: Appl. Phys.* **29**, 939–949 (1996).
- [3] Mitra, A. and Vazquez, M. *J. Phys. D: Appl. Phys.* **23**, 228 (1990).
- [4] Panina, L.V. and Mohri, K. *Appl. Phys. Lett.* **65**, 1189 (1994).
- [5] Vazquez, M. and Adenot-Engelvin, A.-L., *J. Magn. Magn. Mater.*, **321**, 2066–2073(2009)
- [6] A. Aharoni, *Introduction to the Theory of Ferromagnetism*, second ed., Oxford University Press, Oxford, 2000
- [7] Ulitovsky, A. V. *Pribory I Technika Eksperimenta* **3**, 115 (1957).
- [8] Kavesh, S. US Patent 3 960 200 (1976).
- [9] Taylor, G. F. *Phys. Rev.* **23**, 665 (1924).
- [10] Pirota et. al. *Adv. Func. Mater.* **14**, 226 (2004).
- [11] Y. Wu, K. Li, J. Qiu, Z. Guo, and G. Han, *Appl. Phys. Lett.* **80**, 4413 (2002); M. Albrecht, A. Moser, C. T. Rettner, S. Anders, T. Thomson, and B. D. Terris, *Appl. Phys. Lett.* **80**,3409 (2002);
- [12] Jung, H. S., Kuo, M., Malhotra, S. S. and Bertero, G., *Appl. Phys. Lett.* **91**, 212502 (2007); Shamaila, S., Liu, D. P., Sharif, R., Chen, J. Y., Liu, H. R. and Han, X. F., *Appl. Phys. Lett.* **94**, 203101-1 (2009).
- [13] Mourachkine, A., Yazyev, O. V., Ducati, C. and Ansermet, J. -Ph., *Nano Letts.* **8** (11) 3683 (2008).
- [14] Yan, M., Kákay, A., Gliga, S. and Hertel, R., *Phys. Rev. Lett.* **104**, 057201 (2010).

- [15] Boone, C. T., Katine, J.A., Carey, M., Childress, J. R., Cheng, X. and Krivorotov, I.N., Phys. Rev. Lett. **104**, 097203 (2010).
- [16] Tretiakov, O.A., Liu, Y. and Abanov, Ar., Phys. Rev. Lett. **105**, 217203 (2010).
- [17] Sun, Z. Z. and Schliemann, J., Phys. Rev. Lett. **104**, 037206 (2010).
- [18] Perkin, S. S. P., Hayashi, M., Thomas, L., Science **320**, 190 (2008).
- [19] Hayashi, M., Thomas, L., Rettner, C., Moriya, R. and Perkin, S. S. P., Nature Physics **3** 21 (2007).
- [20] Martin, J.I., Nogues, J., Liu, K., Vicent, J.L., Schuller, I. K., J. Magn. Magn. Mater. **256**, 449–501(2003).
- [21] Schwarzacher, W., Attenborough, K., Michel, A., Nabiyouni, G. and Meier, J.P., J. Magn. Magn. Mater. **165** 23-29(1997); Piraux, L., George, J. M., Despres, J. F., Leroy, C., Ferain, E., Legras, R., Ounadjela, K. and Fert, A., Appl. Phys. Lett. **65**, 2484 (1994).
- [22] Martin, J.I., Nogues, J., Liu, K., Vicent, J.L., Schuller, I. K., J. Magn. Magn. Mater. **256**, 449–501(2003).
- [23] George, E. P., Rev. Sci. Instrum. **41**, 772 (1970).
- [24] Kawai, S. and Ueda, R., J. Electrochem. Soc. **122**, 32-36 (1975).
- [25] Tsuya, N., Saito, Y., Nakamura, H., Hayano, S., Furugohri, A., Ohta, K., Wakui, Y. & Tokushima, T. J. Magn. Magn. Mater., **54**, 1681-1682 (1986).
- [26] Huysmans, G. T. A., Lodder, J. C. & Wakui, J., J. Appl. Phys., **64**, 2016-2021 (1988).
- [27] Zhang, L. C. & Lodder, J. C., J. Magn. Magn. Mater., **88**, 236-246 (1990).
- [28] Whitney, T. M., Jiang, J. S., Searson, P. C., Chien, C. L., Science **261**, 1316 (1993).

- [29] Fischer, B. E. and Spohr, D., *Rev. Mod. Phys.* **55**, 907 (1983); Fleischer, R. L., Price, P. B., Walker, R. M., *Nuclear Tracks in Solids - Principles and Applications* (Univ. of California Press, Berkeley, 1975).
- [30] Masuda, H. and Fukuda, K., *Science* **268**, 1466 (1995).
- [31] Sellmyer, D. J., Zheng, M. and Skomski, R., *J. Phys.: Condens. Matter* **13**, R433–R460 (2001); Sugawara, A., Streblechenko, D., McCartney, M. and Scheinfein, M. R., *IEEE Trans. Magn.* **34**, 1081(1998).
- [32] Cullity, B. D. and Graham, C. D., *Introduction to magnetic materials*, 2nd Edition, Wiley-IEEE Press, November 2008.
- [33] Reininger, T., Kronmüller, H., Gómez-Polo, C. and Vázquez, M., *J. Appl. Phys.*, **73**, 5357 (1993).
- [34] Frei, E. H., Shtrikman, S. and Treves, D., *Phys. Rev.* **106**, 446 (1957).
- [35] Bryant, P. and Suhl, H., *Appl. Phys. Lett.* **54** (1) 78 (1988).
- [36] Aharoni, A., *J. Appl. Phys* **68** (6) 2892 (1990).
- [37] Ross, C. A., Farhoud, M., Hwang, M., Smith, I. H., Redjdal, M. and Humphrey, F. B., *J. Appl. Phys.* **89**, 1310.(2001).
- [38] Ross, C.A., Hwang, M., Shima, M., Smith, H. I., Farhoud, M., Savas, T.A., Schwarzacher, W., Parrochond, J., Escoffier, W., Neal Bertram, H., Humphrey, F.B., Redjdal, M., *J. Magn. Magn. Mater.* **249**, 200–207 (2002); Ross, C. A., Haratani, S., Castan, F. J., Hao, Y., Hwang, M., Shima, M., Cheng, J. Y., Vogeli, B., Farhoud, M., Walsh, M., and Smith, H. I., *J. App. Phys.* **91**(10), 6848 (2002).
- [39] Bogdanov, A. N., Rößler, U. K., Müller, K. -H., *J. Magn. Magn. Mater.* **242-245**, 594-596 (2002).
- [40] Aharoni, A., *J. Appl. Phys.* , **82**, 1281-7(1997).
- [41] Rosler, U. K., Bogdanov, A. N. and Müller, K. -H., *IEEE Trans. Magn.* **38** (5) 2586 (2002).

- [42] Jackson, J. D., *Classical Electrodynamics*, Jhon Wiley & Sons, Inc. (1999).
- [43] Grimsditch, M., Jaccard, Y. and Schuller, I.K., *Phys. Rev. B* **58**(17), 11539 (1998).
- [44] Rivas, J., Kazadi, A., Bantu, M., Zaragoza, G., Blanco, M.C., Lopez-Quintela, M. A., *J. Magn. Magn. Mater.* **249** 220-227 (2002) ; Sánchez-Barriga, J., Lucas, M., Radu, F., Martin, E., Multigner, M., Marin, P., Hernando, A. and Rivero, G., *Phys. Rev. B* **80**, 184424 (2009) ; Encinas-Oropesa, A., Demand, M., Piraux, L., Huynen, I., Ebels, U., *Phys. Rev. B* **63**, 104415 (2001).
- [45] Raposo, V., Garcia, J.M., Gonzalez, J.M., Vazquez, M., *J. Magn. Magn. Mater.* **222**, 227-232 (2000).
- [46] Clime, L., Ciureanu, P. and Yelon, A., *J. Magn. Magn. Mater.* **297**, 60-70 (2006).
- [47] Wernsdorfer, W., Doudin, B., Maily, D., Hasselbach, K., Benoit, A., Meier, J., Ansermet, J. P. and Barbara, B., *Phys. Rev. Lett.* **77**, 1873 (1996).
- [48] D. Weller, A. Moser, L. Folks, M. E. Best, W. Lee, M. F. Toney, M. Schwickert, J. U. Thiele and M. F. Doerner, *IEEE Trans. Magn.* **36**, 10 (2000).
- [49] T. Shimatsu, J. C. Lodder, Y. Sugita, and Y. Nakamura, *IEEE Trans. Magn.* **35**, 2697 (1999).
- [50] Jeremy Mallet, K. Yu-Zhang, Chia-Ling Chien, Tom S. Eagleton and Peter C. Searson, *Appl. Phys. Lett.* **84**, 19, 3900 (2004).
- [41] D. Atkinson et al. , *Nature Mater.* **2**, 85 (2003).
- [52] Z. K. Wang, H. S. Lim, H. Y. Liu, S. C. Ng, M. H. Kuok, L. L. Tay, D. J. Lockwood, M. G. Cottam, K. L. Hobbs, P. R. Larson, J. C. Keay, G. D. Lian, and M. B. Johnson, *Phys. Rev. Lett.* **94**, 137208 (2005).
- [53] J. Escrig, P. Landeros, D. Altbir, E. E. Vogel, and P. Vargas, *J. Magn. Magn. Mater.* **308**, 233 (2007).
- [54] K. Nielsch, F. J. Castaño, C. A. Ross, and R. Krishnan, *J. Appl. Phys.* **98**, 034318 (2005).

Chapter 2

Experimental Details

2.1 Preamble

In this chapter, we elaborate various experimental set-ups employed to synthesize the nanostructures along with their characterization processes that are used during the investigations presented in this thesis work. We develop homemade set-ups to synthesize the porous alumina membranes and nanoparticles (NPs). While the nanowires (NWs), nanotubes (NTs) are synthesized employing a commercial electrochemical cell. Thermal evaporation and RF (radio frequency) sputtering techniques to prepare gold thin films on alumina membranes and Si/SiO₂ substrates are described in detail.

The structural and phase characterizations of the samples are done using SEM, FESEM, TEM, HRTEM, EDX, SAED and XRD. The magnetic characterizations are carried out employing MFM, VSM, SQUID-VSM, FMR magnetometer and using a MOKE set-up. The detail of lithography process that is used to make the patterns on Si/SiO₂ substrate for MOKE samples is described here as well.

2.2 Synthesis techniques

2.2.1 Electrochemical anodization

Electrochemical anodization is a simple and elegant way to synthesize porous oxide films on a conducting metal surface such as aluminum (Al).¹⁻³ We engineer porous alumina membranes in our laboratory by two step anodization of pure

aluminum using a homemade electrochemical cell set-up. The schematic diagram of the set-up is shown in Fig. 2.1. The cell consisted of two electrodes: *Cathode* - a thin (~ 1 mm thick) copper (Cu) sheet connected to the negative terminal of a power supply

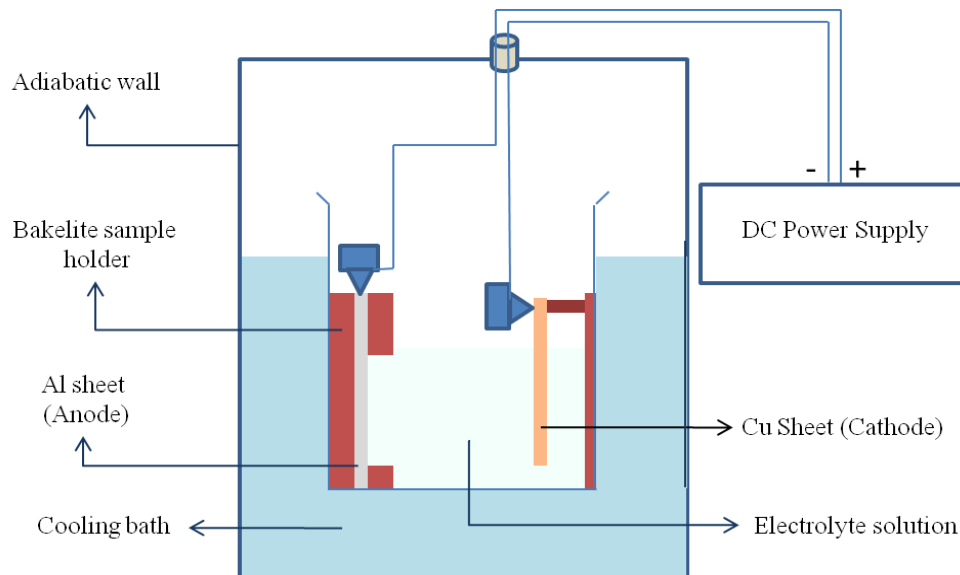


Figure 2.1. Schematic diagram of the experimental set-up for anodization of thin aluminum sheet.



Figure 2.2. Experimental set-up of the anodization of thin aluminum sheet (left), a close view of the electrochemical cell consisting of cathode: Cu ribbon and anode: thin Al sheet inside the bakelite structure (right-top) and a close view of the bakelite structure (right-bottom).

and *Anode* – a thin ($\sim 130 \mu\text{m}$ thick) aluminum (Al) sheet connected to the positive terminal of the power supply. The Cu sheet is connected with the negative terminal of the power supply. The experimental set-up that is developed in our laboratory is shown in Fig. 2.2. The back side and selected portion of front side of the Al sheet is covered by Bakelite to restrict the growth of oxide film only to a selected area on the front side of Al sheet as shown in Fig. 2.2.

Under a suitable constant potential difference across the electrodes, thin porous oxide film starts to grow over the aluminum surface.⁴ In our case we maintained a potential difference within the range of 60 V to 64 V to maintain a constant current density of $\sim 2 \text{ mA} / \text{cm}^2$ across the electrodes. The voltage drops across the electrodes changes with the anodization time due to the growth of non-conducting oxide layer on the aluminum surface.

The growth mechanism and details of synthesized alumina membranes are described in *chapter 4*. The conversion of aluminum in to alumina film on the Al surface is an exothermic reaction. Depending upon suitable choice of electrolyte solution and under a typical potential difference, porous type oxide film develops during the anodization process. The porous oxide film growth with uniform pore distribution is attributed to the thermally assisted, field accelerated dissolution of oxide at the base of pores. This dissolution of oxide layer at pore bottom and formation of new oxide layer at metal/oxide interface needs to maintain a dynamic equilibrium.⁵ In order to attain the equilibrium we maintain a constant temperature of $11 \text{ }^\circ\text{C}$ by immersing the cell in a temperature bath.

2.2.2 Electrodeposition of NWs and NTs

Electrodeposition technique is a cost effective and relatively simple process to synthesize nano-structures compared to the lithography processes e.g. optical, electron beam, ion beam lithography etc.⁶ We employed a commercial set-up (Autolab) in order to prepare ferromagnetic NWs and NTs within the nano pores (diameter ~ 50 – 300 nm) of alumina and polycarbonate membranes having thickness of ~ 5 and 60 μm respectively.

The set-up consists of an electrochemical cell and a power supply. Schematic diagram of the set-up is shown in Fig. 2.3. The electrochemical cell consists of three electrodes: *working*, *counter* and *reference electrodes*. The working electrode is generally the substrates on which the required electrochemical depositions are carried out. To deposit the metal ions in the pores of membranes in order to synthesize NWs and NTs, we use the membrane as a working electrode. One side of the membranes is therefore coated with a conductive gold layer of ~ 100 nm thickness by RF sputtering technique. In case of metal deposition from the aqueous solutions of their salts, the working electrode is connected to the negative terminal of the power supply.

During the deposition, the electrochemical reaction is carried out between the working and counter electrodes. We use either a gold or a platinum wire as the counter electrode having the purity of ~ 99.99% commercially purchased from sigma-aldrich.⁷ The reference electrode is a Ag/AgCl calomel electrode that is used to measure the other electrode potentials with respect to it. The set-up used in our laboratory is shown in Fig.2.4. The cell has the volume capacity of ~ 20 cm^3 for the electrolyte solutions.

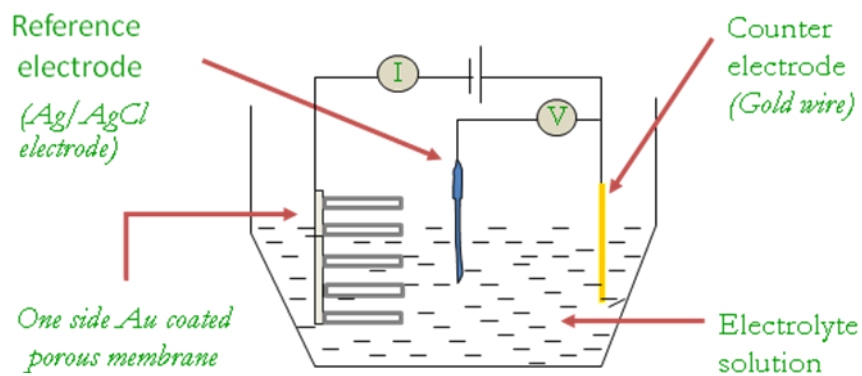


Figure 2.3. Schematic diagram of three electrode electrochemical cell used to deposit NWs and NTs in alumina membranes.

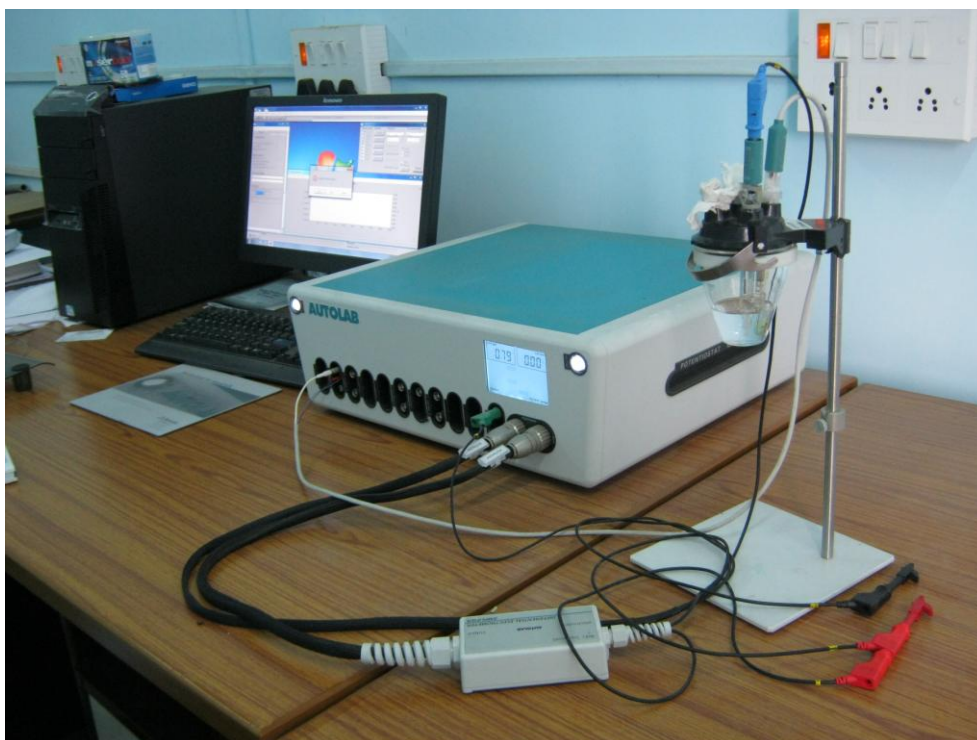


Figure 2.4. Electrodeposition set-up used to deposit NWs and NTs

NWs and NTs are deposited in the pores of alumina membranes by choosing typical potential of corresponding depositions from linear sweep voltametry (LSV). The LSV gives us a *voltage versus current* profile for a particular electrolyte solution for a particular choice of electrodes. LSV scanned between 0 to -1.5 is presented in Fig. 2.5. Up to a certain value of the applied voltage, the current remain near zero value with the increase in voltage indicating no deposition of cations at cathode. After which the current suddenly increases and attain a maximum value followed by saturation. The sudden increase in current indicates metal ion deposition at cathode. Simultaneously, the pH value of the solution during the LSV scan is also recorded. The pH graph shows a spike near the potential where the sudden jump in current value has started. We choose a potential of deposition just after the pH spike and very near to the start of the jump in current value. Choosing higher potentials may incorporate foreign ions (e.g) depositions and hence avoided.

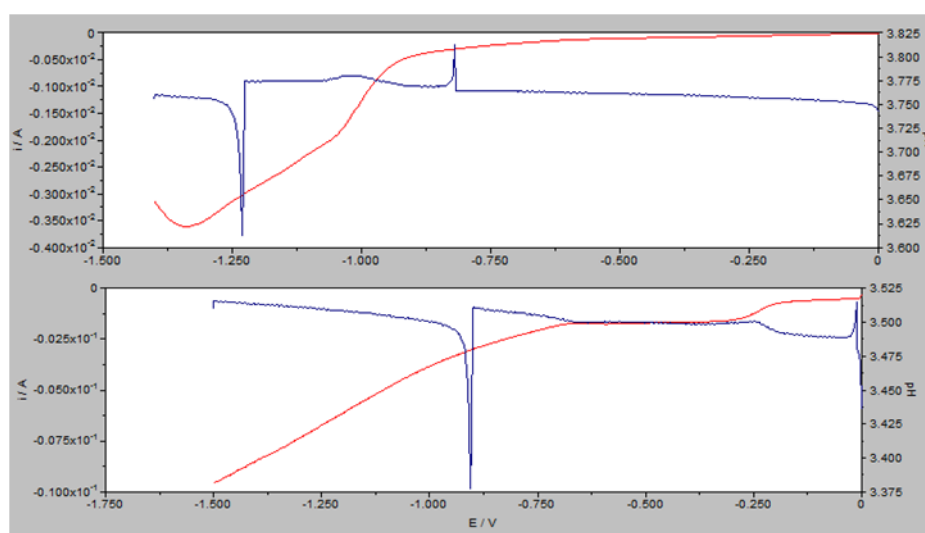


Figure 2.5. LSV profile for typical Ni (top), Co (bottom) NWs deposition in porous alumina template.

Formation of NWs is the consequence of metal ions depositions on gold thin film at the pore bottoms in the nano channels of the membranes. Usually higher rate of ion deposition leads to formation of NW whereas the lower rate leads to NT formation within the nano channels. We prepare Ni and Co NWs under the constant potential of

~ 0.85, 0.9 V respectively (see Fig. 2.5). Details of all the NWs including NiFe alloy NWs and Ni NTs are described elaborately in the following chapters of the thesis.

2.2.3 Thermal deposition

Thermal evaporation is a technique commonly used to deposit thin films of metals. The metal source is heated up to evaporate in a vacuum chamber that maintains a pressure of $\sim 10^{-6}$ mbar. At an elevated temperature, the thermal energy of surface atoms of the metal becomes greater than the binding energy of the same and they become free from the metal surface. Under such high vacuum atmosphere the typical mean free paths of the evaporated particles are in the range of few meters. That large mean free path allows the particles (atoms/molecules) to travel to the target object (substrate) where they deposited. On the substrate, the deposited particles lower their energy through the dissipation of heat and make a thin film of the source material. Generally a diffusion pump is employed to achieve such high vacuum within the chamber to extract all unwanted gaseous particles within the chamber. However, hot objects within the chamber (e.g. heating filament, molybdenum boat in our case) produce unwanted vapors that limit the quality of the vacuum. A cooling system is employed to keep the chamber and substrate holder temperature at normal.

In case of metallic oxide thin film deposition, the deposition is carried out in the presence of oxygen so that the metal can react to produce oxide film. Perhaps, the oxygen atoms can collide with the metallic particles within the chamber and reduce the amount of vapor that reaches the substrate. The quality of the film (i.e. uniformity in thickness, contamination free) is mostly depending on the quality of vacuum within the chamber and the quality of the substrate on which the film is deposited. As the evaporated materials approach the substrate from a particular direction, the rough surface of the substrate thus leads a non uniform deposition of thin film. A schematic diagram of the set-up is shown below in Fig. 2.6.

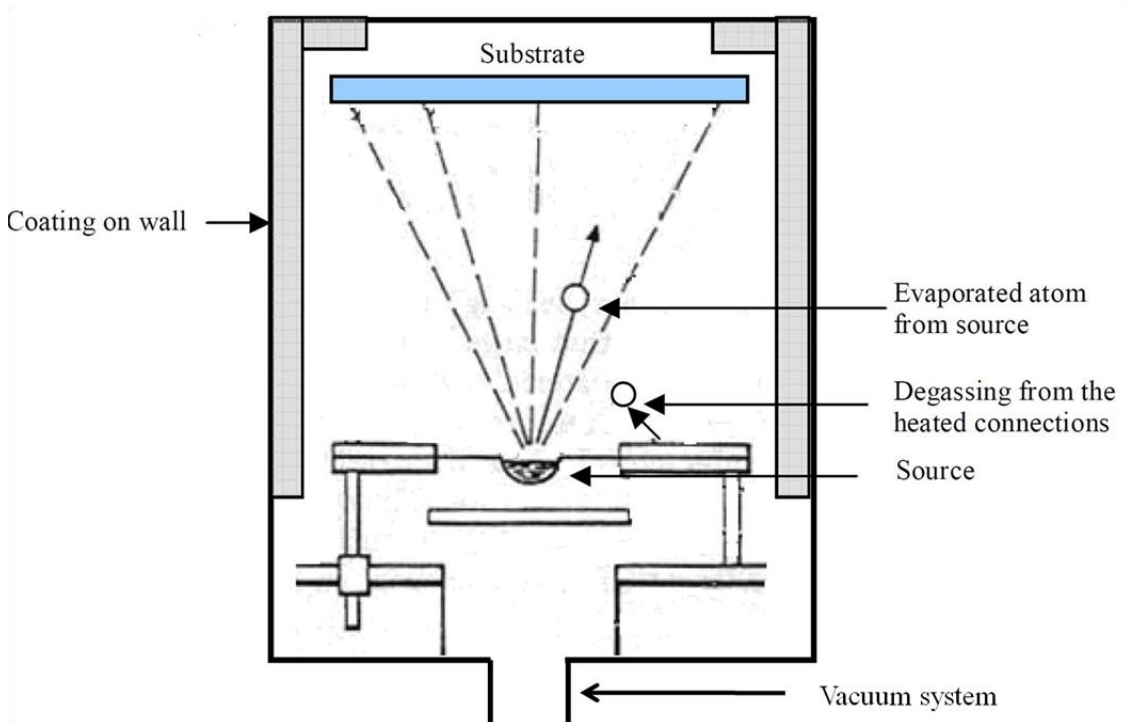


Figure 2.6. Schematic diagram of thermal evaporation.

2.2.4 Sputtering deposition

DC (direct current) Sputter deposition is a physical vapor deposition process for depositing thin films of metals. Sputtering means ejecting material from a target and depositing it on a substrate. Fig. 2.7 shows the schematic diagram of a sputter deposition system. The target is the source material. Substrates are placed in a vacuum chamber and are pumped down to a prescribed process pressure. Prior to the sputtering coating process a vacuum of $\sim 10^{-5}$ mbar must be achieved. Once the appropriate pressure has been reached a controlled flow of an inert gas such as argon is introduced. Sputtering starts when a potential difference is applied between the target and substrate holder causing a plasma or glow discharge. The negative terminal is connected to the target material. Positive charged gas ions generated in the plasma region are attracted

to the negatively biased target plate at a very high speed. This collision creates a momentum transfer and can eject atomic size particles from the target.

If the energy transferred to a lattice site is greater than the binding energy, primary recoil atoms can be created which can collide with other atoms and distribute their energy via collision cascades. A surface atom becomes sputtered if the energy transferred to it normal to the surface is larger than about three times the surface binding energy (approximately equal to the heat of sublimation). These particles are deposited as a thin film into the surface of the substrates. A schematic diagram of the deposition technique is shown below.

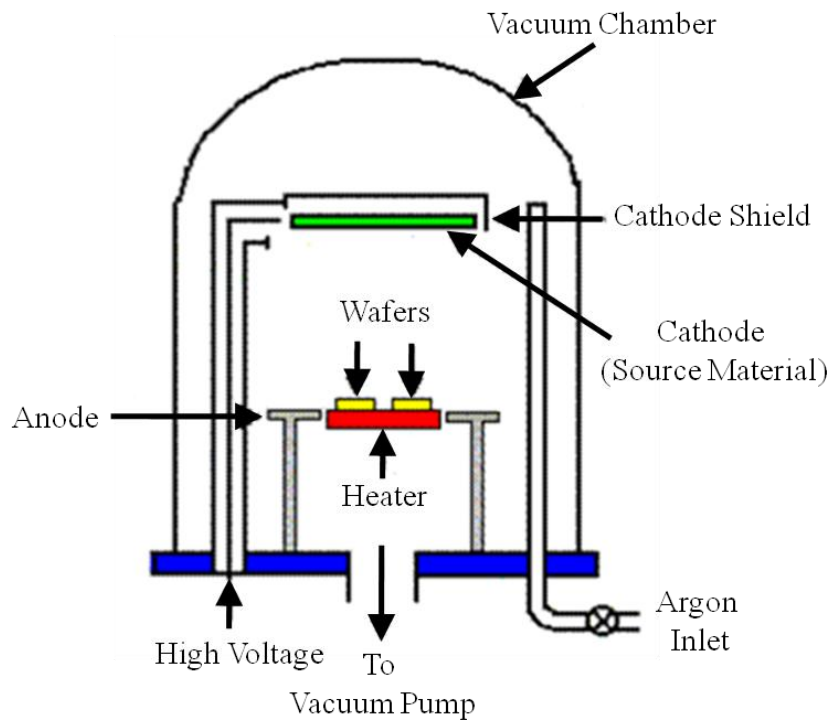


Figure 2.7. Schematic diagram of sputter deposition.

For efficient momentum transfer, the atomic weight of the sputtering gas should be close to the atomic weight of the target, so for sputtering light elements neon is preferable, while for heavy elements krypton or xenon are used. Reactive gases can also be used to sputter compounds. The compound can be formed on the target surface, in-flight or on the substrate depending on the process parameters.

Magnetron sputtering can be done either in DC or RF (radio frequency) modes. DC sputtering is done with conducting materials. If the target is a non conducting material the positive charge will build up on the material and it will stop sputtering. In such a situation, RF sputtering is employed. In magnetron sputtering which has almost no restrictions on target materials, magnets are used to increase the percentage of electrons that take part in ionization of events and thereby increase the probability of electrons striking the Argon atoms, increase the length of the electron path, and hence increase the ionization efficiency significantly.

Table 2.1 shown below is describing the differences of two deposition processes, e.g. evaporation and sputtering.

EVAPORATION	SPUTTERING
low energy atoms	high energy atoms
high vacuum path <ul style="list-style-type: none"> • few collisions • line of sight deposition • little gas in film 	low vacuum, plasma path <ul style="list-style-type: none"> • many collisions • less line of sight deposition • gas in film
larger grain size	smaller grain size
fewer grain orientations	many grain orientations
poorer adhesion	better adhesion

Table 2.1. Differences between evaporation and sputtering deposition.

2.2.5 Electron Beam (E-beam) Lithography

E-beam lithography technique uses a focused beam of electrons to create patterns on desired substrate e.g., Si wafer at sub-micrometer length scale, in contrast with optical lithography which uses light for the same purpose in creating larger patterns.^{8, 9} Electron lithography offers higher patterning resolution¹⁰ than optical lithography because of the shorter wavelength possessed by the 10-50 keV electrons that it employs. Electrons can induce the deposition of substances onto a surface

(additive), or etch away at the surface (subtractive). E-beam lithography is particularly important in micro electronics, which require extremely precise placement of micro sized circuit elements. E-beam lithography allows scientists to design and place elements at the smallest possible scale. Because electrons are charged particles, it is necessary to perform E-beam lithography inside a vacuum.

E-beam Components

Fig. 2.8 shows schematic diagram of E-beam lithography system with a detail view of electron optics used in the system. The process of E-beam lithography (EBL) is simple, however, the schematics and the parts required are quite complex. A typical EBL system mainly consists of the following parts:

- 1) An electron gun or electron source that supplies the electrons.
- 2) An electron optical column that 'shapes' and focuses the electron beam.
- 3) A mechanical stage that positions the substrate (Si wafer) under the electron beam.
- 4) A computer system that controls the equipment.

Electron Gun

The electron gun which is the centerpiece behind E-beam lithography is an apparatus that is able to “shoot” a beam of electrons in a specific direction. Two common E-beam emitters are lanthanum hexaboride crystal and a zirconium oxide coated tungsten needle. The emitter is first heated to produce and excite electrons on the surface. Then, when a high voltage is applied, the excited electrons accelerate towards a structure called the anode. By varying this voltage, the trajectory and the focus of the beam can be manipulated.

Electron Optical Column

The electron optical column is a system of lenses that, by a combination of electromagnetism and optics, has the ability to focus the electrons into a concentrated beam in a desired direction. Two parallel plates inside the column can be electrostatically charged to a precise degree; the resulting electric field is able to bend the beam in a desired direction.

The mechanical stage positions the substrate (Si wafer) under the electron beam which is automated by a computer. The computer system can control the whole equipment.

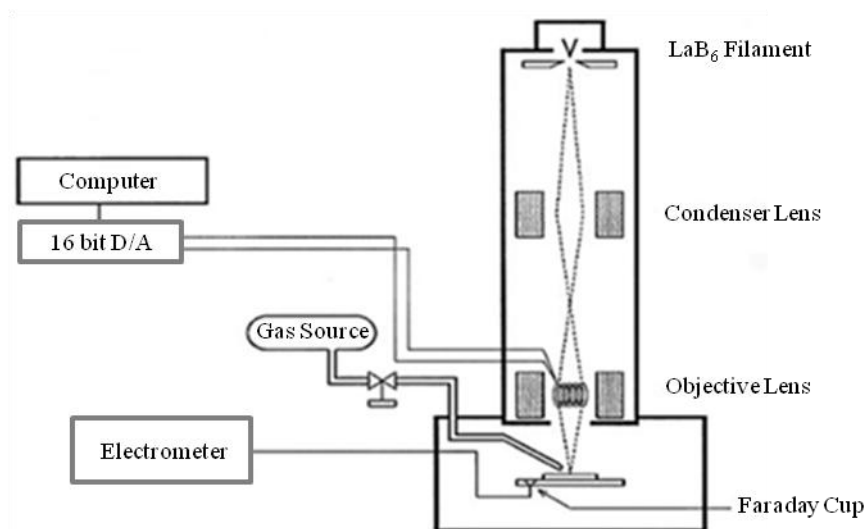


Figure 2.8. Schematic diagram of E-beam lithography system.

Substrate manipulation

After the beam is directed and concentrated by the optical column, it is ready to be focused on the surface of substrate. As with most lithography techniques, a substance called a photoresist covers the surface. However, E-beam photoresists are not as specific as other types. Technically, high energy electron bombardment will cause bond breakage in any polymer. When the beam hits the surface, either an

additive or subtractive reaction takes place as shown schematically in Fig.2.9. An additive writing method uses the electrons to induce a deposition of a compound on the surface. Subtractive writing methods use the e-beam to remove the sections of the resist and surface. This method is common in creating masks for other lithographic techniques such as UV lithography.

PMMA (poly methyl methacrylate) is the most commonly used photo-resist for E-Beam. Before exposing the Si substrate under the electron beam, a thin/thick film of PMMA is made on the wafer employing a spin coater. Knowing the film thickness for particular spin speed the film is made with desired thickness.

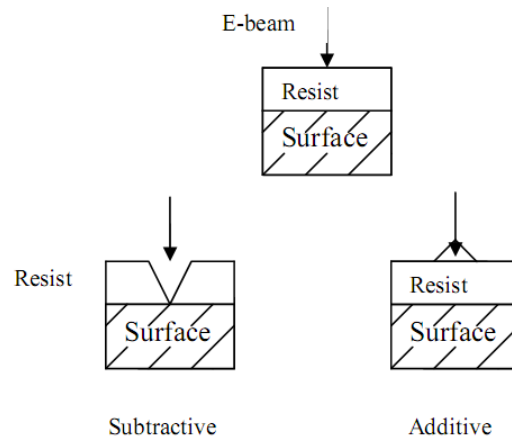


Figure 2.9. Interaction of E-beam with resist (subtractive and additive).

Scanning Methods

Raster Scan: The e-beam is swept across the entire surface, pixel by pixel, with the beam being turned on and off according to the desired pattern (see Fig.2.10). This method is easy to design and calibrate, however, because the beam is scanned across the entire surface, sparse patterns take the same amount of time to write as dense patterns, making this method inefficient for certain types of patterns.

Vector Scan: The e-beam “jumps” from one patterned area to the next, skipping unwanted areas (see Fig.2.10). This makes the vector scan much faster than the raster scan for sparse pattern writing. Adjustments to the beam can also be made relatively easily. However, it takes longer for the beam to settle, making it more difficult to maintain accurate placing for the beam.

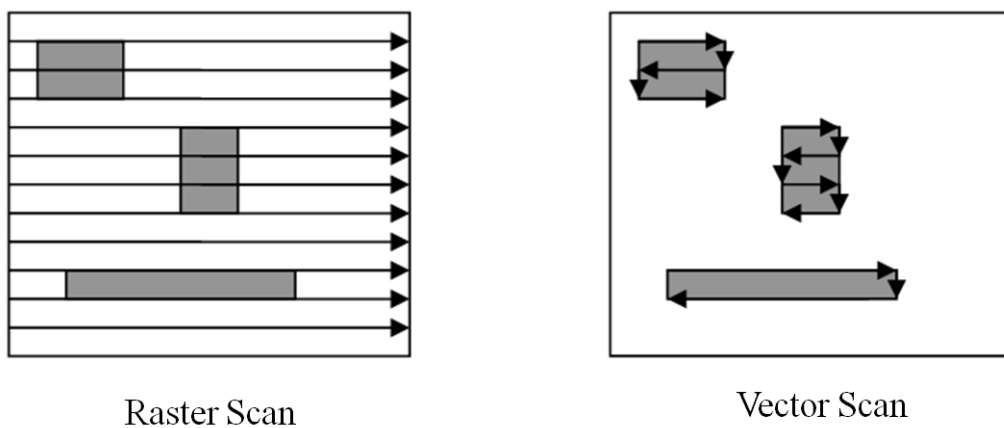


Fig.2.10. A schematic diagram of raster scan and vector scan technique.

Disadvantages

The resolution of optical lithography is limited by diffraction, but this is not a problem for electron lithography. The reason for this is the short wavelengths (0.2-0.5 angstroms) exhibited by the electrons in the energy range that they are being used by EBL systems. However, the resolution of an electron lithography system may be constrained by other factors, such as electron scattering in the resist and by various aberrations in its electron optics.

When electrons are subjected directly to a surface, they tend to “scatter” quickly. This phenomenon, known as electron backscattering,¹¹⁻¹³ causes unwanted reactions to take place outside of the focused electron beam. As a result, the resolution of an E-beam is not limited to only the size of the focused beam. In addition to

backscattering, the focused E-beam hitting the surface produces secondary electrons, which can expose the resist as much as several micrometers away from the point of exposure. These proximity effects¹⁴⁻¹⁶ can cause critical variations when dealing with surfaces that need to be exact on the submicron level.

2.2.6 Micellar technique to synthesis NPs

CoPt alloy nanoparticles with various compositions of Cobalt and Platinum are prepared by micellar technique. A micelle is an aggregate of surfactant molecules dispersed in a liquid colloid. A typical surfactant molecule has a hydrophilic head and a hydrophobic tail. While they form a spherical micelle in an aqueous solution, they aggregate their hydrophobic “tail” regions in the micelle center and the hydrophilic “head” regions in contact with surrounding solvent at the outside of the micelle. Reverse micelle is just the opposite case of micelle with hydrophobic heads in the micelle centre and hydrophilic tails at the outside in contact with the solvent. Fig. 2.11 below shows schematic diagram of a micelle and reverse micelle. By using elegant synthesis techniques, nanoparticles of different materials can be synthesized at the centre of reverse micelles.

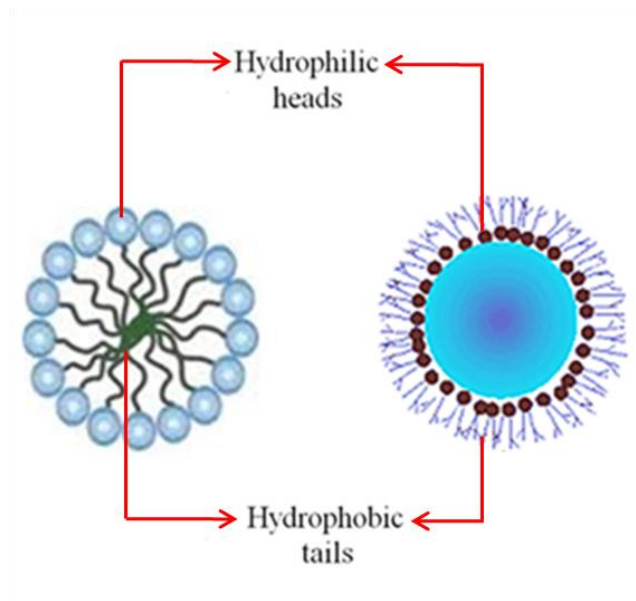


Figure 2.11. Schematic diagrams of micelle and reverse micelle.

We use all the reagents of analytical grade and purchased from Sigma-Aldrich. The water used is of Millipore grade. Cobalt sulfate and hexachloro platinate salts are used as sources of Co and Pt, respectively. These salts are taken in different ratios and are dissolved in TX-100 micellar medium under Argon atmosphere in a round bottom flask as shown in Fig 2.12. The laboratory set-up for the synthesis is shown in Fig. 2.12. The mixture is stirred for 30 min then it is heated at 80 °C. Sodium borohydride and oleic acid are added to it under stirring and heating condition. The solution turned into black after the addition of sodium borohydride. The particles are separated from the mixture by the method of centrifugation and purified by washing the particles several times by ethanol to remove TX-100 micelles. We prepare CoPt alloy nanoparticles with different ratios of Co and Pt such as Co:Pt = 90:10, 75:25, 50:50, 25:75 and 10:90 in at%. The particles are dispersed in hexane and dropped on silicon wafer to make the thicker film of all five samples. These films are subjected for heat treatment at 900 °C for 1 hour under N₂ and H₂ atmosphere and different measurements are done on the samples before and after the heat treatment to investigate the properties of the particles.

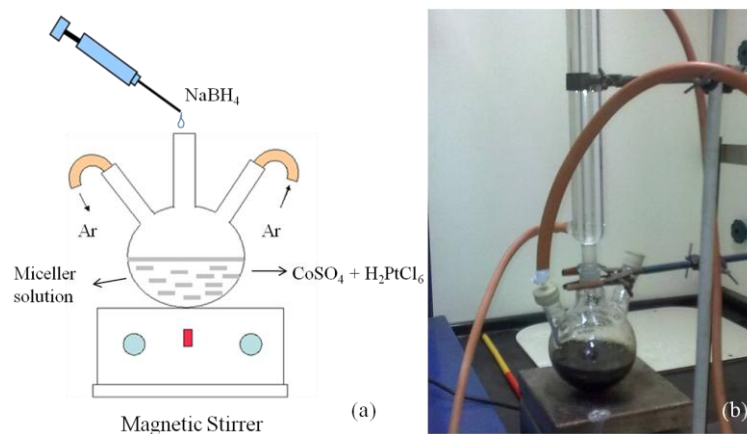


Figure 2.12. Schematic diagram of synthesis of NPs employing micellar technique (a), laboratory set-up for the synthesis (b).

2.3 Surface morphological and structural characterization techniques

2.3.1 Electron Microscopes (EMs)

Electron Microscopes are microscopic instruments that use a beam of highly energetic electrons to examine objects on a very fine scale of submicron length.¹⁷ This examination can yield information about the topography (surface features of an object), morphology (shape and size of the particles making up the object), composition (the elements and compounds that the object is composed of and the relative amounts of them) and crystallographic information (how the atoms are arranged in the object). EMs function exactly as their optical counterparts except that they use a focused beam of electrons instead of light to "image" the specimen and gain information as to its structure and composition. The Transmission Electron Microscope (TEM) was the first type of EM to be developed first in 1931 and is used to "see through" the specimen.¹⁸ However, the Scanning Electron Microscope (SEM) debuted in 1935 with the first commercial instruments around 1965.¹⁹⁻²⁰ Its late development was due to the electronics involved in "scanning" the beam of electrons across the sample.

Scanning Electron Microscope (SEM)

The basic steps involved in all EMs are the following: A stream of electrons is formed in high vacuum (by electron guns). This stream is accelerated towards the specimen (with a positive electrical potential) while is confined and focused using metal apertures and magnetic lenses into a thin, focused, monochromatic beam. It is basically similar to the electron optical column described in E-beam lithography system earlier (see Fig. 2.8). The sample is irradiated by the beam and interactions occur inside the irradiated sample, affecting the electron beam. These interactions and effects are detected and transformed into an image. The above steps are carried out in all EMs regardless of type.

In SEM (Schematically shown in Fig. 2.13), the electron beam is thermionically emitted from an electron gun fitted with a tungsten filament cathode and focused in vacuum into a fine probe that is rastered over the surface of the

specimen. The electron beam passes through scan coils and objective lens that deflect horizontally and vertically so that the beam scans the surface of the sample. SEM works on a voltage between 2 to 50kV and its beam diameter that scans the specimen is 5 nm-2 μm . Other types of electron emitters include lanthanum hexaboride (LaB_6) cathodes and field emission guns (FEG),²³ which may be of the cold-cathode type using tungsten single crystal emitters or the thermally-assisted Schottky type, using emitters of zirconium oxide. When the primary electron beam interacts with the sample, the energy exchange between the electron beam and the sample results deceleration of incident electrons through the energy dissipation and produces a variety of signals. These signals include secondary electrons, backscattered electrons, diffracted backscattered electrons, characteristic X-rays, visible light (cathodoluminescence) and heat. Secondary and backscattered electrons are conventionally separated according to their energies.²⁴ Detectors of each type of electrons are placed in the microscope in proper positions to collect them.

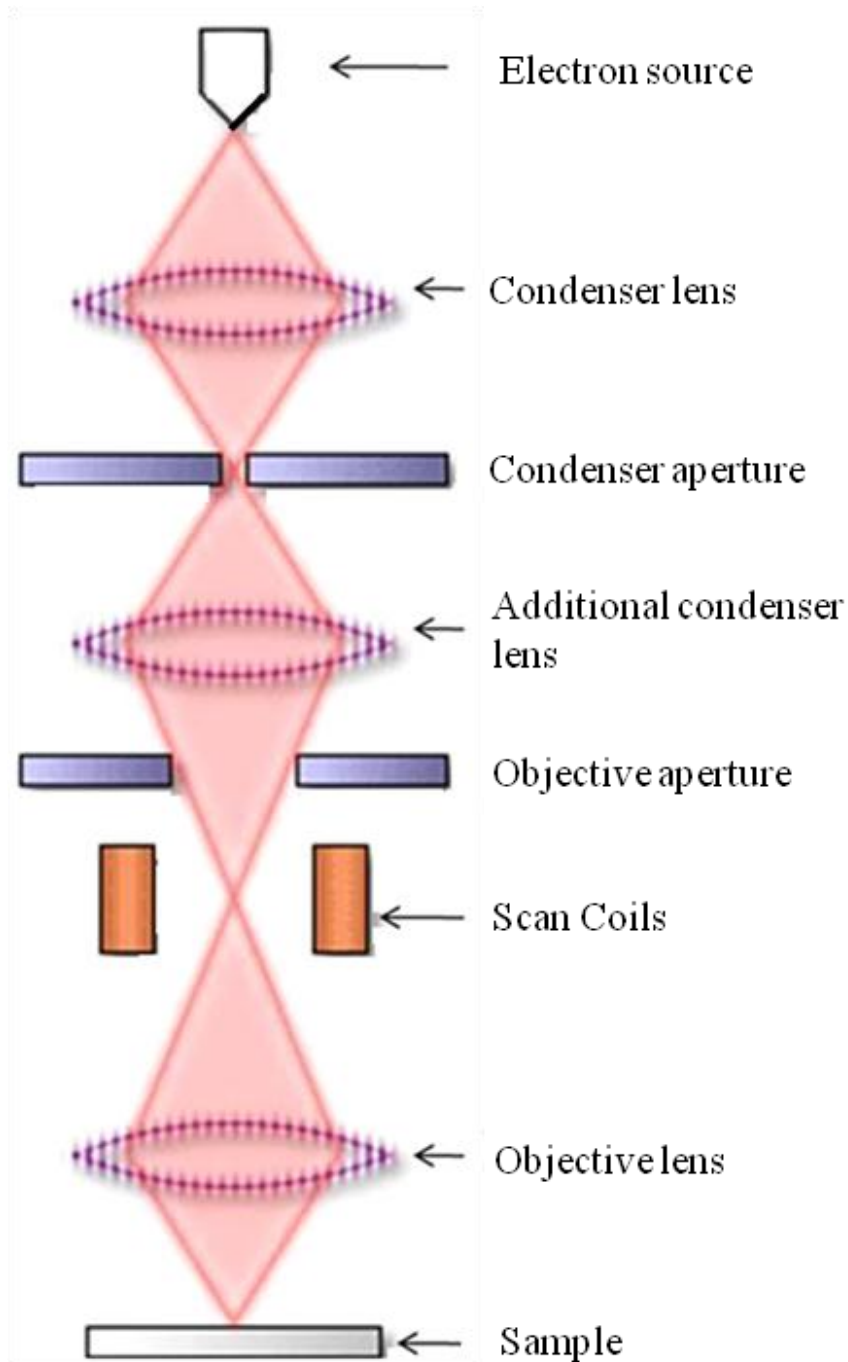


Figure 2.13. Schematic diagram FESEM shows the parts of the microscopes.

Emission of secondary electrons by inelastic scattering of incident electrons produces the SEM micrograph of the sample. Due to the very narrow electron beam, SEM micrographs have a large depth of field yielding a characteristic three-dimensional appearance useful for understanding the surface structure of a sample. Whereas, characteristic X-rays produced by inelastic collisions of the incident

electrons with electrons in discrete orbitals (shells) of atoms in the sample are used for elemental analysis. The process is known as energy dispersive analysis of X-ray (EDAX).

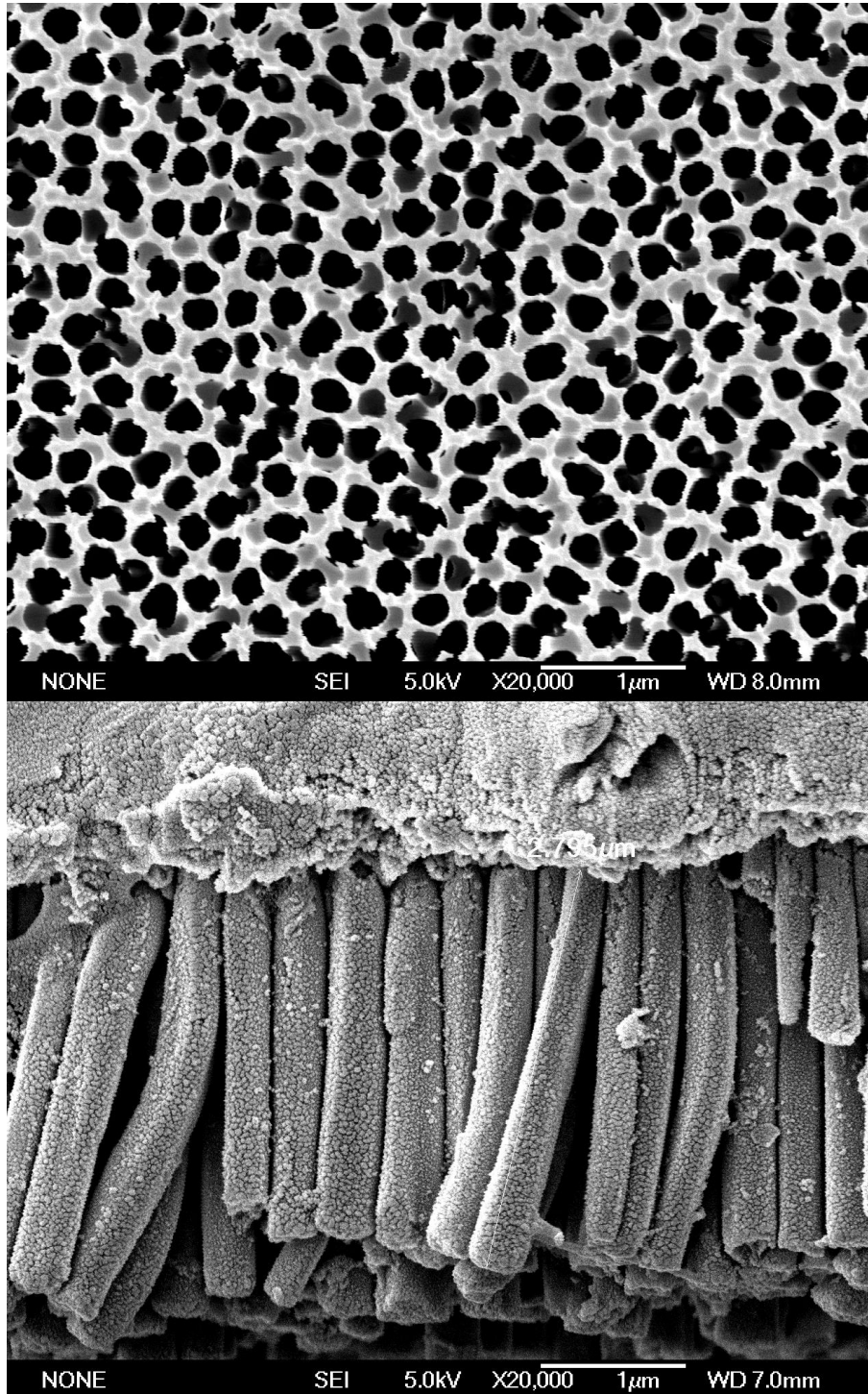


Fig.2.14. FESEM micrograph of alumina membrane (top) and Ni NWs (bottom).

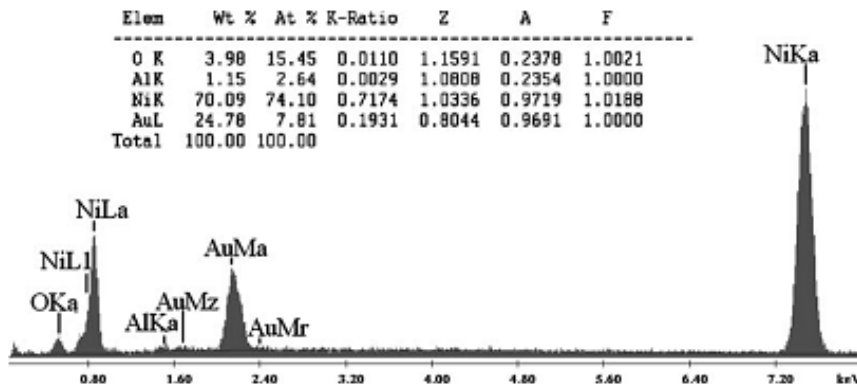


Fig.2.15. EDAX spectra obtained from Ni NWs.

A field-emission cathode in the electron gun of a SEM (FESEM) provides narrower probing beams at low as well as high electron energy, resulting in both improved spatial resolution and minimized sample charging and damage. The sample preparation include a thin gold coating on the sample (mainly for electrically non conducting samples) to avoid static charge accumulation during SEM imaging. Fig. 2.14 shows the FESEM micrographs of alumina membrane and Ni NWs. The EDAX spectrum of Ni NWs is shown in Fig. 2.15.

Transmission electron microscope (TEM)

Our use of TEM mainly exploits two different interactions of electron beam-specimen; unscattered electrons (transmitted beam) and elastically scattered electrons (diffracted beam). Schematic diagram of a TEM is shown in Fig. 2.16.

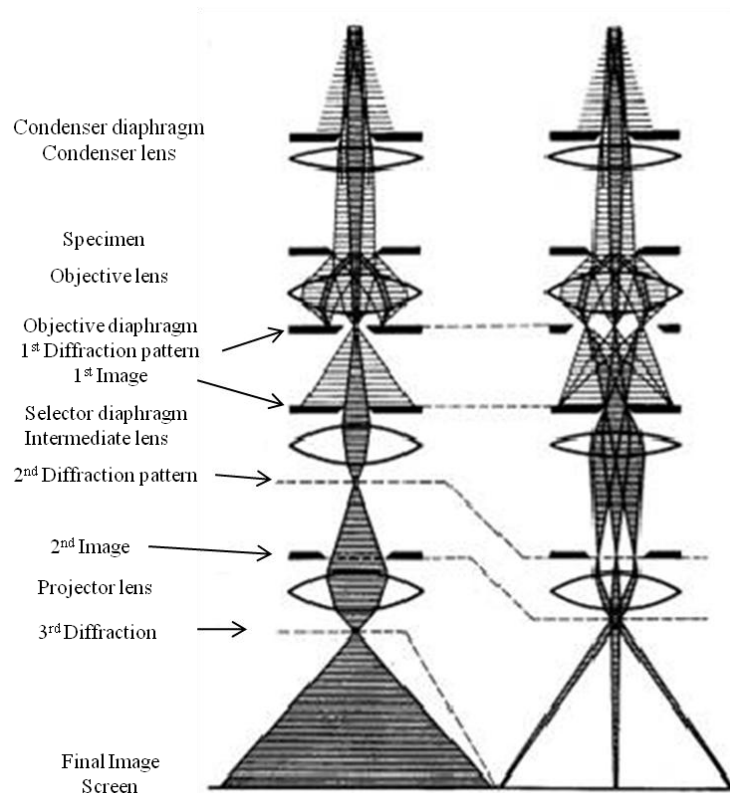


Figure 2.16. Schematic diagram of electron optics of a TEM.

In case of transmitted beam, incident electrons are transmitted through the thin specimen without any interaction occurring inside the specimen. The transmission of unscattered electrons is inversely proportional to the specimen thickness. Areas of the specimen that are thicker will have fewer transmitted unscattered electrons and so will appear darker, conversely the thinner areas will have more transmitted and thus will appear lighter. This mode of operation to create contrast in image is known as bright field imaging mode. In order to take microscopic images of ferromagnetic nanowires (NWs) and nanoparticles (NPs), we place them on carbon grids that are specially made for TEM imaging purpose.²¹ Standard TEM grid has typical diameter of ~ 3.05 mm with a thickness and mesh size ranging from a few to $100 \mu\text{m}$. Pretreatments of the NWs and NPs are done before placing them on carbon grid. Alumina and polycarbonate membranes that are used to prepare the NWs are dissolved chemically using 2M NaOH and chloroform solution respectively. NWs are washed carefully using distilled water and then the residual is ultra-sonicated in ethyl alcohol for few

minutes to free the bare NWs from gold thin film. The sonication also helps to detach the magnetic NWs from each other. In case of NPs, ultra-sonication has done to the particles in ethyl alcohol to detach the magnetic particles from each other. After sonication, we drop the ethyl alcohol solutions containing NWs and NPs on the TEM grids using micropipette. Proper pretreatment is necessary to get good quality images of nanostructures. Fig. 2.17 shows the TEM micrograph of 200 nm Co NWs.

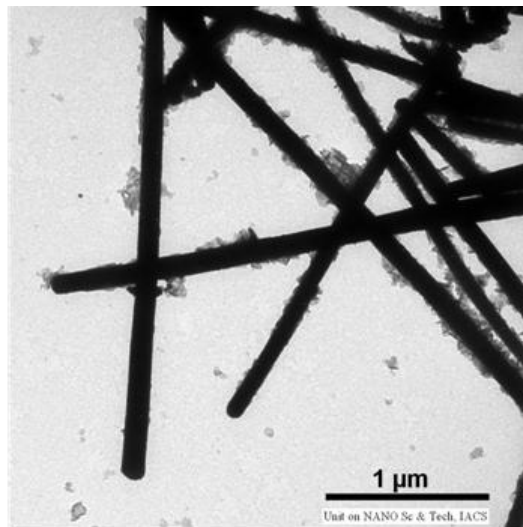


Fig.2.17. TEM micrograph of Co NWs.

In case of crystalline sample, the electron beam undergoes Bragg scattering and disperses electrons into discrete locations in the back focal plane as shown in Fig.2.18 below. The desired Bragg reflections can be selected by specific placement of objective apertures at back focal plane. Thus only parts of the sample that are causing the electrons to scatter to the selected reflections will end up projected onto the imaging apparatus producing diffraction contrast.

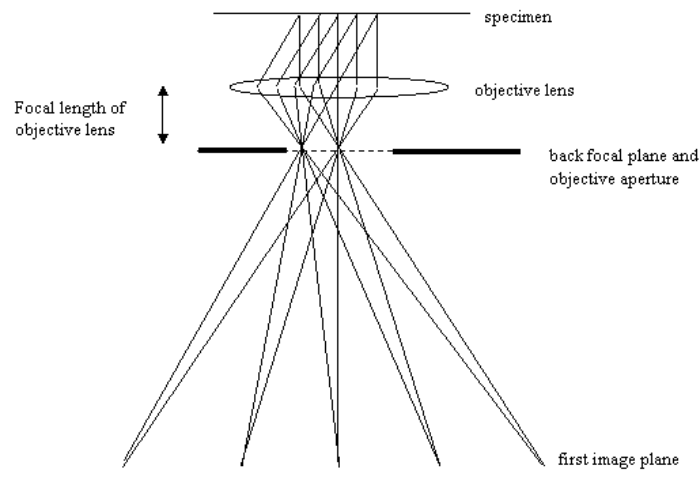


Figure 2.18. Schematic diagram of image forming by E-beam.

Another part of the incident electrons are scattered (deflected from their original path) by atoms in the specimen in an elastic fashion (no loss of energy). These scattered electrons are then transmitted through the remaining portions of the specimen. All electrons follow Bragg's Law and are scattered according to

$$2d \sin \theta = n\lambda \quad [2.1]$$

Where λ is the wavelength of the rays, θ is the angle between the incident rays with respect to the surface of the crystal and d is the spacing between layers of atoms. All incident electrons have the same energy (thus wavelength) and enter the specimen normal to its surface. All incident electrons that are scattered by the same atomic spacing will be scattered by the same angle. These scattered electrons can be collated using magnetic lenses to form a pattern of spots; each spot corresponding to a specific atomic spacing (or crystalline plane). This pattern can then yield information about the orientation, atomic arrangements and phases present in the area being examined. Fig. 2.19 shows electron diffraction patterns of polycrystalline and single crystalline Co NWs.

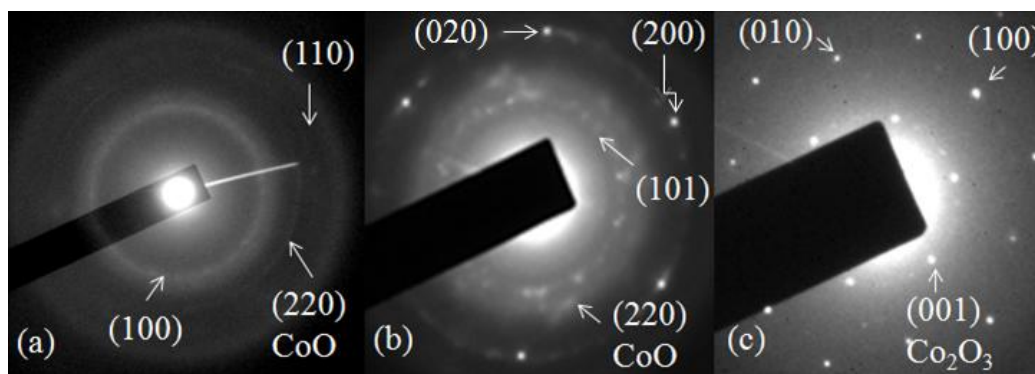


Fig. 2.19. SAED patterns of Co NWs.

The radius of circular rings in the diffraction patterns are measured using the microscopic length scale and then compared with the standard diffraction data of the corresponding elements or compounds provided by ICSD (Inorganic Crystal Structure Database).²²

2.3.2 X-Ray Powder Diffraction

X-ray crystallography relies on the dual wave/particle nature of x-rays to discover information about the structure of crystalline materials. X-ray powder diffraction is a common technique for the study of crystal structures and atomic spacing.

The physics and mathematics describing the generation of monochromatic X-rays and the diffraction of those X-rays by crystalline powders are very complex. However in precise, X-rays are generated by a cathode ray tube, filtered to produce monochromatic radiation, collimated to concentrate, and directed toward the sample.²⁵ X-rays can be considered waves of electromagnetic radiation. Upon incidence on crystalline sample, atoms within the sample elastically scatter the X-ray waves, primarily through the atom's electrons. The regular array of scatterers (electrons) within a crystalline sample produces a regular array of outgoing spherical waves of scattered X-rays. Although these waves cancel one another out in most

directions through destructive interference, they add constructively in a few specific directions, determined by Bragg's law stated in Eq. 2.1. These diffracted X-rays are then detected, processed and counted. By scanning the sample through a range of 2θ angles, all possible diffraction directions of the lattice should be attained due to the random orientation of the powdered material. Conversion of the diffraction peaks to d-spacings allows identification of the elements/compound present in the sample because each element/compound has a set of unique d-spacings. Typically, this is achieved by comparison of d-spacings with standard reference patterns (ICSD).

Powder diffractometers come in two basic varieties: θ - θ in which the X-ray tube and detector move simultaneously or a θ - 2θ in which the X-ray tube is fixed, and the specimen moves at $\frac{1}{2}$ the rate of the detector to maintain the θ - 2θ geometry. Our X-ray Panalytical system is a θ - 2θ system. In both systems the geometry shown in the diagram in Fig.2.20 is maintained during data collection.

The angles and intensities of diffractions are recorded electronically using a detector, electronics and specialized software resulting in a plot of 2θ (horizontal axis) vs. intensity (vertical axis) for the specimen. Fig. 2.21 shows a typical XRD pattern obtained from fcc crystalline Ni NWs.

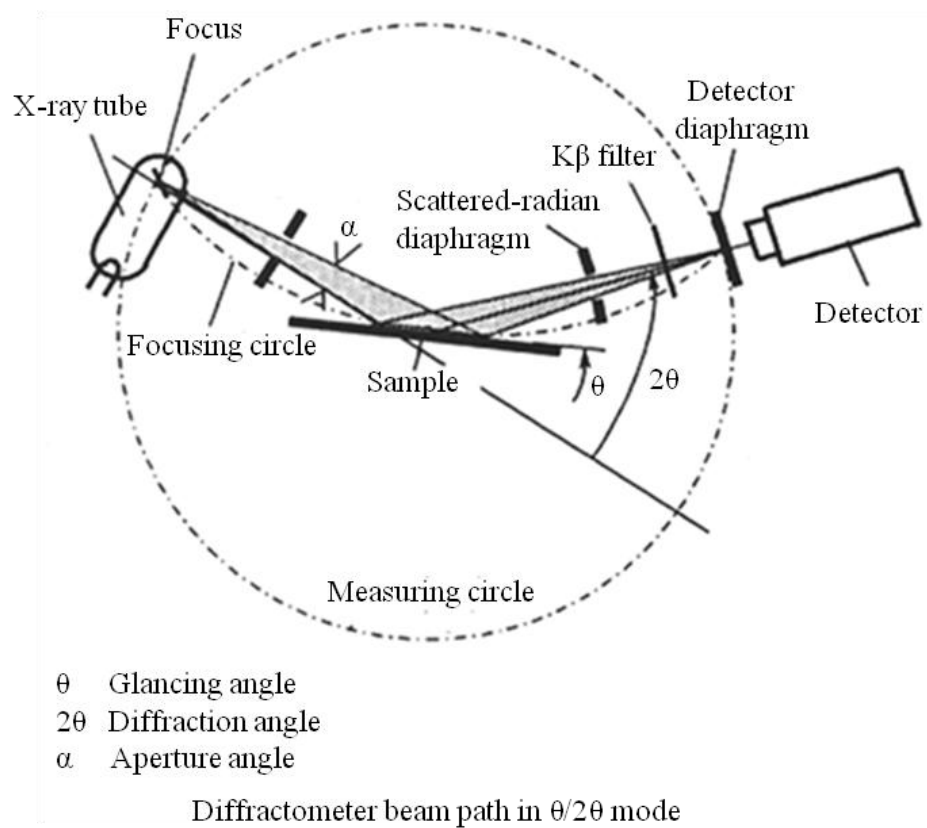


Fig.2.20. X-ray Diffraction optics used in $\theta/2\theta$ mode.

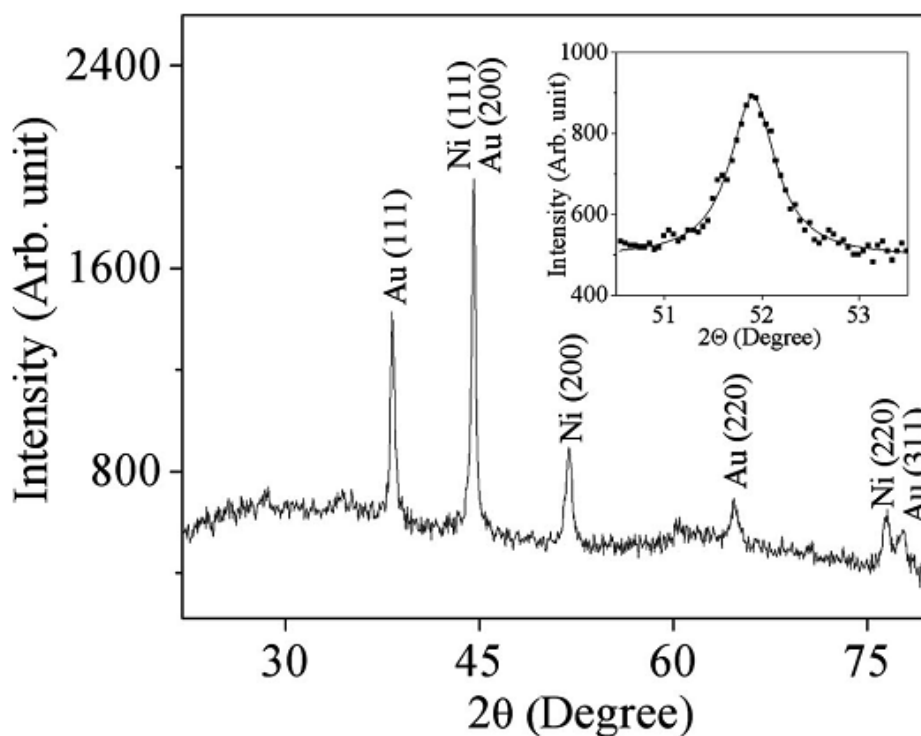


Fig.2.21. XRD pattern of Ni NWs.

2.4 Magnetic characterization techniques

2.4.1 Magnetic Force Microscopy (MFM)

MFM is a special type of Scanning Probe Microscopy (SPM)²⁶ where a sample can be scanned by a magnetic probe in order to gather information about the properties of the surface of a magnetic sample.²⁷ Another type of SPM is Atomic Force Microscopy (AFM).

In case of AFM, the probe is a very tiny sharp tip at the end of cantilever. Cantilever can be made of single-crystalline silicon, silicon dioxide (SiO₂), or silicon nitride (Si₃N₄). With AFM the force between the surface and the probe is measured. There are two different modes to achieve this goal. In contact mode, the tip is directly in contact with the surface and the interaction force is dominated by Van der Waals interaction. Whereas, the tapping mode is a non contact mode.

A drive signal is applied by a piezoelectric crystal with typical frequencies ranging from 10 kHz to 1 MHz²⁸ to the "Tapping Piezo", mechanically oscillates the probe at or near its resonance frequency. The interaction between the tip and the surface changes the cantilever oscillation amplitude or the phase relative to the Drive Signal (see schematic in Fig. 2.22).

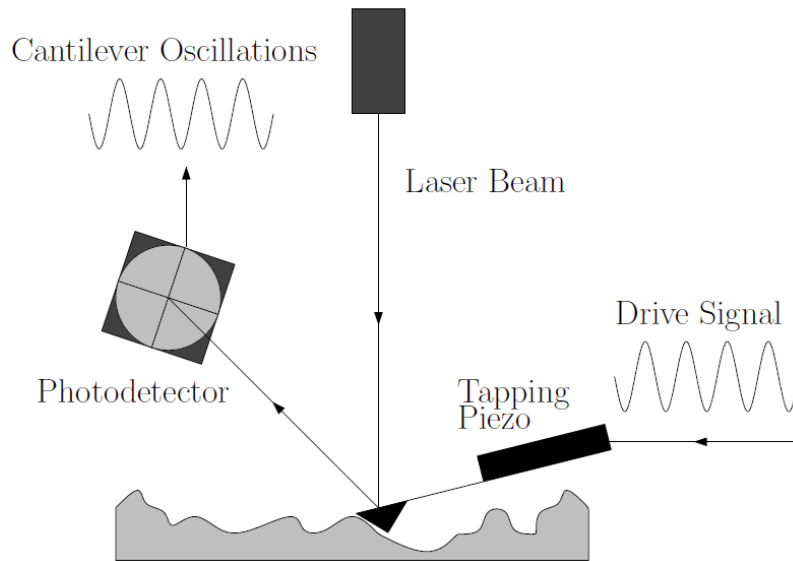


Figure 2.22. Schematic of the Tapping Mode

In case of MFM, the AFM Tips are coated with a thin (< 50 nm) magnetic film (such as Ni or Co), which not have negligible coercivity, so that the tip magnetic state (or magnetization \mathbf{M}) does not change during the imaging. The magnetic tip is sensitive to the out-of-plane component of the stray field originating from a magnetic sample (e.g. from a domain wall). During these modes each scan line is recorded twice. First, the topographic information of the line is recorded using the AFM Tapping Mode. This information is used during the second scan in order to keep the cantilever always at a certain probe sample distance, called *Lift Height*. During this scan the magnetic tip is only sensitive to the magnetic stray field from the sample. Therefore the combination of these two modes enables an accurate localization of the magnetic stray fields on the magnetic structure along with a good matching of topological artifacts.

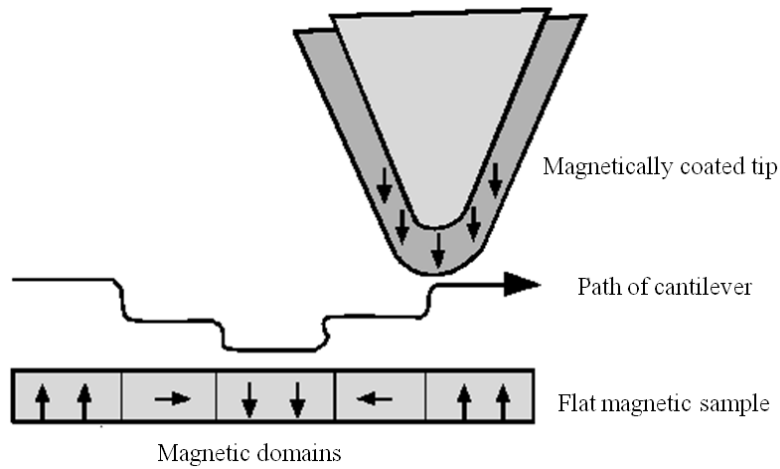


Figure 2.23. Schematic diagram of MFM tip scan over a magnetic surface.

In MFM measurements, the magnetic force between the sample and the tip can be expressed as

$$F = \mu_0 (\mathbf{m} \cdot \nabla) \mathbf{H} \quad [2.2]$$

Where \mathbf{m} is the magnetic moment of the tip (approximated as a point dipole), \mathbf{H} is the magnetic stray field from the sample surface, and μ_0 is the magnetic permeability of free space. The stray magnetic field from the sample can affect the magnetic state of the tip, and vice versa. Thus, interpretation of the MFM measurement is not straightforward. For instance, the geometry of the tip magnetization must be known for quantitative analysis. Fig. 2.23 shows schematic diagram of the magnetic tip movement over a magnetic sample. The stray field of the MFM tip magnetizes the sample surface locally along its own direction of magnetization as it close to the sample area. Typical resolution of 30 nm can be achieved,²⁹ although resolutions as low as 10 to 20 nm are attainable.³⁰ Fig. 2.24 below shows typical AFM and MFM micrographs of Ni NWs. In MFM micrographs, the bright spots corresponding to the magnetic stray field at the portion of the sample upward from the page and the black regions corresponds to the downward stray field.

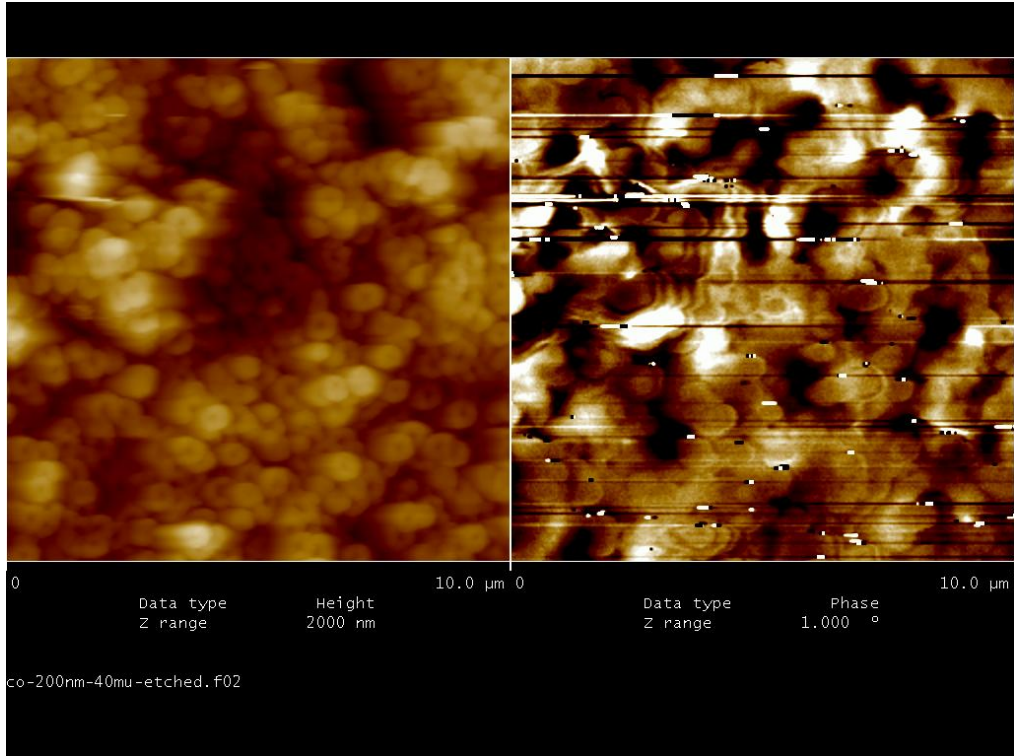


Fig. 2.24. AFM (left) & MFM (right) micrographs of Ni NWs.

2.4.2 Vibrating Sample Magnetometer (VSM)

Vibrating sample magnetometer (VSM) is based on Faraday's law that states, an emf (electromotive force) will be generated in a coil if there is a change in flux linking the coil. The induced emf in a coil with 'n' turns with a cross-sectional area of 'a' can be written as,

$$V = -na(dB/dt) \quad [2.3]$$

When the coil is positioned in a constant magnetic field,

$$\mathbf{B} = \mu_0 \mathbf{H} \quad [2.4]$$

Now if we place a magnetic sample having magnetization ' \mathbf{M} ' near the coil, then

$$\mathbf{B} = \mu_0 (\mathbf{H} + \mathbf{M}) \quad [2.5]$$

The corresponding flux change can be written as

$$\Delta \mathbf{B} = \mu_0 \mathbf{M} \quad [2.6]$$

The induced emf in pick-up coils expressed at the beginning thus can be rewritten as

$$V dt = -n a \mu_0 M \quad [2.7]$$

The above equation implies that the output signal of the coil is proportional to the magnetization \mathbf{M} but independent of the magnetic field in which the magnitude of \mathbf{M} is to be determined.

Schematic diagram of a VSM is shown in Fig. 2.25. In a VSM, the sample is subjected to a sinusoidal motion (of frequency ν) and the corresponding voltage is induced in suitably located stationary pickup coils.

The electrical output signals of these latter coils has the same frequency ν . Its intensity of proportional to the magnetic moment of the sample, the vibration amplitude and the frequency ν . The schematic diagram of the set-up is shown in fig f below. The sample to be measured is centered in the region between the poles of a electromagnet which can generate a uniform magnetic field \mathbf{H}_0 . A thin vertical non magnetic sample rod (made of plastic/quartz) connects the sample holder with a transducer assembly located above the magnet. The transducer converts a sinusoidal as drive signal (generated by an oscillator/amplifier circuit) into a sinusoidal vertical vibration of the sample rod. The sample is thus subjected to a sinusoidal motion in the magnetic field \mathbf{H}_0 .

Pickup coils made of copper and mounted on the poles of the magnet pick up the signal resulting from the motion of the sample. However, though the pick-up coil signal at the vibration frequency ν is proportional to the magnitude of the moment of the sample, it is also proportional to the vibration amplitude and frequency. Thus the moment readings taken simply by measuring the amplitude of the signal are subject to errors due to variation in amplitude and frequency of vibration. In order to avoid this

difficulty, a nulling technique is introduced employing a vibrating capacitor for generating a reference signal that varies with moment, vibration amplitude and frequency in the same manner as the signal from the pickup coils. When these two signals are processed in an appropriate manner, it is possible to eliminate the effects of vibration amplitude and frequency shifts. In that case, one obtains readings that vary only with the moment of the sample.

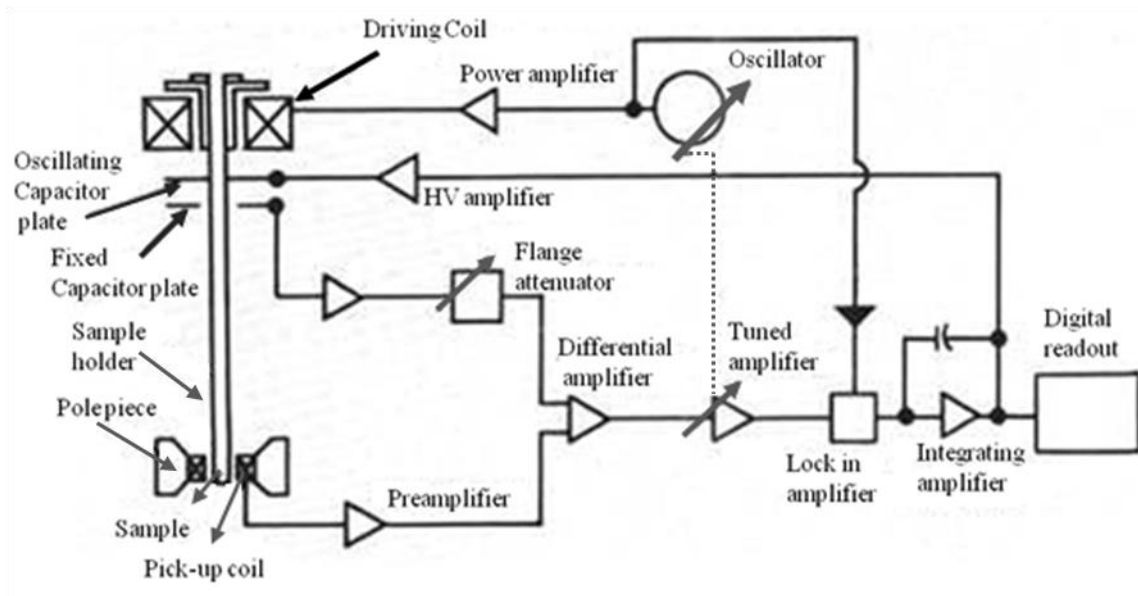


Fig. 2.25. Schematic diagram of VSM.

In case of NWs, we measured the corresponding hysteresis loops at two different orientations of the samples as shown in Fig. 2.26. The NWs are placed either parallel to the external uniform magnetic field H_0 named as out-of-plane (OP) configuration or perpendicular to H_0 named as in-plane (IP) configuration. The phrases ‘out-of-plane’ (OP) and ‘in-plane’ (IP) are coined from the orientation of the flat planes of alumina or polycarbonate membranes within which the NWs are deposited. The magnetization per unit volume or per unit mass of the NWs is difficult to measure as the NWs are within the membranes (which are very fragile and pores are not well arranged). We rather interested in the nature of magnetization curve of the NWs and

want to do comparative studies of the magnetization processes of the nanostructures. Hence, we normalized the magnetic moment values in hysteresis loops recorded by VSM. We follow the same technique later for V-SQUID measurements.

The VSM in our laboratory (Lakeshore make) has maximum magnetic field generating capability of 2.1 T without cryogenic system and 1.76 T can be achieved with LN₂/LHe dewar between the coils. The moment versus temperature or temperature dependent hysteresis loops can be measured using a cryogenic system (Liq. N₂) that can operate within a temperature range of 80 to 400 K with temperature stability of ± 0.2 K and temperature resolution of 0.001 K. Noise level of 1.25 μ emu (RMS value) in moment measurement can be achieved using the system.³¹

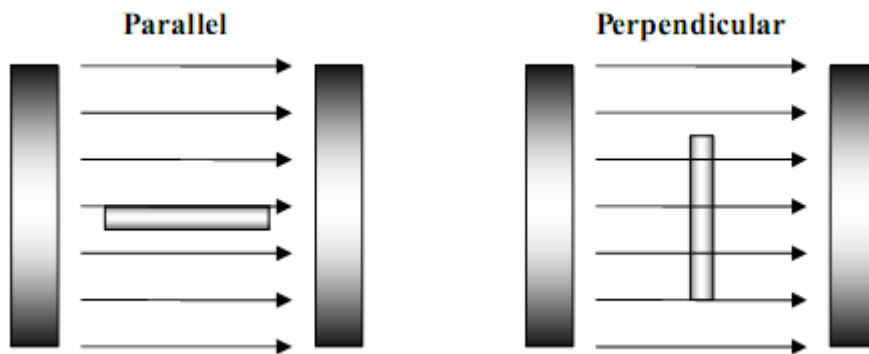


Fig.2.26. placement of NW samples between the pole pieces of VSM magnet.

2.4.3 Superconducting Quantum Interference Vibrating Sample Magnetometer (S-VSM)

S-VSM or SQUID -VSM is the most sensitive and effective device available till now to detect magnetic moment/field in less time compared to the usual SQUID magnetometer. This magnetometer is a kind of combination of two magnetometers, the conventional high speed VSM and the high sensitive SQUID. Unlike the copper detection coils in a conventional VSM, magnetic flux in SQUID-VSM is detected by

SQUID sensors. Signal created by sample vibration is frequency modulated to separate the sample signal from the instrumental artifacts. The size of the signal is independent of the vibration frequency. Similar to a SQUID, a superconducting second order gradiometer detection coil used in MPMS SQUID–VSM detection coil produces a current in response to local magnetic field disturbances, rather than to a change in magnetic flux as in the case of the VSM coils. Figure 2.27 is a simplified model of the MPMS SQUID–VSM detection hardware. The current in the detection coil is a function of the sample position. The detection coil can be considered as consisting of three loops, the upper loop has a single turn wound clockwise, the middle one has two turns wound anti-clockwise and the lower one has a single turn wound clockwise. The sensor in the MPMS SQUID–VSM is the well-known Josephson junction, which is a device consisting of superconducting-insulating-superconducting (SIS) tri-layer junction. The basic equations governing the Josephson junction are

$$U(t) = \frac{\hbar}{2e} \frac{\partial \phi}{\partial t}, \quad I(t) = I_C \sin \phi(t) \quad [2.8]$$

Here, $U(t)$ and $I(t)$ are the voltage and current through the Josephson junction, I_c is the critical current of the junction and $\phi(t)$ is the phase difference between the wave functions in the two superconductors. In case of no emf is applied through the Josephson junction, a constant DC current flows through it. If a constant DC voltage is applied then an ac current flows with a frequency $(2e/h)U$. When a magnetic moment is kept in the loop containing a Josephson junction,³² an emf is induced in the loop, which induces a current with a frequency decided by the Josephson equations. The MPMS SQUID–VSM detects the change in currents or frequency to deduce the magnetic moment of the sample.

There are two types of SQUIDS, DC or AC. The MPMS SQUID–VSM works on the principle of DC SQUID, consisting of two Josephson junctions connected in parallel so that the electrons tunneling through the junctions demonstrate quantum interference depending upon the magnetic field within the loop.

The MPMS SQUID–VSM is capable of providing magnetic fields in the range ± 70 kOe with field ramp possible as high as 700 Oe/s and sample temperature ranging from 1.8 K to 400 K. Sensitivity is 1×10^{-8} emu at zero magnetic field and 5×10^{-8} emu at 70 kOe with 4 seconds data averaging.³³

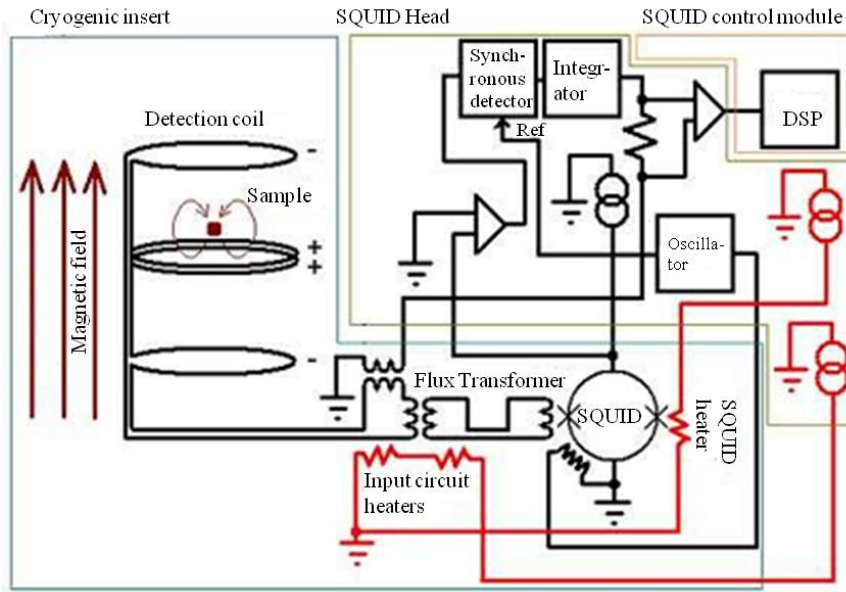


Fig.2.27. Schematics of the SQUID-VSM detection system

2.4.4 Ferromagnetic Resonance (FMR) Spectrometer

FMR is a spectroscopic (FMR) method to measure magnetic properties by detecting the precessional motion of the magnetization in a ferromagnetic sample. FMR absorption is the analog of paramagnetic and nuclear resonance absorption. The ferromagnetic effect was found originally by Griffiths³⁴ and further confirmation has been reported by Yager and Bozorth.³⁵ A theory of the resonance effect has been proposed by C. Kittel.³⁶

From a macroscopic point of view, the applied static magnetic field H_0 causes the total magnetic moment to precess around the direction of the local field H_{eff} , before relaxation processes damp this precession and the magnetization aligns with H_{eff} . If the sample is irradiated with a transverse radio frequency field (microwaves of typically 1–35 GHz), and if the rf frequency coincides with the precessional frequency, the resonance condition is fulfilled and the microwave power is absorbed by the sample. The motion of the magnetization is described by the Landau-Lifshitz-Gilbert equation:

$$\frac{\partial \mathbf{M}}{\partial t} = -\gamma (\mathbf{M} \times \mathbf{H}_{eff}) + G/\gamma (M_s)^2 [\mathbf{M} \times \frac{\partial \mathbf{M}}{\partial t}] \quad [2.9]$$

The first part in right hand side corresponds to the precession. However, the second part introduces a viscous damping (Gilbert damping constant G). The effective magnetic field H_{eff} includes the applied DC field, the rf microwave magnetic field component, the demagnetizing field (shape anisotropy) and the magnetocrystalline anisotropy field. γ is the gyromagnetic ratio $\gamma = g\mu_B/\hbar$. The principal result of the theory³⁶ is that the resonance condition for a plane surface should be given by

$$\omega_0 = \gamma (BH)^{1/2} \quad [2.10]$$

Instead of the Larmor condition $\omega_0 = \gamma H$; here ω_0 is the frequency at resonance; γ is the magneto-mechanical ratio for an electron spin; H is the strength of the static magnetic field and B is the magnetic induction in the specimen.

Microscopically, the H field creates a Zeeman splitting of the energy levels, and the microwave excites magnetic dipole transitions between these split levels. Since it is difficult to vary the microwave frequency over larger ranges, the DC magnetic field H_0 is varied instead.

Usually the absorption derivative is measured. During the measurements, the angular orientation of pumping field and static field are maintained as depicted in Fig. 2.28 while the schematic diagram of the set-up is shown in Fig. 2.29. The resonance signal resembles a Lorentzian lineshape. The resonance field position H_{res} depends on the angles, anisotropy parameters, g -factor, and magnetization of the sample. The linewidth ΔH is directly connected to the relaxation processes.

In ultrathin films, Gilbert damping is commonly used to describe the relaxation. But several other possible relaxation paths are also known, e.g. two-magnon scattering, spin-pumping effect, etc., which can contribute to the linewidth. The anisotropy constants can be easily deduced from angle dependent measurements of single crystalline samples. For magnetic multilayers, also the interlayer exchange coupling constant can be determined by FMR in absolute units.

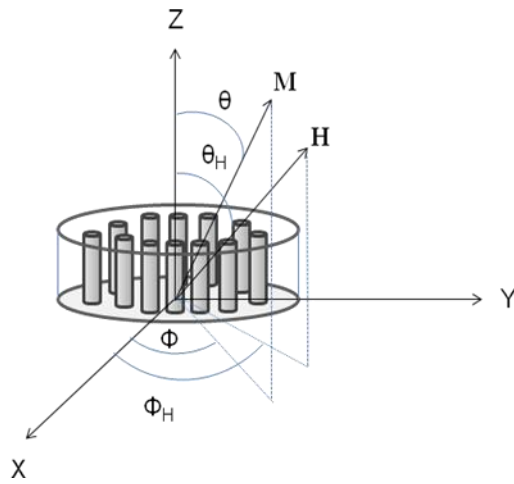


Figure 2.28. Orientation of static and dynamic magnetic field in a right angle FMR configuration.

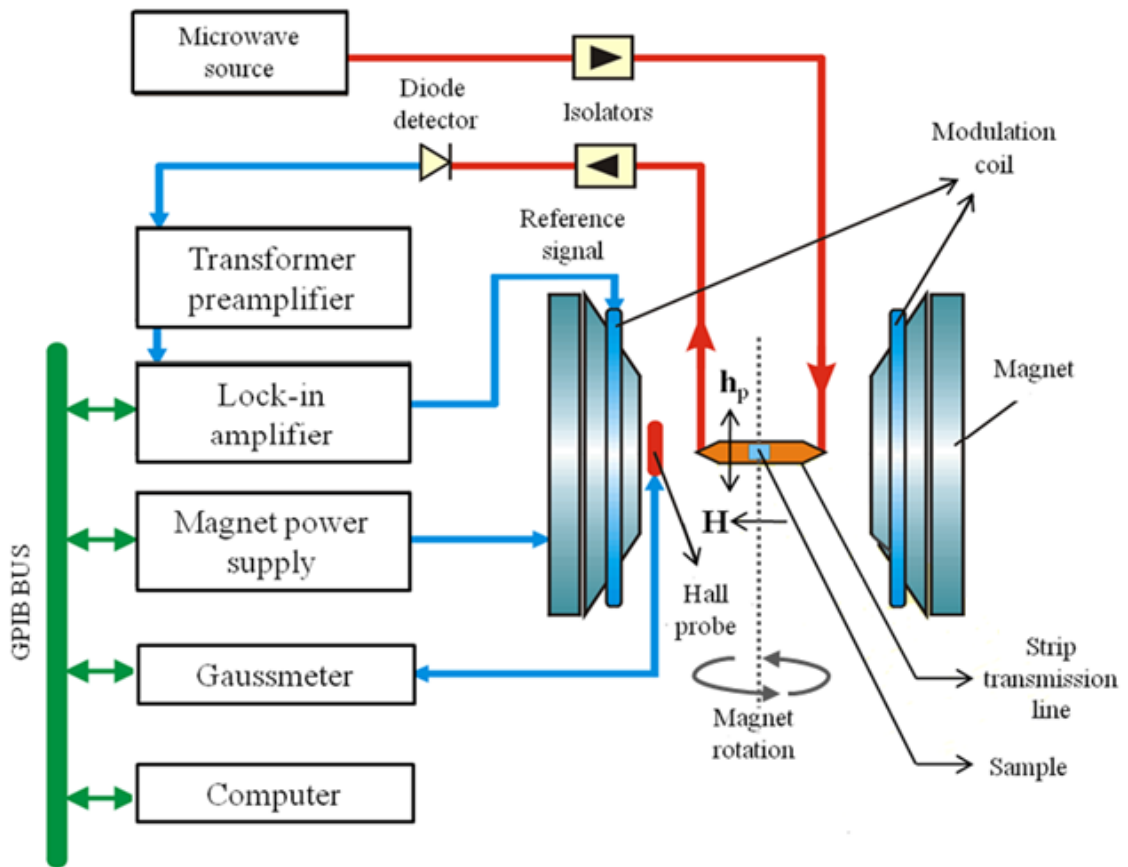


Figure 2.29. Schematic diagram of FMR set-up.

2.4.5 Magneto Optical Kerr Effect (MOKE) magnetometer

We use the magneto-optical Kerr effect (MOKE) to assess the magnetization behavior of electrodeposited NWs. Membranes are dissolved chemically in order to free the NWs employing an ultra-sonicator. Individual NWs are then placed on Si/SiO₂ substrates and then used as sample for MOKE measurement. In this non-destructive surface sensitive technique, polarization-modulated LASER light reflects from the surfaces of magnetic NWs in the presence of a sweeping magnetic field. Since the LASER is an electromagnetic field, the magnetic field of the sample interacts with the light to cause a very slight change in the incident LASER's polarization and ellipticity. We measure these changes in the LASER light as an intensity change through nearly-crossed polarizers, recording the intensity as a function of the applied magnetic field.

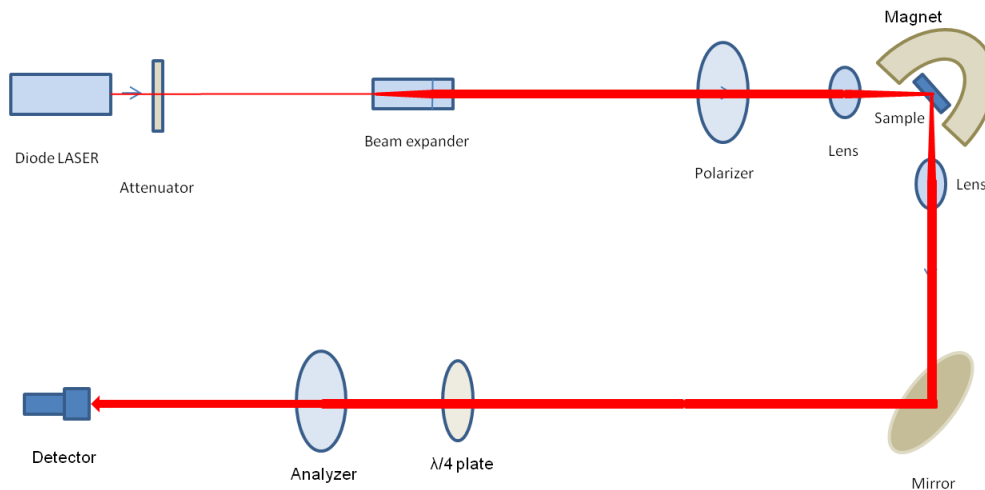


Figure 2.30. Schematic diagram of the table top MOKE set-up.

We measure the longitudinal or transverse magneto optical Kerr effect where the magnetization lies in the plane of sample substrate. Schematic diagram of the set-up is shown in Fig. 2.30. The polarizer and analyzer are kept at crossed with respect to each other before the measurement starts. An attenuator is used to decrease the LASER power of the diode LASER source to 3.5 mW. Beam expander expands the

beam which is later converged to a fine elliptical LASER spot of dimension $5 \times 7 \mu\text{m}$ using a plan-concave lens. The reflected beam is diverged and parallel beam is produced using another lens. The intensity of the reflected beam is detected by a high resolution Si detector. All the parts are available from Thorlabs. In presence of an alternating magnetic field ($f \sim 17 \text{ Hz}$) produced by the external magnet placed near the sample (see Fig. 2.30), the magnetization of the sample changes followed by a change in polarization angle of the reflected beam. Thus the intensity detected at the detector is change which is proportional to the change in magnetization of the sample. The $\lambda/4$ plate is introduced to reject the change in ellipticity of the beam reflected from the sample substrate. The laboratory set-up is shown in Fig. 2.31.

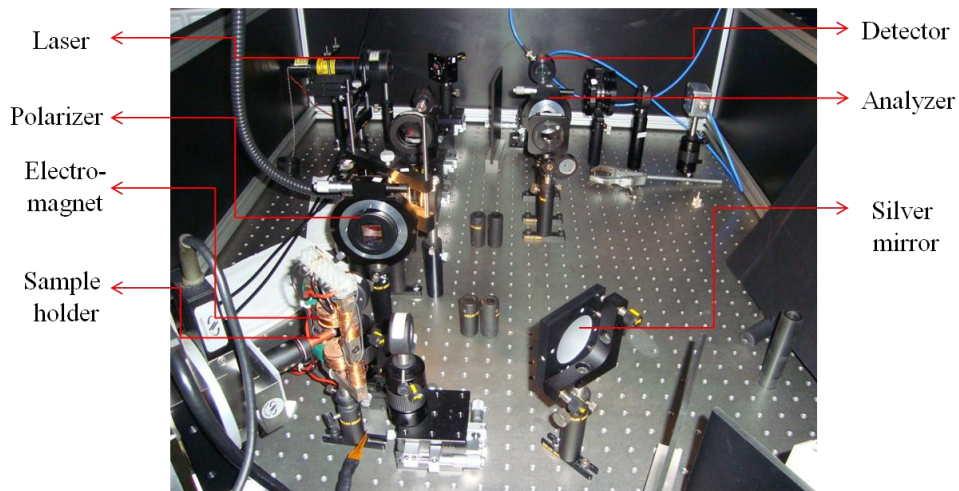


Figure 2.31. Laboratory set-up of MOKE measurements for NWs.

Bibliography

- [1] Asoh, H., Nishio, K., Nakao, M., Tamamura, T. and Masuda, H., *J. Electrochem. Soc.*, **148**, B152-B156 (2001).
- [2] Brown, F. and Mackintosh, W.D., *J. Electrochem. Soc.*, **120**, 1096 (1973).
- [3] Kobayashi, K., Shimizu, K., Thompson, G.E. and Wood, G.C., *J. Appl. Electrochem.*, **15**, 781 (1985).
- [4] Wang, H. and Wang, H. W., *Mater. Chem. Phys.*, **97**, 213-218 (2006).
- [5] O'Sullivan, J. P. and Wood, G. C., *Proc. Roy. Soc. Lond. A*, **317**, 511-543 (1970).
- [6] Martín, J.I., Noguès, J., Liu, K., Vicent, J.L., Schuller, I. K., *J. Magn. Mater.*, **256**, 449-501 (2003).
- [7] Sigma-Aldrich Corp., St. Louis, MO, USA
- [8] Madou, M. J., *Fundamentals of Microfabrication and Nanotechnology*, CRC Press, 3rd edition (July 13, 2011).
- [9] Herriott, D.R., Collier, R.J., Alles, D.S. and Stafford, J.W., *IEEE Trans. On Electron Devices*, **22** (7), 385 (1975).
- [10] Broers, A.N., Molzen, W.W., Cuomo, J.J. and Wittels, N.D., *Appl. Phys. Lett.* **29**, 596 (1976).
- [11] Chang, T.H.P., *J. Vac. Sci. Technol*, **12**, 1271 (1975).
- [12] Parikh, M. and Kyser, D.F., *J. Appl. Phys.*, **50**, 1104 (1979).
- [13] Rishton, S.A. and Kern, D.P., *J. Vac. Sci. Technol. B*, **5**, 135 (1987).
- [14] Parikh, M., "Corrections to Proximity Effects in Electron Beam Lithography," Research Report RC-2254 (30447), IBM T.J. Watson Research Center, Yorktown Heights, NY, (1978).
- [15] Broers, A.N., "Resolution Limits for Electron Beam Lithography", *IBM J. RES. Develop.* **32**, 502 (1988).
- [16] Chang, T.H.P., et. al., "Nanostructure Technology," *IBM J. RES. Develop.* **32**, 462 (1988).

- [17] Erni, R., Rossell, M. D., Kisielowski, C., Dahmen, U., "Atomic-Resolution Imaging with a Sub-50-pm Electron Probe". *Phys. Rev. Lett.*, **102** (9), 096101(2009).
- [18] Ruska, E., "Ernst Ruska Autobiography". Nobel Foundation. Retrieved 2010-01-31 (1986).
- [19] Knoll, M., "Aufladepotential und Sekundäremission elektronen-bestrahlter Körper". *Zeitschrift für technische Physik* **16**, 467–475 (1935).
- [20] Cambridge Scientific Instrument Company, USA.
- [21] ProSciTech, Australia.
- [22] Fachin formations zentrum (FIZ) Karlsruhe (c) FIZ Karlsruhe (2007).
- [23] Groves, T.R., Pfeiffer, H.C., Newman, T.H. and Hohn, F.J., *J. Vac. Sci. Technol. B*, **6**(6), 2028 (1988).
- [24] Brundle, C. R., Evans, C. A. Jr., Wilson, S., *Encyclopedia of materials characterization*, Butterworth-Heinemann publications, 1992.
- [25] Cullity, B. D., Stock, S. R., *Elements of X-ray Diffraction*, 3rd Edition, Prentice Hall (2001).
- [26] Bonnell, D.A., *Scanning Probe Microscopy and Spectroscopy*, 2nd edition, Wiley-VCH (2000).
- [27] Jiles, D. C., *Introduction to Magnetism and Magnetic Materials*, 2nd edition, Springer (1998).
- [28] Hopster, H. and Oepen, H.P., *Magnetic Microscopy of Nanostructures*, Springer (2005).
- [29] Abelmann, L., Porthun, S. *et al.* "Comparing the resolution of magnetic force microscopes using the CAMST reference samples". *J. Magn. Magn. Mater.*, **190**, 135–147(1998).
- [30] Nanoscan AG, Quantum Leap in Hard Disk Technology.
- [31] Lake Shore Cryotronics, Inc., USA.
- [32] Josephson, B. D., *Rev. Mod. Phys.* **46** (2) 251–254 (1974).
- [33] Quantum Design Inc., USA.

[34] Griffiths, J. H. E., Nature **158**, 670 (1946).

[35] Yager, W. A. and Bozorth, R. M., Phys. Rev. **12**, 80 (1947).

[36] Kittel, C., Phys. Rev. **71**, 270 (1947).

[37] Thorlabs, New Jersey, USA.

Chapter 3

Study of glass coated amorphous MWs

3.1 Preamble

Among the soft magnetic materials, wire shaped amorphous magnetic materials exhibit peculiar magnetic behavior due to their novel synthesis techniques. Amorphous wires with diameter $\leq 100 \mu\text{m}$ (therefore termed as microwire, MW) show excellent soft magnetic properties. MWs with large positive magnetostriction show bistable magnetic hysteresis loop. Sharp change in magnetization makes them ideal for “jitterless” pulse generator.¹ Whereas, MWs with near zero or vanishing magnetostriction show giant magnetoimpedance (GMI) effect. Observed GMI effects in MWs pointing towards their possible applications in stress sensors.² Furthermore, the MWs have gained the interest of researchers in order to get a better understanding of micromagnetism for their simple magnetic domain structure. The MWs that have been most widely investigated are composed of $\text{TM}_x\text{Si}_y\text{B}_z$ where TM is one of the transition metals (e.g. Fe, Ni, Co) with the index x ranges typically from 0.7 – 0.8.³ On the other hand, y and z are typically in the range of 0.1-0.2. Other transition metals such as Cr occasionally added to improve corrosion resistance.³

There are mainly two ways to synthesize the MWs: In-rotating-water-quenching technique and quenching & drawing technique. In the first case, the molten metal stream is ejected from the orifice of a quartz tube and then projected onto a water layer formed by centrifugal force on the internal surface of a rotating cylinder. The technique is first introduced by Ohnaka.⁴ The second process uses Pyrex like glass tube which is placed within a high frequency induction heater.^{5, 6, 7} The alloy with desired composition in the form of a pellet is put inside the glass tube. At an elevated temperature, the metal melts within the tube and the temperature is also sufficient to

melt the Pyrex or similar insulating glass. The molted alloy took the form of a droplet. During the process, a glass envelope form on the metal droplet. A glass capillary is then drawn from the viscous melt and wound on a rotating drum. A running cold water jet solidifies the melt rapidly followed by the formation of metallic MW with the glass coated on its outer surface. The typical inner metallic core diameter that can be achieved by the process is about $\sim 1 - 30 \mu\text{m}$ and the glass coating has thickness of $\sim 2 - 10 \mu\text{m}$. The insulating coating of glass provides corrosion resistance to the MWs and offers electrical insulation. Due to lack of crystal structure, the magnetocrystalline anisotropy is almost negligible in these materials. Internal stresses developed within the MWs during the rapid solidification of the melt gives rise to magnetoelastic anisotropy, the main source of anisotropy.

In this chapter we are investigating the magnetic domain structure of the MWs via the magnetic hysteresis loops measurements of the MWs under different physical conditions. These studies will help us to understand the domain structure and magnetic properties of magnetic nanowires which are discussed in the following chapters.

3.2 Experimental

We study cobalt rich glass coated amorphous MWs with two different compositions of $\text{Co}_{83.2}\text{Mn}_{7.6}\text{Si}_{5.8}\text{B}_{3.3}$ and $(\text{Co}_{0.93}\text{Fe}_{0.07})_{63}\text{Ni}_{10}\text{Si}_{11}\text{B}_{16}$. The microwires were received from Instituto de Magnetismo Aplicado, Madrid, Spain. The surface morphology of the MWs is studied by scanning electron microscope (SEM). Before the microscopic study we remove the glass coatings from the surface of the MWs very carefully using sharp edges, for example razor blades. The DC magnetic hysteresis loops of the MWs are measured by a conventional DC magnetization set-up where the MWs are magnetized using a air core solenoid and the change in magnetic flux through a pick-up coil is recorded and then integrated using a fluxmeter. Magnetic hysteresis loops are measured under different stresses applied to the MWs. The MWs are stressed out using different weights applied at one end of the MWs keeping the other end fixed [see Fig.3.1(a)] and magnetic hysteresis loops are recorded for each load. The stresses are calculated by knowing the weights and the cross sectional area

of the MWs. DC magnetic hysteresis loops are also measured after passing different number of current pulses through the MWs. The pulses are generated by an electronic circuit using IC 555 [see Fig. 3.1(b)] that produces current pulses of 12 sec width and 100 mA DC current amplitude. During the passage of the current pulses through the MWs, the MWs are subjected to joule heating accompanied by a circumferential magnetic field according to Ampere's law. The effect of the short duration heat annealing of the DC magnetic hysteresis loops of the $\text{Co}_{83.2}\text{Mn}_{7.6}\text{Si}_{5.8}\text{B}_{3.3}$ MWs in the presence of the magnetic field is then studied by their DC magnetic hysteresis loops measurements.

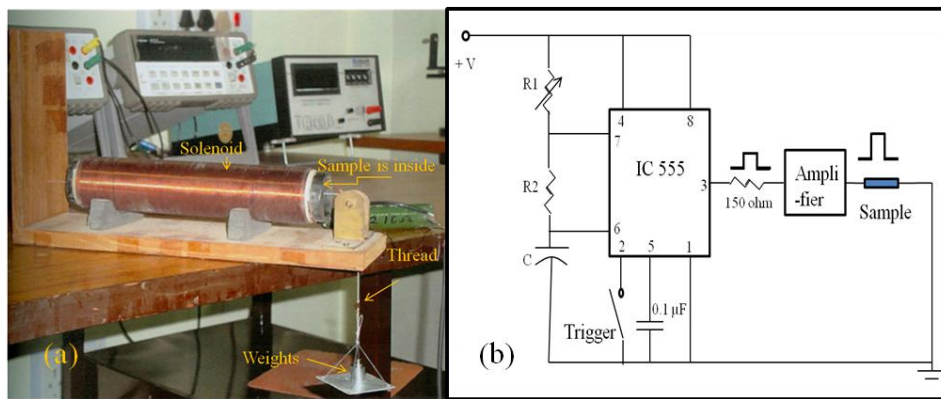


Figure 3.1. (a) Laboratory arrangement for applying pressure to the MWs and (b) Current pulse generating circuit using IC555.

3.3 Results and Discussions

3.3.1 Structural properties

Fig. 3.2 (a) and Fig. 3.2 (b) show the SEM micrographs of the $\text{Co}_{83.2}\text{Mn}_{7.6}\text{Si}_{5.8}\text{B}_{3.3}$ and $(\text{Co}_{0.93}\text{Fe}_{0.07})_{63}\text{Ni}_{10}\text{Si}_{11}\text{B}_{16}$ MWs respectively. From the micrographs the glass coating on the surfaces of the metal core of the MWs is evident. It is observed that the diameter of the metal core and the thickness of the surrounding glass coating are uniform throughout the length of the MWs. In case of $\text{Co}_{83.2}\text{Mn}_{7.6}\text{Si}_{5.8}\text{B}_{3.3}$ MWs, the glass coating has a thickness of $\sim 5.3 \mu\text{m}$ while the inner

metallic core has the diameter of $\sim 14.7 \mu\text{m}$. The $(\text{Co}_{0.93}\text{Fe}_{0.07})_{63}\text{Ni}_{10}\text{Si}_{11}\text{B}_{16}$ glass coated microwires have a thickness of glass coating $\sim 5.4 \mu\text{m}$ and the inner core has the diameter of $\sim 20.5 \mu\text{m}$.

The synthesis procedure (quenching & drawing procedure) of the MWs supports the formation of several centimeter long MWs with smooth surfaces of the metallic core covered by glass coating. This is observed in SEM micrographs where we merely have seen any surface defects. The scratches observed in SEM micrographs are believed to be due to the cutting of the MWs before the SEM study.

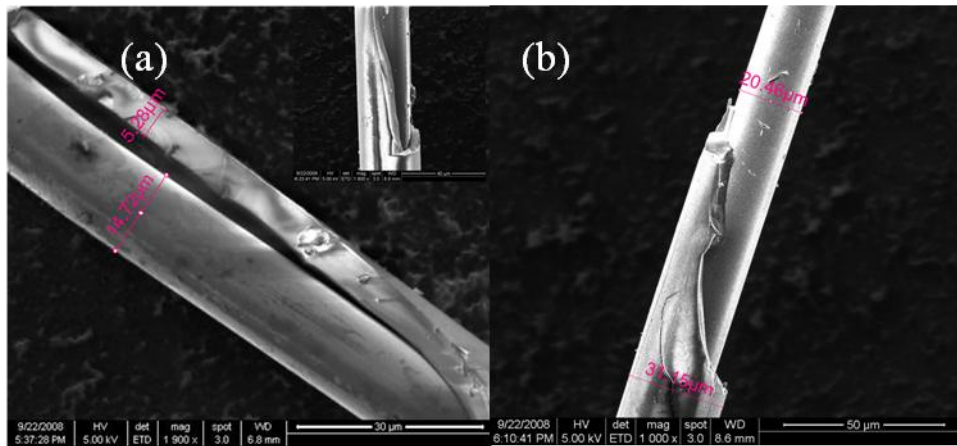


Figure 3.2. Scanning Electron Microscopy (SEM) image of glass-coated amorphous (a) $\text{Co}_{83.2}\text{Mn}_{7.6}\text{Si}_{5.8}\text{B}_{3.3}$ microwire and (b) $(\text{Co}_{0.93}\text{Fe}_{0.07})_{63}\text{Ni}_{10}\text{Si}_{11}\text{B}_{16}$ microwire.

3.3.2 Magnetic properties and Domain structure

Fig. 3.3 shows three hysteresis loops of a $\text{Co}_{83.2}\text{Mn}_{7.6}\text{Si}_{5.8}\text{B}_{3.3}$ MW under three different stresses e.g. 0, 220 and 440 MPa. The external magnetic field applied along the axis of the MWs has the upper limit of 10 Oe. The hysteresis loops show sharp jump at the start of the switching followed by a slow increase in magnetization towards saturation with the increase of external magnetic field along the opposite direction. The loops are thus not square in shape. It is to be noted that the switching of magnetization in the MWs is observed to be increases with the increase in applied

tensile stress (i.e. $0 \text{ MPa} < 220 \text{ MPa} < 440 \text{ MPa}$). In contrast, the slow saturation process of MWs after the switching (i.e. when the applied field is directed at opposite direction) is decaying slowly with the increase in stress. The coercivity of the hysteresis loops is also observed to be decreasing with the increase in stress. In precise we can state that, the hysteresis loss of the MWs is decreasing with the increase of applied tensile stress.

Fig. 3.4 shows the hysteresis loops of $\text{Co}_{83.2}\text{Mn}_{7.6}\text{Si}_{5.8}\text{B}_{3.3}$ MW before and after heat treatment with different current pulses (e.g. 1, 2, 3 and 4 current pulses). Hysteresis loops are found to shear as the MWs are treated by the current pulses. Furthermore, the shear nature of the loops (i.e. low initial susceptibility) increases as we increase the number of pulses passing through the wires. The sharp switching is prominent in as-quenched sample which is also observed in the MW after single pulse heat treatment. However, the sharp switching starts to disappear after the MW is treated with two pulses and completely disappear in the MW which is treated with four consecutive pulses (see Fig. 3.4).

In order to explain the observed experimental results, it is necessary to understand the domain structure of the glass coated amorphous MWs. The MWs are synthesized in quenching and drawing procedure followed by the rapid cooling from melt. The process accompanied by a strong mechanical stress on the metal core induced by the surrounding glass coating due to their different thermal coefficient. However, the composition of the alloy defines the magnetostriction of the MWs. For example, Fe based alloy shows positive magnetostriction while Co based alloy show negative magnetostriction.³ On the other hand, MWs containing $\text{Co} : \text{Fe} \approx 16 : 1$ can show nearly zero magnetostriction.³ It is believed that the unique stress distribution within the metallic core and the nature of magnetostriction of the MW together define all the unique magnetic characteristics of the MWs.⁸ The corresponding magnetoelastic and shape anisotropies determines the domain structure and hence the magnetization process.^{9, 10}

During the rapid quenching of the melt in the synthesis procedure, the outer layer of the melt solidifies first followed by shrinking of inner core of the same. The delay in shrink of inner core of the melt develops a radial tension in the wire. Perhaps

the radial tension increases towards the centre of the MWs due to the differential cooling process and as a consequence, an axial stress is developed in the inner core. In summary, two distinct regions are developed within the wires: inner core where the axial stress exists and outer layer where the radial stress exists. The transition between these two regions is expected to occur gradually over a few atomic layers. Volumes of the two regions depend largely on the magneto-elastic coupling of the material. The stresses are long range in character and play a crucial role in defining the domain structure of the MWs. Domain structure of the MWs can be derived from axial magnetic hysteresis loops combined with domain observation by magneto optical Kerr effect or Bitter technique.¹¹ In case of glass coated MWs, it is difficult to observe the domain structure by the later techniques due to their reduced dimension compared to the water quenched MWs.⁷ However, the domain structure in glass coated MWs is very similar to the water quenched MWs. Detail study on domain structure can be found in literature^{8-10, 12, 13} all of which indicate the possible domain structure in amorphous MWs as shown in Fig. 3.5 and Fig. 3.6.

Fig. 3.5 shows the typical domain structure of a negative magnetostrictive amorphous MW. Whereas, Fig. 3.6 shows the same for a positive magnetostrictive MW. The domain structure consist of a single domain core (inner core or IC) having magnetization parallel to the axis of the MW and a multidomain outer shell (outer shell or OS) with transversely oriented magnetization. In case of negative magnetostrictive MW, the OS magnetization is circular (see Fig. 3.5) and for positive magnetostrictive MW, it is radial (see Fig. 3.6).

The sharp switching observed in the hysteresis loops of as quenched $\text{Co}_{83.2}\text{Mn}_{7.6}\text{Si}_{5.8}\text{B}_{3.3}$ MW (Fig.3.3) as discussed earlier is a consequence of switching of the IC domain upon reversing the external field. After the switching, the slow saturation in the opposite direction is attributed to the OS magnetization. As we applied an external stress (220 MPa) along the axis of MW, the IC increases in volume results an enhanced sharp switching (Fig.3.3). On the other hand, the slow saturation after the switching decreases perhaps due to the decrease in OS volume. Hysteresis loop corresponds to 440 MPa shows further enhancement of sharp switching for greater IC volume whereas less OS signature is evident.

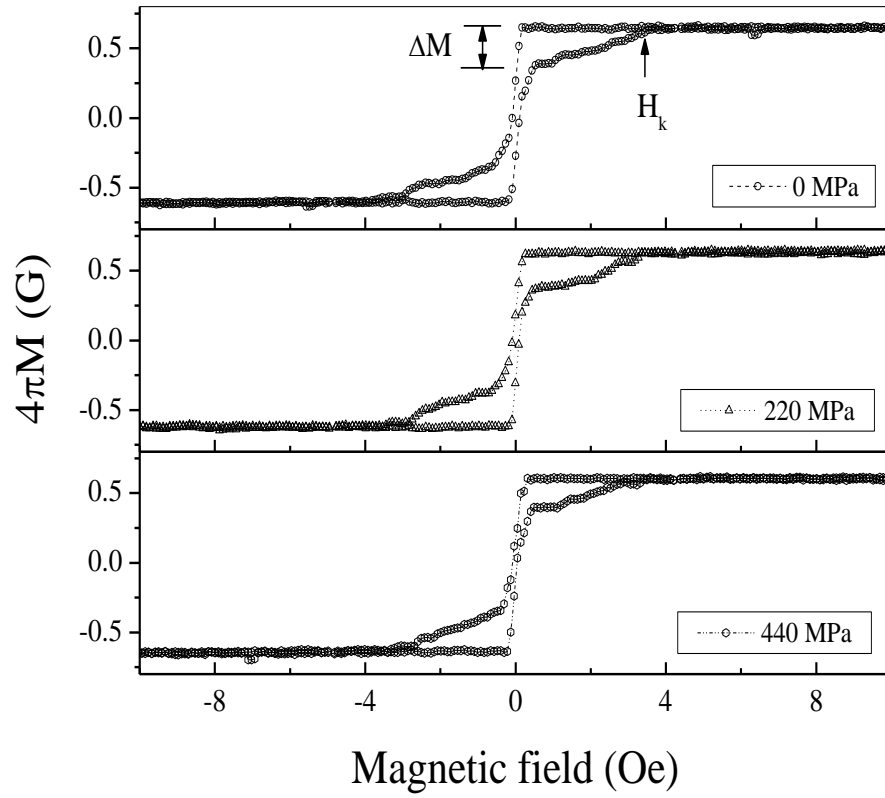


Figure 3.3. Axial hysteresis loops of the amorphous $\text{Co}_{83.2}\text{Mn}_{7.6}\text{Si}_{15.8}\text{B}_{3.3}$ MW at various stress values.

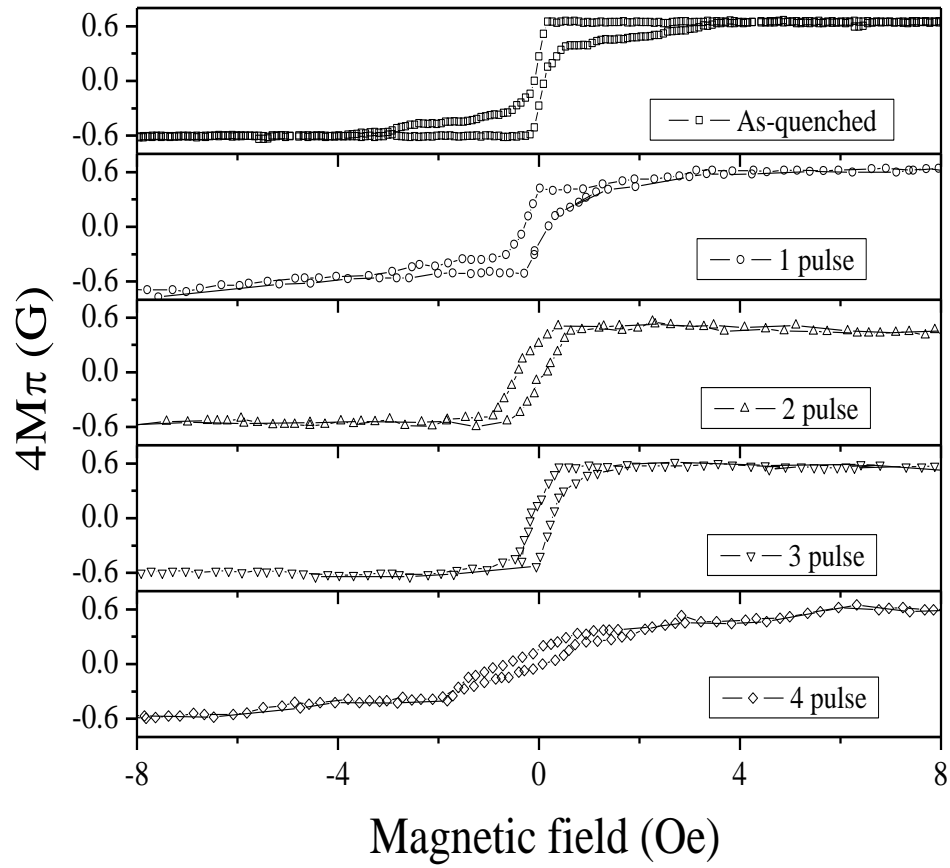


Figure 3.4. Axial hysteresis loops of the as-quenched and heat-treated amorphous $\text{Co}_{83.2}\text{Mn}_{7.6}\text{Si}_{5.8}\text{B}_{3.3}$ microwires.

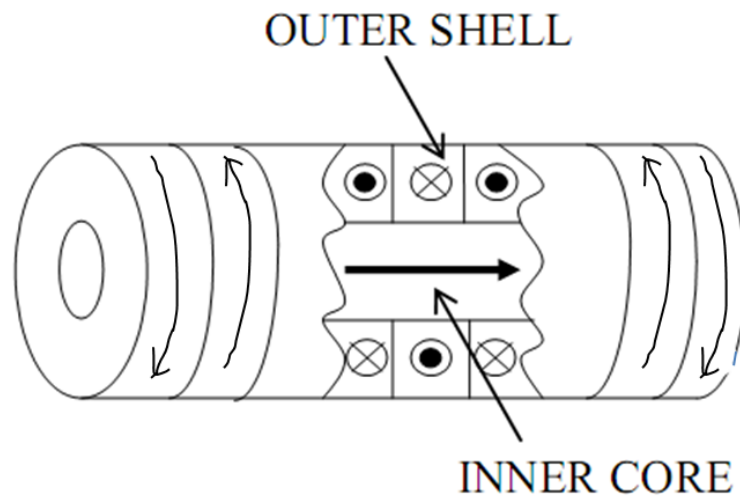


Figure 3.5. Possible domain structure of a negative magnetostrictive wire-shaped amorphous magnetic material.

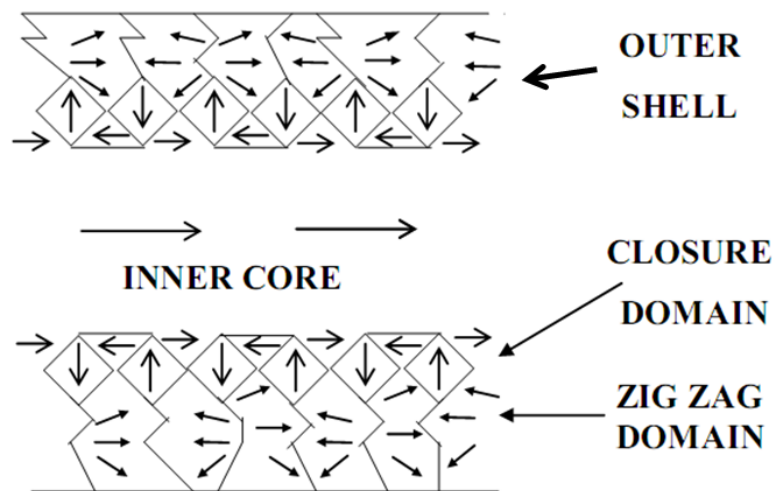


Figure 3.6. Possible domain structure of positive magnetostrictive wire-shaped amorphous magnetic material.

In contrast to the stress dependent results, heat treatment using current pulses indicates an opposite response of the MWs (Fig. 3.4). It is seen that, the sharp jump in magnetization near zero field is decreased in the MW treated with single current pulse. Upon increasing the number of current pulses, the sharp jump observed during switching slowly disappears and it completely disappears on sending four current pulses. On the other hand, the slow rise at higher field is increased in the current pulse treated MW indicating an enhancement of OS volume. The current pulse generates heat to the MW which allows the OS to expand in volume at the cost of the IC. The volume enhancement of the OS is more preferable because of the presence of circular magnetic field corresponding to the current pulse. As the IC volume decrease, the sharp jumps during switching disappear with increasing number of pulse. This is just the opposite case of application of a tensile stress to the MWs where the IC volume increases upon increasing the stress.

We studied another amorphous microwire with the composition $(\text{Co}_{0.93}\text{Fe}_{0.07})_{63}\text{Ni}_{10}\text{Si}_{11}\text{B}_{16}$. We plot the hysteresis loops of as quenched and stress induced MWs in consecutive panels in Fig. 3.7. We observe, the applied stresses (209 MPa and 431 MPa) enhanced the sharp switching in the MWs compared to the as quenched condition. These indicate the enhancement of IC volume.

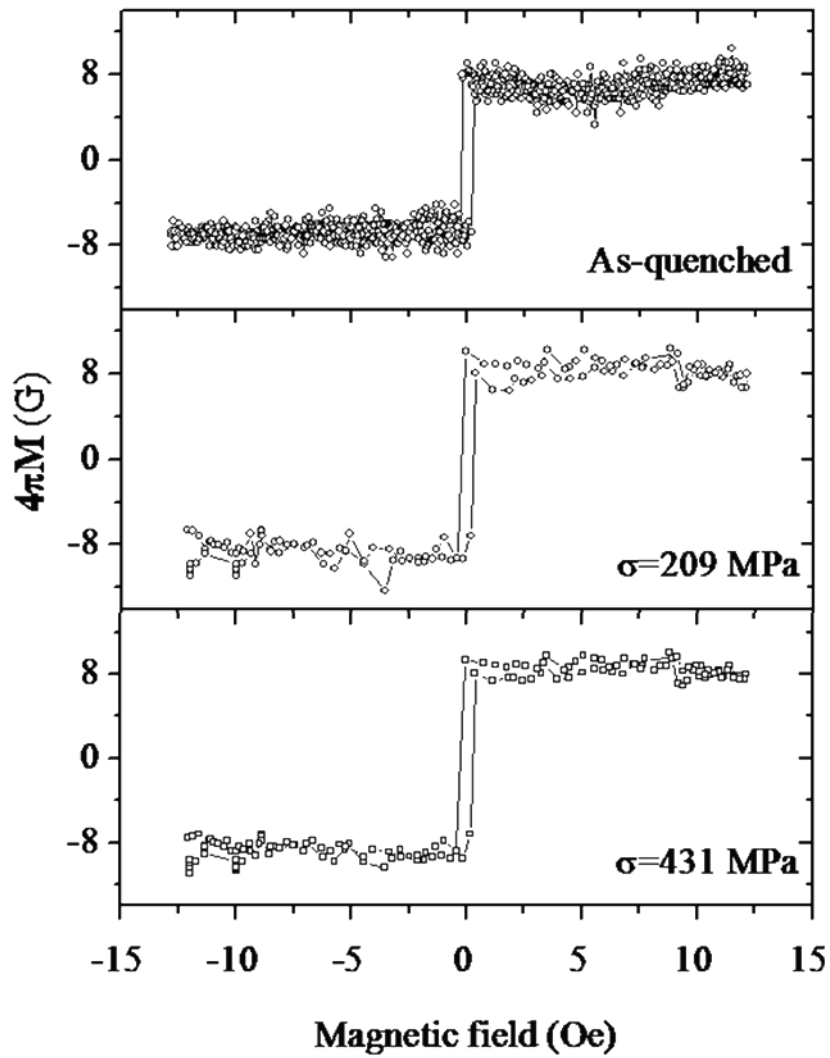


Figure 3.7. The dc magnetic hysteresis loops of the glass-coated amorphous $(\text{Co}_{0.93}\text{Fe}_{0.07})_{63}\text{Ni}_{10}\text{Si}_{11}\text{B}_{16}$ microwire in absence of stress, in presence of 209 MPa and 431 MPa stress.

3.4 Conclusions

Magnetization process of amorphous glass coated MWs with the composition of $\text{Co}_{83.2}\text{Mn}_{7.6}\text{Si}_{5.8}\text{B}_{3.3}$ and $(\text{Co}_{0.93}\text{Fe}_{0.07})_{63}\text{Ni}_{10}\text{Si}_{11}\text{B}_{16}$ MWs are studied in detail under different stressed and current annealing conditions. Surface morphological characterizations done by electron microscope shows the MWs are uniform in diameter throughout their length. Inner metallic core of the MWs have average diameters of ~ 14.7 and $20.5 \mu\text{m}$ respectively with the glass coating thickness of $\sim 5 \mu\text{m}$. It is assumed that, magnetic domains in MWs have two distinct regions, namely IC and OS. IC is a single domain with magnetization along the axis of the MWs. Whereas, the OS is a multidomain region with transverse magnetization. Low field DC magnetic hysteresis loops are recorded at different conditions of the MWs. MWs subjected to external tensile stress along their length show increase in sharp switching indicating the increase of IC volume increases at the cost of OS. Conversely, sending current pulses (100 mA) of short duration (12 sec) have reverse effect on the MWs. They heated up the MWs in the presence of circular magnetic field associated with the current sending through the MWs. As a result, the OS volume increased at the cost of IC which is just reverse the case of stressed MWs. All the results are in accordance with the inner core-outer shell domain structure of the MWs.

Bibliography

- [1] Mohri, K., Humphrey, F. B., Yamosaki, J., Okamura, K., *IEEE Trans Mag*, **20**, 1409 (1984).
- [2] Panina, L. V., Mohri, K., *Appl. Phys. Lett.*, **65**, 1189 (1994).
- [3] Jiles, D. C., *Acta Materials*, **51**, 5907 (2003).
- [4] Ohnaka, I., Melt-spinning into liquid cooling medium, Japanese Patent, **64**, 948 (1980).
- [5] Taylor, G. F., *Physical Review*, **23**, 655 (1924).
- [6] Ulitovsky, A. V., *Pribory I Technika Eksperimenta*, **3**, 115 (1957).
- [7] Larin, V. S., Torkunov, A. V., Panina, L. V., et al. UK Patent GB0108373.2. (2002).
- [8] Humphrey, F. B., Mohri, K., Yamasaki, J., et al. In Proceedings of the Symposium on Magnetic Properties of Amorphous Metals, Hernando, A., Madurga, V., Sanchez, M. C., and Vázquez, M. (EDAX.), North-Holland: Amsterdam, p. 110.
- [9] Vázquez, M., Chen, D-X., *IEEE Trans. Magn.*, **31**, 1229 (1995).
- [10] Vázquez, M., Zhukov, A., *J. Magn. Magn. Mater.*, **160**, 223 (1996).
- [11] Reininger, T., Kronmüller, H., Gómez-Polo, C., Vázquez, M., *J. Appl. Phys.*, **73**, 5357 (1993).
- [12] Squire, P. T., Atkinson, D., Gibbs, M. R. J., Atalay, S., *J. Magn. Magn. Mater.*, **132**, 10 (1994).
- [13] Chiriac, H., Ovari, T. A., *Progress in Materials Science*, **40**, 333 (1996).

Chapter 4

Synthesis and characterization of anodic alumina membrane

4.1 Preamble

Nanotechnology is a result of miniaturization of devices and the development of specific instrumentations leads us to the nanoworld. It allows us to do surface engineering at nano scale resolution. One of the main aspects of nanotechnology is to fabricate various nanostructures, particularly the inexpensive formation of periodically ordered structures (e.g., nanopores, nanotubes and nanowires arrays) with a periodicity of less than 100 nm, has triggered extensive activities in research. The unique properties of the arrays or of an integral functional unit consisting of multiple nanostructures are the result of collective behavior and interactions among them producing response of the system as a whole.¹ Highly ordered nano materials have potential use in the future technologies in the fields as nanophotonic, photocatalytic, microfluidic and sensing devices, as well as functional electrodes and magnetic recording media.¹⁻³

Lithography patterning is the earliest technique to produce various nanostructures (e.g. nanoparticles, nanowires, nanotubes) arranged in highly ordered arrays.⁴ Following all the processing steps of various lithography techniques (e.g. electron-beam, ion-beam, X-ray, interference or holography lithography) with ultra high precision, it is possible to fabricate highly ordered nanostructures with periodicity less than 50 nm.⁵⁻⁸ However, two serious drawbacks that exist in these processes are: low aspect ratio (the ratio of length to diameter) of the formed nanostructures and the high cost of their preparations. These limit the applications of lithography techniques to the laboratory scale. In order to overcome such drawbacks, nanoimprint lithography (NIL) as a high-throughput and low-cost method has been developed for fabricating

nanometer-scale patterns.⁹ Template synthesis in nanometer scale however proved now another elegant, inexpensive and technologically simple approach for the fabrication of various nanoscale sophisticated materials (e.g. arrays of nanowires, nanotubes).^{10, 11} The templates can be synthesized by electrochemical anodization of thin metal sheet (thickness of micrometer length scale) of aluminum, tin or zinc. Depending upon various anodization conditions and surface topology of the metal surfaces, nano sized pores start to form in the oxide layer on the metal surface. Directional growth of the pores within the metal oxides can give rise to an oxide membrane (have a thickness of several microns) with highly ordered nano-channels (diameters of the channels are in nanometer length scale) with a periodicity within a range from few nanometers to several nanometers. We synthesize highly ordered porous alumina templates by electrochemical process. In this chapter we discuss the synthesis procedure of the templates and their structural and magnetic properties.

4.2 Types of alumina oxide films

Alumina templates or membranes consist of self-organized nanopores can be made by anodization of thin aluminum sheet in an electrochemical cell. The detail of the experimental set-up is discussed earlier in *chapter 2*. The anodization of aluminum can result in two different types of oxide films: a barrier type film, and a porous oxide film. Films of controlled morphology may be developed by appropriate selection of electrolyte and film-forming conditions. Thus, films grown at high current efficiency in largely near-neutral electrolytes at ambient temperatures are highly uniform in thickness and relatively compact; such films are termed as barrier films. It has been seen that barrier films may develop at current efficiencies of film formation above approximately 60%.^{12, 13} However, irrespective of the current density, the relatively high field developed across the alumina gives rise to Al^{3+} egress and O^{2-} or OH^- ingress through the anodic film.

In acidic electrolytes, or selected alkaline electrolytes, the relatively compact barrier-type anodic films on aluminum no longer develop as a result of anodic

polarization. Examination of the resultant film at appropriate magnification and resolution reveals a relatively regular porous oxide film.¹⁴ The pores, of cylindrical section, pass normally to the macroscopic aluminum surface but are separated from it by a relatively compact barrier layer of scalloped appearance.

In an alumina membrane, each hollow pore is surrounded by alumina wall and can be consider as a cell. Hence, the pore diameter is defined as the diameter of the pores, wall thickness is the thickness of the alumina wall separating two nearest neighbor pores and interpore distance is the centre to centre distance of two consecutive pores. Ideally, an alumina template will consist of closed packed arrays of hexagonally arranged cells and can be represented schematically as shown in Fig. 4.1 below. The alumina templates or membranes consist of nanopores and are generally characterized by given parameters such as pore diameter, wall thickness, barrier layer thickness and interpore distance.

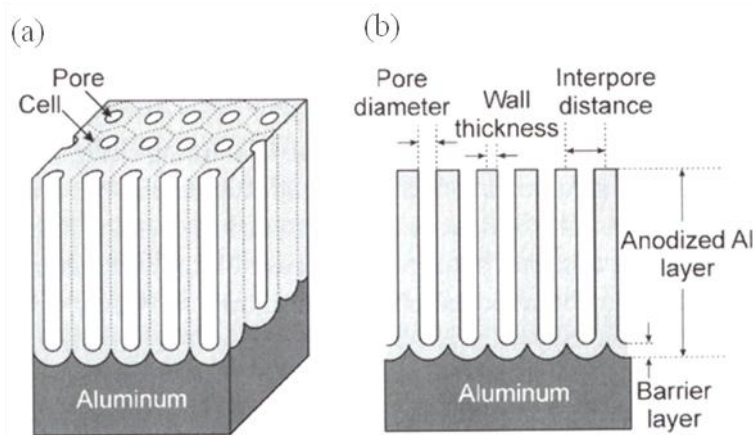


Figure 4.1. (a) Schematic diagram of idealized structure of porous alumina template obtained from anodization of thin aluminum sheet and (b) a cross sectional view of the anodized layer

The pore diameters of the membranes can range from few nanometers to hundreds of nanometers by altering the anodization conditions. On the other hand, the depth of the fine parallel channels can even exceed 100 μm . Research on the growth, morphology and composition of porous anodic films on aluminium have received tremendous attention due to high level of perfection that can be achieved quite easily at various stages in their development. It is known that the major anodic film

parameters (such as, barrier layer thickness and pore and cell diameters) are directly dependent upon the anodization voltage.¹⁵

4.3 Growth mechanism

A particular barrier and porous type anodic films with particular surface morphology can be synthesized by anodizing pure aluminum under specific conditions in various electrolytes allows incorporation of species from the electrolyte. Such an ability to control morphology, particularly for porous anodic films, as well as up-take of electrolyte species, enables tailor making of anodic films for particular applications. For example, relatively large diameter pores are generated by anodizing at high voltages in phosphoric acid compared with the fine pores in the anodic films which are developed rapidly by anodizing in sulphuric acid.

It was previously accepted that the nature of electrolyte used for anodization of alumina is the key factor which determines the type of oxide grown on the surface.¹⁶⁻¹⁸ However, more detail studies later revealed that, there is no distinct difference in the selection of an electrolyte used for the formation of barrier or porous films during the anodization of aluminum.¹⁹⁻²² For porous oxide film of alumina, the film growth is associated with localized dissolution of oxide, as a result of which pores start to form on the barrier type oxide film.

It is possible to fabricate alumina oxide membrane by two step anodization of a thin sheet of aluminum using proper acidic solution. In the first anodization, the barrier layer formed followed by the pore nucleation on the aluminum surface. The oxide removal from the surface of the oxide film is carried out by keeping the sample in a mixture of 6% phosphoric acid and 1.8% chromic acid at an elevated temperature of 60⁰ C for 10-15 minutes. Following the chemical removal of oxide, a periodic concave triangular pattern formed on the aluminum surface acts as self-assembled masks for the second anodizing. The second time anodization leads to the growth of the pores inside the aluminum and form a porous membrane. During the anodization of aluminum, the growth of oxide layer takes place at the metal/oxide interface at the

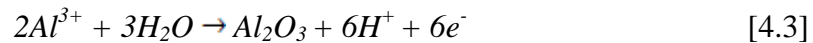
pore bottom, and involves the conversion of a preexisting, naturally occurring film on the surface into a barrier-type film and further into a porous oxide layer. The porous oxide growth accompanied with a thin and compact barrier layer at the pore bottom/electrolyte interface which continuously dissolved by locally increased field, and a new barrier layer at the metal/oxide interface rebuild.

However, the growth mechanism of porous alumina oxide is not known very clearly e.g. which oxygen carrying anion species O^{2-} or OH^- ions are involved in the anodic process. The generation of OH^- ions in an anodizing electrolyte solution can occur in two ways: the simple splitting of water or by cathodic reduction of water followed by the reaction with dissolved oxygen as described below,

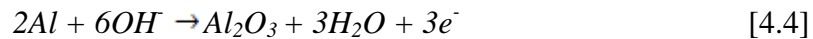


The possible ways of the generation of O^{2-} ions at the electrolyte/oxide interface are: adsorption of OH^- ions by oxygen vacancy annihilation¹² or from water following the interaction with adsorbed electrolyte anions¹³ in the process as shown in Fig. 4.2. In the latter process, OH^- ions may also be produced.

The anodic polarization of the Al sheet in acidic electrolyte solution leads to the formation of amorphous oxide film growth on the surface of the Al sheet according to the following reactions:



and



The growth of oxide occurs mainly at oxide/metal interface for typical acidic electrolyte solutions containing sulfuric, phosphoric, chromic, acetic, oxalic acids etc. It is widely accepted that, the pore formation is attributed to the thermally assisted, field accelerated dissolution of oxide at the base of the pores. The growth of porous

alumina involves the inward migration of oxygen containing ions (O^{2-} / OH^-) from the electrolyte through the barrier layer and simultaneous outward drift of Al^{3+} ions across the oxide layer (shown in Fig. 4.2). In the steady state of the process, i.e. during the formation of porous oxide structure, a dynamic equilibrium is maintained between the local field assisted dissolution of barrier layer at pore bottom/electrolyte interface and the rate of new barrier layer formation at metal/oxide interface.

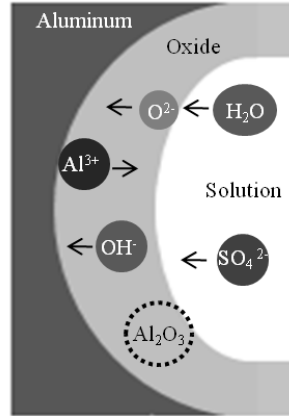


Figure 4.2. Schematic illustration of ions movement and dissolution of oxide barrier layer at pore bottom in a typical sulfuric acid solution.

The side reactions that are responsible for the evolution of oxygen¹⁴⁻¹⁵ near metal/oxide interface are as follows:



Or alternately,



At high anodizing potential, it is observed that the generation of oxygen is also possible through the following reaction:



The evolution of oxygen bubbles may enhance further near the metal/oxide interface due to the presence and compositions of impurities or second phase

particles.^{15, 16} It is suggested that oxygen evolution is directly connected with the growth of porous alumina film and it is useful for testing from barrier-type to porous-type coatings.¹⁷

For steady state porous oxide growth, the locally increased field at the electrolyte/oxide interface affects the dissolution of oxide in the pore bases.¹⁸ Moreover, the oxide growth rate at the metal/oxide interface increases due to the increasing field assisted dissolution of oxide. The field assisted dissolution starts from the polarization of Al-O bonds, followed by the removal of Al³⁺ ions from the oxide structure.¹⁹ The removal of Al³⁺ ions occurs more easily in the presence of the field.

4.4 Synthesis and microstructures of porous oxide films

In order to prepare alumina membrane in a more simple way, we first try to anodize a thin sheet of aluminum (Al) with the thickness of ~ 135 nm and dimension of ~ (5 × 10) mm using phosphoric acid. The aluminum sheet has the purity of ~ 99.998% and purchased from Sigma Aldrich. The sheets are available with prior electro-polished. One side of the sheets is covered by a Bakelite structure (Fig. 2.2 in *chapter 2*) so that only the other side of aluminum comes to the contact of electrolyte solution. The concentration of the phosphoric acid solution is 0.42 M. A constant voltage of 34 V is applied between the Al thin sheet and Au wire (the cathode). The anodization is carried out at room temperature for 10 minutes. After the first anodization, the FESEM images are taken and shown in Fig. 4.3. The cross sectional view of the membrane shows the formation of channels with a radius of ~ 80 nm and length of ~ 2 to 2.5 μm. Moreover, the channels are seems to be cross linked with each other. The pore initiation from the top surface (Fig. 4.3) is neither regular nor easy to observe as most of the pores on the surface are blocked with alumina. In order to see the effect of time, we increased the time and did an anodization for 1 hour and the FESEM micrograph of the resultant alumina film as shown in Fig. 4.4. In this case, the pores can be seen from the top surface of the film with an average radius of ~ 80 nm. The surface of the film has seen to be covered with residual alumina confirmed by

EDX and XRD which are started to dissolve during the anodization by phosphoric acid solution.

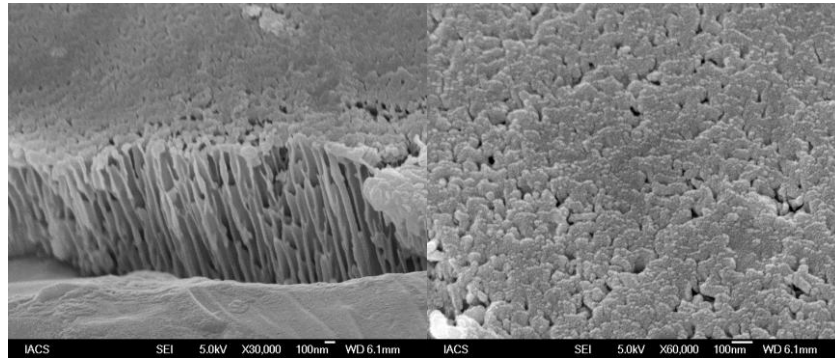


Figure 4.3. Alumina membrane prepared using 0.42 M H_3PO_4 under a constant potential of 34 V for 10 minutes at room temperature: (left) side view, (right) top view.

The time and voltage both are then increased to 14 hours and 64 V respectively. The right panel in Fig. 4.4 shows the FESEM micrograph of top surface of the alumina film. In this case, the top surface of the alumina film is free from residual alumina due to the long time interaction of film surface with the phosphoric acid. However, most of the pores are blocked on the surface whereas the pores with lower diameters get opened in the process.

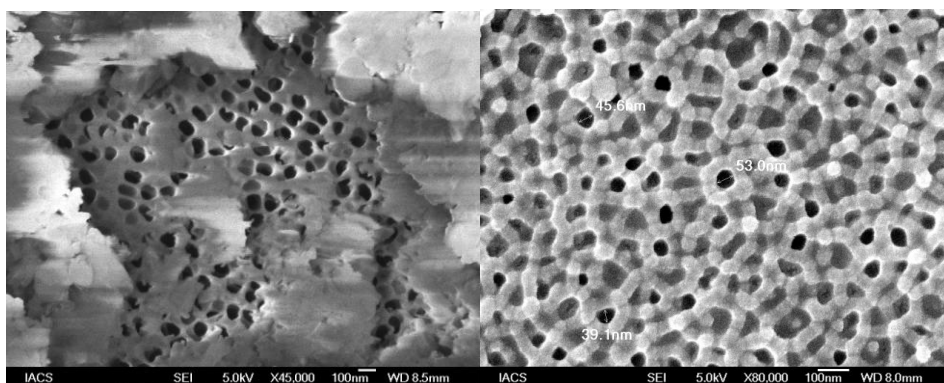


Figure 4.4. Top view of alumina membrane prepared at room temperature using 0.42 M H_3PO_4 under a constant potential of 34 V for 1 hour (left) and at 68 V for 14 hours (right).

In order to accelerate the pore opening process by etching out the alumina from top surface of the film, we add 0.001 M of chromic acid. We hoped, the growth of the nano channels through the aluminum would also enhance by the use of chromic acid. An anodization of a similar aluminum sheet is carried out for 1 hour and 40 minutes keeping the voltage constant at 34 V. The SEM study reveal (see Fig. 4.5), the pore formation on the surface of the alumina film is quite irregular. The diameter also varies in a wider range from ~ 50 nm to 250 nm.

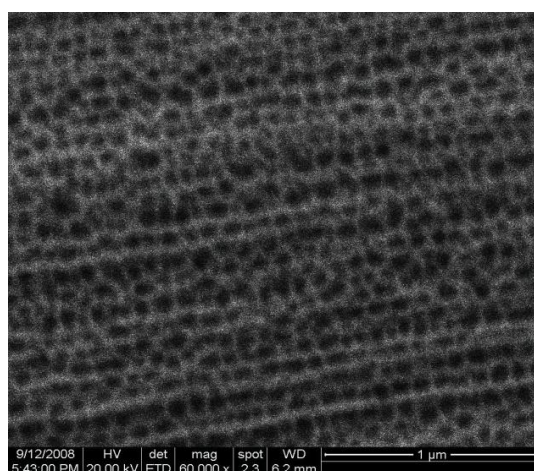


Figure 4.5. Top view of the alumina membrane prepared by using 0.001 M H_2CrO_4 mixed with 0.42 M H_3PO_4 solution under a constant potential of 34 V for 1 hour 40 minutes at room temperature.

As far we observe, the single step anodization using phosphoric acid or mix with chromic acid is not good for preparing highly ordered porous membrane with parallel nano channels through the membrane without any cross link among them.

With the target fixed for getting highly ordered porous membrane, we use oxalic acid ($\text{C}_2\text{H}_2\text{O}_4$) electrolyte solution. The concentration of oxalic acid is taken as 3 wt% as the voltage maintained at a constant value of ~ 60 to 62 V to achieve a current density of $2\text{mA}/\text{cm}^2$. The anodization is carried out at 11°C to dissipate the heat generated during the exothermic reaction of conversion of aluminum in to alumina. The first anodization is carried out for 10-30 minutes. After the first anodization, oxide removal from the surface of the film is carried out as described earlier. The self-assembled mask on aluminum after the first anodization followed by oxide removal is shown in the SEM micrograph in Fig. 4.6.

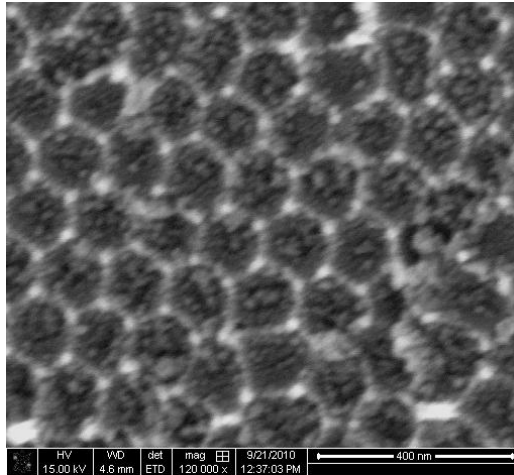


Figure 4.6. FESEM micrograph of alumina layer on aluminum sheet after first anodization followed by post treatment.

The second anodization is conducted then at same potential used for the first anodization. Finally the hexagonally arranged nanopores structure is detached from the base aluminum using mercury chloride (HgCl_2) solution. If desired, the pore opening and widening of the resultant alumina membrane can be done using 5% phosphoric acid solution. The alumina membranes are then characterized by SEM, FESEM and the micrographs are shown in Fig.4.7.

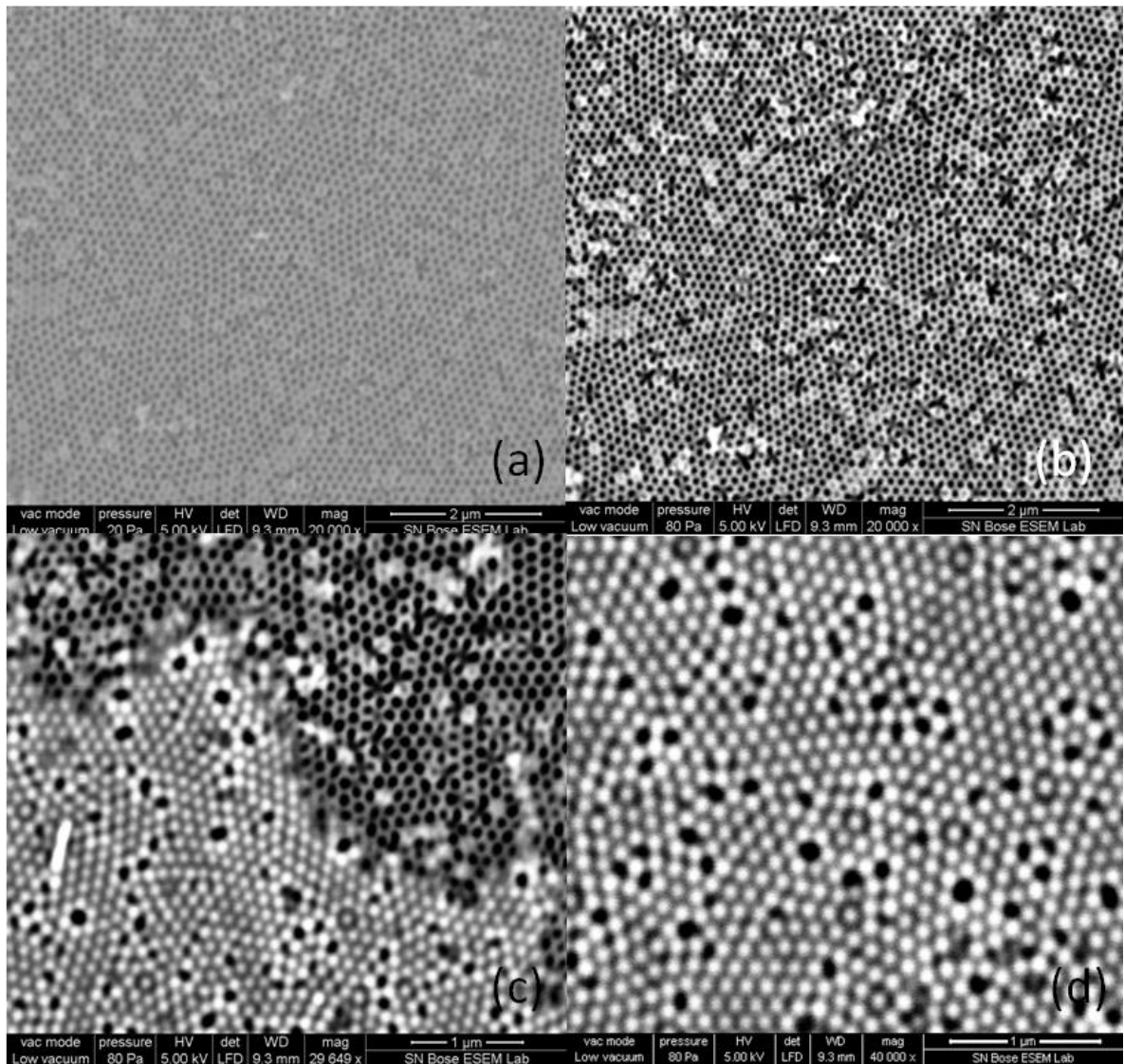


Figure 4.7. FESEM micrographs of alumina membranes obtained after two step anodization at 60 V for 2 hrs. (a) & (b) The top surface of the membrane. (c) Back side of the membrane after partial pore opening treatment using phosphoric acid. (d) The pore bottoms on the backside of membrane.

The FESEM micrographs of the resultant membrane show uniform pore formation [Fig.4.7(a), 4.7(b)] on the top side of alumina membrane though a large region. Whereas the backside of the membrane after partially pore open region is shown in Fig.4.7(c). A close view of the pore bottom is shown in Fig. 4.7(d). It is observed that the pores are arranged in a hexagonal pattern within the membrane. In Fig.4.8 we can see a closer view of a selected region of the top surface of the membrane. It shows an average pore diameter of ~ 73 nm with an average pore separation of ~ 145 nm.

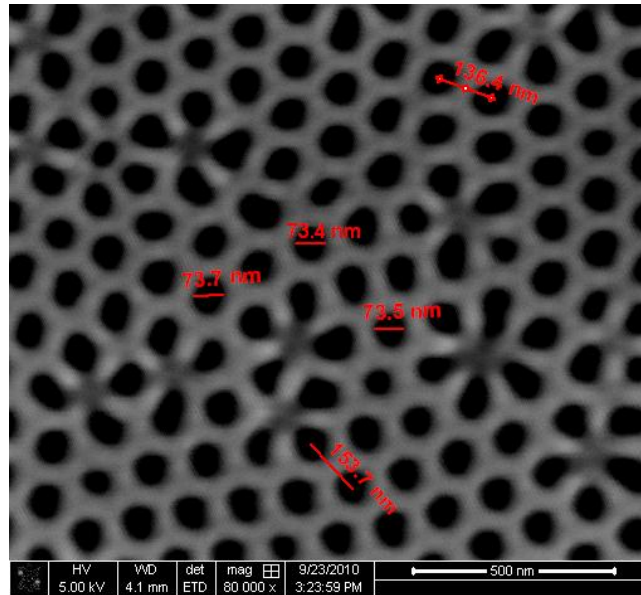


Figure 4.8. A high resolution FESEM micrograph of the top surface of alumina membrane after two step anodization at 60 V for 2 hrs.

Different pore diameters can be achieved using different potentials of anodization and different time of pore widening treatment. Fig.4.9 shows the SEM micrographs of the top surface of membrane obtained after two step anodization under a potential difference of ~ 64 V followed by a pore widening treatment in phosphoric acid. It shows a wide range formation of uniform pores. The average diameter of the pores is ~ 100 nm. Pore widening process is a sophisticated process during which the alumina going to dissolve in acidic solution at some elevated temperature (typically $\sim 60^{\circ}$ C) and widened the pore diameter. Here, the applied potential is nearly same as previous but with the pore widening treatment the average pore diameter of ~ 100 nm is obtained.

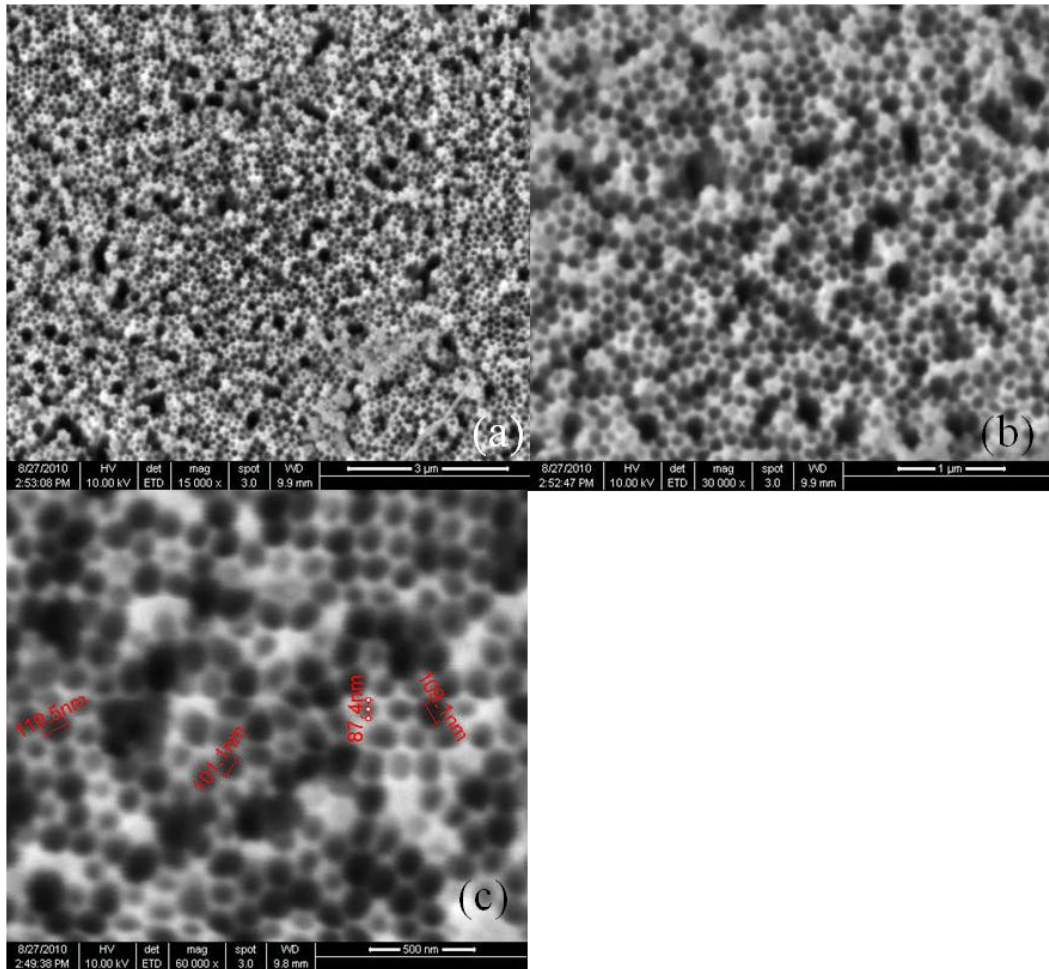


Figure 4.9. SEM micrograph of top surface of alumina membrane prepared using a potential of ~ 64 V for 2 hrs followed by a pore opening and widening treatment in phosphoric acid. (a) Long range formation of uniform pores, (b) a close view (c) a closer view with pore parameters measurements.

Fig.4.10 shows the FESEM micrographs of alumina membrane prepared by two step anodization process under a potential of ~ 55 V. The pore opening treatments are partially performed in this case. The micrographs clearly show the hexagonal shape of the cells with a hexagonal close-packed arrangement among themselves. The average pore diameter is of ~ 50 nm with an average center to center distance between the pores is of ~ 134 nm.

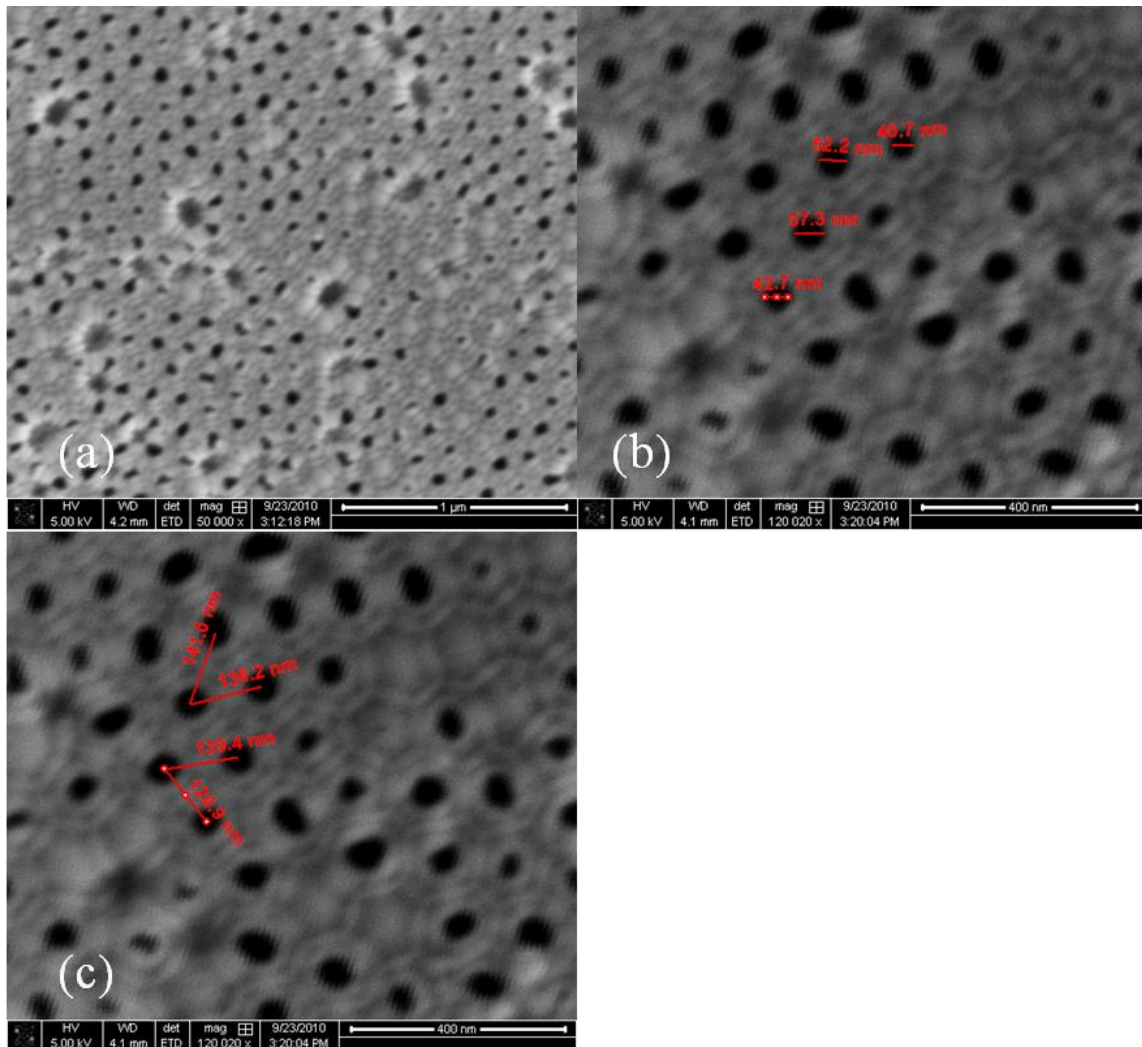


Figure 4.10. FESEM micrograph of alumina membrane obtained by two step anodization using a potential difference of ~ 55 V for 2 hrs (a) followed by a partial pore opening treatment, (b) a close view of the surface with pore diameter measurements, (c) a close view of the surface with pore separation measurements.

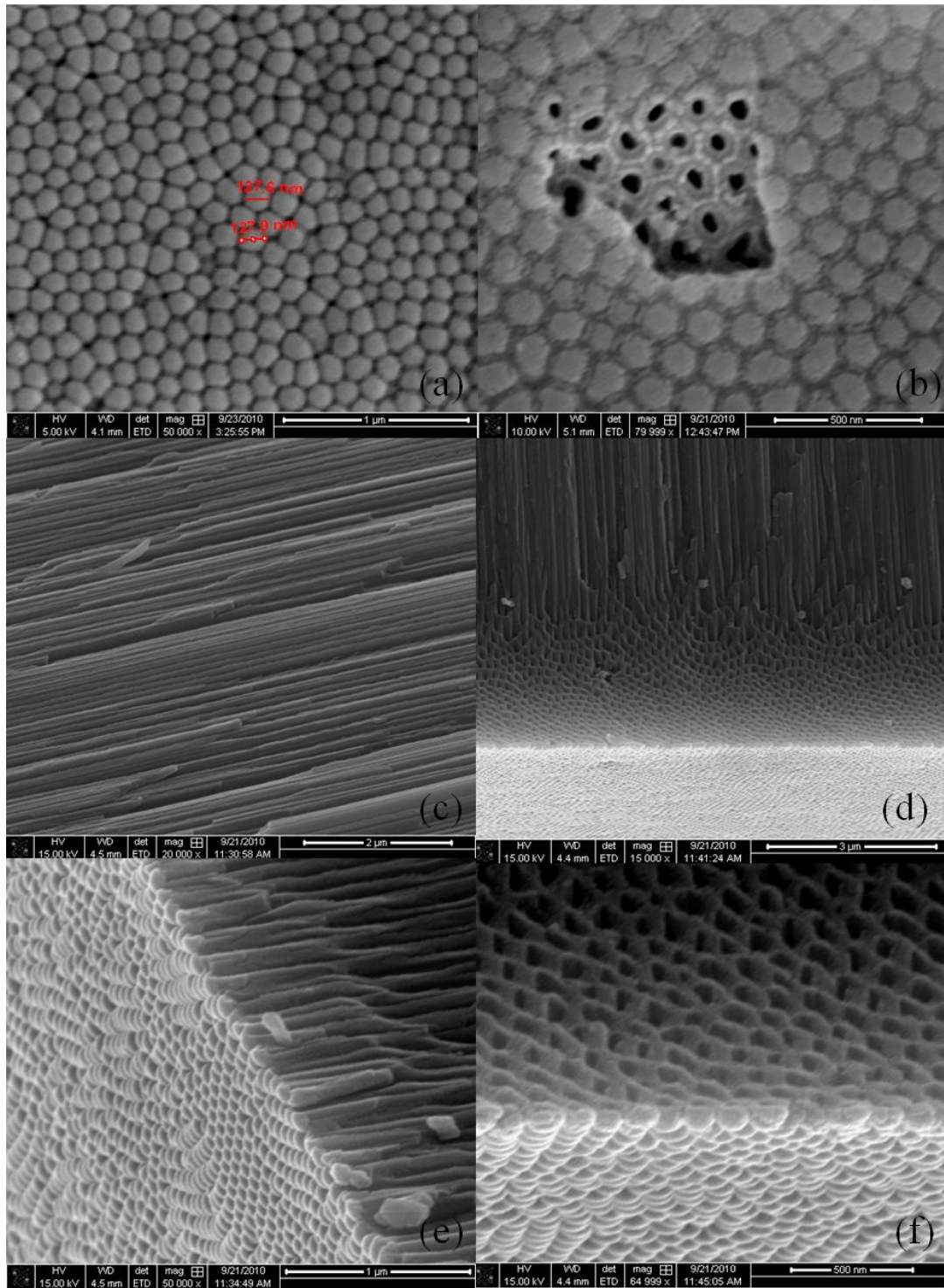


Figure 4.11. FESEM micrographs of the alumina membrane prepared using two step anodization under a potential of ~ 55 V for 2 hrs (a) pore bottoms at the back side of the membrane after dissolving the aluminium base by HgCl_2 (b) A closer view of the pore bottom with a partially open region (c) & (d) cross sectional view of the membranes (e) & (f) typical views of the edges of the membranes.

The pore bottoms of the membrane are shown in Fig.4.11 (a) and (b). The closer view of the pore bottom on the back side of the membrane [Fig.4.11 (b)] shows a clear hexagonal structure of the pore cell. The cross sectional view of the membrane [Fig.4.11(c), 4.11(d)] shows the uniform growth of the channels through the membrane and are not cross linked with each other. The typical edges of the membranes are shown in Fig 4.11(e) and 4.11(f) which shows the sharp edges of the membranes. The second anodization performed under a potential difference within a range of 55-64 V for 2 hour duration typically produce a membrane with thickness 41.25 μm and is shown in Fig.4.12.

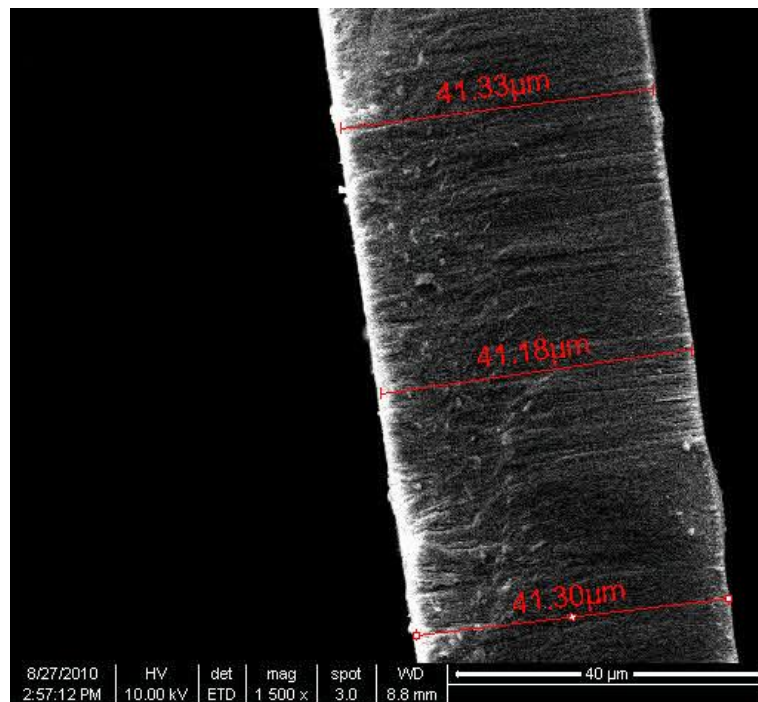


Figure 4.12. FESEM micrograph of a cross sectional view of a typical membrane synthesized by two step anodization process using different potential differences from 55 to 64 V for 2 hrs.

4.5 Elemental and crystalline phase characterization

Elemental study of the membranes is performed by EDAX. The EDAX spectra are shown in Fig. 4.13 and indicate the presence of Al and O. The XRD pattern obtained from powder diffraction of the alumina membrane after dissolving the Al base shown in Fig.4.14. The powder diffraction has no distinct peak and indicates the amorphous nature of the membrane synthesized using oxalic acid solution.

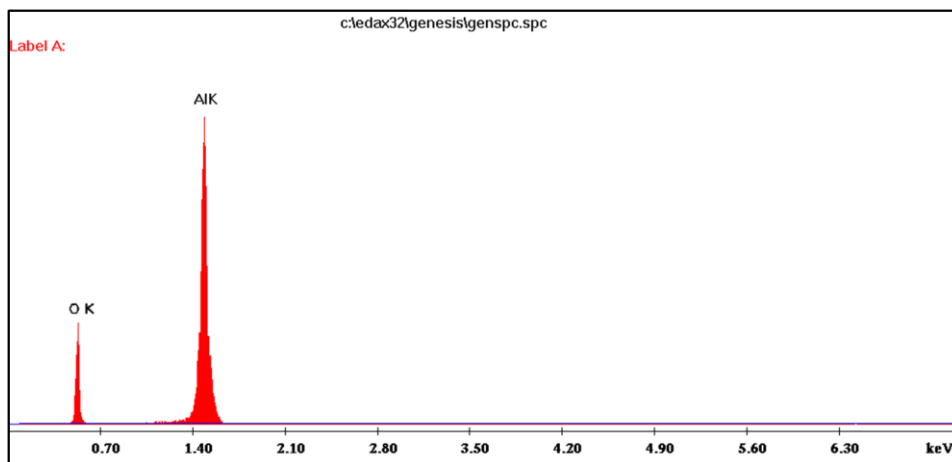


Figure 4.13. EDAX spectra of alumina membranes prepared in lab.

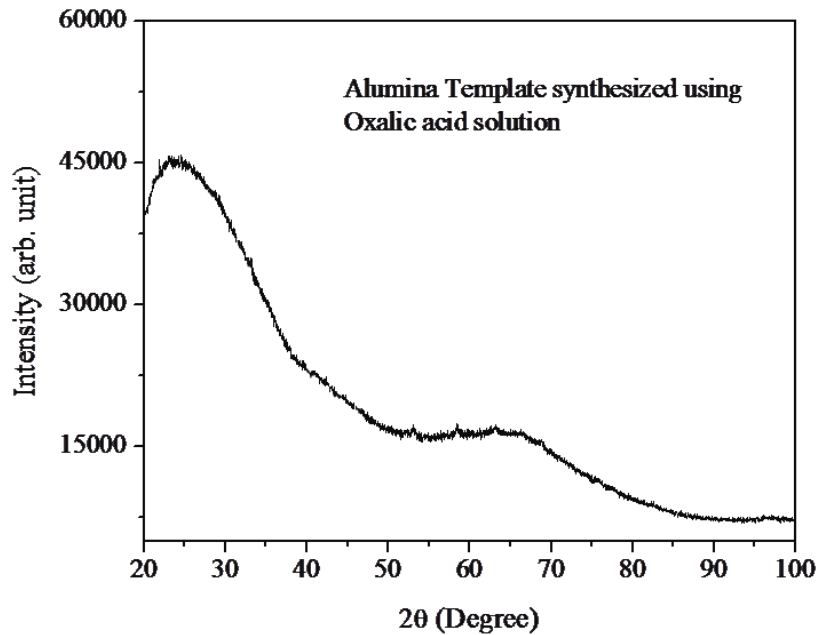


Figure 4.14. XRD spectra of alumina membranes prepared using oxalic acid solution.

4.6 Magnetic characterization

It is well known that, pure aluminum is paramagnetic in nature at room temperature. During the anodization of aluminum, the conversion of aluminum to alumina oxide started to form on the surface of aluminum. The magnetic state of alumina membrane after being taken out from the aluminum base has been studied by VSM. Magnetization loop of the membrane measured at room temperature indicates diamagnetic phase as shown in Fig. 4.15. The data points (red) in up-side down triangle indicate the MH loop of a membrane placed in a diamagnetic sample holder used for VSM. The data points in triangular symbol (green) indicate the MH loop of the sample holder only. However, the linearly fitted curves of the MH loops are represented by orange and deep green solid lines for membrane with sample holder and bare sample holder respectively. The solid line in violet color thus indicates the sample holder subtracted diamagnetic MH loop of the membrane only. From the curve it is observed that the membrane has a weak diamagnetic property with lower initial

susceptibility than the sample holder. The Al and O are both paramagnetic in nature but while they form the amorphous Al_2O_3 , it becomes diamagnetic because of the covalent bond form between them.

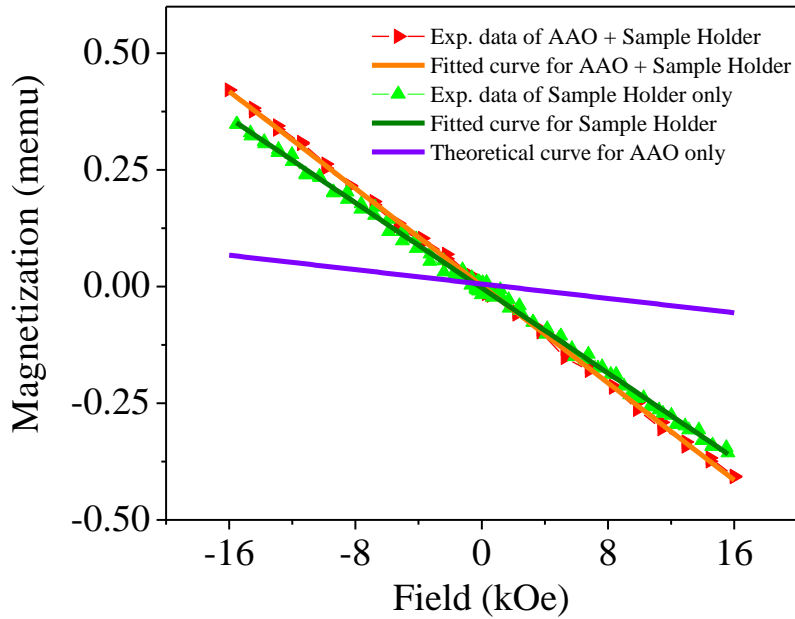


Figure 4.15. Experimental MH loops of AAO membrane with sample holder (red triangle with up-side down) and of sample holder only (green triangle). Linearly fitted straight lines for membrane with VSM sample holder (orange) and for VSM sample holder only (deep green). Sample holder subtracted theoretical straight line for AAO membrane only (solid line in violet color).

4.7 Synthesis of Zinc-Oxide nanowires using the AAO membrane

Two dimensional arrays of Zinc-Oxide (ZnO) NWs using the alumina membranes have been synthesized by simple wet chemical process. The membranes with an average pore diameter of 50 nm have been used in this purpose. The NWs are formed within the pores of the membranes by dipping the membranes into saturated 0.1 M solution of $\text{Zn}(\text{CH}_3\text{COOH}) \cdot 2\text{H}_2\text{O}$ prepared in ethanol followed by drying and

annealing of the membranes. The membranes are used to dipped within the solution for four to five days so that the solution can reach inside the nanopores. The surfaces of the membranes are washed very carefully to remove the acetate solution from the surface. The membranes then kept at room temperature till they become dry. Thermal annealing of the membranes at 450°C for 2 hrs has done at the last stage of the synthesis procedure. During the annealing of the templates, arrays of ZnO NWs form within the nanopores through the decomposition of the acetate salt. In order to dope the NWs with different atomic % of Potassium (K), one can add selective amount of potassium acetate to the zinc acetate solution.

The SEM characterizations of the NWs are performed after dissolving the membranes in 2 M NaOH solution and are shown in Fig. 4.16 (a). It shows the clear formation of the NWs. The X-ray diffraction patterns confirm the formation of undoped and K-doped ZnO hexagonal wurztite crystal structure as are shown in Fig. 4.16 (b). The XRD patterns clearly show the distinct peaks of ZnO. The diffraction peaks correspond to Al is because of the presence of aluminium substrate beneath the alumina membrane.

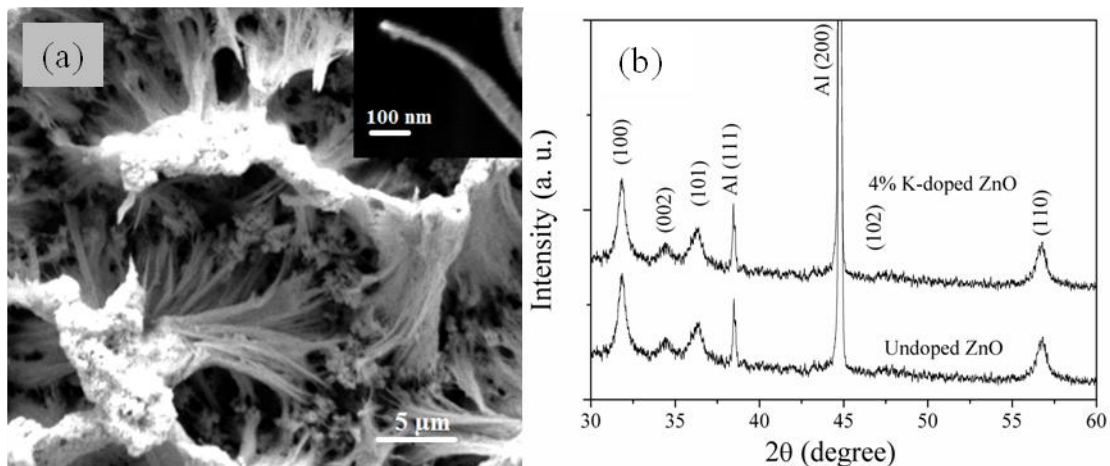


Figure 4.16. (a) SEM micrograph of ZnO NWs after dissolving the membrane by NaOH solution with an inset showing a single NW and (b) XRD spectra of undoped and K-doped ZnO NWs.

The elemental analysis of the NWs has performed by EDAX whereas the optical and magnetic properties have been characterized by photoluminescence spectroscopy and vibrating sample magnetometer respectively and the detail of the work can be found in reference [33].

4.8 Conclusions

We successfully prepare the Alumina membranes using oxalic acid solution by a two step anodization process. Structural characterizations done by electron microscopes clearly show the formation of uniform pores with hexagonal cell structure. A dynamical equilibrium between the local field assisted dissolution of the barrier layer and conversion of Al into Al_2O_3 at metal/oxide interface help to grow the nano-channels through the oxide film converting all the sample into porous membrane.

Anodization of Al is an exothermic reaction. At an elevated temperature, phosphoric acid solution can open the pore on the anodized surface of Al. But, one step anodization is no good even using a mix solution of chromic and phosphoric acid. Post anodization treatments both after the anodization are crucial to clean or open or widen the pores. It is possible to grow pores with different diameters by using different anodization potential and employing different post anodization treatments. The elemental analysis is done by EDAX whereas the amorphous nature of the membrane is confirmed by XRD patterns.

Magnetic measurements are astonishing as we observe weak ferromagnetic hysteresis loops for the Al base and Al base/AAO film composite. The samples are prepared and measured with highest sincerity to avoid any contamination. The measurements repeatedly show ferromagnetic nature of the samples. The Al base/AAO composite and the annealed Al bases show enhanced ferromagnetism compared to mere Al base and un-annealed Al base respectively. As there are no other sources of ferromagnetism present in those sample, we believe the ferromagnetism is originated

from the localized defects that form within the Al base and Al base/barrier layer interface during the anodization.

Bibliography

- [1] Rosei, F., *J. Phys. Condens. Matter*, **16**, S1373-S1436 (2004); Chik, H. and Xu, J. M., *Mater. Sci. Eng. R*, **43**, 103-138 (2004).
- [2] Letant, S. E., van Buuren, T. W. and Terminello, L. *J. Nano Lett.*, **4**, 1705-1707 (2004).
- [3] Islam, T., Mistry, K. K., Sengupta, K. and Saha, H. *Sensors Mater.*, **16**, 345-356 (2004).
- [4] Martin, J. I., Nogues, J., Liu, K., Vicent, J. L. and Schuller, I. K. *J. Magn. Magn. Mater.*, **256**, 449-501 (2003).
- [5] Duvail, J. L., Dubois, S., Piraux, L., Vaures, A., Fert, A., Adam, D., Champagne, M., Rousseaux, F. and Decanini, D., *J. Appl. Phys.*, **84**, 6359-6365 (1998).
- [6] Lodder, J. C., *J. Magn. Magn. Mater.*, **272-276**, 1692-1697 (2004).
- [7] Miramond, C., Fermon, C., Rousseaux, F., Decanini, D. and Carcenac, F. *J. Magn. Magn. Mater.*, **165**, 500-503 (1997).
- [8] Turberfield, A. J. *MRS Bulletin*, August, 632-636 (2001).
- [9] Chou, S. Y., Krauss, P. R. and Renstrom, P. R. *J. Vac. Sci. Technol. B*, **14**, 4129-4133 (1996).
- [10] Sun, L., Searson, P. C. and Chien, C. L. *Appl. Phys. Lett.*, **74**, 2803-2805 (1999).
- [11] Ross, C.A., Hwang, M., Shima, M., Smith, H. I., Farhoud, M., Savas, T.A., Schwarzacher, W., Parrochon, J., Escoffier, W., Bertram, H. N., Humphrey, F.B., Redjda, M., *J. Magn. Magn. Mater.*, **249**, 200-207 (2002).
- [12] Brown, F. and Mackintosh, W.D., *J. Electrochem. Soc.*, **120**, 1096 (1973).
- [13] Kobayashi, K., Shimizu, K., Thompson, G.E. and Wood, G.C., *J. Appl. Electrochem.*, **15** (1985) 781.

- [14] O'Sullivan, J.P. and Wood, G.C., Proc. Roy. Soc. London, **A317**, 511 (1970).
- [15] Wood, G.C., Skeldon, P.G., Thompson, E. and Shimizu, K., J. Electrochem. Soc., **143**, 74 (1996).
- [16] Keller, F., Hunter, M. S. and Robinson, D. L. J. Electrochem. Soc., **100**, 411-419 (1953).
- [17] Young, L. Anodic Oxide Films, Academic Press, London and New York, pp. 193-221 (1961).
- [18] Despic, A. R. J. Electroanal. Chem., **191**, 417-423 (1985).
- [19] Wang, H. and Wang, H. W. Mater. Chem. Phys., **97**, 213-218 (2006).
- [20] Jia, Y., Zhou, H., Luo, P., Luo, S., Chen, J. and Kuang, Y. (2006) Surf. Coat. Technol., **201**, 513-518.
- [21] Mozalev, A., Poznyak, A., Mozaleva, I. and Hassel, A. W. *Electrochem. Commun.*, **3**, 299-305 (2001).
- [22] Shingubara, S., Morimoto, K., Sakaue, H. and Takahagi, T. *Electrochem. Solid State Lett.*, **7**, E15-E17 (2004).
- [23] Siejka, J. and Ortega, C., J. Electrochem. Soc., **124**, 883-891 (1977).
- [24] O'Sullivan, J. P. and Wood, G. C. Proc. Roy. Soc. Lond. A, **317**, 511-543 (1970).
- [25] Zhu, X. F., Li, D. D., Song, Y. and Xiao, Y. H. Mater. Lett., **59**, 3160-3163 (2005).
- [26] Shimizu, K., Habazaki, H. and Skeldon, P. Electrochim. Acta, **47**, 1225-1228 (2002).
- [27] Crossland, A.C., Habazaki, H, Shimizu, K., Skeldon, P., Thompson, G. E., Wood, G. C., Zhou, X. and Smith, C. J. E., Corros. Sci., **41**, 1945-1954 (1997).
- [28] Zhu, X. F., Li, D. D., Song, Y. and Xiao, Y. H., Mater. Lett. **59**, 3160-3163 (2005).

- [29] Thompson G. E., Thin Solid Films, **297**, 192-201 (1997).
- [30] O'Sullivan, J. P. and Wood, G. C. Proc. Roy. Soc. Lond. A, **317**, 511-543 (1970).
- [31] Sigma-Aldrich Corp. USA.
- [32] Khan, G. G., Mukherjee, N., Mondal, A., Bandyopadhyay, N.R., Basumallick, A., *Matts. Chem. Phys.* 122, 60 (2010).
- [33] Ghosh, S., Khan, G. G., Das, B. and Mandal, K., *J. App. Phys.* **xx**, xxxx (2011).

Chapter 5

Structural and magnetic properties of 2- dimensional arrays of Ni NWs

5.1 Preamble

Research on ferromagnetic NWs has attracted increasing interest in material science because of their potential applications in various fields, particularly in high density perpendicular magnetic storage.¹⁻⁴ Highly ordered arrays of magnetic NWs show novel and interesting magnetic properties different from those of bulk and thin films and sensitively depend on their sizes, shapes, and the interactions between them.⁵⁻⁷

Among the various methods for preparing NWs, electrodeposition technique is widely used because of its simplicity, cost effective and sophistication. In this method, various ferromagnetic metals such as Fe, Co, Ni and their alloys can deposit into the nanopores of silica, alumina, or polycarbonate porous substrates or membranes by the electrodeposition technique.⁸⁻¹⁰ The process leads to the formation of two dimensional (2D) arrays of thousands of NWs within the membranes with their long axes parallel to each other. Elongated shape of the NWs determined their shape anisotropy that plays a dominating role in governing the magnetic properties of a single NW such as, magnetic easy direction, coercivity, remanence etc.

Magnetic behavior of the arrays of NWs is determined by the magnetic nature of individual NWs controlled by the geometrical shape and orientation of crystal axes, texture as well as by the magnetostatic interactions among the NWs. In the present work, Ni NWs with diameters of ~ 150 and 275 nm are prepared in alumina membrane

by the electrodeposition method. Surface morphology and structural characterization of the NWs are done in detail. Magnetic properties of the arrays of NWs, such as magnetic hysteresis loops and hence the coercivity, squareness are studied at various temperatures between 80 and 350 K for different aspect ratio AR (= length/diameter) of the NWs. The experimental results suggest the development of magnetic easy axis perpendicular to the wire axes with vortex remanent state^{4, 5, 11} in the NWs. Attempt has made to investigate the magnetic hysteresis loops of three isolated NWs by magneto optical Kerr effect (MOKE) measurement.

5.2 Experimental

Synthesis of Ni NWs

2D arrays of Ni NWs are fabricated within the pores of alumina membranes by simple DC electrodeposition method. The thickness of a 13 millimeter circular alumina membrane is approximately 60 μm with nano-sized pores of average diameter of $\sim 150, 275$ nm and a pore density of $\sim 10^9$ / cm^2 . To use it as an electrode, one side of it was coated with a conductive gold layer of ~ 0.1 μm thickness by the thermal evaporation technique. All electrochemical deposition of Ni NWs is carried out in a three electrode electrochemical cell supported by a potentiostat as described in *chapter 2*.

The gold-coated membrane is used as working electrode and acts as cathode whereas a platinum (or gold) wire and a saturated Ag/AgCl electrode are used as the counter and reference electrodes respectively. Ni is electrodeposited at room temperature using an aqueous electrolyte containing 0.57 M of NiSO₄ and 0.32 M of H₃BO₃. Boric acid is used as buffer solution and the pH of the solution is adjusted between ~ 3.5 and 4.0. The constant potential for the electrodeposition is chosen as -0.85 V followed by linear sweep voltametry results. Electrodeposition is performed for different durations in order to obtain NWs with different lengths (hence different aspect ratios, ARs).

5.3 Results and discussions

5.3.1 Structural and elemental properties

In structural characterization of the NWs, we study the geometrical structure of the NWs by scanning electron microscope (SEM). The micrographs obtained through the study gives us an idea of surface morphology of the NWs and determine their length and diameter. We did structural characterization of the NWs using powder X-ray diffraction (XRD) and the elemental study is done by energy dispersive analysis of X-ray (EDAX). In order to do the SEM, FESEM study and EDAX analysis of NWs, the alumina membranes are dissolved in 2 M of NaOH solution at room temperature. SEM micrographs of NWs are also often taken without dissolving the alumina membranes. Ni NWs with the diameter of 150 nm are shown in the SEM micrographs in Fig. 5.1. The left micrograph in Fig. 5.1 shows the NWs, within alumina membrane, having length of 1.4 μm i.e. the AR ~ 9 and the right micrograph shows the NWs, without alumina membrane, having length of 28.4 μm i.e. the AR ~ 189 . The micrographs also indicate the uniformity in length and diameter of the NWs.

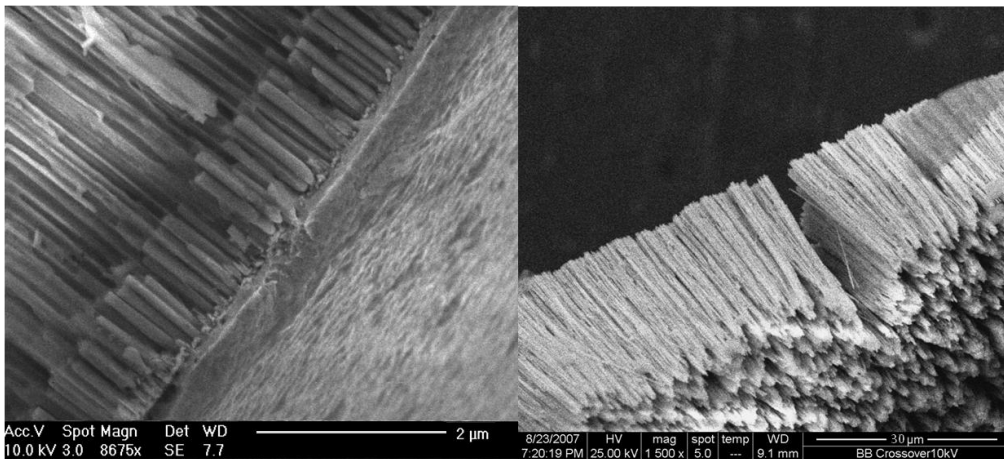


Figure 5.1. SEM micrographs of Ni 150 nm NWs (left) having length of $\sim 1.4 \mu\text{m}$ within the alumina pores and (right) having length of $\sim 28.4 \mu\text{m}$ after dissolving the alumina membrane.

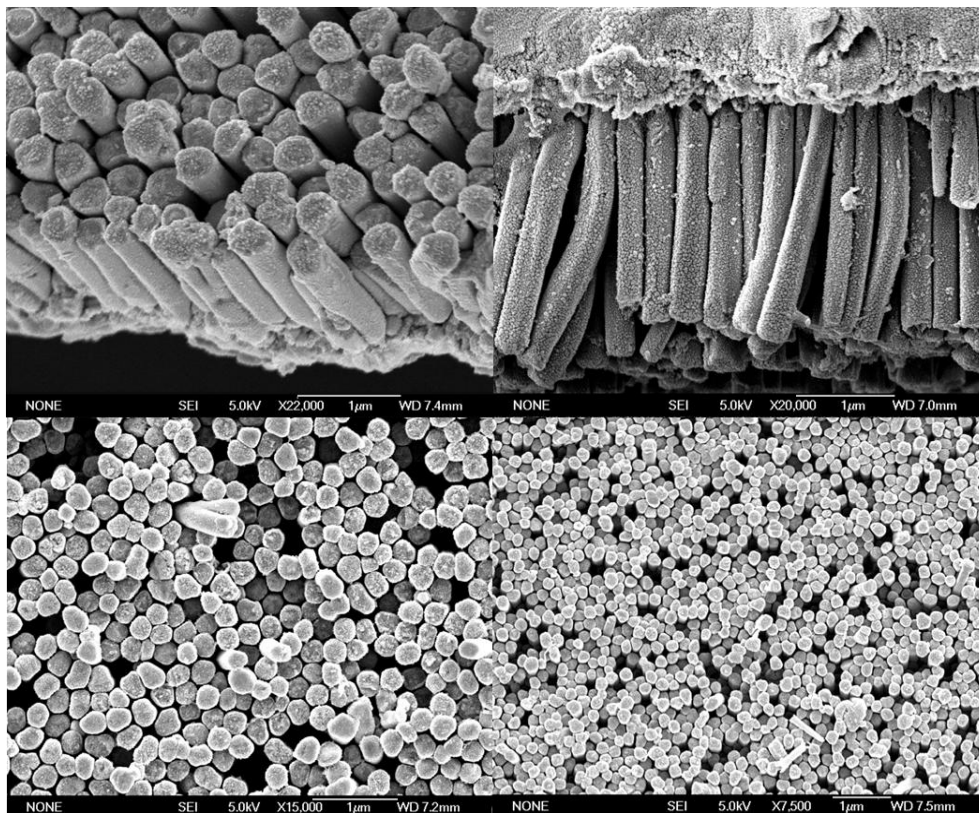


Figure 5.2. FESEM micrographs of Ni 275 nm showing the NWs after dissolving the alumina membranes. (top left) Side view of the NWs having average length of $\sim 1.37 \mu\text{m}$, (top right) side view of the NWs having average length of $\sim 2.1 \mu\text{m}$, (bottom left) top view of $1.37 \mu\text{m}$ long NWs and (bottom right) top view of $2.1 \mu\text{m}$ long NWs.

Fig. 5.2 shows the FESEM micrographs of 275 nm NWs after dissolving the alumina membranes. Micrographs clearly show that the NWs are very stable and did not break due to the alumina dissolving process. Different lengths of the NWs, confirmed from SEM and FESEM micrographs, are obtained by changing the time of deposition of Ni within alumina membranes during the electrochemical deposition. The length of the 150 nm NWs is varied from $1.4 \mu\text{m}$ (AR ~ 9) to $28.4 \mu\text{m}$ (AR ~ 189) whereas the same for 275 nm NWs is varied from $1.37 \mu\text{m}$ (AR ~ 5) to $7.7 \mu\text{m}$ (AR ~ 28).

Powder X-ray diffraction pattern of 275 nm NWs is recorded and shown in Fig. 5.3. The XRD peaks correspond to either face-centered-cubic Ni or gold as shown in

this figure. The average crystallite size in the NWs calculated from various peaks of XRD using the Scherer equation is ~ 29 nm. The (200) peak of Ni in the XRD pattern is fitted with Lorentzian for determining the crystallite size and shown in the inset of Fig. 5.3. EDAX spectra obtained from the NWs is shown in Fig. 5.4 and indicate that the NWs are free from sulphur and boron contamination as they are developed under the negative potential of -0.85 V and the SO_4^{2-} and BO_3^{3-} anions did not get deposited.

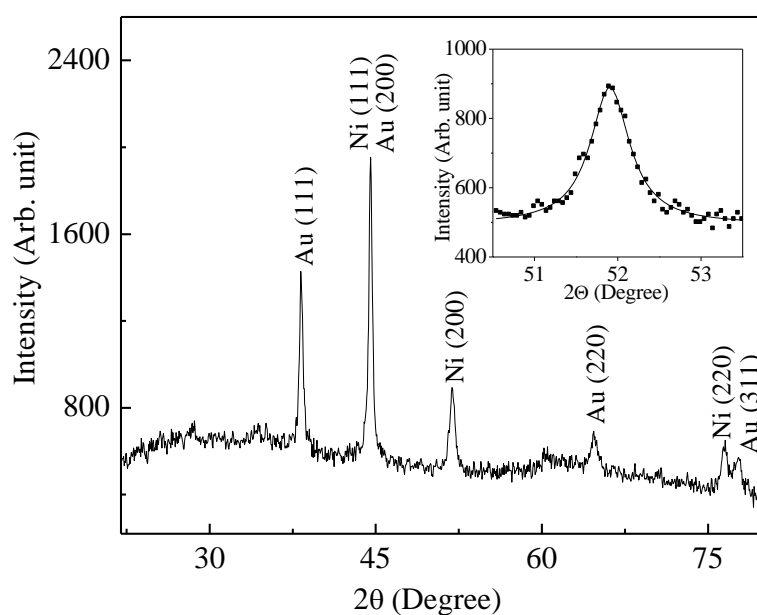


Figure 5.3. X-ray diffraction pattern of 275 nm Ni NWs. Inset: (200) peak of fcc Ni fitted with Lorentzian.

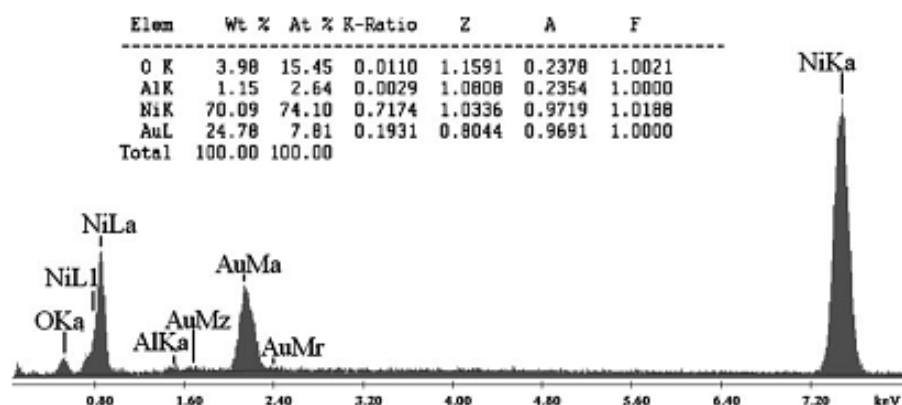


Figure 5.4. Energy dispersive analysis of X-ray (EDAX) spectra of Ni NWs.

5.3.2 Magnetic properties of arrays of Ni NWs

The magnetic measurements of the arrays of NWs are done by keeping the membranes intact. Fig.5.5 shows the OP (external applied field parallel to the wire-axis) and IP (external applied field perpendicular to the wire axis) isothermal magnetic hysteresis loops of arrays of 150 nm NWs with different aspect ratios (ARs) recorded at room temperature. For all the samples, we observe that, the rate of increase in magnetization with the external magnetic field in the OP hysteresis loops is much slower than that in the corresponding IP hysteresis loops. Remanence in the OP direction is also much smaller compared to the IP counterpart. Along the IP direction, magnetization saturates at a lower field compared to the OP direction. All these characteristics indicate the direction of the easy magnetization of the NWs is perpendicular to the wire axis. Similar behavior of having IP easy magnetic axis in 275 nm NWs is observed in Fig. 5.6 which shows the magnetic hysteresis loops in IP and OP directions for different ARs of 275 nm NWs.

The remanence ($< 0.45M_s$, M_s the saturation magnetization) and coercivity (< 300 Oe) of the hysteresis loops are quite small for the NWs. The reversal of the NWs is an important aspect of the remanent state of the NWs. It is important to know the remanent state of the NWs with the help of micromagnetism. In order to investigate

the magnetic properties of arrays of NWs, it is first obvious to understand the domain structure or the magnetic spin distribution within a single NW.

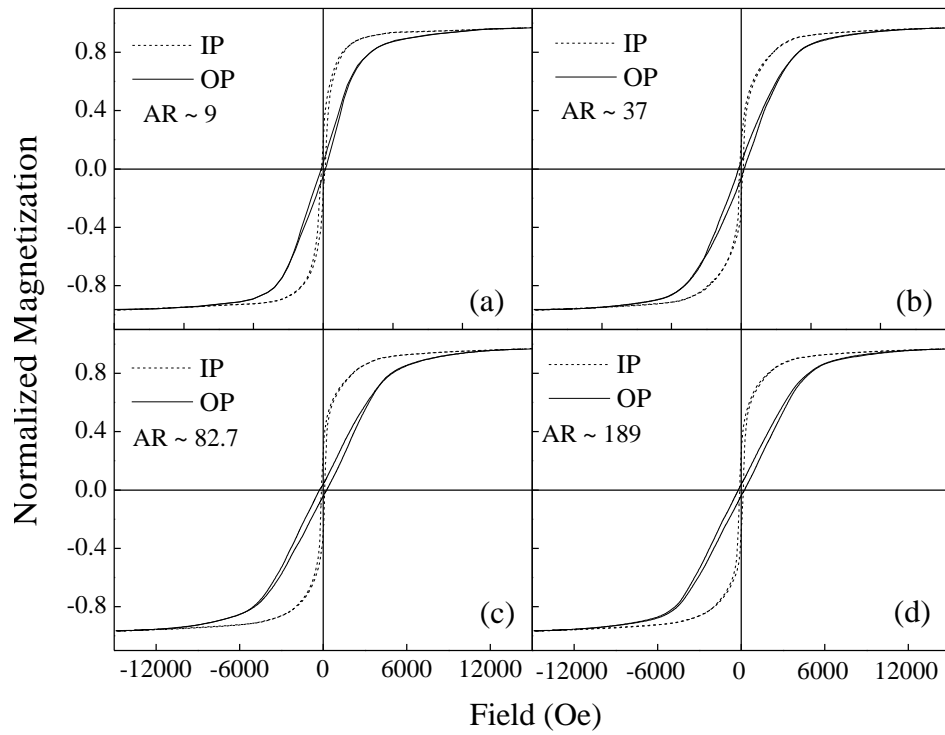


Figure 5.5. IP and OP magnetic hysteresis loops of arrays of 150 nm Ni NWs having an aspect ratio of (a) ~ 8 (b) ~ 37 (c) ~ 82.7 and (d) ~ 189 .

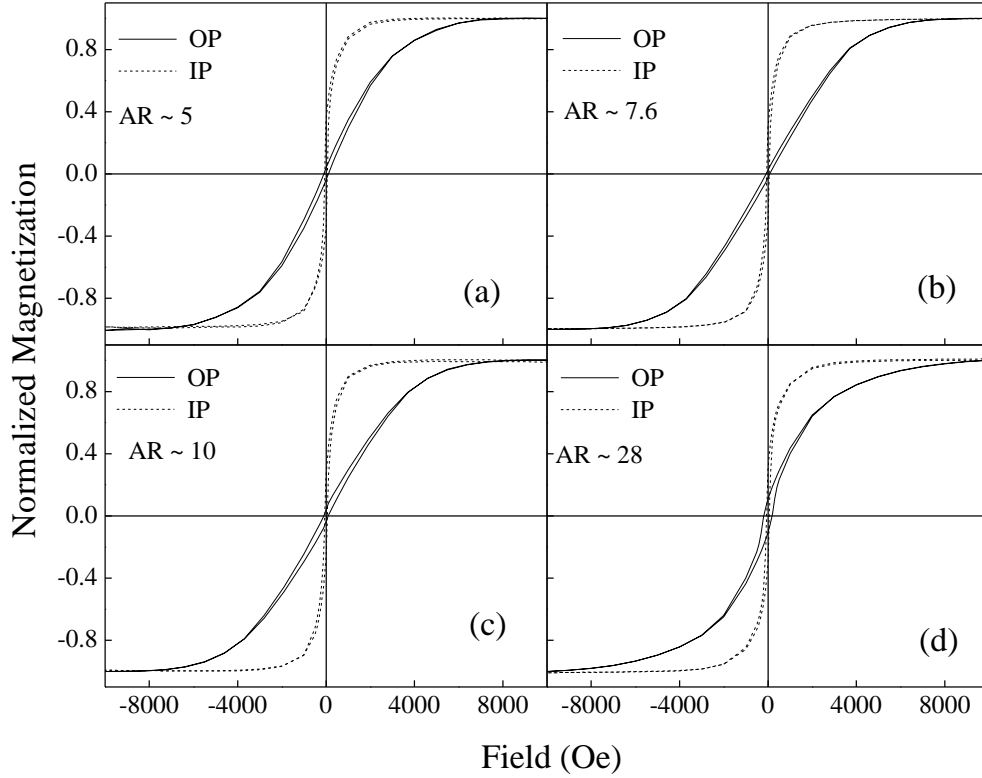


Figure 5.6. IP and OP magnetic hysteresis loops of arrays of 275 nm Ni NWs having an aspect ratio of (a) ~ 3.2 (b) ~ 7.3 (c) ~ 10 and (d) ~ 20 .

The magnetic spin distribution within a NW is determined by its exchange interaction, shape anisotropy (originated from the self demagnetizing field), magnetocrystalline anisotropy (originated from spin-orbit coupling of crystalline structure of the NW), surface anisotropy (uneven coordination number of the spins near the surface of the NW) etc. Diameters of the NWs, which are about few nanometers, are often comparable to the magnetic domain wall widths that make them hard to accommodate multidomain structures and promote to form single domain structure. However, various micromagnetic calculations were performed in this regard based on *Landau Lifschitz–Gilbert* equations to determine the remanent states of cylindrical shaped magnetic materials.^{4, 5, 11} In case of NWs with diameter below $3.5\lambda_{\text{ex}}$, λ_{ex} being the exchange length, the spin magnetic moments within the NW lie parallel to each other and directed along the length of the NW with a small radial tilt at both ends. This configuration produces very high axial remanence M_r ($\sim M_s$, the

saturation magnetization) and is termed as the “flower” state. With the increase in diameter, more precisely above $3.5\lambda_{\text{ex}}$, the spin magnetic moments, within the NW, begin to tilt in the circumferential direction, giving rise to a “vortex” configuration. The axial remanence decreases as the vortex develops. Though the calculations were done mostly for the cylindrical NWs with low ARs (< 3) but, it is still significant for high ARs.^{4, 5, 11} It was shown earlier somewhere else^{12–14} that the surface-induced anisotropy stabilizes vortex states in cylindrical ferromagnetic NWs at high ARs.

In case of magnetic thin films with a thickness in the nanometer range, uniaxial anisotropy along the direction normal to the layer surface is developed due to induced orbital moments near the surface and interfaces.^{15, 16} This well established fact in thin films^{12–14} suggests that magnetic anisotropy can also be induced in NWs by the lateral surfaces because of a similar microscopic origin. In some materials, this surface-induced anisotropy exceeds the magnetocrystalline anisotropy by orders of magnitudes and stabilizes the vortex configuration when the length of the wire is much higher than the diameter.¹² For Ni, $\lambda_{\text{ex}} = 20$ nm and thus the critical diameter of Ni NWs is 70 nm.¹¹ However, compared to flower structure, it is relatively easy to move a vortex wall through the wire with vortex structure. Hence, the observed low remanence and coercivities of the hysteresis loops in Fig. 5.5 and 5.6 indicate vortex remanent state within the NWs.

In case of two dimensional (2D) arrays of NWs, magnetostatic interactions among the NWs play an important role in governing their magnetic properties, especially when the length or diameter of the NWs are comparable to the inter-wire distance.¹⁷ For simplicity, each NW can be consider as magnetic dipole. Therefore, the dipolar magnetostatic interaction field produced by surrounding NWs on a particular test NW in a 2D arrays system can have two contributions: the field $2\pi M_s f$ produced by the charges on the cylindrical wire surfaces of surrounding NWs which tries to make the perpendicular direction of the test NW as easy magnetic direction and the field $4\pi M_s f$ produced by the free charges at both ends of the surrounding NWs which tries to make the axial direction of the test NW as magnetically hard, where f is the filling factor of the NWs or porosity of the alumina membrane (it is the ratio of the total cross sectional area of the pores to the membrane’s flat surface area). Hence,

combining these two contributions with the shape anisotropy of the test NW, the net effective magnetostatic field (H_{eff}) can be written as¹⁷

$$H_{eff} = 2\pi M_S - 2\pi M_S f - 4\pi M_S f \quad [5.1]$$

Here, f is the filling factor and $f \propto d/D$, the ratio of the NW diameter (d) to the inter-wire distance (D). In Eq.5.1, the first term is the self-demagnetizing field $2\pi M_S$ of a NW, i.e. the shape anisotropy. The Eq. 5.1 can be rewritten as

$$H_{eff} = 2\pi M_S - 6\pi M_S f \quad [5.2]$$

Eq.5.2 show, how the magnetostatic interaction field ($6\pi M_S f$) determines the magnetic easy axis either along axial (OP direction) or along the transverse (IP direction) direction of the NWs. In case of the NWs that are well separated, due to self-demagnetization field and relatively small magnetostatic interaction among them, it is possible that the direction of easy magnetization lies parallel to the axes of the NWs, giving rise to a large OP remanence.^{3, 4} But, the easy axis can turn in to the perpendicular direction of the NWs if the NWs are close enough (a large value of f) to produce a strong magnetostatic interaction field greater than the shape anisotropy field. In our study, the pores and hence the NWs are randomly arranged. Thus, an exact calculation of the filling factor f considering a square or hexagonal mesh of NWs within the membranes may give wrong information. However, the observed transverse or IP magnetic easy axes of the 150 and 275 nm NWs in Fig. 5.5 and 5.6 can be qualitatively explain by the dipolar interaction field for a dense arrays system as described above.

The variation of squareness ($= M_r/M_s$, M_r being the remanent magnetization measured from hysteresis loops) with the AR in case of 150 and 275 nm NWs are shown in Fig. 5.7 and Fig. 5.8 respectively. The squarenesses (Fig.5.7) of 150 nm NWs at different ARs are measured at room temperature (300K). It shows an increase in IP squareness and slow decrease in OP squareness with the AR of the NWs. On the other hand, the squarenesses of 275 nm NWs at different ARs are measured both at 80 and 300 K (see Fig. 5.8). Here, the change in AR changes the IP and OP squarenesses significantly. After an initial decrease at lower values of the ARs, the squarenesses started to increase at higher ARs. Here, the trends of variation of both squarenesses are

almost same at both the temperatures and the values are almost same in case of OP squarinesses at all the ARs. Micromagnetic calculations^{3-5, 11, 14} states that, the transition from flower to vortex state takes place when a tilt in the magnetization develops near the base of a cylindrical-shaped particle and the magnetization forms a helical structure. The magnetization lies closer to the base plane due to the increase in particle size. In the flower state, the squariness is close to 1 and decreases monotonically as the vortex develops resulting small values of squarinesses. Furthermore, as the magnetic easy direction of a single NW is along the length of the NW dominated by shape anisotropy, the OP squariness must be higher than the IP squariness. However, the magnetostatic interactions among the NWs can change the scenario. We have dense arrays of NWs with inter-wire distances comparable to the diameter of the NWs and smaller than the lengths of the NWs. Hence, the magnetostatic interactions among the NWs are strong enough to dominate over the shape anisotropy of individual NW. Here in Fig. 5.7 and 5.8, the higher IP squarinesses compared to OP squarinesses of all the NWs is the signature of IP easy axes which is a consequence of domination of magnetostatic interaction over the shape anisotropy of the NWs. With the increase in length (i.e. AR) of the NWs, the magnetostatic interaction increase among the NWs due to stronger magnetic field produced by the neighboring NWs. Point to note here, the IP interaction field ($2\pi M_{sf}$) produced by free charges on the cylindrical surfaces of NWs tries to make the transverse direction of NWs as easy. And, the OP interaction field ($4\pi M_{sf}$) produced by free charges at both ends (the flat surfaces) of NWs tries to make the axial direction of NWs as hard. As a consequence, with the increase in AR, the OP direction becomes magnetically harder and the IP direction becomes easier direction of magnetization. The increase in IP squareness and slow decrease in OP squareness in 150 nm NWs with increase in AR, though not very clearly but indicate the increase in interaction field with the increase in AR (length) of the NWs. In case of 275 nm NWs, the inter-wire separation (i.e. the separation between the cylindrical surfaces of two neighboring NWs ~ 35 nm) is very smaller than the NW diameter ~ 275 nm. In this circumstance, the array system can be considered as continuous distribution of NWs similar to thin film. Thus, as the AR (length) of the NWs increase (the situation as similar to the increase in thickness of a thin film), the OP direction becomes magnetically easier (explains the increase in OP

squarness in Fig. 5.8) and IP direction becomes the harder (explains the decrease in IP squarness in Fig. 5.8). However, influence of NWs characteristic is also present in the array systems resulting in the increment of IP squarnesses at higher ARs of the NWs (Fig.5.8). Near the same values of OP squarnesses at 80 and 300 K for all the ARs of 275 nm NWs (Fig.5.8) indicate no change of self demagnetization values (or the strength of shape anisotropy) of the NWs in the arrays (or the demagnetization values of the approximated thin film systems) with temperature. Using the same argument one can assume that, no change in magnetostatic interaction among the NWs. But, a significant change in IP squarnesses is observed with the change in temperature. At low temperature (at 80K), the IP squarnesses are low compared to OP squarnesses measured at relatively higher temperature of 300K. The phenomena are more clearly depicted in the plot of squarness at different temperatures for different ARs of 275 nm NWs in Fig. 5.9. OP squarness does not change significantly for the change in temperature and the IP squarness remain higher than OP squarness and increase slowly with temperature. For Ni NWs with fcc polycrystalline structure, magnetocrystalline anisotropy is small as Ni fcc structure has a low magnetocrystalline energy of $\sim -0.5 \times 10^5$ ergs/cm³. The alumina has low thermal expansion coefficient ($\sim 5 \times 10^{-6}$ meter/milliKelvin) compared to Ni ($\sim 13 \times 10^{-6}$ meter/milliKelvin) and we prepare the NWs at room temperature. Thus, the stress induced anisotropy is also low. Thus, it is not very clear to us that, who increases the IP squarness upon increasing the temperature.

Change in coercive field value with respect to ARs of 150 and 275 nm NWs are plotted in Fig. 5.10 and Fig. 5.11 respectively. Coercivities of 150 nm NWs are measured only at room temperature (300K). The coercivities of 275 nm NWs are measured at various temperatures. Coercivities at 80 K and 300 K of 275 nm NWs at various ARs are plotted in Fig. 5.11. The OP and most often the IP coercivity increase with the increase in AR in both the NWs. At a particular temperature, the OP coercivity is always higher than the IP coercivity at all the ARs. Fig.5.12 shows the change in coercivity of 275 nm NWs having different ARs with respect to temperature. It also shows the OP coercivity is always higher than the IP one for any particular arrays of NWs. It is previously discussed that, the low coercivity observed in the NWs (< 280 Oe) is a consequence of vortex remanent state of the NWs. However, for a

single NW, the strong shape anisotropy along OP direction can produce higher coercive field value compared to IP direction. But, a dipolar kind of magnetostatic interaction in a 2D array of NWs tries to reduce the OP coercivity to attain a lower energy state of the array system. However, the interaction does not remain dipolar in nature in case of vortex NWs during magnetization reversal (more specifically below the saturation fields in hysteresis loops) as then the individual NWs cannot be treated as magnetic dipoles. Because, within a vortex NW, the spins are not parallel to each other rather orient in circumferential direction. The nature of interaction is complex for vortex NWs and not clearly known which makes it tough to predict its effect on coercivity of the arrays. It may be possible that, in defining the coercive field value of arrays of NWs, the shape anisotropy of individual vortex NW took a decisive role that makes the OP coercivity higher than the IP one (Fig.5.11, 5.12) through a curling reversal. The nanopores of alumina membranes are not always cylindrical with inner surfaces perfectly smooth enough to create NWs without any domain wall pinning site. During the reversal, any significant surface roughness of NWs can act as pinning site of vortex wall which results in an increment of coercive field values upon increasing the AR (length) of the NWs (Fig.5.10, 5.11). OP and IP coercivities of the NWs decrease with the increase in temperature (Fig.5.12). With the increase in temperature, the thermal fluctuations of spin magnetic moments within the NWs increase which results in a decrement of coercivity as observed in most of the ferromagnetic materials.

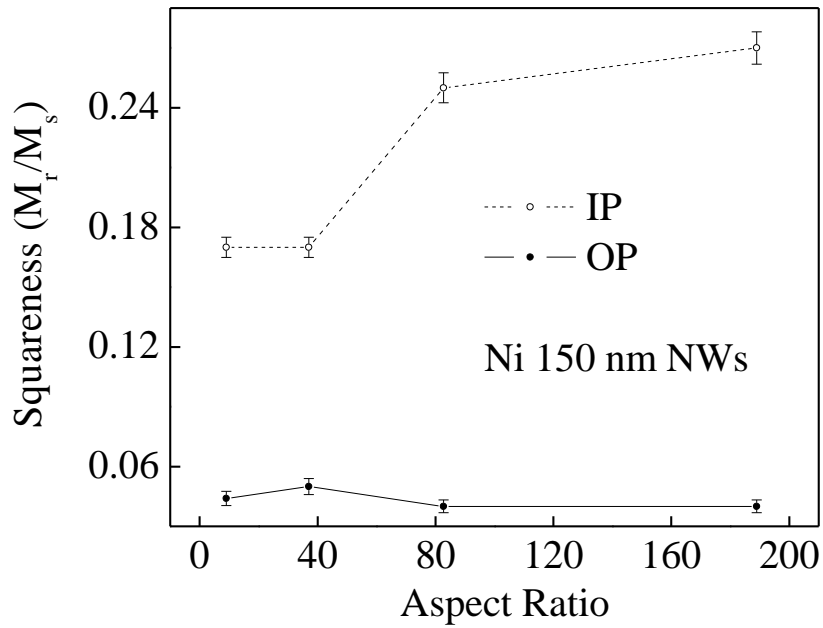


Figure 5.7. Variation of squariness (M_r/M_s) of Ni 150 nm NWs with respect to aspect ratio at room temperature.

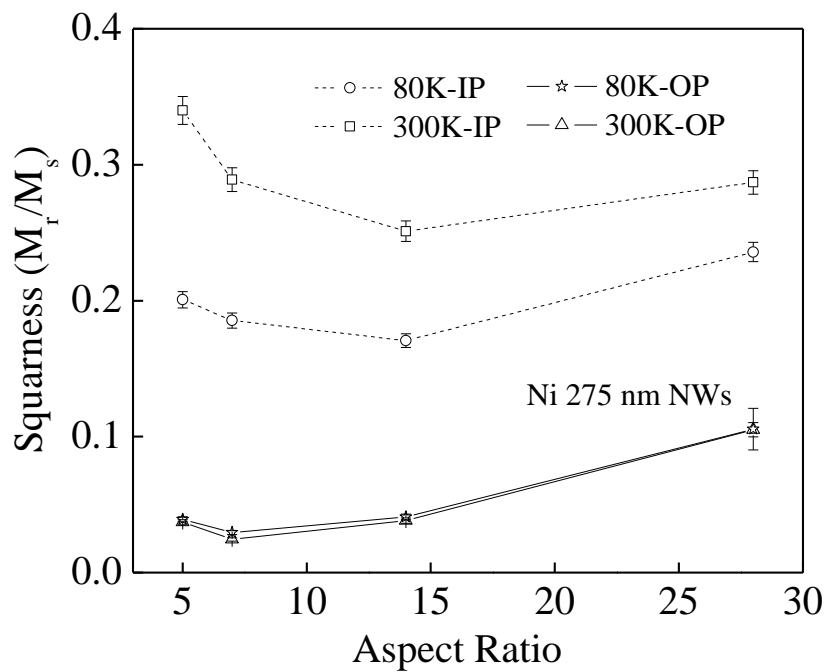


Figure 5.8. Variation of squariness (M_r/M_s) of Ni 275 nm NWs with respect to aspect ratio at room temperature (300K) and at 80K.

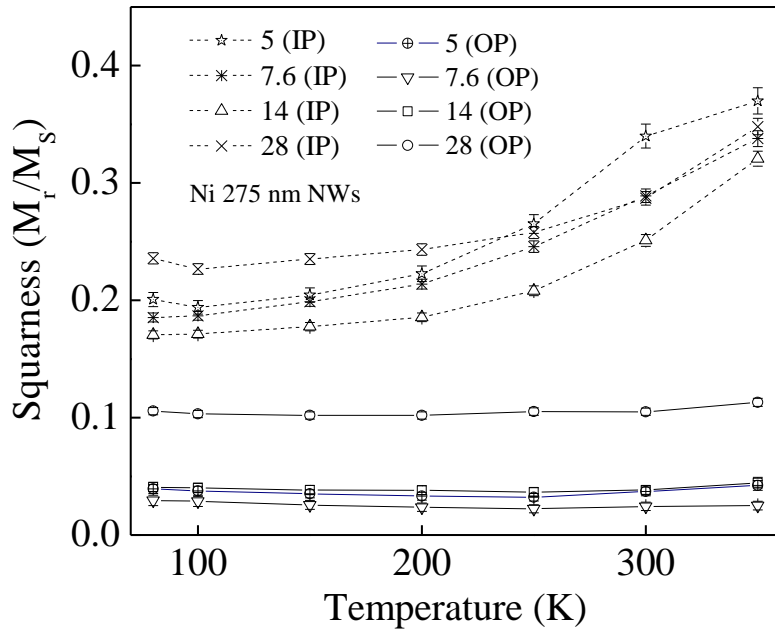


Fig.5.9. Variation of IP and OP squariness of all the NWs having different ARs with respect to temperature.

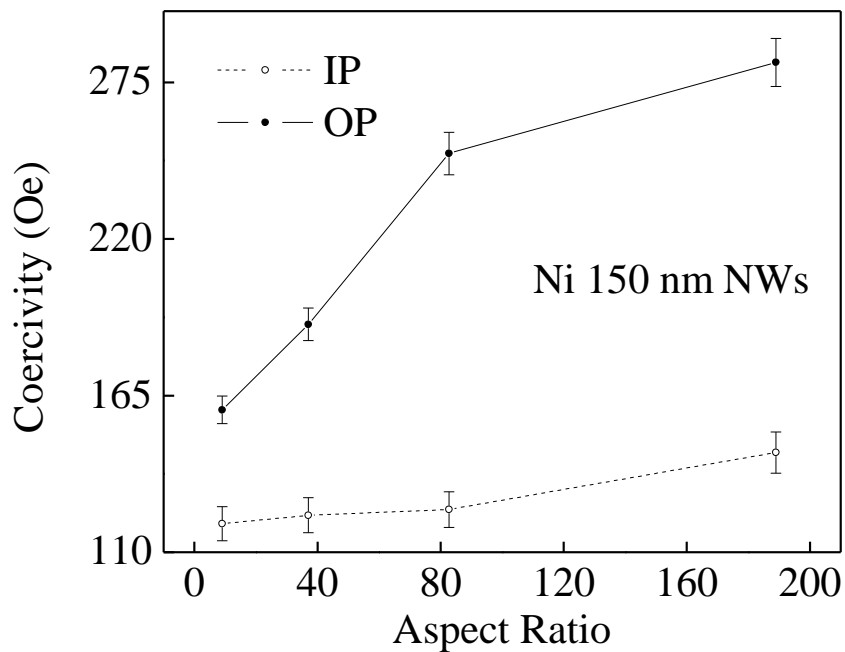


Fig.5.10. Variation of coercivity of Ni 150 nm NWs with respect to aspect ratio measured at room temperature (300K).

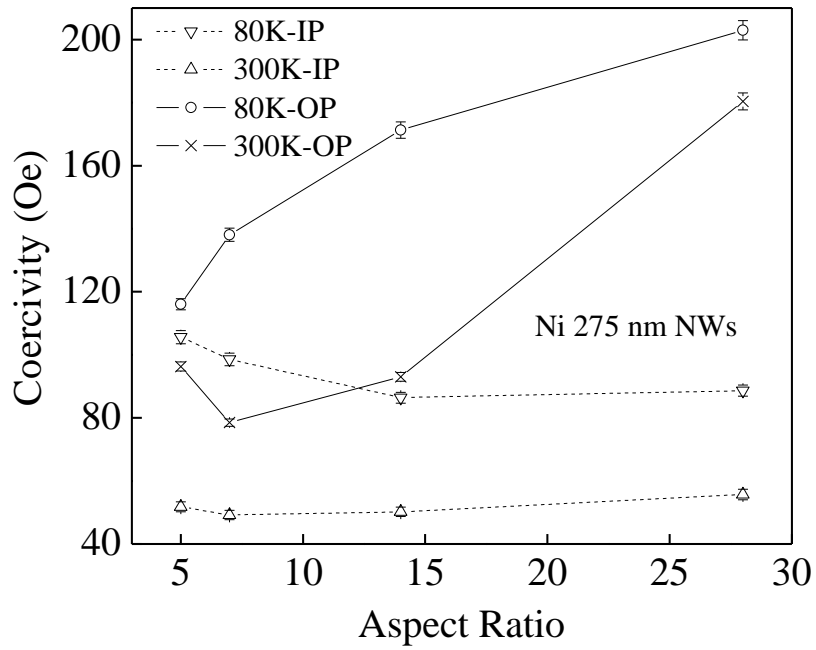


Fig.5.11. Variation of coercivity of Ni 275 nm NWs with respect to aspect ratio of NWs measured at 80 and 300K.

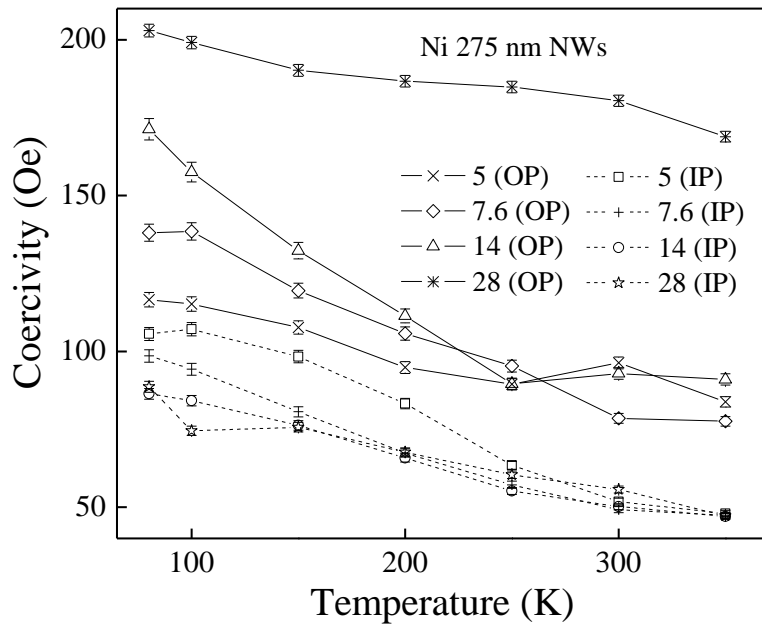


Fig.5.12. Temperature dependence of IP and OP coercivities of Ni NWs having different ARs.

5.3.3 Magnetization measurement of three isolated Ni NWs

In order to understand the magnetization dynamics of arrays of NWs it is always important to understand the dynamics for a single NW. We tried to measure the magnetic hysteresis loops of single NW employing a magneto optical Kerr effect (MOKE) set-up. The schematic diagram of the set-up is shown in Fig. 2.30 in *chapter 2*. The detail of the set-up is also described in the same chapter. In MOKE measurement, we projected an unpolarized LASER ray on the sample and measured the Kerr rotation of the ray after being reflected from the sample kept under an alternating magnetic field. It is assumed that the change in Kerr rotation is linearly proportional to the change in magnetization of the sample under the external magnetic field. Thus the change in Kerr rotation with the change in external magnetic field gives the MH loop of the sample.

We separate the NWs by ultrasonication after dissolving the alumina membrane using NaOH solution. Then we place the NWs on Si/SiO₂ chips. However, it is a challenging task to detect MOKE signals coming from the NWs. For an isolated single NW, it is obvious that the signal (S) to noise (N) ratio (S/N) extremely small. Moreover, it is also a rather difficult task to find the isolated NWs on the Si/SiO₂ substrate. To locate the NWs on the chips we make gold patterns on the Si/SiO₂ chips by E-beam lithography. The detail of the technique is described in *chapter 2*. A thin film of PMMA is prepared on the chip and various gold patterns of micro-meter dimensions are made on that by E-beam lithography. The micro patterns are shown in Fig. 5.13 taken by an optical microscope.

The NWs are placed on the gold patterned Si/SiO₂ chip and then found by using scanning electron microscope (SEM). Knowing the coordinates of the identified NWs on the chips (see Fig.5.14 (a) for three isolated NWs on Si/SiO₂ substrate), the NWs are then investigated by MOKE set-up. The SEM micrographs of such an isolated bunch of three NWs are shown in Fig. 5.14 (b).

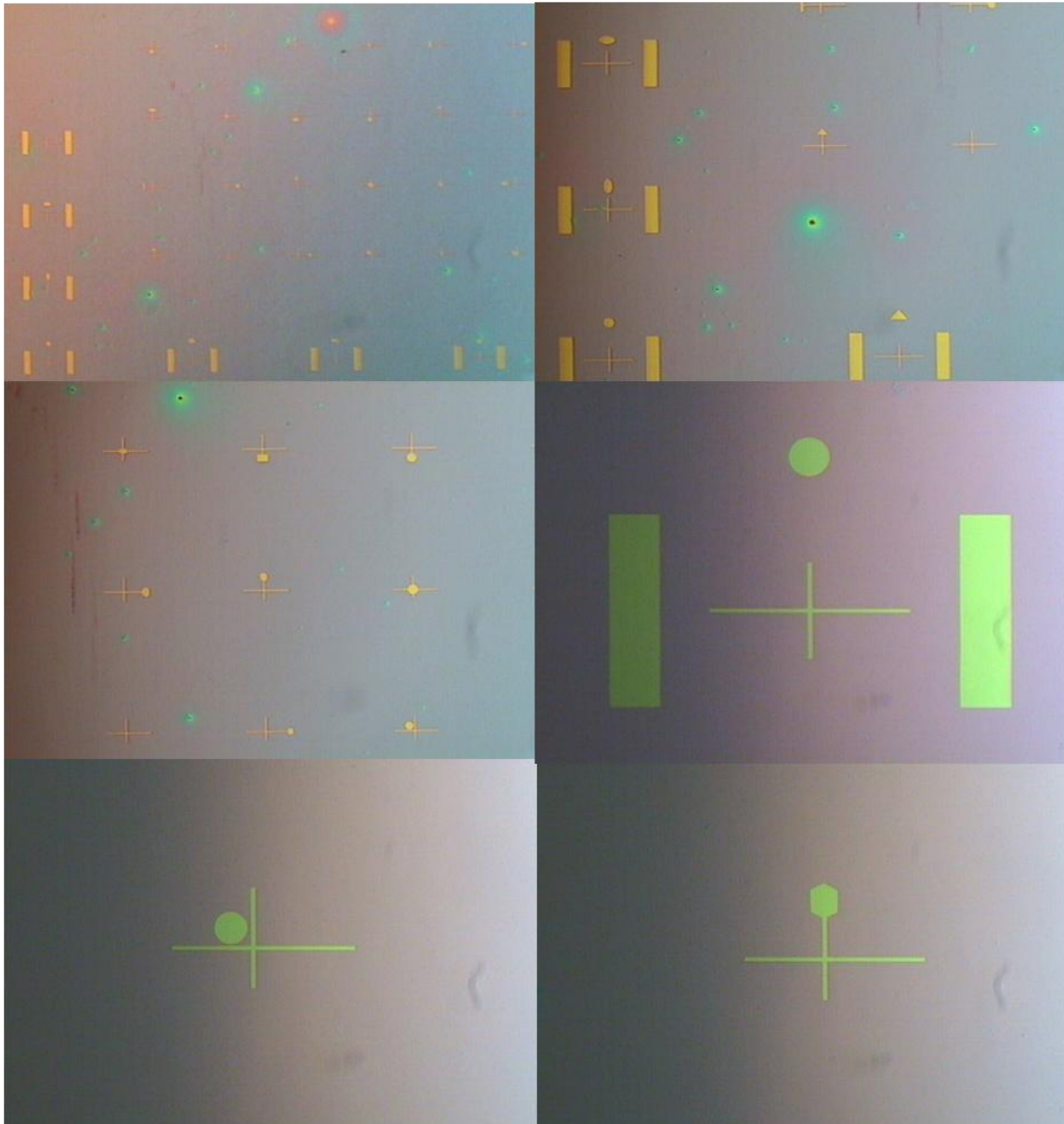


Figure 5.13. Optical images of gold micro patterns on Si/SiO₂ chips made by E-beam lithography.

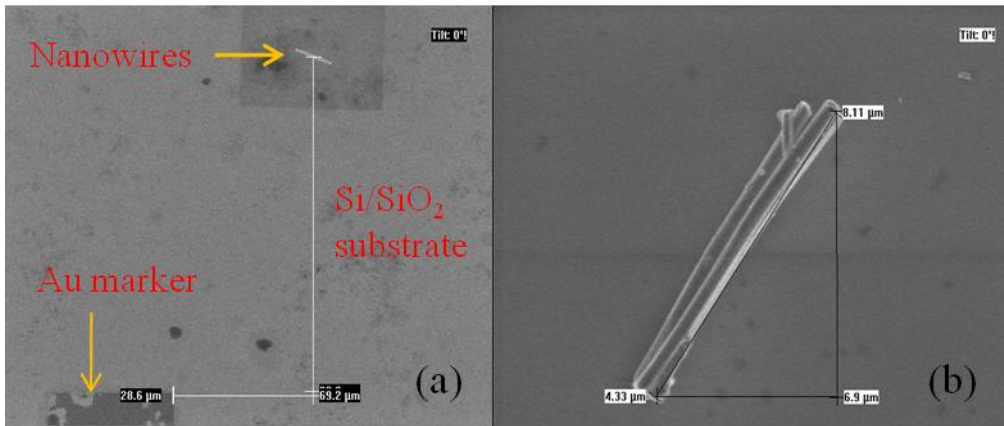


Figure 5.14. SEM micrograph of (a) three isolated NWs with gold markers on Si/SiO₂ substrate and (b) the three isolated NWs in a close view.

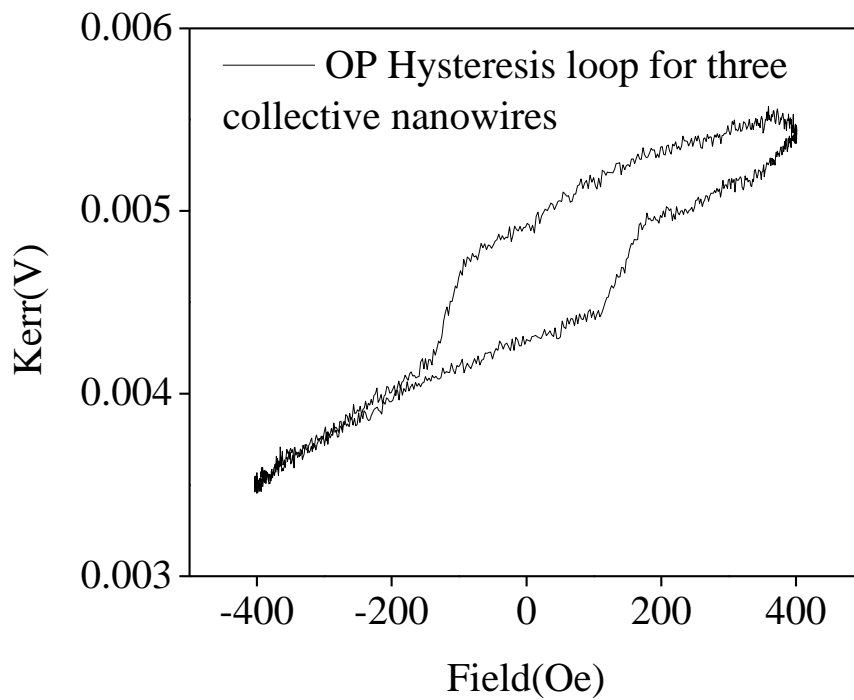


Figure 5.15. MOKE hysteresis loop for three isolated Ni NWs placed on Si/SiO₂ chip. The external magnetic field is parallel to the NWs axes.

It is clear in the SEM micrograph that, the NWs are parallel and attached to each other. The diameter of the NWs is ~ 300 nm with an average length of ~ 7 μm . The MOKE signals are detected by a high resolution Si diode detector while the external alternating magnetic field has a maximum strength of ~ 400 Oe with a frequency 17 Hz. The spot size of the LASER beam is about 5×6 μm . The magnetic hysteresis loop recorded for the three isolated NWs is shown in Fig. 5.15. The loop is recorded while the magnetic field is kept parallel (OP configuration in VSM measurements) to the NWs axes.

In Fig. 5.15, a sharp jump during reversal is observed in the hysteresis loop. In contrast, arrays of NWs show a sheared hysteresis loop in OP direction in VSM measurement (Fig. 5.6). This is due to the magnetostatic interaction among the NWs. We change the angle between the applied magnetic field and NW axis from 90° to 0° and measure the hysteresis loops at few different angles. Fig. 5.16 shows the magnetic hysteresis loop of the NWs while the applied field is perpendicular the NWs axes (IP configuration in case of arrays of NWs). The reversal here is not as in OP direction and becomes sheared. The VSM measurements indicate vortex remanent state in the NWs. Here in OP direction magnetization the relatively sharper jump in reversal compared to VSM measurement indicate the absence of magnetostatic interaction among the NWs which generally tries to shear the jump. The three NWs are attached to each other here and thus may be treated as a unified system.

We plotted the change in coercive field with the applied external field angle and is shown in Fig. 5.17. The coercivity of the loops decreases slowly upon increasing the angle of applied field. This is perhaps due to the decrease in shape anisotropy as we increase the angle between the applied field and NW axes. The other anisotropies such as magnetocrystalline, magnetostatic interaction among the NWs are weak to counter act the shape anisotropies of the NWs.

It is difficult to detect the MOKE signals for such isolated cylindrical NWs as the most of the incident beam is randomly scattered by the cylindrical surface of the NWs. Moreover, the gold pattern Si/SiO₂ substrate adds some additional noise and decrease the S/N ratio. MOKE signal detection from single NW is thus really a challenging task and need more sophistication in the set-up and in sample preparation.

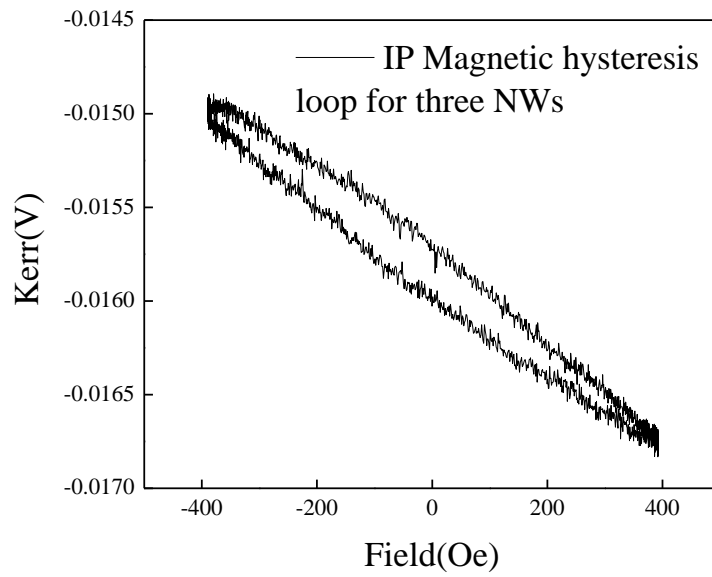


Figure 5.16. MOKE hysteresis loop for three isolated NWs while the external magnetic field is perpendicular to the NWs axes.

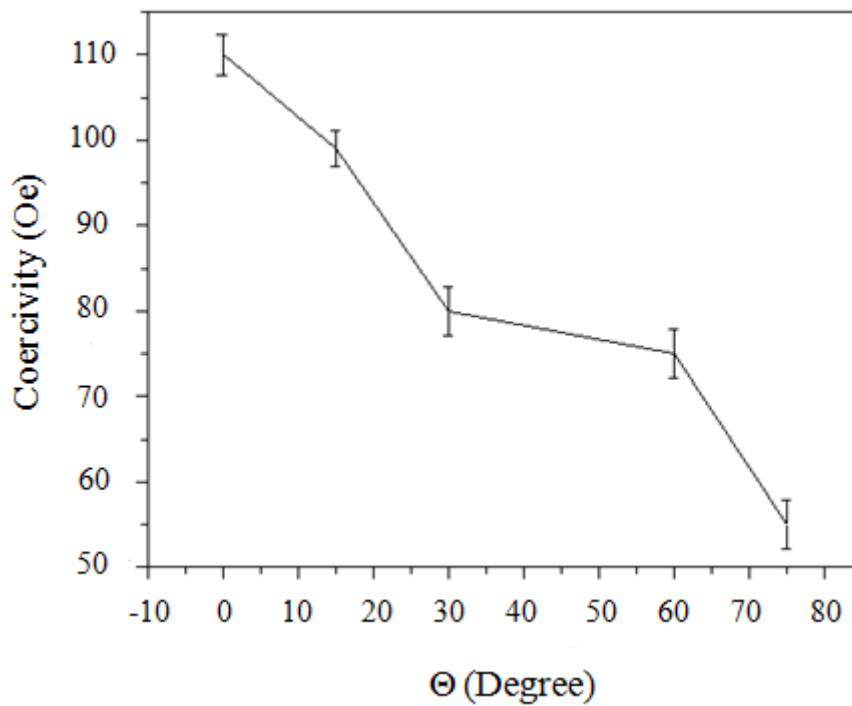


Figure 5.17. Plot of coercive field with respect to the external applied field angle.

5.4 Conclusions

Highly uniform and dense arrays of nickel NWs with an average diameter of ~ 200 nm are prepared varying the AR from 3.5 to 28. Structural characterization of the NWs reveals the fcc crystalline phase of the NWs and are free from any contamination as confirmed by EDAX spectra. The typical crystallite size is found to be of ~ 29 nm. Room temperature isothermal magnetic hysteresis loop measurements in IP and OP configuration of the external magnetic field indicate the magnetic easy axis of the arrays of NWs along their perpendicular direction (IP). The experimental results are in accordance with the vortex configuration of NWs. With this configuration, substantial OP coercivity and remanence are possible at high ARs of the NWs.

MOKE measurement of three isolated NWs shows sharp magnetization reversal indicating OP easy axis due to shape anisotropy and low magnetostatic interaction among the NWs. The decrease in coercivity upon increasing the angle of applied external field indicates the decrease in shape anisotropy in perpendicular direction (IP) of the NWs.

Bibliography

- [1] Wu, Y., Li, K., Qiu, J., Guo, Z., and Han, G., *Appl. Phys. Lett.* **80**, 4413 (2002); Albrecht, M., Moser, A., Rettner, C. T., Anders, S., Thomson, T., and Terris, B. D., *Appl. Phys. Lett.* **80**,3409 (2002)
- [2] Jung, H. S., Kuo, M., Malhotra, S. S., and Bertero, G., *Appl. Phys. Lett.* **91**, 212502 (2007); Shamaila, S., Liu, D. P., Sharif, R., Chen, J. Y., Liu, H. R. and Han, X. F., *Appl. Phys. Lett.* **94**, 203101-1 (2009).
- [3] Ross, C. A., *Annu. Rev. Mater. Res.* **31**, 203 (2001).
- [4] Vázquez, M., Vélez, M. H., Pirota, K., Asenjo, A., Navas, D., Vélezquez, J., Vargas, P., and Ramos, C., *Eur. Phys. J. B.* **40**,489 (2004).
- [5] Ross, C. A., Farhoud, M., Hwang, M., Smith, I. H., Redjda, M. and Humphrey, F. B., *J. Appl. Phys.* **89**, 1310 (2001).
- [6] Hassel, C., Brands, M., Lo, F. Y., Wieck, A. D. and Dumpich, G., *Phys. Rev. Lett.* **97**, 226805 (2006).
- [7] Ferré, R., Ounadjela, K., George, J. M., Piraux, L. and Dubois, S., *Phys. Rev. B* **56**, 14066 (1997).
- [8] Vázquez, M., Pirota, K., Torrejón, J., Navas, D. and Vélez, M. H., *J. Magn. Magn. Mater.* **294**, 174 (2005).
- [9] Chaure, N. B., Stamenov, P., Rhen, F. M. F. and Coey, J. M. D., *J. Magn. Magn. Mater.* **290–291**, 1210 (2005).
- [10] Xu, C.-L., Li, H., Zhao, G.-Y. and Li, H.-L., *J. Magn. Magn. Mater.* **253**, 1399 (2006).
- [11] Ross, C. A., Hwang, M., Shima, M., Smith, H. I., Farhoud, M., Savas, T. A., Schwarzacher, W., Parrochon, J., Escoffier, W., Bertram, H. N., Humphrey, F. B. and Redjda, M., *J. Magn. Magn. Mater.* **249**, 200 (2002).

- [12] Rossler, U. K., Bogdanov, A. N. and Müller, K.-H., IEEE Trans. Magn. **38**, 2586 (2002).
- [13] Bogdanov, A. N. and Rößler, U. K., Phys. Rev. Lett. **87**, 037203 (2001).
- [14] Bogdanov, A. N., Rößler, U. K. and Müller, K.-H., J. Magn. Magn. Mater. **242–245**, 594 (2002).
- [15] Bruno, P., Phys. Rev. B **39**, 865 (1989).
- [16] Dürr, H. A., Guo, G. Y., Laan, van der G., Lee, J., Lauhoff, G. and Bland, J. A. C., Science **277**, 213 (1997).
- [17] Oropesa, A. E., Demand, -M., Piraux, L., Huynen, I. and Ebels, U., Phys. Rev. B **63**, 104415 (2001).
- [18] Ramos, C. A., Brigneti, E. V. and Vázquez, M., Physica B (Amsterdam) **354**, 195 (2004).

Chapter 6

Magnetic behavior of 2-dimensional arrays of Cobalt nanowires: Influence of aspect ratio

6.1 Preamble

A renewal of interest in ferromagnetic nanowires (NWs) has surged recently triggered by their possible use in spintronic devices and more specifically in non-volatile memory (MRAM), magnetic logic devices¹⁻³ and low Ohmic loss devices.⁴ Fabrication and magnetic properties⁵ of two dimensional (2D) arrays of NWs are important not only from the fundamental physics point of view but also from the technological aspect, owing to their potential applications in perpendicular recording media⁶ and in field, current and biological sensors based on the giant magneto-resistance effect.⁷⁻¹²

Magnetic properties of a NW are governed by various anisotropy energies such as shape, magnetocrystalline, surface anisotropy of the NW.¹³ But in case of 2D arrays of such NWs, another anisotropy developed due to the magnetostatic interaction among the NWs¹⁴, which can play a dominating role over the other anisotropies as seen earlier in case of array of nanodots.¹⁵ Each NW can be assumed as magnetic dipole and the interaction may be dipolar in nature if the diameter of the NWs is negligible compared to the inter-wire distance. But, when the NWs are closely spaced i.e., when the inter-wire distance is comparable to the NW diameter, the interaction among the NWs may not be considered as dipolar interaction. In the present chapter, we describe the synthesis procedure of 2D arrays of Co NWs electrodeposited in alumina and polycarbonate membranes in detail. The typical diameters of the NWs are 50, 150 and 275 nm. We did a detail study of the structural properties of the 2D arrays as well as of the individual NWs. The NWs show a change in crystal texture on

decreasing the wire diameter. We investigate the static and dynamic magnetic response of the arrays. Study of magnetic properties revealed that NWs had vortex state and the magnetostatic interaction among the NWs, which is complex in nature, changed the magnetic easy axis from the axial to the transverse direction of the NWs at some higher aspect ratios ($AR = \text{length/diameter}$) on increasing their length.

6.2 Experimental

Synthesis of Co NWs

Arrays of Co NWs are prepared employing electrodeposition method within the pores of polycarbonate membrane with average pore diameter $d \sim 50$ ($\sigma \sim 2$) nm and of alumina membrane with $d \sim 150$ ($\sigma \sim 6$) and 275 ($\sigma \sim 7$) nm, where σ is the standard deviation. The membranes are commercially available from Whatman (UK).¹⁶ The average thickness of the polycarbonate membrane is ~ 6 ($\sigma \sim 1$) μm and that of alumina membranes is ~ 60 ($\sigma \sim 1$) μm . The average inter-pore distance (D), i.e. the center to center distance of the nanopores is 250 nm ($\sigma \sim 80$) for the pores of diameter 50 nm and ~ 185 ($\sigma \sim 6$) and 310 ($\sigma \sim 9$) nm for the pores of diameter 150 and 275 nm respectively. All electrochemical depositions of Co NWs are carried out at room temperature using an AUTOLAB-30 potentiostat. To use the membrane as an electrode, one side of it is coated with a conductive gold layer of ~ 0.1 μm thick using thermal evaporation technique. The gold-coated membrane is used as a working electrode (cathode) whereas a platinum foil and saturated Ag/AgCl are used as the counter and reference electrode respectively. The backsides of the membranes are covered by adhesive plastic tapes to prevent deposition on that side during electrodeposition. The deposition is carried out at a constant voltage of 0.9 Volt maintained between the working and counter electrodes. The potential of deposition is determined by linear sweep voltametry in a conventional three-electrode cell (20 c. c. capacity) for the particular electrolyte and for the above mentioned electrodes used for the synthesis. A saturated Ag/AgCl electrode is to be chosen as the third electrode, i.e. the reference electrode. Co is electrodeposited from an aqueous electrolyte solution of

0.9 M of CoSO_4 and 0.8 M of H_3BO_3 . The pH of the solution is maintained at ~ 3.4 ($\sigma \sim 0.5$) recorded by a pH meter. Under the constant potential, the Co^{2+} ions move towards the working electrode (gold coated alumina membranes) and enter in to the nano channels (nano pores) within the membranes. The ions are then become electrically neutral as soon as they come in contact with the gold film at the pore bottoms.

6.3 Results and discussions

6.3.1 Structural properties

The NWs are expected to take the cylindrical shape of the nano-channels of the membranes used for the synthesis. In order to do the structural characterization of the NWs, the alumina membranes are dissolved in 2M solution of NaOH at room temperature. The polycarbonate membranes are dissolved using chloroform solution. A field emission scanning electron microscope or FESEM (JEOL, JSM –6700 F) is employed to study the surface morphology of the NWs and to determine their length and diameter. The crystal structures of the samples are confirmed by x-ray diffraction (X'Pert Pro, Panalytical) and selected area electron diffraction (SAED) pattern is taken by a high resolution transmission electron microscope or HRTEM (JEOL-2010). Composition of the NWs is determined by energy dispersive x-ray scattering or EDAX spectra obtained from the isolated NWs during their imaging by FESEM.

FESEM micrographs of the nanowires taken after dissolving the membranes clearly show the formation of Co-nanowires with uniform length and diameter and are shown in Fig. 6.1 (a), (b) and (c) for the NWs with diameters of ~ 50 nm, 150 and 275 nm, respectively. Fig. 6.1 (d) shows the top view of the 275 nm NWs array after dissolving the alumina membrane. All the micrographs indicate that the lengths of the nanowires are uniform. We did the microscopic study for various NWs synthesized by electrodeposition process using different deposition time. We found the length of the NWs is linearly proportional to the time of deposition. Therefore the ARs of the NWs

for a particular diameter are varied by changing the length of the NWs. For each diameter, length of the NWs is varied by changing the deposition time and hence AR of the NWs. The ARs of the NWs are varied from ~ 3.7 to 410.

The lengths of the NWs are varied by changing the time of deposition of the NWs during synthesis. Lengths of the NWs obtained by using different deposition time are confirmed by FESEM study and are shown in Fig. 6.2 for 275 nm NWs. The plot of the length of NWs against deposition time is shown in Fig. 6.3. It clearly shows the length of the NWs is a linear function of deposition time. EDAX study of the NWs confirms that, the NWs are composed of cobalt (see Fig. 6.4). The residual alumina membrane in the etched samples is the source of Al in EDAX pattern. The observed Au peaks in EDAX spectra are due to the presence of Au thin film beneath the alumina membrane. Presence of oxygen peaks indicates the surface oxidation of the nanowires on removing the template. Similar results are obtained for the NWS with other diameters.

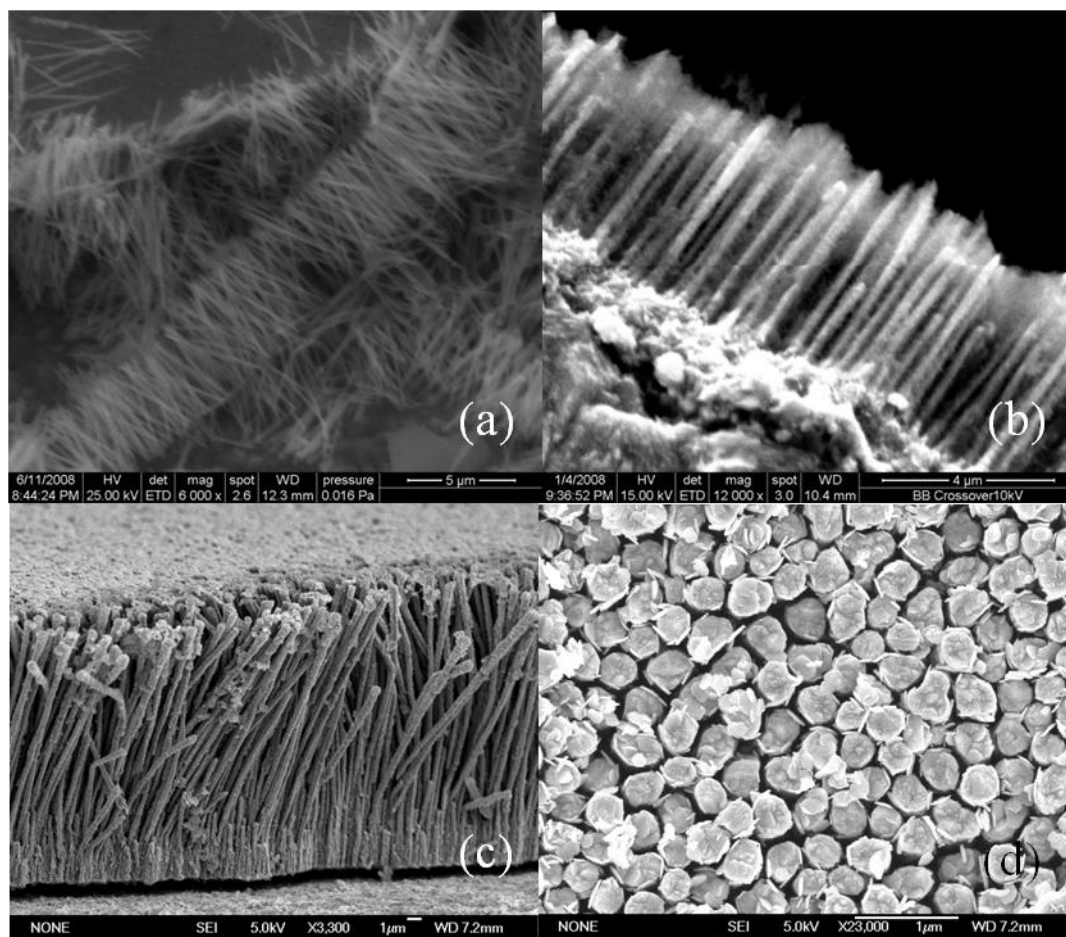


Figure 6.1. FESEM micrographs of the NWs with average diameters (a) 50 nm (b) 150 nm and (c) 275 nm. (d) Top view of 275 nm NWs.

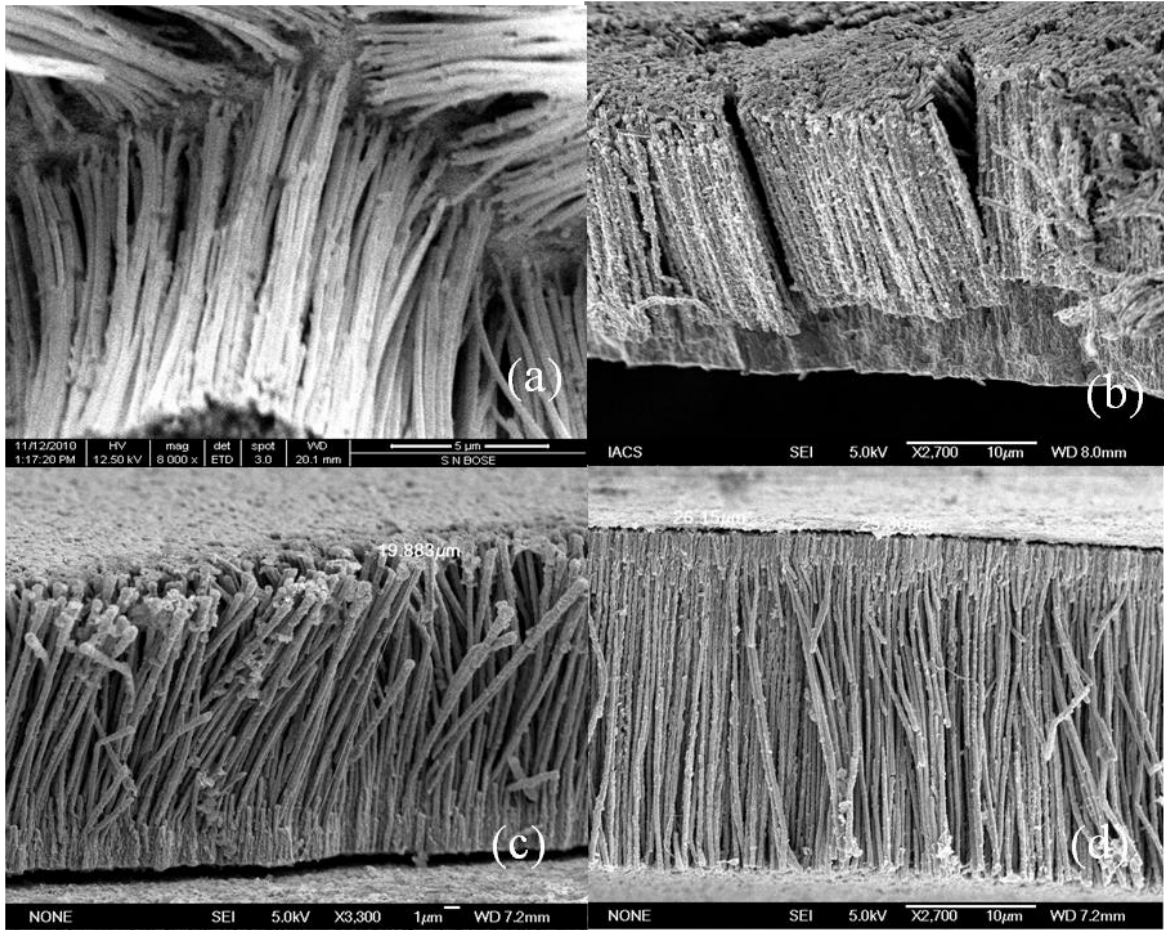


Figure 6.2. SEM micrographs of Co 275 nm NWs obtained for the deposition time of (a) 45 min, (b) 55 min, (c) 65 min & (d) 90 min.

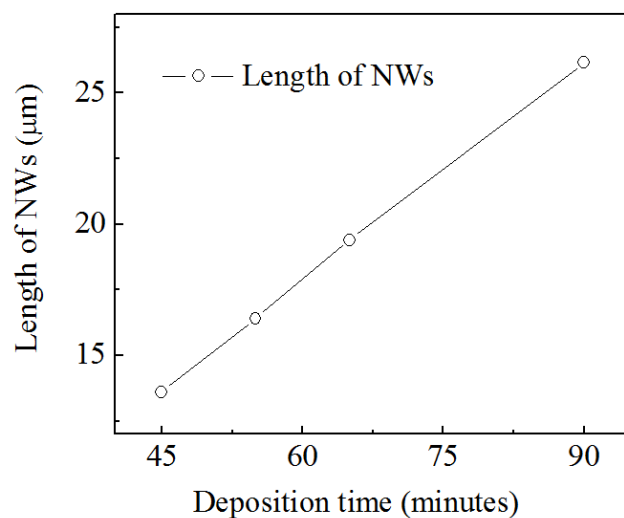


Figure 6.3. Length of NWs against the deposition time of NWs indicating a linear relationship between them.

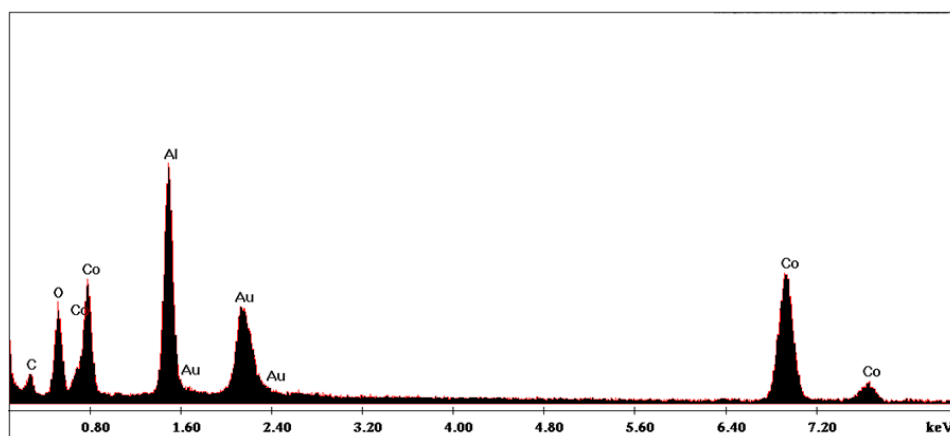


Figure 6.4. EDAX pattern of 275nm NWs after dissolving the membrane in NaOH solution.

X-ray diffraction (XRD) pattern for the arrays of 275nm NWs is shown in Fig. 6.5. The XRD pattern of the NWs is recorded keeping the membranes intact. The two peaks at $2\theta=41.53^\circ$ and 75.81° correspond to hcp (100) and (110) planes of Co

respectively which indicating the hcp phase of the NWs. It further indicates that Co NWs are not oxidized. It is perhaps because of the membranes which prevents the surface oxidation of the NWs. The second peak also corresponds to the (220) peak of the fcc structure of cobalt. But, the absence of most intense peak of fcc Co, i.e. the (111) peak in the spectra indicate that the NWs have no fcc phase.

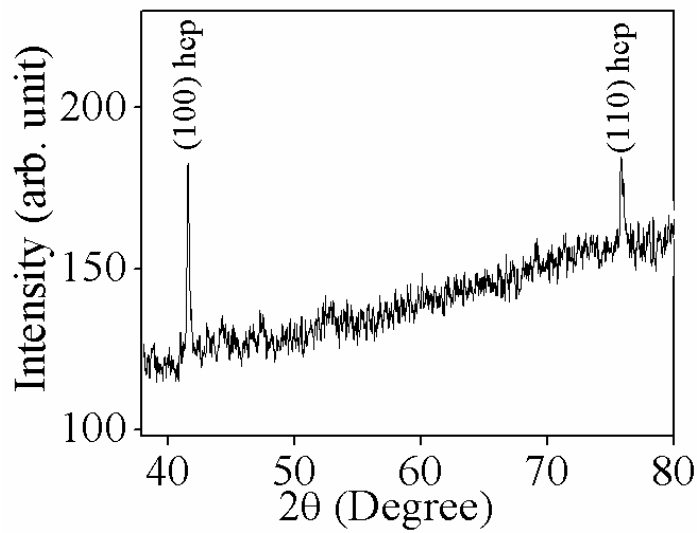


Figure 6.5. XRD pattern of 275nm NWs indicating hcp phase of Co NWs.

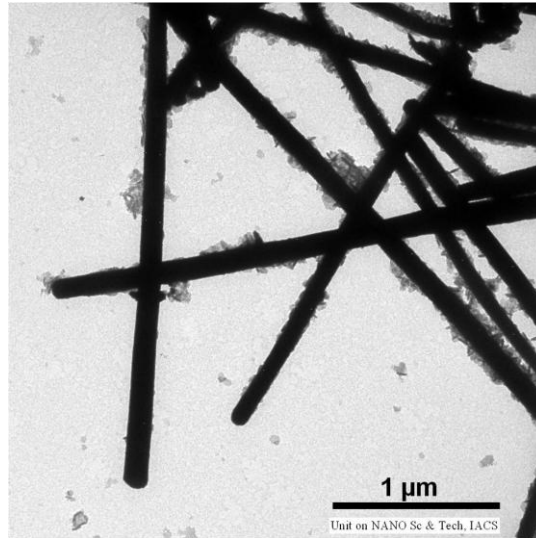


Figure 6.6. TEM micrograph of 150 nm NWs after dissolving the membrane in NaOH solution.

Transmission electron microscopic (TEM) studies of the NWs are performed after dissolving the alumina and polycarbonate membranes in NaOH and chloroform solutions for respectively. Such a TEM micrograph of 150 nm NWs is shown in Fig. 6.6. It clearly shows the cylindrical shape of the NWs with a uniform diameter throughout the length. These kinds of NWs are ideal for transport property measurements if the surfaces of the NWs are cleaned properly.

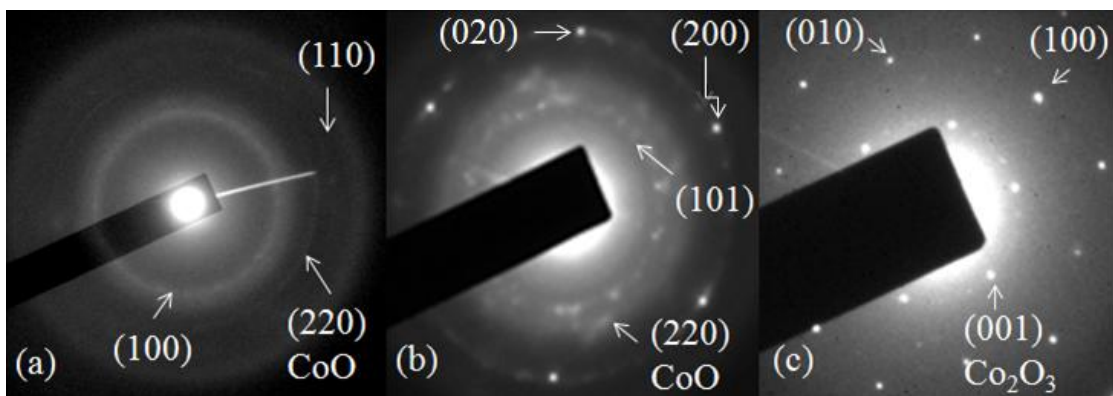


Figure 6.7. SAED patterns of (a) 275nm, (b) 150nm and (c) 50nm NWs after releasing the NWs from the membranes. The electron beam incidents on the curved surface of the NWs and perpendicular to their axes.

The crystal structure of the NWs after releasing them from the membranes are also studied by selected area electron diffraction (SAED) study. SAED patterns obtained from a single NW with diameter 275nm, 150nm and 50nm are shown in Fig. 6.7 (a), (b) and (c), respectively. The diffuse rings from the 275nm wire indicate its polycrystalline structure and shows the diffraction patterns obtained from (100) and (110) plane of hcp phase. The observation is consistent with the XRD pattern.

However, the texture of the hcp crystal phase improved as we decrease the nanowire diameter. In 150nm wire diameter, circular ring with hexagonal spots of hcp phase are observed from (200) and (020) planes and the circular ring corresponds to polycrystalline (101) plane of hcp Co. SAED pattern of 50nm wire diameter shows single crystalline hcp (hexagonal close packed) phase with diffraction spots from (010) and (100) planes. During the study, the electron beam was projected perpendicularly to the axes of NWs and the patterns indicate the textured c-axis perpendicular to the length of the NWs.

The increase in crystalline texture on decreasing the diameter is the consequence of increased pressure at smaller diameter during the electrodeposition¹⁷ as other parameters during synthesis are kept the same. Diffraction patterns of cobalt oxide are also identified in SAED patterns (Fig.6.7) as expected in bare NWs after dissolving the membranes.

As the NWs are magnetic, we employed a magnetic force microscope (MFM) along with an atomic force microscope (AFM) to study the bare NWs coming out from the gold thin film after chemically dissolving the membranes. The MFM micrographs along with the AFM data are shown in Fig. 6.8 and Fig. 6.9.

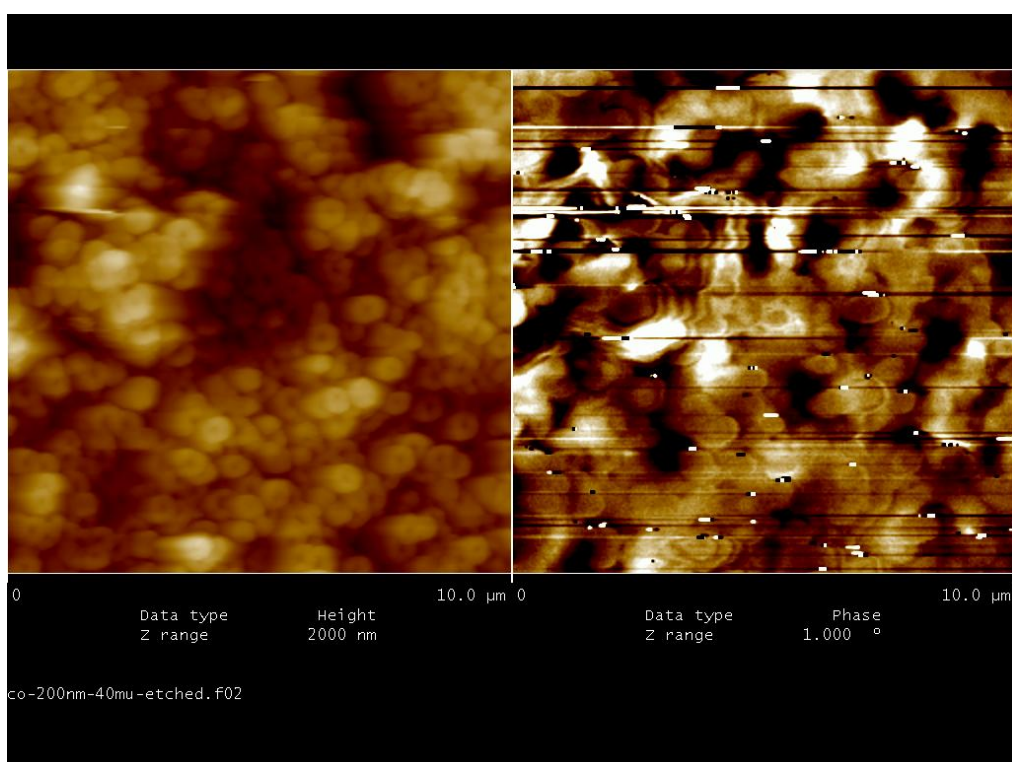
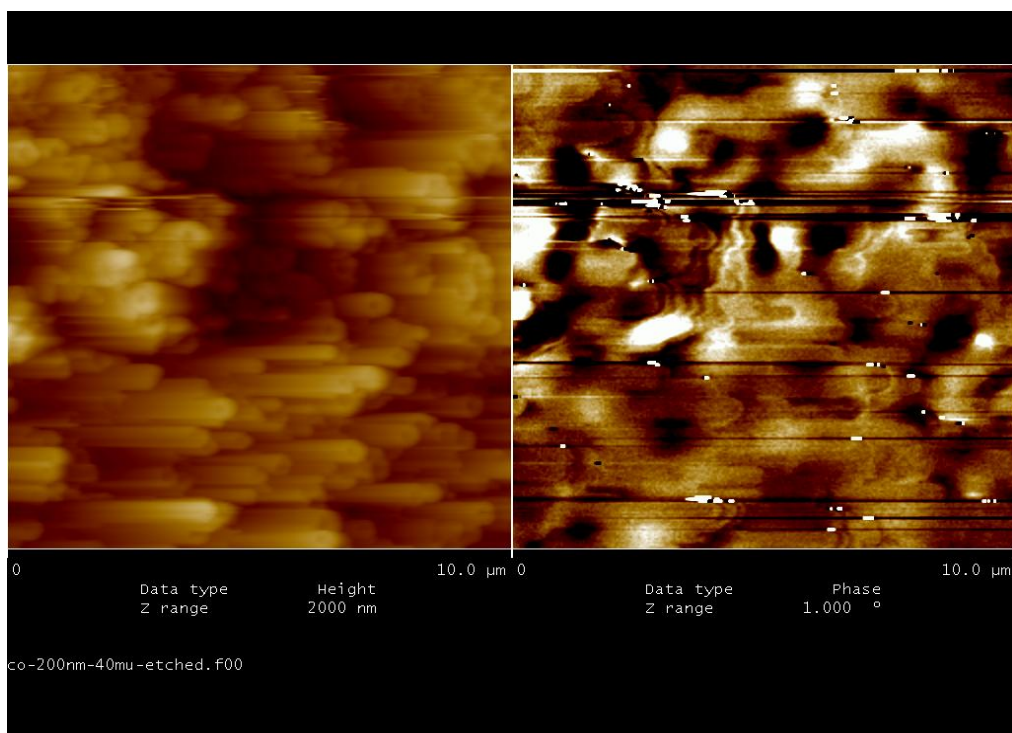


Figure 6.8. AFM (left) and MFM (right) micrographs of bare 275nm Co NWs after dissolving the membrane.

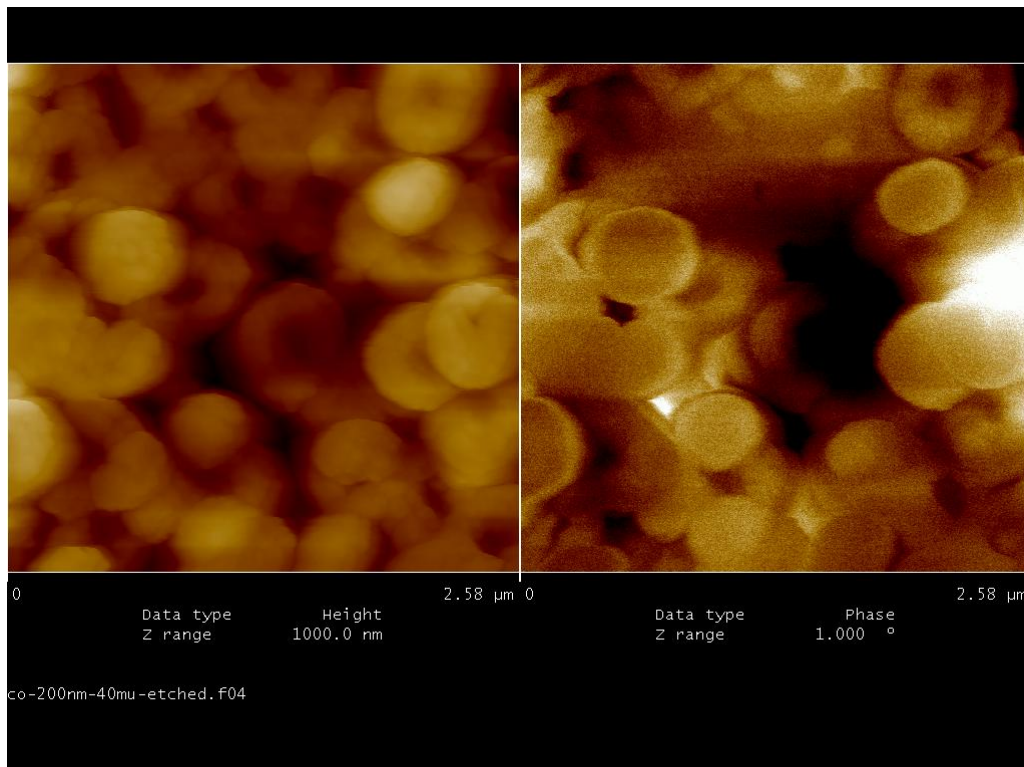


Figure 6.9. AFM (left) and MFM (right) micrographs of bare 275nm Co NWs after dissolving the membrane.

The magnetic tip of MFM magnetizes the NWs in a close vicinity of the tip. Colors in the micrographs indicate the intensity of magnetization of the nanostructures within the samples. The brightest (white) and darkest (black) colors signify the spin upped and spin downed NWs respectively. The MFM micrographs show the most of surface area of the samples are covered with neither white nor black spots, indicating perpendicular magnetization of the NWs with respect to their length. The corresponding AFM micrographs show clear formation of NWs of the same samples.

6.3.2 Magnetic properties

All the magnetic measurements of the arrays of NWs are done keeping the membranes intact. The room temperature isothermal magnetic hysteresis loops of the arrays of NWs are measured by a SQUID (Quantum Design, MPMS) and a vibrating sample magnetometer or VSM (Lakeshore). Dynamic response of the arrays of NWs with the diameter 150 nm having the ARs of 50 and 400 are studied by a ferromagnetic resonance set-up (Bruker make) at room temperature.

In Fig. 6.10, 6.11 and 6.12 we plotted the magnetic hysteresis loops recorded for 50, 150 and 275 nm NWs respectively at two different orientations of the external applied magnetic field H_a : parallel to the length (L) of the NWs, described as the “Out of plane” (OP) and perpendicular to it, denoted as “In plane” (IP) configuration. In above mentioned figures, hysteresis loops in solid lines correspond to the IP configuration and the same in dotted line correspond to the OP configuration. In both the configurations, we observed that the hysteresis loops are tilted and non-quadrilateral in shape with remanence magnetization $M_r < 0.45M_s$ and coercivity $H_c < 540$ Oe, where M_s is the saturation magnetization.

Here it is noteworthy to remember that, in absence of an external magnetic field, the equilibrium state of magnetization of a ferromagnetic nanostructure is determined by the exchange interaction and other anisotropy fields like shape, magnetocrystalline and surface anisotropy field.¹⁸ At sub-micrometer length scale, various micromagnetic calculations based on Landau-Lifschitz-Gilbert equations suggest two remanent states of an isolated cylindrical shaped NW: *flower states* at lower diameters of NWs and *vortex states* at higher diameters of NWs.¹⁹⁻²⁵

In flower state, the spins are parallel to each other and are oriented along the NW axis. It follows a coherent magnetization reversal and produces square shaped hysteresis loop with $M_r \approx M_s$. Whereas in the vortex state, the magnetic spins are tilted in the circumferential direction and make a certain angle to each other. In this state, curling type of reversal takes place giving rise to a tilted non-quadrilateral hysteresis loops with much low remanence and coercivity. A complex vortex state may also be possible on increasing the diameter further.

It is to be noted that, inside a cylindrical shaped bulk magnetic structure, one can observe multi-domain structure defined by Neel or Bloch domain walls¹³. However, in case of MWs (diameter $\sim 100 \mu\text{m}$), we know there exist a long (\sim lengths of MWs) cylindrical single domain inner core (IC) and a multidomain outer shell (OS). The inner core cylindrical single domain can have radius more than 50% radius of the MWs.²⁶ Therefore, we can expect that, the NWs (diameter up to $\sim 275\text{nm}$) in our present study can also possess single domain. However in micromagnetic frame work, the NWs should have either flower or vortex structure instead of very well defined domains separated by Neel or Bloch domain walls. The remanent state is in turn modified by the magnetostatic interaction among the NWs when they are in arrays.^{22, 23}

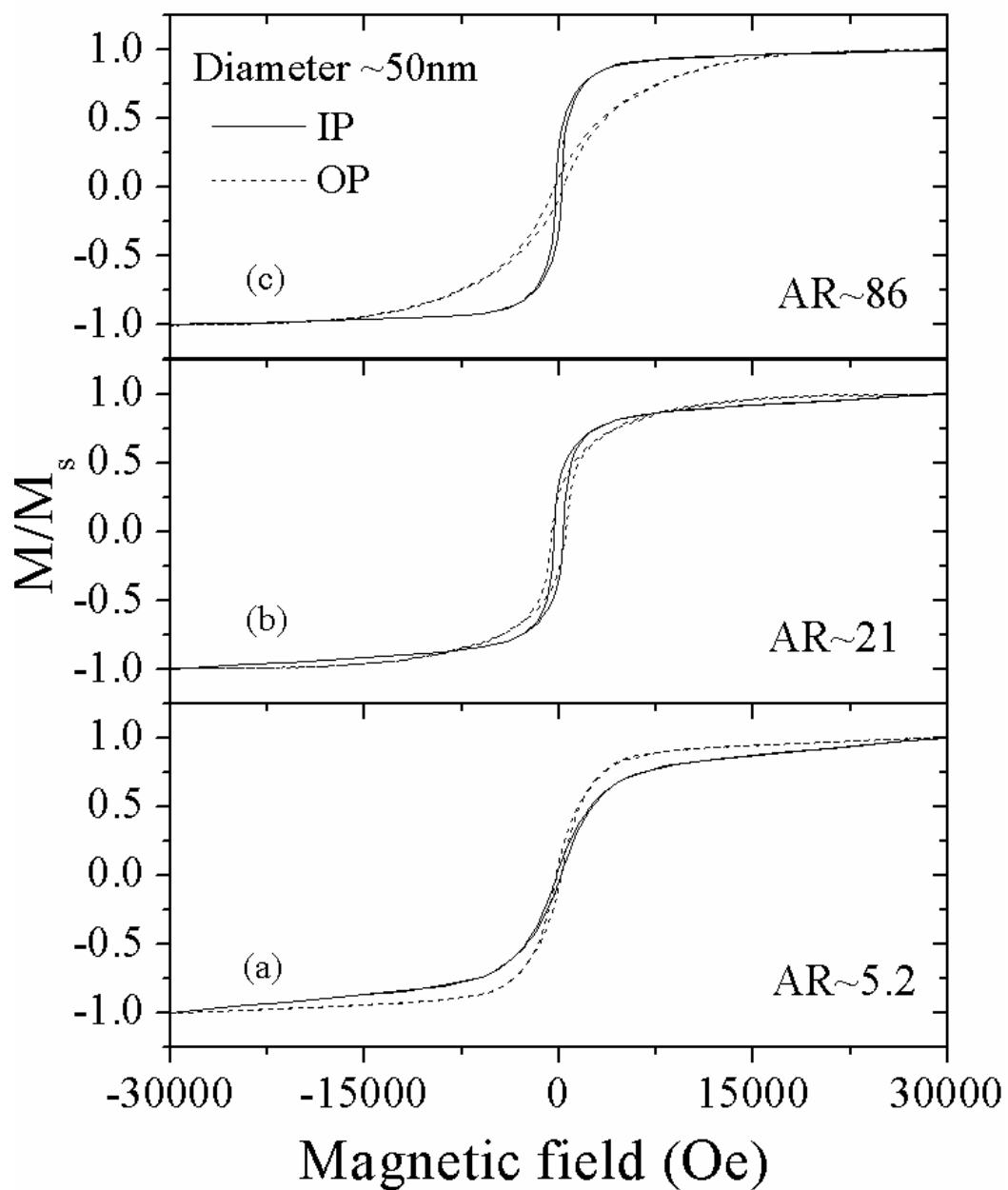


Figure 6.10. Hysteresis loops of the NWs with diameter 50nm having AR ~ (a) 5.2 (b) 21 and (c) 86. The dotted and solid curves are for applied field parallel (OP) and perpendicular (IP) to the axes of the NWs respectively.

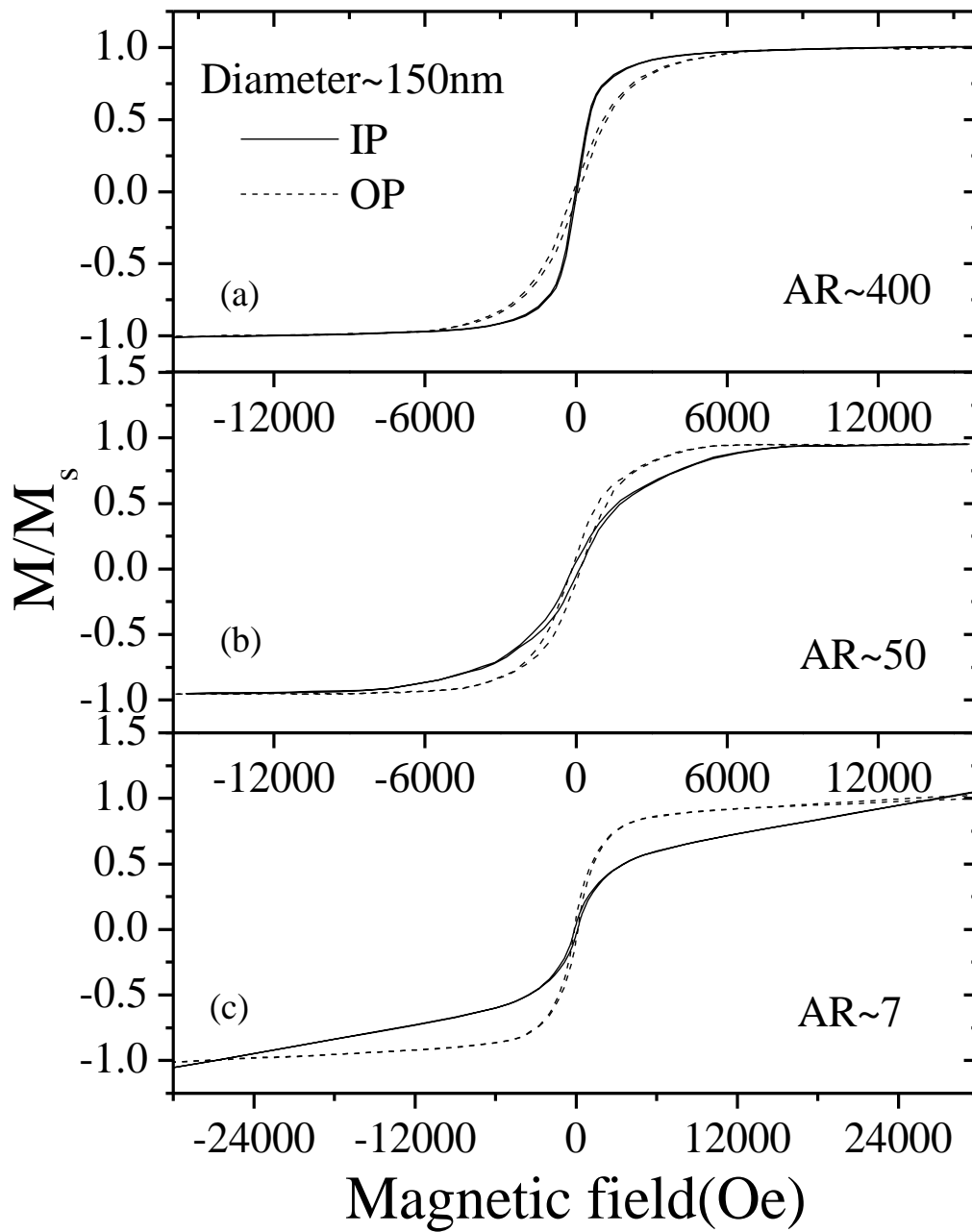


Figure 6.11. Hysteresis loops of the NWs with diameter 150nm having AR ~ (a) 400, (b) 50 and (c) 7. The dotted and solid curves are for applied field parallel (OP) and perpendicular (IP) to the axes of the NWs respectively.

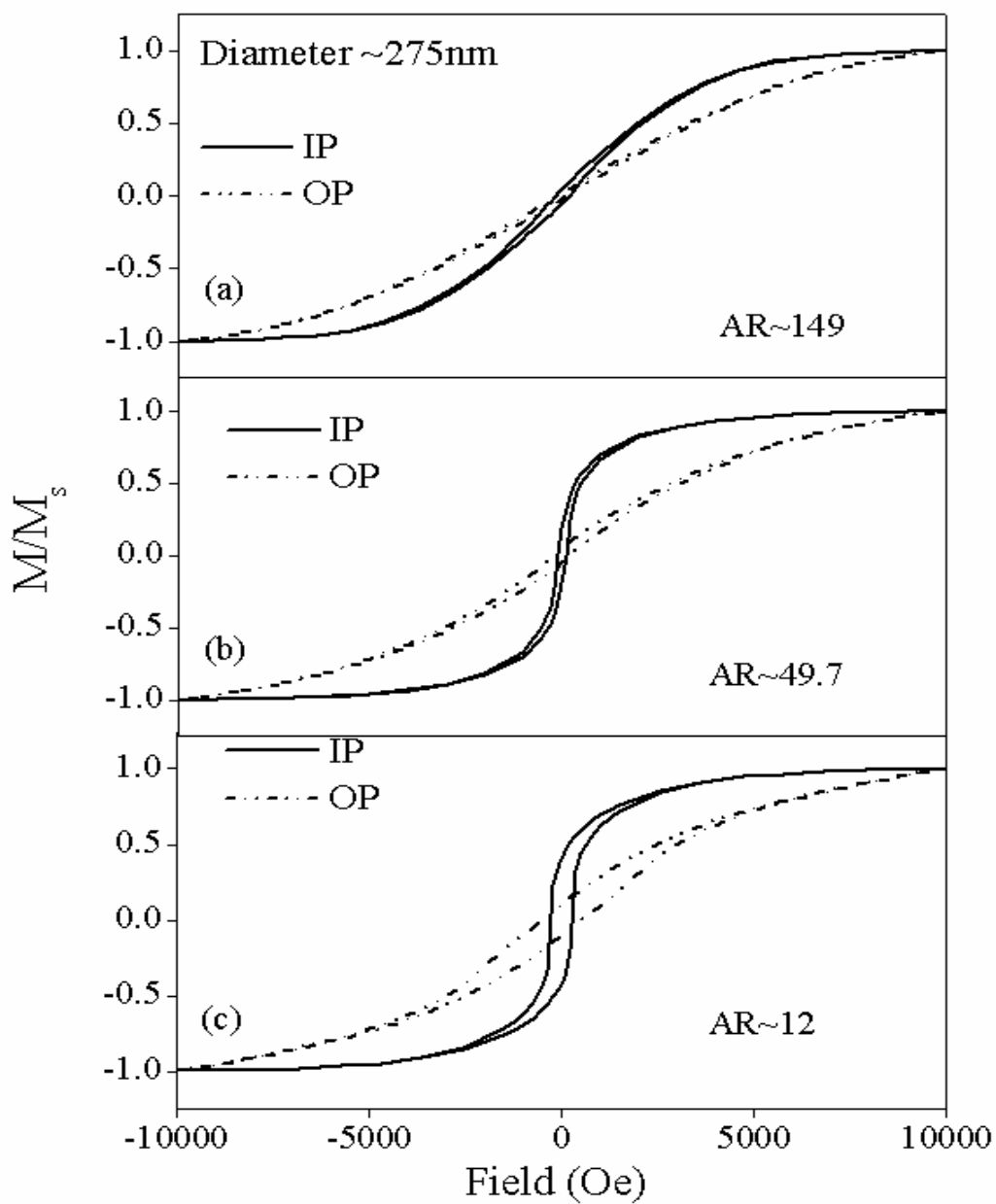


Figure 6.12. Hysteresis loops of the NWs with diameter 275nm having AR ~ (a) 149, (b) 49.7 and (c) 12 respectively. The dotted and solid curves are for applied field parallel (OP) and perpendicular (IP) to the axes of the NWs respectively.

It is known that, the critical diameter (D_c) of a magnetic cylinder, beyond which the flower state is unstable and vortex state develops, is proportional to magnetic exchange length, $\lambda_{ex} = \sqrt{A / M_s}$ of the material, where A is the exchange constant and M_s , the saturation magnetization of the material.^{23, 27} Ross et. al. found²³ the D_c for a pure Co cylinder with AR within the range of 0.9 to 3.5 is about 24.5 nm. Furthermore in case of infinite cylinder, the surface induced anisotropy²⁸ stabilize the vortex state in it²⁵ and the value of D_c may even become lower due to less magnetostatic energy.²⁹ Here, we have the NWs with minimum diameter 50 nm. Hence, all the experimental evidences indicate towards vortex remanent state within the NWs used in our study.

In Fig. 6.10 (a) and Fig. 6.11 (c), 6.11 (b) for low ARs of the 50 and 150 nm NWs respectively, we notice near the zero external magnetic fields, the OP magnetization increases faster with the external field than the IP magnetization. This type of sharper hysteresis loops along OP direction of the NWs indicates the OP as their easy direction of magnetization. On the other hand, in Fig. 6.10 (b), 6.10 (c) and 6.11 (a), we notice IP easy axis at higher ARs of the NWs (AR ~ 21, 86 for 50 nm and ~ 400 for 150 nm NWs). In Fig.6.12, the IP hysteresis loops for 275 nm NWs were always sharper than OP loops for all values of AR (~ 12, 49.7, 149) and no change in easy direction is observed.

We estimate the squarenesses (M_r/M_s) and initial susceptibilities ($\chi_{initial}$) from the hysteresis loops for all the NWs and plotted in Fig. 6.13 and 6.14 respectively. Here the solid and dotted lines are the best fitted polynomial curves for the experimental data obtained in IP and OP directions respectively.

We see the IP squareness is lower than the OP squareness for lowest two ARs of the 50 nm NWs. As the AR increases, a crossover among the IP and OP squareness is observed. At higher ARs of the NWs, the OP squareness is almost saturated i.e. no change in squareness is observed there, while the IP squareness decreases slowly at higher ARs. The phenomena of crossover the IP and OP easy axis is consistent with the change in easy axis from OP to IP direction as observed in their corresponding

hysteresis loops. In case of 150 nm NWs, OP squareness is always higher than the IP squareness and no crossover is observed. Squareness in both the directions increases first with the increase in AR, then decrease at higher ARs. At the highest AR ~ 400, the OP squareness tries to merge with IP one indicating a tendency towards the change in easy direction from OP to IP. However, the IP squareness is always remaining higher than OP direction in case of 275 nm NWs.

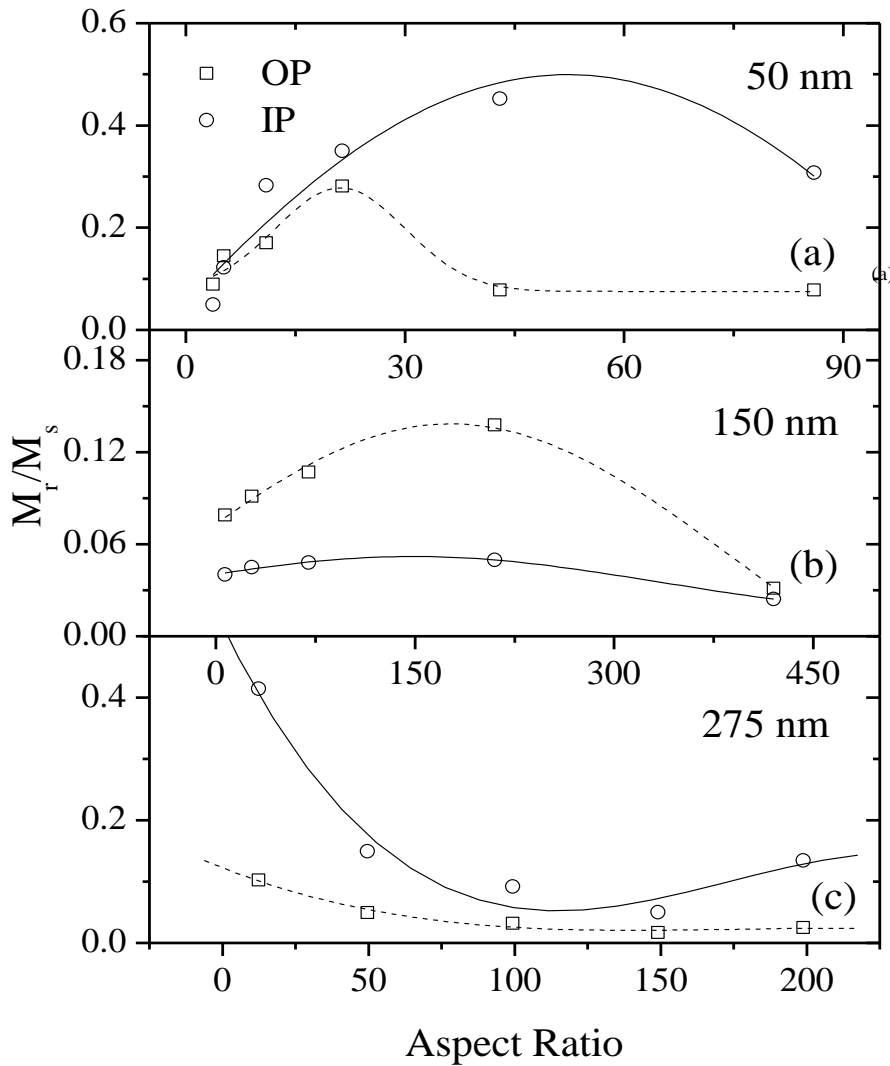


Figure 6.13. Squareness (M_r/M_s) along IP (open circles) and OP (open boxes) direction plotted against the ARs of the (a) 50 nm (b) 150 nm and (c) 275 nm NWs. Solid and dotted lines corresponds to the best fitted polynomial plot in IP and OP directions.

The crossover of easy axes is more prominent in the plot of initial susceptibilities along IP (χ_{IP}) and OP (χ_{OP}) as a function of AR of the NWs in Fig. 6.14 (a) for 50 nm, 6.14 (b) for 150 nm and 6.14 (c) for 275 nm NWs.

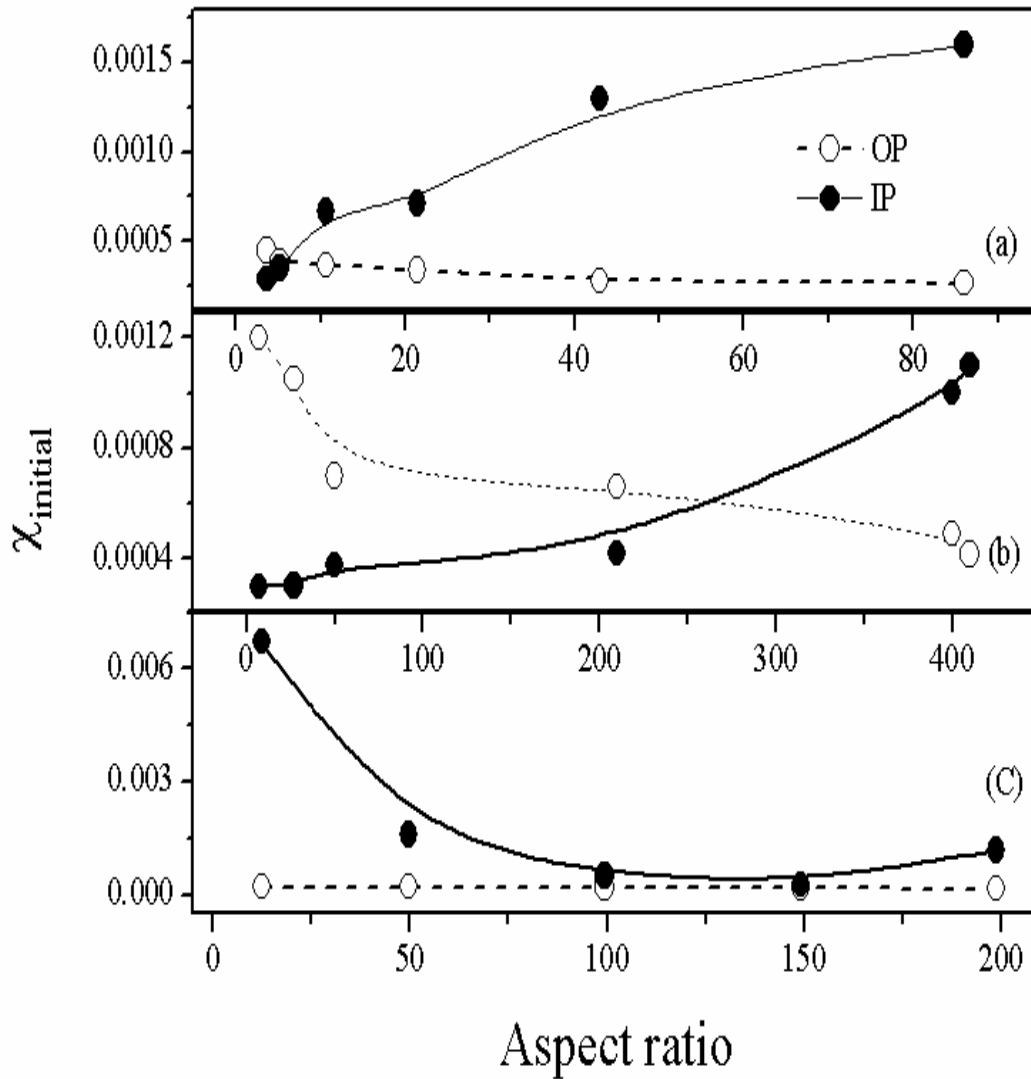


Figure 6.14. Initial susceptibility, $\chi_{initial}$ vs. AR plot for both the IP and OP configurations of the NWs with diameter (a) 50nm, (b) 150nm and (c) 275nm.

χ_{OP} is initially higher than χ_{IP} at low ARs of 50 and 150 nm NWs. Upon increasing the AR, a crossover between χ_{IP} and χ_{OP} has been seen at AR ~ 6 and 265 for 50 and 150 nm NWs respectively. These indicate a change in easy axis from OP to IP on increasing the AR of the NWs. Whereas in Fig.6.14(c), the 275nm NWs show higher χ_{IP} compared to χ_{OP} for all values of AR indicating no change in easy direction on increasing the AR. The above mentioned directional change of easy axes can be explained by considering the anisotropies present in the NWs.

The anisotropies that determine the shape of the magnetic hysteresis loops of a NW are mainly the shape and magnetocrystalline anisotropies. In order to get an estimate of shape anisotropy of a NW, demagnetization factors (N_d) of the NWs with different ARs are calculated along their length (N_d^{OP}) and perpendicular to the NW axis (N_d^{IP}).²⁹ In Fig.6.15, we plotted the demagnetization fields along IP direction, $H_d^{IP} = N_d^{IP} M_s$ (closed circles) and along OP direction, $H_d^{OP} = N_d^{OP} M_s$ (open circles) where $M_s = 1422$ emu/cc of bulk Co is taken. It indicates, irrespective of the diameter of NWs, the shape anisotropy along OP direction ($\sim H_d^{OP}$) of a NW increases sharply up to the AR ~ 43 beyond which it becomes almost saturated at a value $\sim 2\pi M_s = 8930$ Oe.

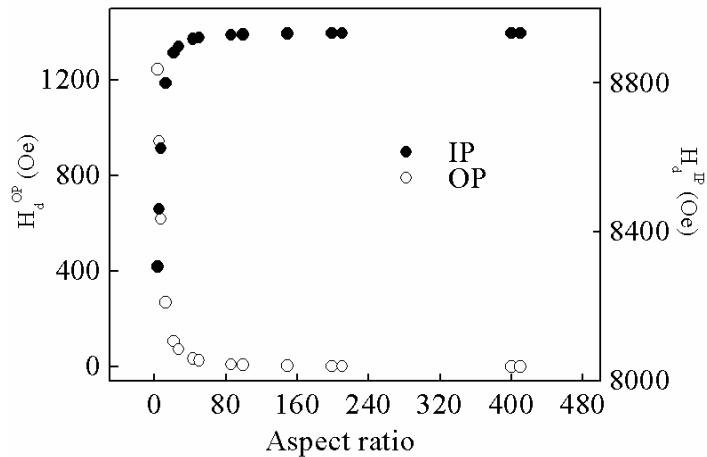


Figure 6.15. Plot of calculated demagnetization field of the NWs with respect to their AR along OP and IP direction.

Therefore it is clear that, the shape anisotropy of the NWs in our study always tries to make the OP as easy direction and remain constant beyond AR ~ 43 . Hence, it has nothing to do with the crossover of easy axis of NWs from OP to IP on increasing the ARs of NWs.)

On the other hand, the magnetocrystalline anisotropy (H_k) remains constant for a particular wire diameter irrespective of its AR and depends only on the crystallinity of the NW. The magnetocrystalline anisotropy field for NWs used in our study can achieve its highest value $\sim 2K_1/M_s = 7032$ Oe for single crystalline NWs with diameter 50 nm, where K_1 is the first order anisotropy constant and is equal to 5×10^5 erg/cc for hcp phase.²⁹ H_k is much lesser in 150 nm NWs as they consist of textured hcp as well as polycrystalline phase. The direction of H_k is along the IP direction of the NWs which is the direction of c-axis of hcp crystalline phase. The NWs with diameter 275 nm have poly-crystalline phase and thus have negligibly small magnetocrystalline anisotropy. Thus the shape anisotropy always dominates over the crystalline anisotropy for all the NWs we used in our study. As a consequence, the OP easy axis of a single NW is determined by the resultant of these two anisotropies of a NW³⁰ contrary to the IP easy axis observed in some of our arrays of NWs.

In case of NWs arranged in a 2D dense array similar to ours, it is obvious to consider the magnetostatic interaction (H_{int}) among the NWs. The shape anisotropy does not change beyond AR ~ 43 and the magnetocrystalline anisotropy remain constant at all ARs for a particular diameter of NWs. These indicate that, it is the magnetostatic interaction that dominates over all other anisotropies and changes the direction of easy axis from OP to IP (Fig. 6.14) opposed by shape anisotropy.

The simplest and almost well established model of the interaction among the NWs is the dipolar interaction^{31, 32} while assuming the NWs themselves as magnetic dipoles. In this model, it has assumed that the dipolar field of interaction increases linearly with the volume of the NWs and inversely proportional to third power of inter-wire distance. The dipolar interaction field can derive as follows.

Given a single dipole P_0 surrounded by an array (dimension $m \times n$) of dipoles on a 2D square lattice P_m , the interaction energy is

$$E = \sum_i (\mathbf{P}_0 \cdot \mathbf{P}_m) / r^3 - 3 \{ (\mathbf{P}_0 \cdot \mathbf{r}) (\mathbf{P}_m \cdot \mathbf{r}) \} / r^5 \quad [6.1]$$

This is equivalent to a field H_D acting on the dipole such that: $E = -\mathbf{P}_0 \cdot \mathbf{H}_D$

$$-\mathbf{P}_0 \cdot \mathbf{H}_D = \sum_i (\mathbf{P}_0 \cdot \mathbf{P}_m) / r^3 - 3 \{ (\mathbf{P}_0 \cdot \mathbf{r}) (\mathbf{P}_m \cdot \mathbf{r}) \} / r^5 \quad [6.2]$$

Fig. 6.16 shows a schematic diagram of the dipolar interaction scheme for applied field parallel and perpendicular to the NWs axes. The blue NW at the center of the square grid indicates the P_0 dipole (test NW) and the others indicate the P_m dipoles.

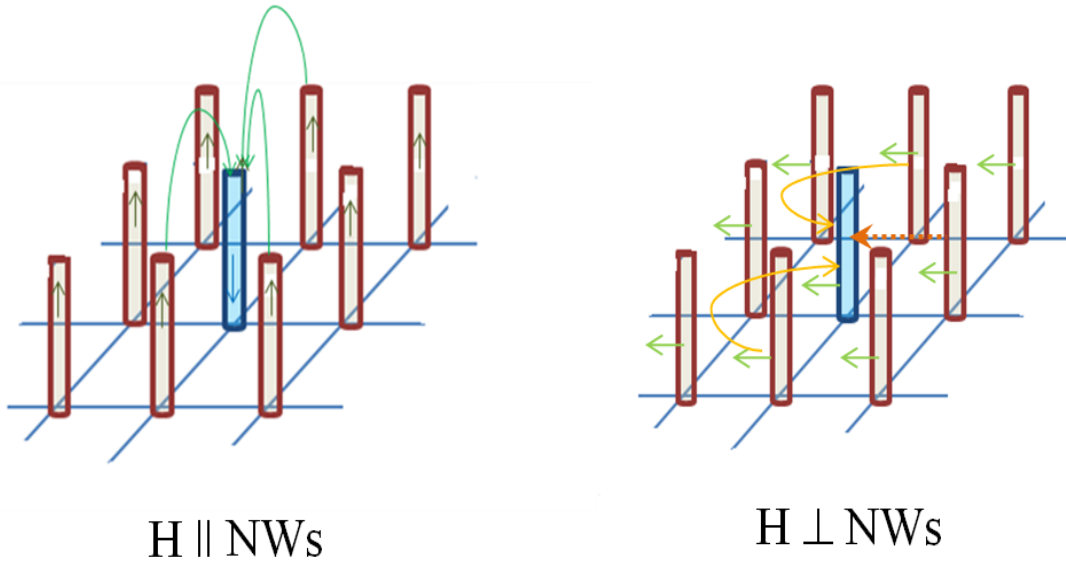


Figure 6.16. Schematic diagram of the dipolar interaction model for applied field parallel and perpendicular to the NWs axes. Blue NW is the test NW (P_0 dipole in Eq. 6.2) and the brown NWs are the nearest neighbor NWs (P_m dipoles in Eq. 6.2).

We assume that the square lattice is of parameter D (average nanowire separation). In order to estimate $H_{D(Z)}$, we take \mathbf{P}_0 directed along the Z axis, $\mathbf{P}_0 = (0, 0, 1)$ and $-\mathbf{P}_0 \cdot \mathbf{H}_D = -H_{D(Z)}$.

At any node (m, n) of the lattice $\mathbf{P}_m = (P_x, P_y, P_z)$, and $\mathbf{r} = (mD, nD, 0)$, hence $\mathbf{P}_0 \cdot \mathbf{r} = 0$, $\mathbf{P}_0 \cdot \mathbf{P}_m = P_z$.

The field $H_{D(Z)}$ is then,

$$H_{D(Z)} = - \sum_{m,n=-\infty,\infty} (P_Z / r^3) = - \sum_{m,n=-\infty,\infty} \{P_Z / D^3 (m^2 + n^2)^{3/2}\} \quad [6.3]$$

Taking all surrounding dipoles saturated along Z, $P_Z = M_s V$ with V the total volume:

$$H_{D(Z)} = -M_s V / D^3 \sum_{m,n} 1 / (m^2 + n^2)^{3/2} \quad [6.4]$$

The sum above performed with the conditions $i,j \neq 0$ is explicitly written as

$$\sum_{m,n=-\infty,\infty} 1 / (m^2 + n^2)^{3/2} = 4 \sum_{m,n=1,\infty} 1 / (m^2 + n^2)^{3/2} \quad [6.5]$$

Numerically,

$$\sum_{m,n=1,\infty} 1 / (m^2 + n^2)^{3/2} \approx 1.05 \quad [6.6]$$

Hence,

$$H_{D(Z)} = 4.2 M_s V / D^3 \quad [6.7]$$

We move next to the evaluation of $H_{D(X)}$. Take now \mathbf{P}_0 directed along the X axis, $\mathbf{P}_0 = (1, 0, 0)$, $\mathbf{P} = (P_X, P_Y, P_Z)$ and $\mathbf{r} = (iD, jD, 0)$, the dipolar energy writes

$$E = -\mathbf{P}_0 \cdot \mathbf{H}_D = -H_{D(X)}, \quad \mathbf{P}_0 \cdot \mathbf{P} = P_X \quad [6.8]$$

$$E = - \sum_{m,n=-\infty,\infty} \{r^2 P_X - 3D^2 (m^2 P_X + mn P_Y)\} / r^5 \quad [6.9]$$

Hence,

$$H_{D(X)} = - \sum_{m,n=-\infty,\infty} \{P_X (m^2 + n^2) - 3(m^2 P_X + mn P_Y)\} / D^3 (m^2 + n^2)^{5/2} \quad [6.10]$$

If all the surrounding dipoles are saturated along X, $P_X = M_s V$, $P_Y = 0$, we get

$$H_{D(X)} = (M_s V / D^3) \sum_{m,n=-\infty, \infty} (2m^2 - n^2) / (m^2 + n^2)^{5/2} \quad [6.11]$$

Exploiting the symmetry, we get

$$H_{D(X)} = 4(M_s V / D^3) \sum_{m,n=1, \infty} (2m^2 - n^2) / (m^2 + n^2)^{5/2} \quad [6.12]$$

Numerically,

$$\sum_{m,n=1, \infty} (2m^2 - n^2) / (m^2 + n^2)^{5/2} \approx 0.526 \quad [6.13]$$

Hence,

$$H_{D(X)} = 2.1 M_s V / D^3 = -1/2 H_{D(Z)} \quad [6.14]$$

This proves the dipolar field along X is half its value along Z as used in the text. The negative sign before $H_{D(Z)}$ in Eq. 6.14 indicates the interaction field along OP direction opposes the magnetization. Similarly the positive $H_{D(X)}$ indicates that, it helps the magnetization. In other words, the nature of interaction is anti-ferromagnetic (AFM) kind in OP configuration and the magnitude is double to the ferromagnetic (FM) nature of interaction in IP direction. Ideally the dipolar assumption holds good when the dipoles are infinitely separated from each other as discussed in *chapter 1*. In case of 2D arrays of NWs, when the diameter of the NWs is too small compared to the inter-wire distance D, the approximation holds good.

The magnetostatic interaction influences both the coercive and saturation field effectively. In order to understand the influence while the external field is applied in OP direction, let us consider a couple of wires (Fig. 6.17). At high positive field, both wires have magnetization pointing in the Z direction (OP direction). In such case, the dipolar stray field of the NW opposes to the magnetization of the other wire. This situation reduces the applied field, which is required to reverse magnetization of one wire. Once the magnetization is reversed it creates a dipolar stray field along the same direction of the magnetization of the non-reversed wire.

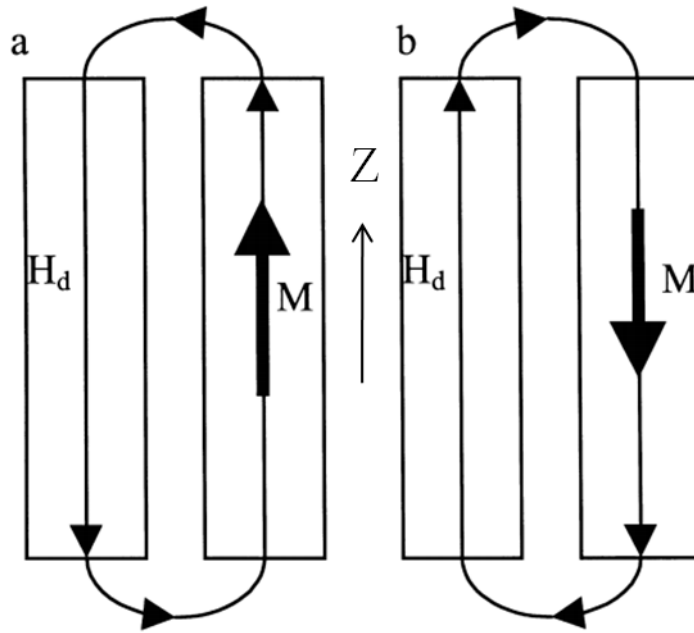


Figure 6.17. Dipolar fields of interacting nanowires (a) with parallel and (b) with opposite magnetization.

So, to produce the reversal of the magnetization of the second wire, a higher negative field is needed. To summarize, the magnetostatic interaction between two wires produce two effects: the coercive field is reduced (compared to the one of a single NW) and the saturation field is increased. If the external field is applied perpendicular to the NWs, the saturation field will reduce according to sign convention of Eq. (6.14).

Considering all the anisotropies, the total anisotropy in IP and OP direction can be written as

$$H_{IP} = H_{D(X)} + H_{crys} = 2.1 M_s V / D^3 + H_{crys} \quad [6.15]$$

And

$$H_{OP} = H_{D(Z)} + H_{sh} = -4.2 M_s V / D^3 + H_{sh} \quad [6.16]$$

Considering the above two equations the crossover of easy axis with the increase in NW volume or AR can be explained. When the magnetostatic interaction among the NWs dominates over the shape and magnetocrystalline anisotropies ($H_{sh} > H_{crys}$), the IP easy direction of the arrays of NWs can be explain [(Fig. 6.10 (b), 6.10 (c) and Fig. 6.11 (a)]. On the other hand when the NW volume V is very small, the interaction field is weak compared to H_{sh} in OP direction resulting an OP easy axis [Fig. 6.10 (a), 6.11 (b) and Fig. 6.11 (c)].

In Fig.6.18 we plotted the IP and OP anisotropy field H_{ani} of the NWs determined from the corresponding hysteresis loops, as a function of AR for each diameter of the NWs. At low ARs, H_{ani} is higher along IP direction for 50 and 150nm NWs. At higher ARs, the opposite behavior was observed.

The crossover between the IP and OP anisotropy fields i.e. the directional change of easy axis observed for 50 and 150 nm NWs at AR ~ 6 and 310 respectively. The directional change in easy axis at relatively lower value of ARs for 50 nm NWs perhaps due to higher inter-wire distance (~ 350 nm) among them compared to 150 nm NW arrays. The directional change of easy axis from OP to IP on increasing the length of 150 nm NWs at quite high values of their ARs contrary to the proposed dipolar interaction model.^{31, 32} This indicate a complex nature of the interaction among the NWs with large ARs. This is because of the uniform magnetic flux line distribution of a dipole around it will change drastically if one increases the length of the dipole infinitely. In such a situation, it is obvious that the flux lines and hence the dipolar field will be more concentrated near the poles of the dipole than their length. Hence, linear dependence of dipolar field strength with the volume of the NWs is certainly doubtful. Furthermore, when the inter-wire spacing among the NWs (of the order of few nanometers) are very small compared to the length of the NWs (of the order of few micrometers) such a straight forward dipole assumption of NWs and the dipolar interaction among them may lead us to wrong results.

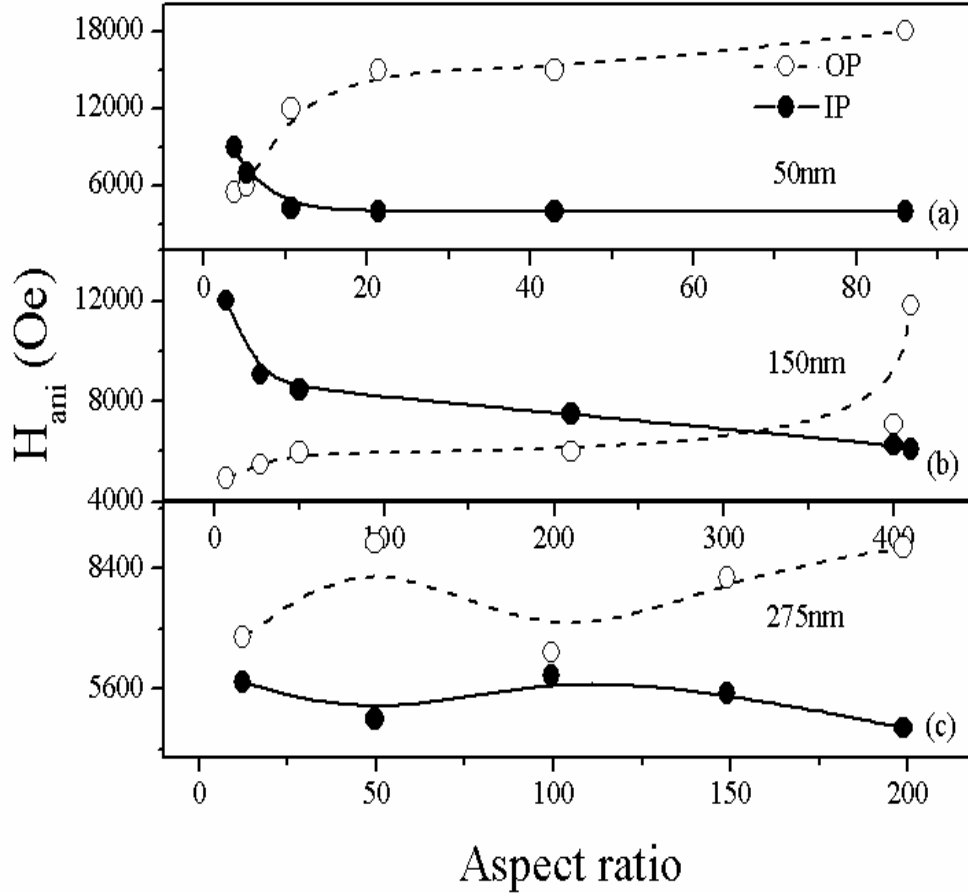


Figure 6.18. H_{eff} vs. AR plot for both the IP and OP configurations of the NWs with diameter (a) 50nm, (b) 150nm and (c) 275nm.

The remanence state of a single NW with such a diameter readily has the vortex state. It lowers the OP remanence of individual NW. If dipolar interaction is there then a crossover between IP and OP squarness is obvious. Only at highest aspect ratio the OP squarness goes down (Fig. 6.13) to a very close value of the IP one. So the observed nature of the squarness (Fig. 6.13) is little abnormal.

The IP squarness first increases and then decreases at highest aspect ratio like the 50nm wire diameter. In 150nm NWs the crystalline anisotropy along IP direction is

less than the 50nm NWs. It also enhances the OP squariness lead by the shape anisotropy. In Fig. 6.13 (c) we assume the effect of thin film for the observed behavior of the squariness as well as of the corresponding hysteresis loops. The IP squariness is decreasing here with the increase in aspect ratio. It is due to the introduction of self demagnetization field at higher aspect ratio produced by the free charges on the curved surfaces of the NWs.

From these observations we can assume here the system of 2D arrays does not attain merely an AFM ground state along the OP direction below the saturation field. The interaction among the NWs is not dipolar in nature below the saturation field perhaps due to the presence of vortex state within the NWs. The dipolar approximation can only give us an intuitive idea about the change in easy axis from OP to IP direction with the increase in aspect ratio. The prediction about the remanence as well as the squariness is little difficult. Because the magnetostatic interaction is itself complex in nature that influence the individual remanent state of a NW and the propagation of vortex wall in more complex way.

In literatures, reports on more realistic theoretical models of the interactions have been found where each saturated NWs are discretized into thousands of elemental cubes within which the magnetization is uniform. Within a NW, the magnetizations of the cubes are parallel to each other and make a resultant dipole. The dipolar interactions are considered between those elemental cubes of two neighboring parallel NWs.³³ Further improvement has been made by L. Clime et. al.³⁴ where they consider both the dipolar and non-dipolar interaction among the NWs depending upon their length. But according to their model, the directional change of easy axis may occur at some lower value of ARs of the NWs. Furthermore, the models^{33, 34} are not complete as well as they are unable to speculate the situations below the saturation fields in hysteresis for vortex NWs.

For 275 nm NWs, the χ_{OP} is always higher than χ_{IP} [Fig. 6.14 (c)] and the anisotropy field along OP is always higher than in IP [Fig. 6.18(c)] indicating no directional change of easy axis on increasing the AR. It may perhaps due to the fact that the NW diameter ~ 275 nm is much greater than the inter-wire separation ~ 35 nm. So, they behave like thin films made of a continuous distribution of NWs in the array.

Similar kind of behavior for arrays of Ni nanowires with diameter $\sim 275\text{nm}$ is previously described in this thesis (*chapter 5*).³⁵ Here interestingly, the initial susceptibility curves for the 275 nm NWs [Fig. 6.14(c)] tend to merge at higher ARs indicating a competition between thin film and NW characteristics of the system.

Ferromagnetic resonance (FMR) study of NWs is believed to be a more sophisticated and direct approach to study the angular dependence of anisotropy field and hence defining the magnetic easy axis of a particular array of NWs with a particular AR.^{11, 14, 32} We investigate here the angular dependence of anisotropy field of 150 nm NWs with two distinct ARs ~ 50 and 400.

FMR studies were performed by placing the membrane of the samples in the resonant cavity in such a way that the axes of the NWs are along the z-axis of a cartesian coordinate system (Fig. 6.19).

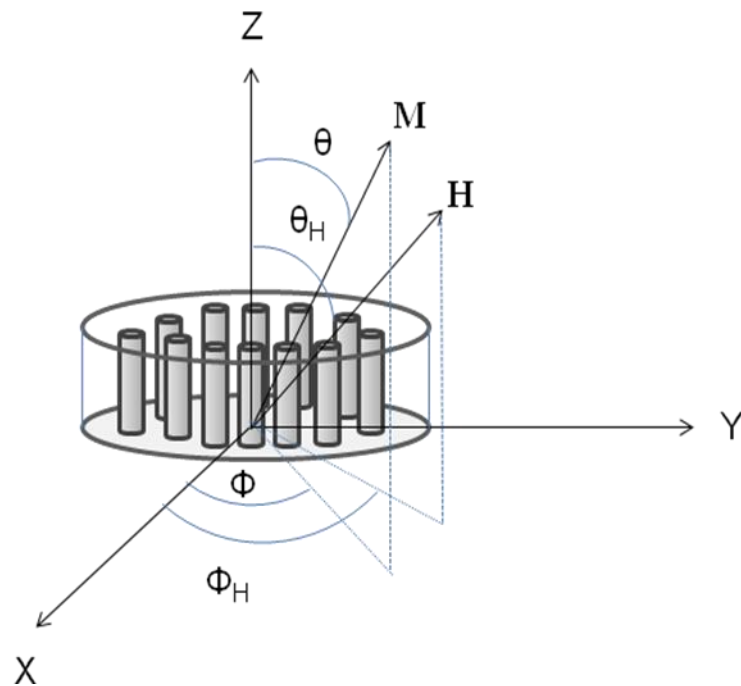


Figure 6.19. Schematic diagram of the NWs arrangement in FMR measurement.

The microwave pumping field h_{rf} with frequency (ν) ~ 24 GHz (k-band) was always oriented perpendicular to the applied bias field H_a and the axes of the NWs. The magnetization \mathbf{M} and applied bias field \mathbf{H}_a can be described by the polar and azimuthal angles (θ, Φ) and (θ_H, Φ_H) respectively in a spherical coordinate system where $H_{a,z} = H_a \cos \theta_H$, the projection of \mathbf{H}_a along Z-axis. We varied the angle θ_H of H_a from 0 to π with respect to the wire axis keeping $\Phi_H = 0$. The strength of the bias field was varied from 0 to 1.7 kOe for each θ_H . FMR derivative spectra at 5° interval of the applied bias field were measured for the arrays of NWs. Typical FMR absorption data for empty resonator, with NW sample (150 nm NWs, AR ~ 50) applying a DC magnetic field at 160° and resonator subtracted the FMR data of the arrays of NWs are shown in Fig. 6.20 (a), (b) and (c) respectively.

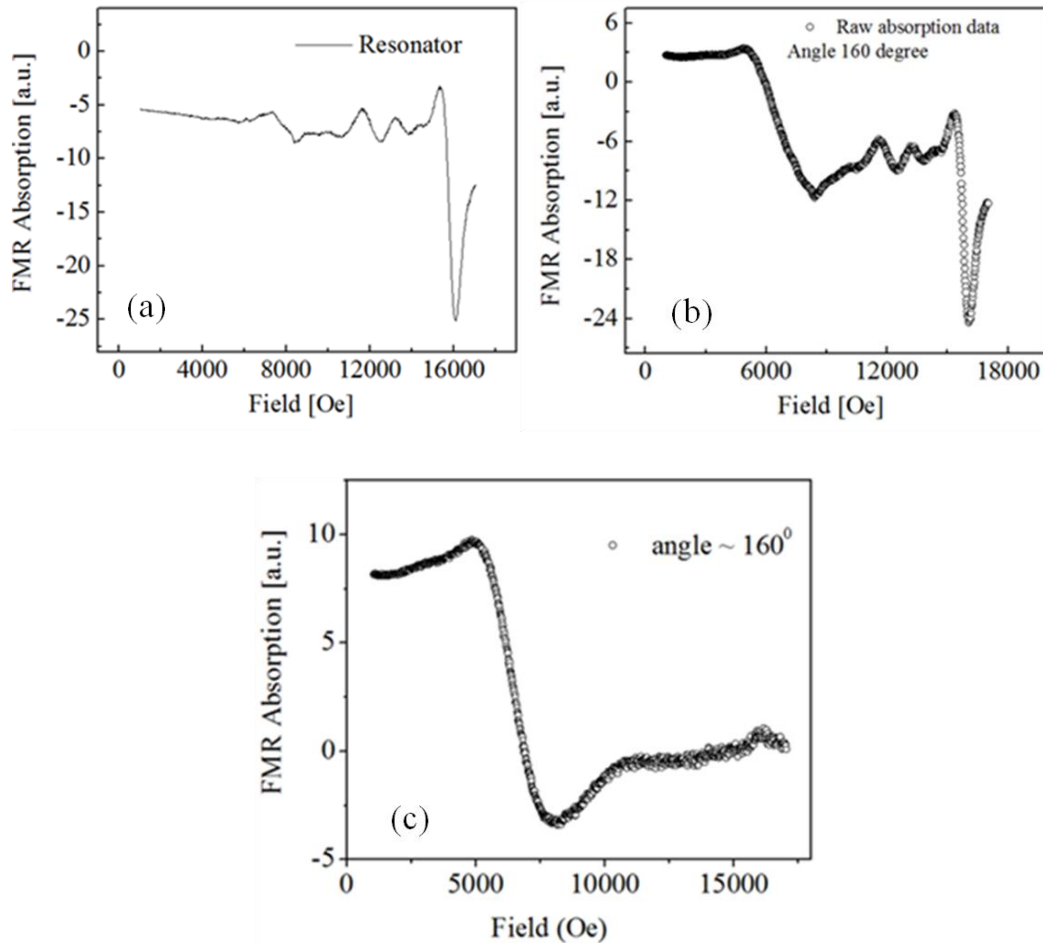


Figure 6.20. FMR absorption data for empty resonator (a), arrays of 150 nm Co NWs having AR ~ 50 with the applied DC magnetic field at 160° (b) and resonator subtracted sample data (c).

Typical sequences of FMR derivative spectra upon sweeping the bias field (H_a) at different θ_H are shown in Fig.6.21 and 6.22 for arrays of NWs with diameter $\sim 150\text{nm}$ and AR ~ 50 and 400 respectively.

The field dependent absorption peaks correspond to FMR absorption peaks and the field corresponds to maximum absorption is taken as the resonance field (H_{res}) from the cobalt NWs. The minor peaks are originated perhaps due to the presence of different crystalline texture and surface anisotropy in the NWs. H_{res} shifts to higher field for shorter NWs and to lower values for longer ones on changing θ_H from 0° (OP direction) to 90° (IP direction). We have measured Φ_H dependence of IP resonance field by rotating the bias field from $\Phi_H=0^\circ$ to 180° and found no change in H_{res} .

For AR ~ 50 (Fig. 6.21), H_{res} significantly increases from $\sim 5398 (\pm 9)$ Oe at $\theta_H=0^\circ$ to $8540 (\pm 12)$ Oe at $\theta_H = 90^\circ$. On the other hand, for AR ~ 400 (Fig. 6.22) a small decrease in H_{res} from $\sim 6627 (\pm 9)$ Oe at $\theta_H=0^\circ$ to $6383 (\pm 9)$ Oe at $\theta_H = 90^\circ$ is observed. The typical skin depth at microwave frequencies in 3d ferromagnetic material is $\sim 100\text{nm}$. Hence the change in H_{res} corresponds to the magnetization of entire NWs and not from their surface only.

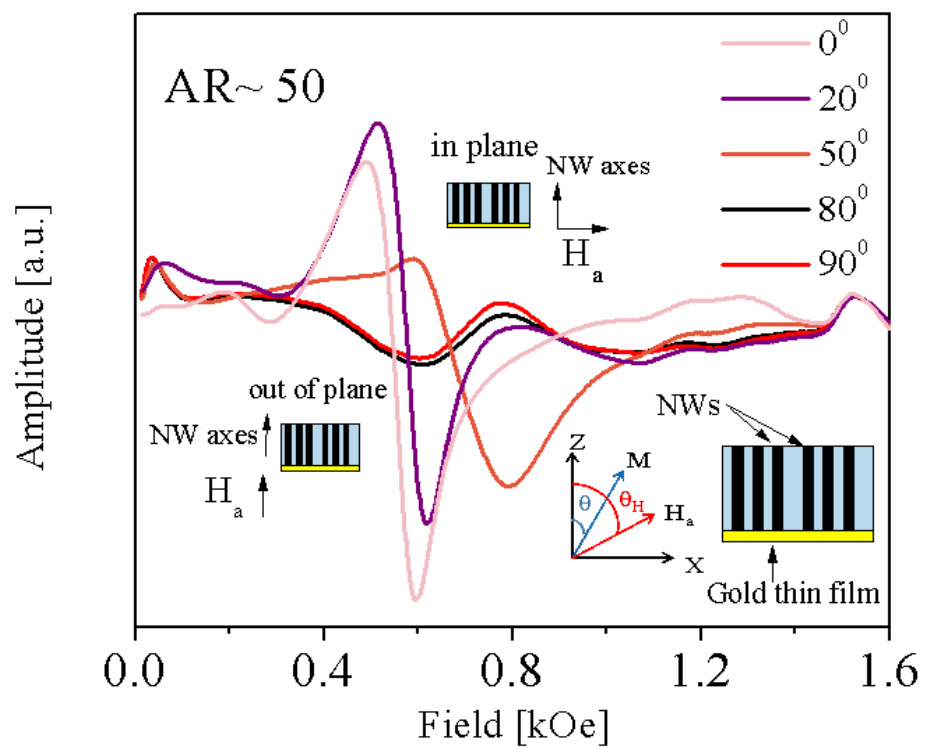


Figure 6.21. FMR spectra at various angles of applied bias field for the 150nm NWs with AR ~ 50. A schematic diagram of the experimental arrangement of FMR study is also shown.

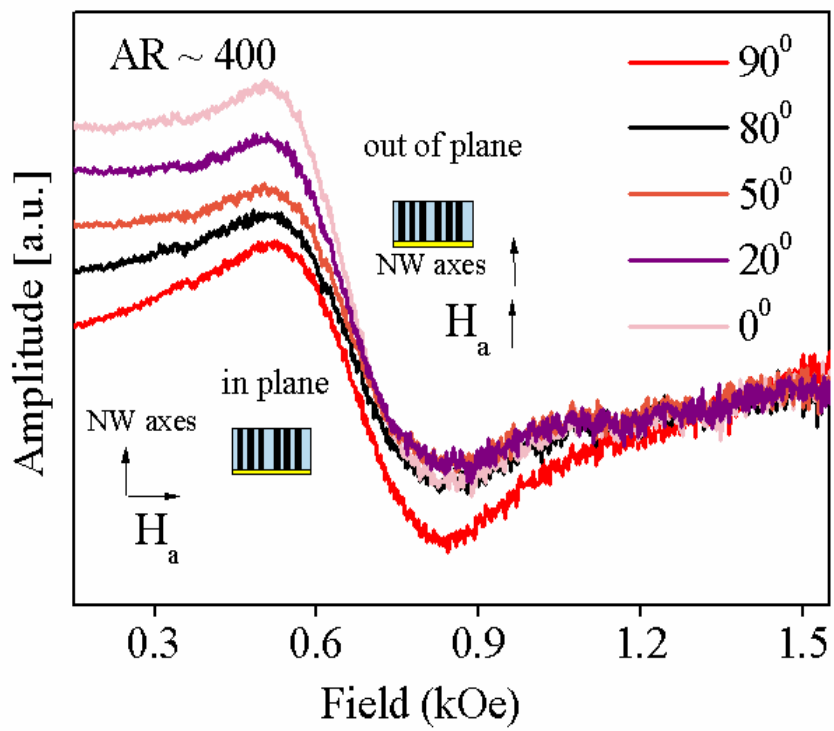


Figure 6.22. FMR spectra at various angles of applied bias field for the 150nm NWs with AR ~ 400.

H_{res} vs θ_H is plotted in Fig. 6.23 for both the samples. It implies the magnetic easy axis changing from OP to IP direction on increasing the AR from 50 to 400 as is observed from the magnetic measurements discussed earlier.

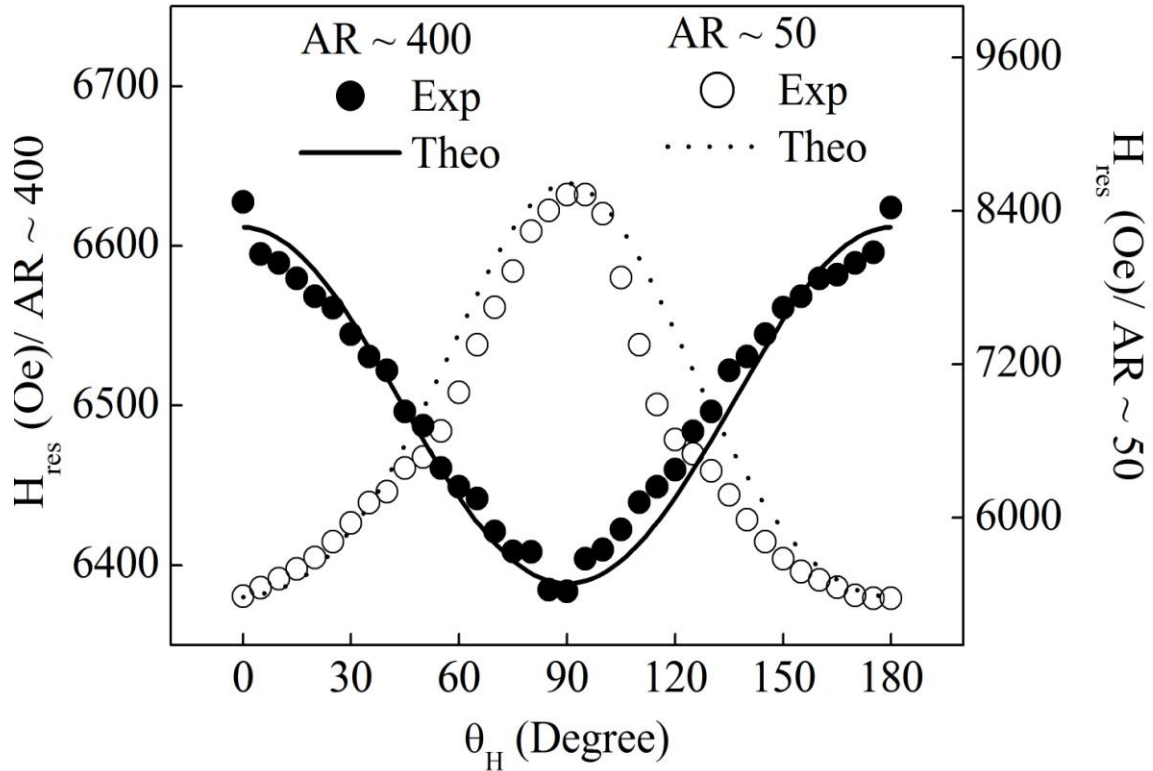


Figure 6.23. Angular dependence of resonance field (H_{res}) of the 150nm NWs with AR~50 (open circles) and AR~400 (solid circles). The best fitted curves using the Eq. (6.18) for AR ~ 50 (dashed line) and AR ~ 400 (solid line) are shown also.

The H_{res} vs θ_H curve can be fitted for uniform FMR mode³⁶ considering the NWs as infinitely long cylinders with an effective uniaxial anisotropy field (H_{eff}) along OP or IP direction depending on AR. The corresponding resonance condition can be derived from the free energy density equation of an infinite cylinder and can be written as,

$$E = M_s H_{eff} \sin^2 \theta - M_s H_{res} \left[\sin \theta \sin \theta_H \cos(\Phi - \Phi_H) + \cos \theta \cos \theta_H \right] \quad [6.17]$$

In our present study with the applied field varying from OP ($\theta_H=0^0$) to IP ($\theta_H=90^0$) direction in a plane of $\Phi = \Phi_H = 0^0$, the resonance frequency ($\omega = 2\pi\nu$) corresponding to the equilibrium angle θ_0 of M is obtained from the second derivative of the energy density Eq. (6.17) by the formalism of Smit and Beljers³⁷ as,

$$(\omega/\gamma)^2 = \left[(H_{eff} \cos 2\theta_0 + H_{res} \cos(\theta_0 - \theta_H)) (H_{eff} \cos^2 \theta_0 + H_{res} \cos(\theta_0 - \theta_H)) \right] \quad [6.18]$$

Here $\gamma = g\mu_B/\hbar$ is the gyromagnetic ratio, taken as positive, μ_B , the Bohr magneton and g , the Landé splitting factor. The equilibrium angle θ_0 of M is determined from the condition $dE/d\theta = 0$ for each field angle θ_H at the corresponding H_{res} . The experimental H_{res} vs θ_H values were fitted with Eq.6.18 and are shown in Fig.6.23 for both the ARs. It gives us the value of $H_{eff} = 2108$ Oe for AR~50 and 149 Oe for AR~400. The value of g calculated from the NWs with AR ~ 50 and OP easy axis is ~ 2.2. We avoided calculating g value from the NWs with AR ~ 400 with IP easy axis as the change in measured H_{res} is only ~ 240 Oe on changing θ_H from 0^0 to 90^0 and can give rise to significant error. The magnetization measurements [Fig. 6.11 (a), (b)] as discussed earlier are in accordance with the FMR results.^{31, 33}

The effective anisotropy field (H_{eff}) is consisted of all the sources of anisotropies that are possibly can exist in the NWs. From SAED study we observed that 150 nm NWs are neither single crystal nor well textured. Therefore their magnetocrystalline anisotropy field (H_k) is much smaller than shape and magnetostatic interaction field. Among the rests, the shape anisotropy field ($H_{sh} = 2\pi M_s$ along OP) and the magnetostatic interaction field H_{int} are the prominent contributions to define the easy direction of the arrays of NWs.

Applying the phenomenological mean field approach suggested by U. Netzelmann³⁸ for the dipolar interaction field in array system, H_{int} has two

contributions : $2\pi M_s P$ due to the charges on the cylindrical wire surfaces which tries to make the IP direction as easy direction and $4\pi M_s P$ for the free charges at the both ends of all the NWs which tries to make the OP direction as magnetically hard where P is the porosity (the ratio of the total cross sectional area of the pores to the membrane's flat surface area) of the membrane. In precise, we can say the magnetostatic interaction has been manifested by the demagnetization fields of thin film (the 2D array) and infinite cylinder (the NW).³² Therefore the resultant H_{int} along IP is $6\pi M_s P$. With $P \sim 0.5$ for 150nm NWs,¹⁶ $H_{\text{int}} = 3\pi M_s$. Combining this with H_{shape} and neglecting H_k , the $H_{\text{eff}} \sim \pi M_s$ (=4466 Oe) along IP direction which explains qualitatively the IP easy axis observed for AR~400 though $H_{\text{eff}} \sim 149$ Oe as obtained from FMR study.

But H_{int} should depend on volume which is not incorporated in the above description and cannot explain the OP easy axis of NWs with AR ~ 50 . For this sample H_{int} is much smaller than $3\pi M_s$ perhaps due to its smaller volume. As a result, H_{eff} along OP direction gives rise to OP easy axis for NWs with AR ~ 50 or less. So the change in the anisotropic direction from OP to IP on increasing aspect ratio is mainly due to the increase of H_{int} for a particular porosity of the membrane. It is thus obvious to incorporate a volume dependency of the interaction term in addition to its porosity dependence.³²

Besides the study of the nature of easy axis of NWs we make a measure of coercive fields for different wire diameter also. In Fig. 6.24 the coercive fields have been plotted with respect to the AR of the NWs. The coercive field value is determined by the reversal process of the system followed by the remanence state of the NWs. At remanence the individual NW has vortex state. They then interact with each other in their own way which is weak and different from dipolar interaction.

However the strength of the interaction at remanence is determined by the saturation state and nucleation process. Regardless the switching of the direction of easy axis with the length of the NWs and typical behavior of squariness, the OP coercivity is almost always higher than the IP direction for all the samples. It is because of the large shape anisotropy along their length (along OP direction) compared to the transverse or IP direction. As they possess vortex state the curling mode of reversal is expected here. Furthermore the magnetostatic interaction, whose

nature is complex in reality, also influences the coercive field values. In 50 and 150nm wire diameter the coercivity first increases with the increase of length. At higher lengths they try to saturate for 50nm may be due to the nature of the movement of vortex wall remain same at higher lengths. The coercivity at higher lengths decreases for 150nm wire diameter. The coercivity decreases with length of the NWs for the 275nm wire diameter, which tries to saturate at higher lengths. The understanding about the reversal process that determines the coercive field value in our NWs need more elaborate investigations both theoretically and experimentally.

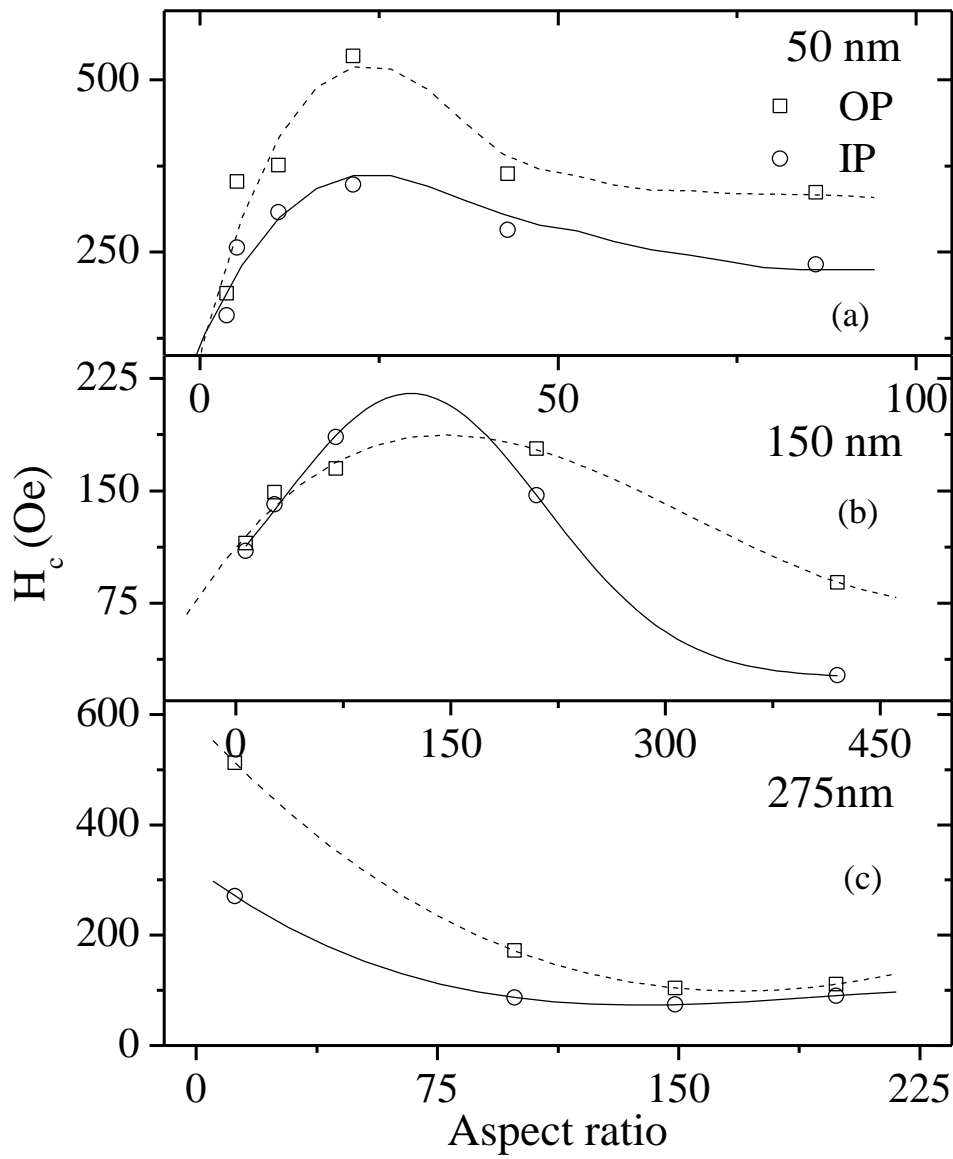


Figure 6.24. Variation of coercive fields in IP (open star) and OP (open box) directions with respect to the AR for the NWs (a) 50 nm (b) 150 nm and (c) 275 nm.

6.4 Conclusions

We have prepared two dimensional arrays of Co NWs having diameters 50, 150 and 275 nm in the pores of polycarbonate and alumina membrane by DC electrodeposition technique. Structural characterizations of NWs show that they are uniform in length and have hcp crystalline phase with c-axis perpendicular to the NW axis. The crystalline texture of the NWs changed from polycrystal to single crystal on decreasing the wire diameter. 150 nm NWs is not merely polycrystal as it shows hcp textured phase. This change in crystalline texture is due to the enhancement of stress as the diameter of the pores is reduced.

Length dependent magnetic properties for these three wire diameters at room temperature have been investigated in detail. The diameters of the NWs are large compared to the critical diameter of the upper bound of flower state of a magnetic cylinder. The observed remanence and coercivities of the hysteresis loops for the samples implies further the presence of vortex state of the NWs at remanence. The observed change in easy direction of magnetization on increasing the length of the NWs for 50 and 150nm wire diameters can be explained by considering magnetostatic interaction among NWs.

A simple model of dipolar interaction can explain the easy axis along the OP direction at small ARs and along IP direction at higher ARs of the NWs. Dipolar interaction between the NWs gives us a qualitative idea about the observed phenomena. The dipolar approximation should not hold good for 150nm NWs as they have the interwire distance of same order of the NW diameter. Though not accurately but hold better in case of 50 nm NWs as the inter-wire distance is about five times the wire diameter. The observed hysteresis loops of the 275 nm NWs are explained by assuming the thin film effect. It is because the continuous distribution of the particles in 2D array increases as the NW diameter increases keeping the wall thickness between two pores same. The 150nm wire diameter shows abnormal variation in the squariness with the aspect ratio.

We study the dynamic response of 150 nm NWs for two different ARs and show the results are consistent with the static magnetization studies. We found the resonance field changes as the bias field changes its direction from axial to transverse direction of the NWs. The NWs are isotropic along the direction perpendicular to the NW axis. We have fitted the experimental data by uniform mode of resonance and have got the effective anisotropy field value and g factor of the material. The directional change in effective anisotropy has been observed upon increasing the aspect ratio.

The observed facts prove the FMR results cannot be explained by a mere packing fraction dependent interaction field and should have a volume dependent term. Furthermore it is not dipolar in nature as the existing theoretical models based on the approximation does not tell us the nature of interaction below the saturation fields in vortex NWs. It needs a complete theoretical formulation to understand clearly the magnetostatic interaction among the NWs with vortex state.

Bibliography

- [1] Sun, Z.Z., Schliemann, J., Phys. Rev. Lett. **104**, 037206 (2010).
- [2] Yan, M., Kakay, A., Gliga, S., Hertel, R., Phys. Rev. Lett. **104**, 057201 (2010).
- [3] Boone, C.T., Katine, J.A., Carey, M., Childress, J.R., Cheng, X., Krivorotov, I.N., Phys.Rev. Lett. **104**, 097203 (2010).
- [4] Tretiakov, O.A., Liu, Y., Abanov, A., Phys. Rev. Lett. **105**, 217203 (2010).
- [5] Zheng, M., Menon, L., Zeng, H., Liu, Y., Bandyopadhyay, S., Kirby, R.D., Sellmyer, D.J., Phys. Rev. B **62**, 12282 (2000).
- [6] Wu, Y., Li, K., Qiu, J., Guo, Z., and Han, G., Appl. Phys. Lett. **80**, 4413 (2002); Albrecht, M., Moser, A., Rettner, C. T., Anders, S., Thomson, T., and Terris, B. D., Appl. Phys. Lett. **80**,3409 (2002); Jung, H. S., Kuo, M., Malhotra, S. S., and Bertero, G., Appl. Phys. Lett. **91**, 212502 (2007); Shamaila, S., Liu, D. P., Sharif, R., Chen, J. Y., Liu, H. R. and Han, X. F., Appl. Phys. Lett. **94**, 203101-1 (2009).
- [7] Piraux, L., George, J.M., Despres, J.F., Leroy, C., Ferain, E., Legras, R., Ounadjela, K., Fert, A., Appl. Phys. Lett. **65**, 2484 (1994).
- [8] Dubois, S., Beuken, J.M., Piraux, L., Duvail, J.L., Fert, A., George, J.M., Maurice, J.L., J. Magn. Magn. Mater. **165**, 30-33 (1997).
- [9] Shakya, P., Cox, B., Davis, D., J. Magn. Magn. Mater. (In Press).
- [10] Ross, C. A., Annu. Rev. Mater. Res. **31**, 203(2001)
- [11] Fert, A. and Piraux, L., J. Magn. Magn. Mater. **200**, 338-358 (1999); Vázquez, M., Vélez, M. H., Pirota, K., Asenjo, A., Navas, D., Vélezquez, J., Vargas, P. and Ramos, C., Eur. Phys. J. B **40**, 489 (2004).
- [12] Schwarzacher, W., Attenborough, K., Michel, A., Nabiyouni, G. and Meier, J.P., J. Magn. Magn. Mater. **165**, 23-29(1997).

- [13] Aharoni, A., Introduction to the theory of ferromagnetism, Oxford Science Publications, second edition (2000).
- [14] Ferre, R., Ounadjela, K., George, J. M., Piraux, L. and Dubois, S., Phys. Rev. B **56** (21), 14066 (1997).
- [15] Grimsditch, M., Jaccard, Y. and Schuller, I. K., Phys. Rev. B **58** (17), 11539 (1998).
- [16] Whatman Inc. Ltd., UK.
- [17] Ye, Z., Liu, H., Luo, Z., Lee, H-G., Wu, W., Naugle, D. G. and Lyuksyutov, I., J. Appl. Phys **105**, 07E126 (2009).
- [18] Brown, W. F., Introduction to the Theory of Ferromagnetism , Oxford University Press, 2nd Edition (2000).
- [19] Frei, E. H., Shtrikman, S. and Treves, D., Phys. Rev. **106**, 446 (1957).
- [20] Bryant, P. and Suhl, H., Appl. Phys. Lett. **54** (1), 78 (1988).
- [21] Aharoni, A., J. Appl. Phys **68**(6), 2892 (1990).
- [22] Ross, C. A., Farhoud, M., Hwang, M., Smith, I. H., Redjda, M. and Humphrey, F. B., J. Appl. Phys. **89**, 1310 (2001).
- [23] Ross, C. A., Haratani, S., Castan, F. J., Hao, Y., Hwang, M., Shima, M., Cheng, J. Y., Vogeli, B., Farhoud, M., Walsh, M. and Smith, H. I., J. App. Phys. **91** (10), 6848 (2002).
- [24] Bogdanov, A. N., Rößler, U. K., Müller, K. -H., J. Magn. Magn. Mater. **242-245**, 594-596 (2002)
- [25] Aharoni, A., J. Appl. Phys. **82**, 1281-7(1997).
- [26] Squire, P. T., Atkinson, D., Gibbs, M. R. J., Atalay, S., J. Magn. Magn. Mater., **132**, 10 (1994).
- [27] Martin, J.I., Nogues, J., Liu, K., Vicent, J.L., Schuller, I. K., J. Magn. Magn. Mater. **256**, 449-501(2003).

- [28] Kim, S. K., Kortright, J.B., Phys. Rev. Lett. **86**, 1347 (2001).
- [29] Cullity B.D. and Graham, C. D., Introduction to Magnetic Materials, John Wiley & Sons Inc. (2009).
- [30] Ross, C. A., Hwang, M., Shima, M., Cheng, J. Y., Farhoud, M., Savas, T. A., Smith, H. I., Schwarzacher, W., Ross, F. M., Redjda, M. and Humphrey, F. B., Phys. Rev. B **65**, 144417 (2002).
- [31] Rivas, J., Bantu, A. K. M., Zaragoza, G., Blanco, M.C., Lopez-Quintela, M. A., J. Magn. Magn. Mater. **249**, 220-227 (2002).
- [32] Encinas-Oropesa, A., Demand, M., Piraux, L., Huynen, I., Ebels, U., Phys. Rev. B **63**, 104415 (2001).
- [33] Raposo, V., Garcia, J.M., Gonzalez, J.M., Vazquez, M., J. Magn. Magn. Mater. **222**, 227-232 (2000); Ramos, C.A., Brigneti, E. V., Vazquez, M., Physica B **354**, 195–197 (2004).
- [34] Clime, L., Ciureanu, P. and Yelon, A., J. Magn. Magn. Mater. **297**, 60-70 (2006).
- [35] Das, B., Mandal, K., Sen, P. and Bandopadhyay, S. K., J. App. Phys. **103**, 013908 (2008).
- [36] Dubowik, J., Phys. Rev. B **54**, 1088 (1996).
- [37] Vittoria, C., *Microwave Properties of Magnetic Films*, World Scientific, Singapore, 1993.
- [38] Netzelmann, U., J. Appl. Phys. **68** (4), 1800 (1990).

Chapter 7

In search of high coercive CoPt alloy nanowires: Influence of alumina membrane

7.1 Preamble

In search of high coercive ferromagnetic material, Cobalt-Platinum alloys are found to be the most promising materials for their large magnetocrystalline anisotropy for some particular compositions of Cobalt (Co) and Platinum (Pt) in the alloy.^{1, 2} At some particular composition, the CoPt and other similar kind of alloys such as FePt (Iron-platinum) possess large anisotropic face centered tetragonal (fct) L1₀ phase that helps them to overcome superparamagnetism even at grain sizes less than 6 nm.^{3, 4} As a consequence, the materials with high coercivity can be used deliberately as magnetic storage elements in high density magnetic recording systems. There are few techniques such as chemical methods, seed layers and heated substrates, also available to obtain films with perpendicular anisotropy or patterned structures which are favorable for even higher areal density.^{5, 6} However, the electrodeposition may be the most cost effective and easier to synthesis CoPt NWs in porous membranes. Thermal annealing of CP (CoPt) NWs with equiatomic compositions can lead to high coercive NWs.⁷ Perhaps, the annealing effects on the NWs to enhance their coercivity are not well studied.

In this chapter, we investigate the effect of thermal annealing on CoPt NWs. We found not only thermal annealing changes the crystalline phase of the NWs but the medium (AAO membrane) also plays an important role in changing the phase. We

study here the magnetic hysteresis behavior of CoPt NWs for different composition of cobalt and platinum. In search of high coercive nanostructure their crystal structure is changed by thermal annealing. The NWs are several microns long with the diameter of ~ 200 nm. The as prepared samples shows fcc crystalline phase and are magnetically soft.

However the NWs show magnetically anisotropic behavior with an easy axis along the perpendicular direction of the axes of the nanowires perhaps due to the strong magnetostatic coupling among the nanowires. We observe the NWs with equiatomic composition changes to $L1_0$ phase after the thermal annealing. The NWs show very high coercivity ~ 6.2 kOe and interestingly become almost isotropic magnetically. In order to study the influence of stress developed during the annealing of the NWs, we compared the results with CoPt nanoparticles (NPs) synthesized in micellar media.⁸ The average particle sizes of the NPs were ~ 6 nm. In case of equiatomic composition, after similar kind of heat treatment, the size of the NPs increased and the crystalline phase changed. NPs with equiatomic composition show enhanced coercivity of ~ 4.4 kOe in the magnetic hysteresis loops. The experimental observations indicate the development of large stress induced anisotropy within the NWs which competes with the magnetocrystalline anisotropy of $L1_0$ phase.

7.2 Experimental

Synthesis of nanoparticles (NPs)

In order to synthesize the NPs⁸ we use the reagents of analytical grade and purchased from Sigma-Aldrich. The water used was of Millipore grade. CoPt alloy NPs with various compositions of Cobalt and Platinum were prepared by micellar technique. Cobalt sulfate and hexachloro platinate salts are used as sources of Co and Pt respectively. These salts were taken in different ratios and were dissolved in TX-100 micellar medium under Argon atmosphere. The mixture was stirred for 30 min then it was heated at 80° C. Sodium borohydride and oleic acid were added to it under

stirring and heating condition. The solution turned into black after the addition of sodium borohydride. The particles were separated from the mixture by the method of centrifugation and purified by washing the particles several times by ethanol to remove TX-100 micelles. We prepared CoPt alloy nanoparticles with different ratios of Co and Pt such as sample A_{NP} (Co:Pt ~ 90:10 in at%), B_{NP} (Co:Pt ~ 75:25 in at%), C_{NP} (Co:Pt ~ 50:50 in at%), D_{NP} (Co:Pt ~ 25:75 in at%) and E_{NP} (Co:Pt ~ 10:90 in at%). The particles were dispersed in hexane and dropped on silicon wafer to make the thicker film of all five samples. These films were subjected for heat treatment at 850 °C for 1 hour under N₂ and H₂ atmosphere and different measurements were done on the samples before and after the heat treatment to investigate the properties of the particles.

Synthesis of nanowires (NWs)

The NWs are electrodeposited in anodic alumina membranes with average pore diameter 200 nm commercially available from Whatman.⁹ The thickness of the membranes is about 60 μm. In order to deposit the conducting Co and Pt inside the pores of non-conducting alumina membrane, one side of the membrane was coated with gold (99.99% pure) having thickness ~100 nm using the thermal evaporation technique. All the electrodeposition was carried out in a conventional three electrode electrochemical cell (Autolab) where we used the gold coated membrane as working electrode. A Pt wire (99.99% pure) and a Ag/AgCl calomel electrode were used as counter and reference electrodes respectively. The backside (gold coated side) deposition of Co and Pt ions were prevented using cello-tape. The deposition was done under a constant potential difference ~ 0.9V, between the working and reference electrodes followed by linear sweep voltametry. The electrolyte solution is consisting of CoSO₄, H₂PtCl₆ and H₃BO₃. All the reagents used were of analytical grade and purchased from Sigma-Aldrich. The molar concentration of CoSO₄ were changed in order to prepare CoPt alloy with three different compositions: sample B_{NW} (Co:Pt 75:25), C_{NW} (Co:Pt ~ 50:50) and D_{NW} (Co:Pt ~ 28:72). The nanowires were then released from the membrane, to perform their structural characterization, by dissolving the membranes in 2M of NaOH solution.

7.3 Results & discussions

7.3.1 Structural characterizations

The crystal phases of the samples are confirmed from the X-ray and electron diffraction spectra using a X-ray diffractometer (X'Pert Pro, Panalytical) and transmission electron microscope (TEM, JEOL-2010) respectively. The geometrical structure, surface morphology and size of the particles are characterized by scanning electron microscope (SEM, JEOL, JSM – 6700 F) and TEM. In order to do SEM study of the NWs, the membranes are dissolved in 2M NaOH solution.

It is known that the solution of water containing micelles is employed as suitable reaction media for the synthesis of nanosized particles.¹⁰ This is achieved by creating micellar core of nano-size and carrying out the reaction inside the core. As a consequence of micellar dynamic motion, the reactant can come in contact and react to each other to form the nuclei of nanoparticles. By the same dynamic process these precursor nuclei are accumulated in some closed micellar core leading to the formation of stable nanoparticles of limited growth.

In our experiment TX-100 micellar medium was used to control the growth of particles in nano-size regime. After preparing the nanoparticles, they are subjected for heat treatment in N₂ and H₂ atmosphere. N₂ and H₂ atmosphere were used to prevent the oxidation. The composition was measured by electron dispersive X-ray (EDX) analysis of each sample. EDX measurement shows that the ratios of Co and Pt in all five samples are nearly same with the ratio of Co and Pt taken as precursor salts. This indicates the complete reduction of the Co and Pt ions present in the salts. Thus in our method it is easy to maintain the ratio of Co and Pt in CoPt alloy.

The crystallinity of the alloy particles has investigated by X-ray diffractometer using Cu-K_α radiation. Before annealing all the samples are in disordered fcc or face centered cubic phase. As Co and Pt in 50:50 composition forms the L1₀ phase on heat treatment above or at ~ 825⁰ C,^{11, 12} all the samples are annealed at 850⁰ C. XRD

pattern for five different sets of particles after annealing at 850⁰ C for 1 hour in the N₂ and H₂ atmosphere are shown in Fig. 7.1.

All the curves show the peaks for (111) and (200) planes of CoPt alloy, in case of sample 'C' some more new peaks are observed in addition to (111) and (222). No separate peak for Co or Pt alone is observed. This confirms the formation of CoPt alloy. In the XRD curve, shifting of the peak position to left region of X-axis, that is, towards lower '2θ' value is observed with the increase of Pt percentage.

From the Bragg's equation, we get $d = k/2\sin\theta$, now k is 1.5418 Å as Cu-Kα radiation source is used in our case and θ is obtained from the XRD peak position of (111) plane. From this equation it is clear that the 'd' increases with decrease of '2θ' position. Applying this equation we have calculated 'd' corresponding to (111) plane for all the five samples and plotted the atomic percentage of 'Pt' vs. 'd' in Fig. 7.2.

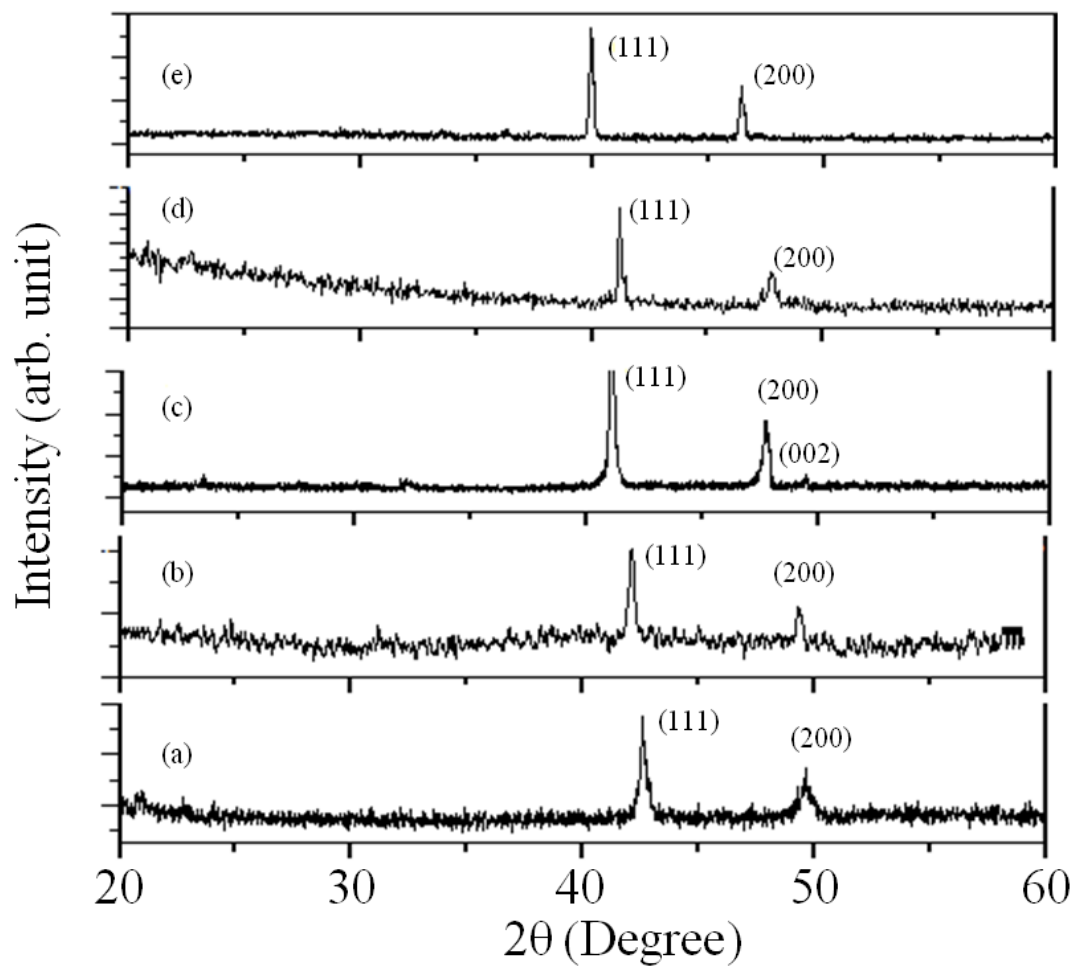


Figure 7.1. XRD spectra of all the samples of CoPt NPs: (a) A_{NP} , (b) B_{NP} , (c) C_{NP} , (d) D_{NP} , (e) E_{NP} .

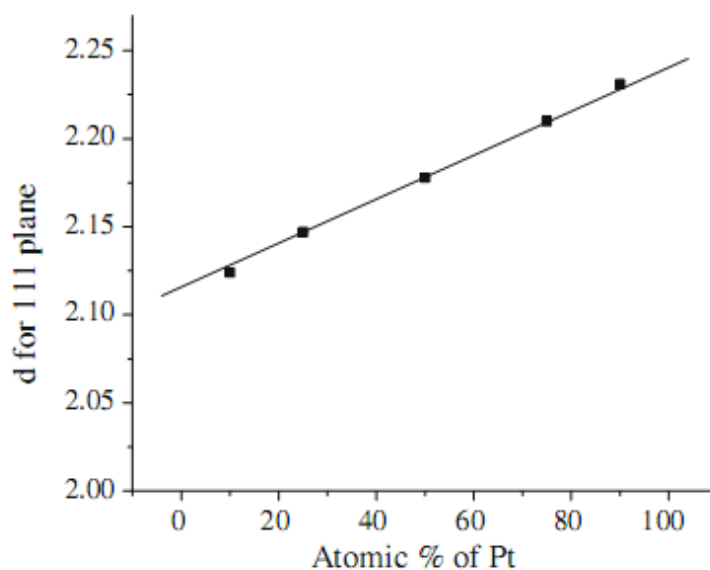


Figure 7.2. Plot of interplanar distance (d) corresponding to (111) plane vs. atomic percentage of Pt for all the five samples A_{NP} to E_{NP} .

The composition of Pt was obtained from EDX measurement for each sample. It is found here that the ‘ d ’ increases from 2.124 to 2.231 Å due to increase of Pt content from 10% to 90%. The error limit of ‘ d ’ is in third decimal place. This change is in good agreement with the Vegard’s law which tells that at a particular temperature, the lattice parameter of the alloys is linearly proportional to the concentrations of the constituent elements. It is well known that Pt atom is larger in size than the Co atom. Therefore the cell parameter as well as the inter-planar distance, ‘ d ’ increases when the smaller Co atom is replaced by the larger Pt atom.

The XRD curve for the sample C_{NP} (50:50) indicates the formation of fct $L1_0$ phase showing all the peaks from (001), (110), (111), (200), (002) planes. Samples of other compositions do not show evolution of such phase. From the equilibrium phase diagram it is known that at room temperature the stability region for $L1_0$ phase of CoPt ranges from about 37% to 53 at% of Pt.^{13, 14} Hence, our result for sample ‘C’ is compatible with this phase diagram.

The TEM micrograph for sample ‘ C_{NP} ’ is shown in Fig. 7.3 (a) and (b) before and after annealing the sample, respectively. Before annealing the particle size is ~ 6

nm and are of almost uniform in size and after heat treatment particle size becomes ~ 7 nm. After heat treatment, particle size increases slightly but do not fuse all together to grow a much larger size. It may be because we have used sodium boro-hydride as reducing agent. Sodium boro-hydride under hydrolysis produces sodium hydroxide which forms sodium oleate with oleic acid. The sodium oleate tries to prevent the coalescence. On the other hand, $L1_0$ phase is an ordered state and thus the unit cell volume is lower than the disordered fcc phase. However, by the process of Ostwald reipening, the particle sizes can increase while annealing.

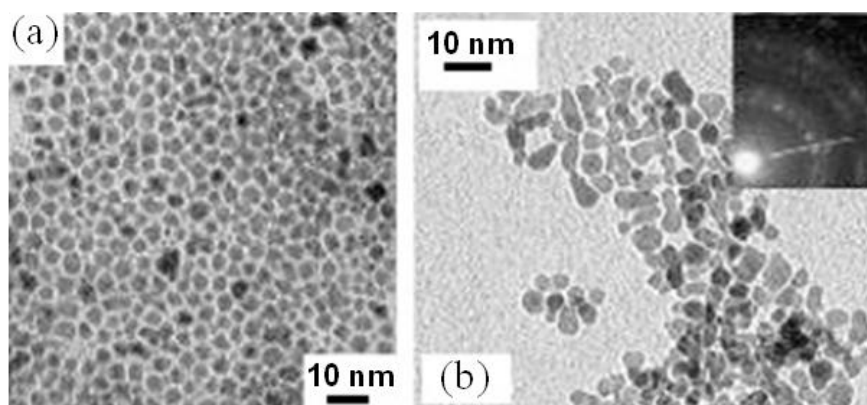


Figure 7.3. TEM micrograph of sample C_{NP} before (a) and after (b) heat treatment. The electron diffraction pattern taken from the sample C_{NP} after heat treatment is given in inset of (b).

We have tested that mixture of sodium hydroxide and oleic acid does not evaporate even at $600^{\circ}C$. But at $850^{\circ}C$ a black colored precipitate is formed which is nothing but carbon particles. These carbon particles may form metal carbide or may remain as carbon coating on the boundary of the CoPt particles after annealing and thus preventing the coalescence of particles even at such high temperature. As this kind of material is amorphous in nature so it does not show any signature in XRD pattern. The electron diffraction pattern taken from sample ' C_{NP} ' after heat treatment is shown in the inset of Fig. 7.3 (b). The analysis of this pattern again indicates the formation of $L1_0$ phase. fcc phase in little amount may be present there. But in this

case it is very difficult to discriminate one from other as rings pattern for (111) and (200) from the $L1_0$ phase overlap on the same from fcc phase.

NWs are first released from alumina membranes in order to characterize them by FESEM and HRTEM. We dissolve the membranes in 2M NaOH solution. The NWs are expected to be free and standing on gold thin films. Fig. 7.4 shows the FESEM micrographs and EDX result of such a sample of B_{NW} .

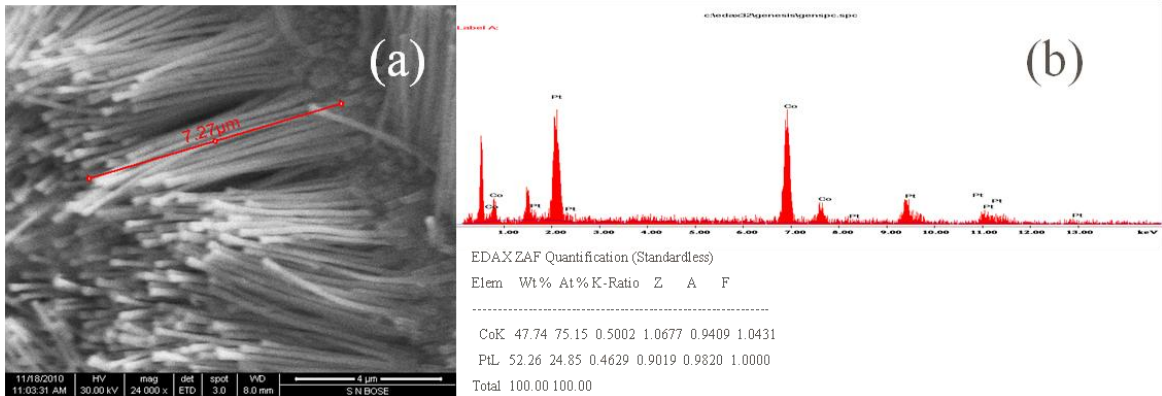


Figure 7.4. FESEM micrograph of sample B_{NW} (a) and EDX spectra with elemental quantification of the sample shows the Co:Pt = 75:25 in at% (b).

We perform the electron microscope studies for the other two samples also and the results are shown in Fig. 7.5 (sample C_{NW}) and Fig. 7.6 (sample D_{NW}). From FESEM micrographs we observe the length of the NWs are uniform throughout the membranes. The NWs have an average diameter of ~ 200 nm (approx). The length of the $B_{NW} \sim 7$ μm , $C_{NW} \sim 15$ μm and of $D_{NW} \sim 9$ μm . Fig. 7.5 (c) shows the EDX results of sample C_{NW} and indicates the Co: Pt = 50 : 50 in at%.

Whereas, Fig. 7.6 (b) shows the EDX results and indicates Co : Pt = 25 : 75 in at%. In order to determine the crystal structures of the samples we did SAED while performing HRTEM of the NWs. In Fig. 7.7 the HRTEM micrograph of sample C_{NW} NWs [7.7 (a)] and SAED [7.7 (b), (c)] results are shown. Fig.7.7 (b) is the SAED spots of the as prepared samples. We got similar spots for other two samples (B_{NW}, D_{NW}). It shows the crystalline phases of the samples are fcc where we can see the circular rings corresponds to (111), (200) and (211) planes.

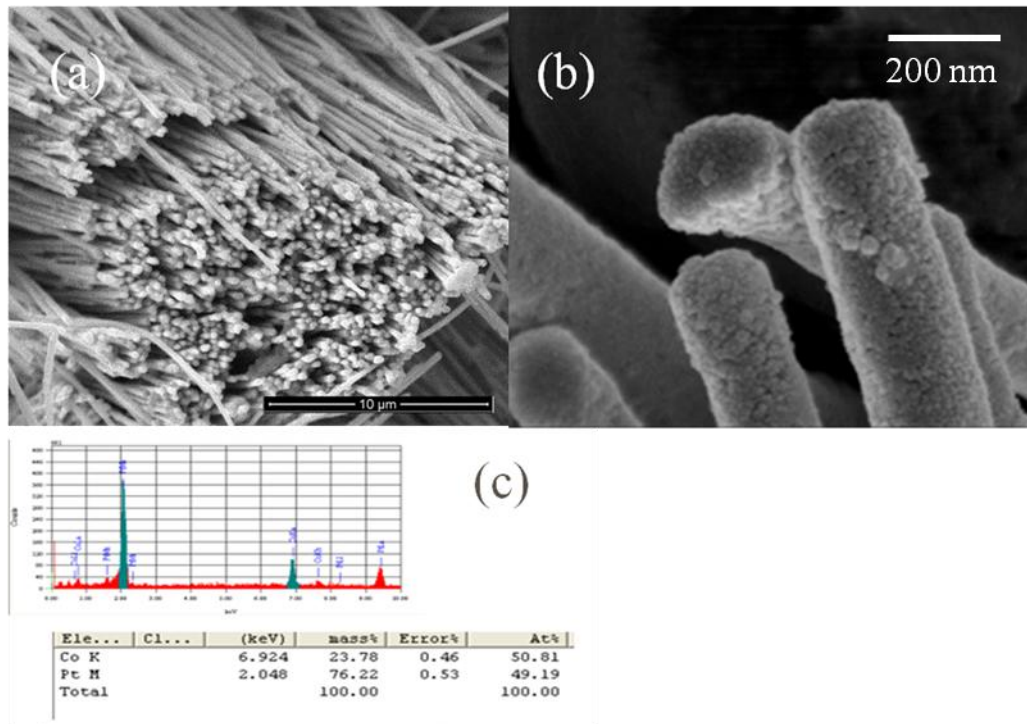


Figure 7.5. FESEM micrograph of sample C_{NW} (a), a close view of the NWs by FESEM (b) and the EDX spectra with elemental quantification of the sample shows the Co:Pt = 50:50 in at% (c).

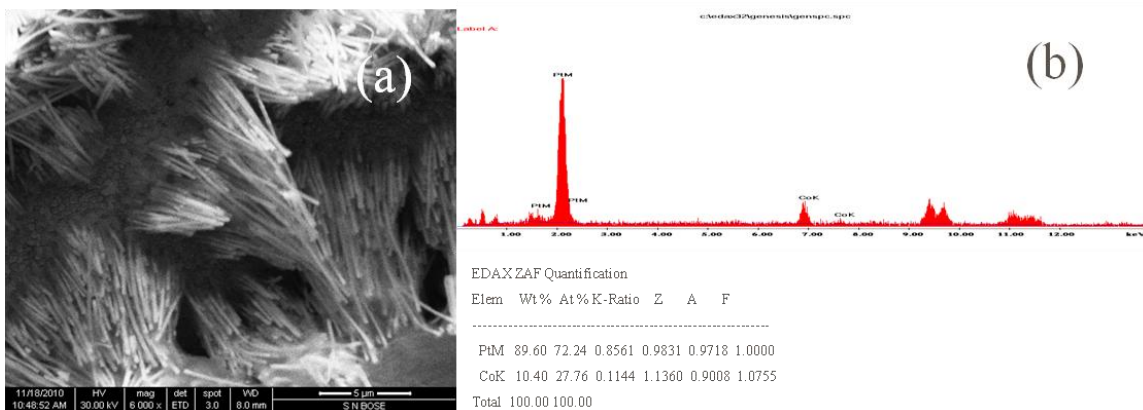


Figure 7.6. FESEM micrograph of sample D_{NW} (a), the EDX spectra with elemental quantification of the sample shows the Co:Pt = 25:75 in at% (b).

We heated up the samples at 650°C for 1 hour in presence of N_2 and H_2 gases. The SAED patterns took after the heat treatment of sample C_{NW} is shown in Fig. 7.7 (c). It clearly shows the circular rings correspond to fct phase $L1_0$ of CoPt. The rings corresponds to (110), (001) and (002) of the fct phase are shown in Fig. 7.7 (c). Contrary, the samples B_{NW} and D_{NW} did not show fct phase.

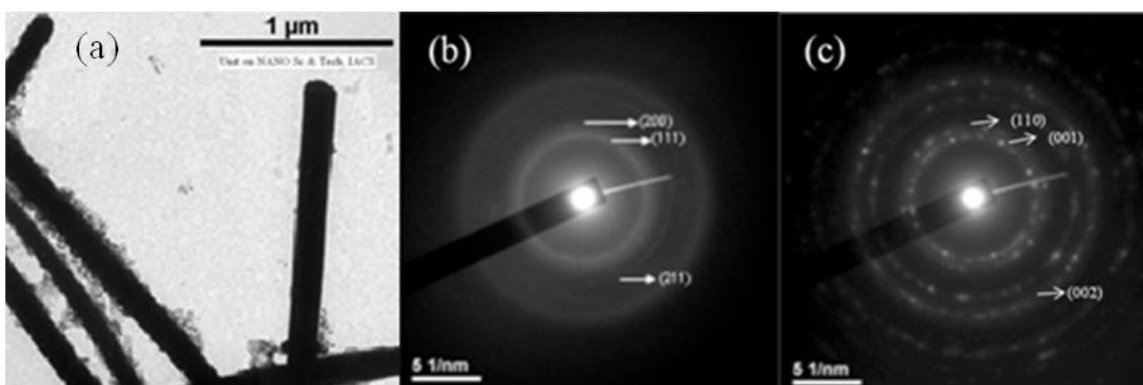


Figure 7.7. HRTEM micrograph of sample C_{NW} (a) and SAED spots of the same CoPt NWs before (b) and after (c) heat annealing.

7.3.2 Magnetic Characterizations

7.3.2.2 Magnetic properties of CoPt NPs

Magnetic hysteresis loops for all the samples ($A_{NP} - E_{NP}$) are measured at room temperature (300 K) with applied magnetic field from -15 to +15 kOe, perpendicular and parallel to the film surface. As the results obtained in both the perpendicular and parallel cases are the same, perpendicular hysteresis loops for all the samples are considered.

In Fig. 7.8 we observe that the coercivity decreases from 1200 (sample A_{NP}) to 800 Oe (sample B_{NP}) due to the change in Co content from 90% to 75%. We have observed that, on decreasing the Co content, lattice constant for the alloy increases. Due to increase in lattice constant, the exchange interaction between the cobalt atoms decreases reducing coercivity of sample B_{NP} . But in case of sample C_{NP} (Co and Pt equiatomic), the coercivity was found to be ~ 4400 Oe due to the change of crystalline phase from fcc to $L1_0$. The $L1_0$ structure is tetragonally elongated along C-axis, which produces very high magnetocrystalline anisotropy and hence such high value of coercivity.

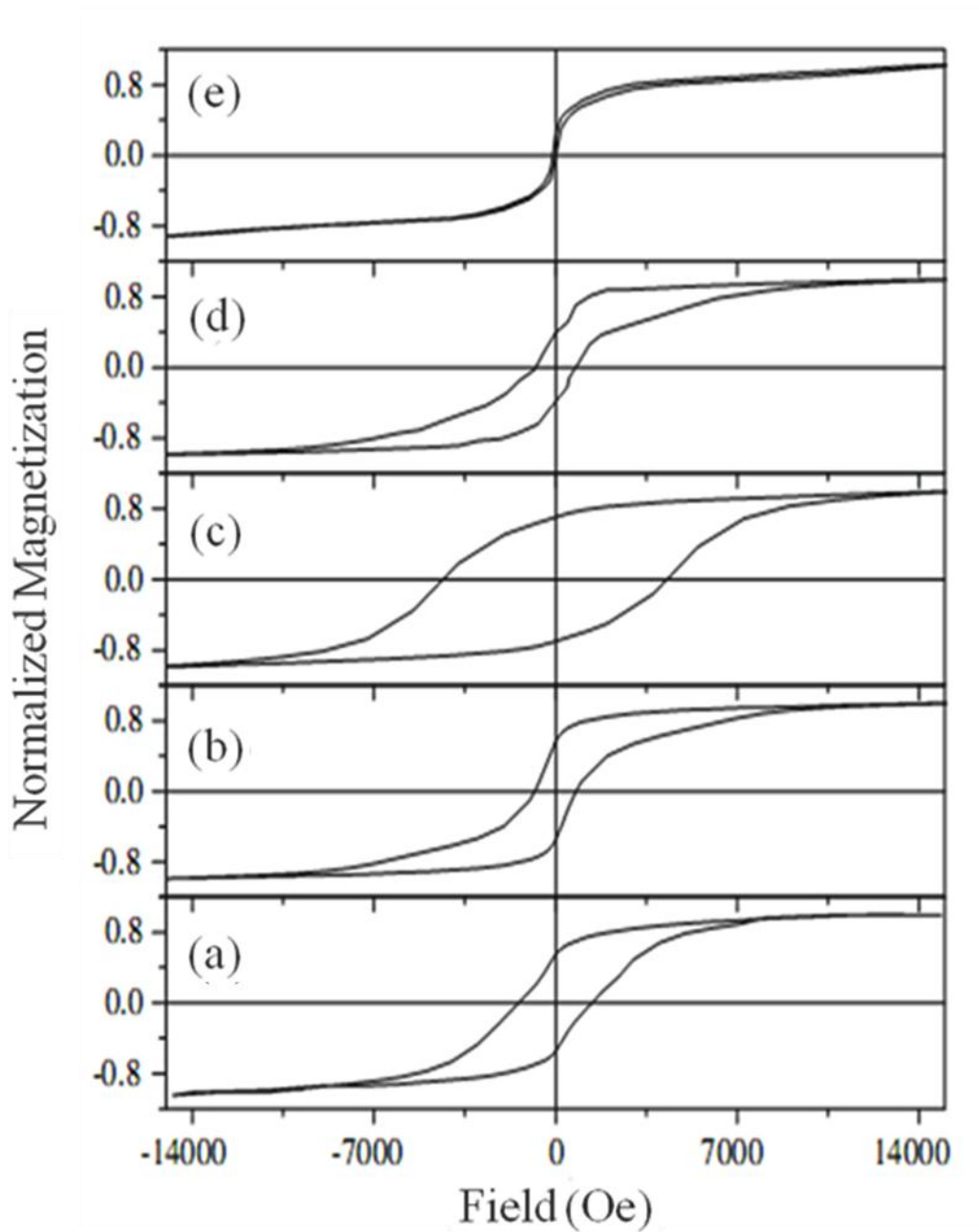


Figure 7.8. Magnetic hysteresis loops measured at room temperature of (a) A_{NP} , (b) B_{NP} (c) C_{NP} (d) D_{NP} and (e) E_{NP} .

Moreover as the particles are single domain in nature, magnetization takes place by rotations resulting further increase in coercivity. In samples D_{NP} and E_{NP} , coercivities are 550 and 100 Oe, respectively, much less than that of sample C_{NP} because of the disordered fcc structures. The ratios, M_r/M_s , where M_r is the residual

magnetization at zero applied field and M_s is the saturation magnetization at the maximum applied field, measured for all of the samples. In this case, M_s is not the ideal saturation magnetization as the available magnetic field cannot saturate the samples completely.

The coercivities and the M_r/M_s measured for all the samples are given in Table 7.1. The larger value of both the coercivity and the M_r/M_s ratio for sample C_{NP} indicates formation of hard phase. Hysteresis loops of the NP_s measured at 80, 100, 150, 200, 250, 300 and 350 K and some of them are shown in Fig. 7.9 for clarity. Coercivity decreases with the increase of temperature as usually observed in case of most of the ferromagnetic materials due to decrease in ordering of the atomic moments. But the magnetization 'M' tries to saturate at higher magnetic field in nearly similar way at 100 and 300 K.

The nanoparticles are of single domain in nature. Hence there is no chance of domain wall shift in these particles. The available field cannot truly saturate the sample. As this M_s is far below from the true saturation magnetization of the sample, so the similar magnetization change at higher magnetic field values is observed. Existence of double jump is also observed in the hysteresis loops. It is due to presence of two phases fcc and fct in the sample. When two hysteresis loops, one for fcc phase and other for fct phase are coupled to one hysteresis loop this kind of behavior is observed. Other samples (A_{NP} , B_{NP} , D_{NP} , E_{NP}) are totally in fcc phase and do not show such jump in their hysteresis loops. The coercive field values and M_r/M_s values of different NPs are listed in Table 7.1 below.

Samples	Coercivity (Oe)	(M_r / M_s)
A_{NP} (CoPt = 90:10)	1200	0.615
B_{NP} (CoPt = 75:25)	800	0.604
C_{NP} (CoPt = 50:50)	4400	0.749
D_{NP} (CoPt = 25:75)	550	0.59
E_{NP} (CoPt = 10:90)	100	0.31

Table 7.1. Coercivities and squariness of nanoparticles with different atomic ratios.

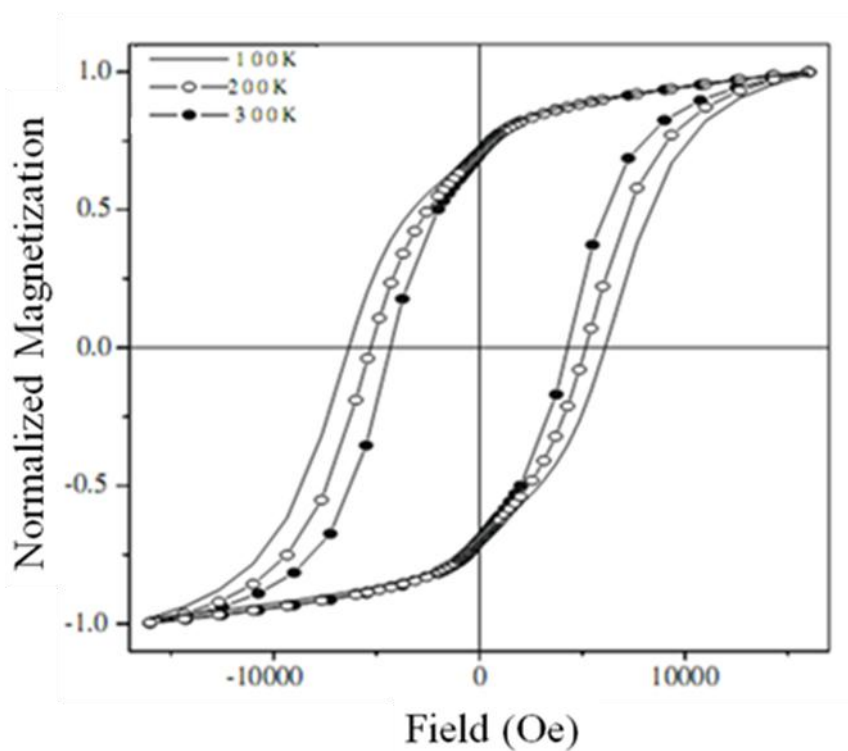


Figure 7.9. Magnetic hysteresis loops measured at three different temperatures for sample ' C_{NP} '.

7.3.2.3. Magnetic properties of CoPt NWs

Magnetic measurements of NWs are carried out keeping the membranes intact. The hysteresis loops were measured for two different orientations of the external applied magnetic field H_a : parallel to the length (L) of the NWs, described as the “Out of plane” (OP) and perpendicular to it, denoted as “In plane” (IP) configuration.

The hysteresis loops are plotted in Fig. 7.10. It shows the magnetization along OP direction increases with H_a much faster than that along the IP direction, i.e. OP hysteresis loop is sharper (greater initial susceptibility) than the IP (lower initial susceptibility) one. This indicates that the OP is the easy direction of magnetization.

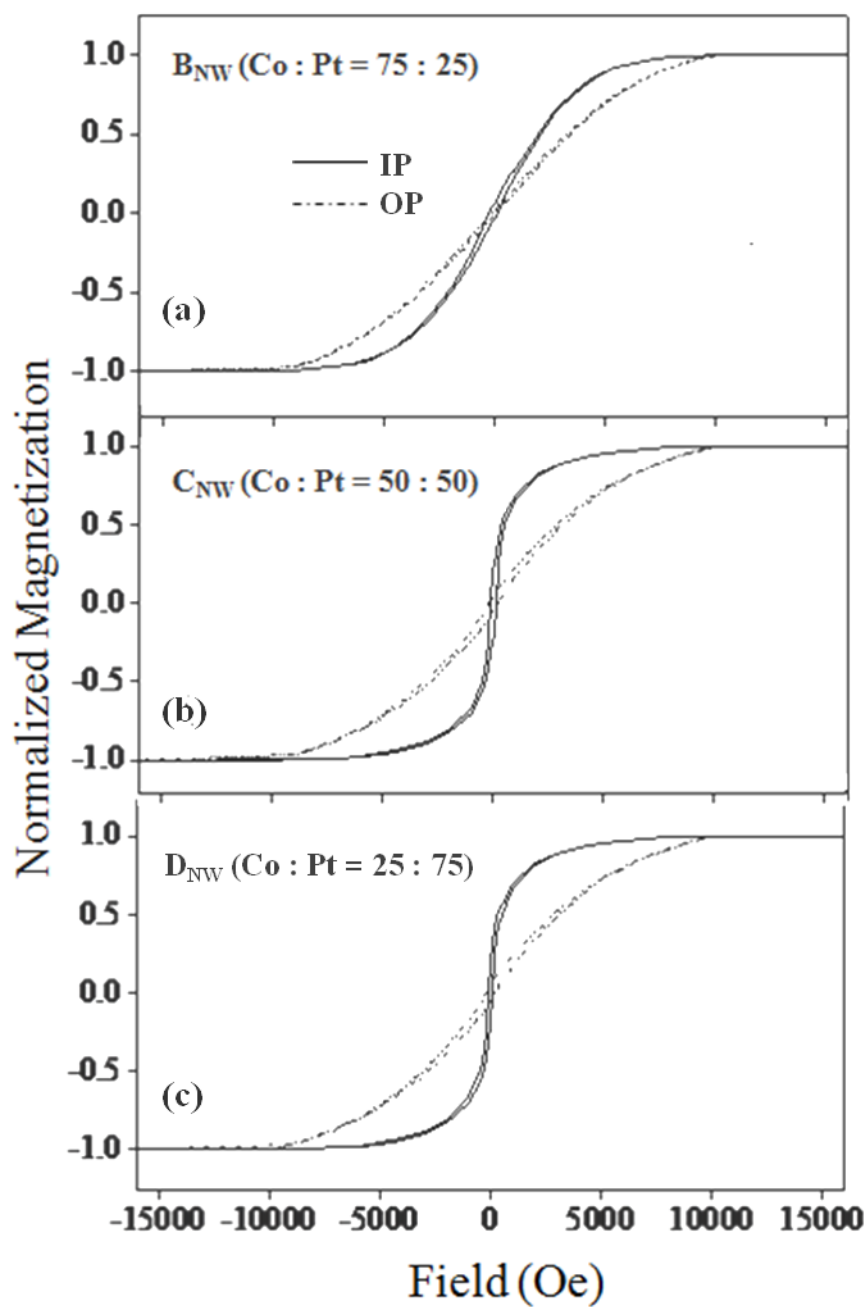


Figure 7.10. Magnetic hysteresis loops in IP and OP configurations for sample (a) B_{NW} , (b) C_{NW} and (c) D_{NW} . The magnetization value is normalized here.

Understanding of the magnetic behavior of individual NW is necessary before explaining the same for the arrays of NWs as discussed in earlier chapters. As to

remind, one may consider each nanowire as a magnetic cylinder made of cobalt. The total magnetic energy (E_{tot}) of such a cylindrical shaped nanowire can be written as¹⁵

$$E_{tot} = E_z + E_{ex} + E_d + E_k + E_s \quad [7.1]$$

Here E_z is the Zeeman energy due to the external field, E_{ex} , the ferromagnetic exchange interaction, E_d , the magnetostatic energy due to the demagnetization field, E_k , the magnetocrystalline anisotropy and E_s , the inhomogeneous surface anisotropy arises from the induced orbital moment¹⁶ due to uneven coordination number of the spins near the surface. Hence taking into account all these energy contributions one can calculate the remanent magnetization state of the cylinder.

At sub-micrometer length scale, various micromagnetic calculations based on Landau-Lifschitz-Gilbert equations suggest two remanent states of an isolated cylindrical shaped NW: *flower states* at lower diameters of NWs and *vortex states* at higher diameters of NWs and discussed elaborately in *Introduction* section of the thesis.¹⁵ A complex vortex state may also be possible on increasing the diameter further. In Micrometer length scale or above, one can get multi-domain structure as derived by Neel or Bloch¹⁵ inside a cylindrical shaped magnetic structure. We observed in our previous study on typical Co rich amorphous alloy microwires (diameter ~ 10-12 μ m) that the typical diameter of inner core domain size is atleast ~ 2-3 μ m (*see chapter 3*). Therefore, we believe that, the NWs (diameter up to ~ 200 nm) in our present study possess either flower or vortex structure. The remanent states are modified when they are in arrays.

Among the various anisotropy energies mentioned in Eq. 7.1, magnetocrystalline and shape anisotropies play the dominating role in governing the magnetic properties of a single NW. Before annealing, the NWs were in fcc phase and polycrystalline. The magnetocrystalline anisotropy is thus negligible with respect to the shape anisotropy $\sim 2\pi M_s$. The shape anisotropy tries to make the long axis of the NWs as easy direction of magnetization. But here it is observed that the perpendicular direction of the NWs as easy direction of magnetization. This is because, in case of NWs arranged in a 2D array, it is obvious to consider the magnetostatic interaction (H_{int}) among the NWs in the array. The anisotropy originated from the interaction

become most prominent anisotropy for a dense array system like the arrays used in the present study.

We believe it is the magnetostatic interaction among the NWs that makes the easy axis of NWs along the IP direction (perpendicular to the NW axis) where OP shape anisotropy is higher than IP magnetocrystalline anisotropy irrespective of the diameter of the NWs. After annealing the samples in inert atmosphere for 1 hr at 650⁰ C, we observe no change in crystalline phase in the samples B_{NW} and D_{NW} and almost no change in their hysteresis loops. In contrast, NWs of sample C_{NW} with equiatomic composition shows enhanced coercivity up to ~ 6.4 kOe at room temperature. Fig. 7.11 shows the magnetic hysteresis loops of the sample C_{NW} after heat treatment.

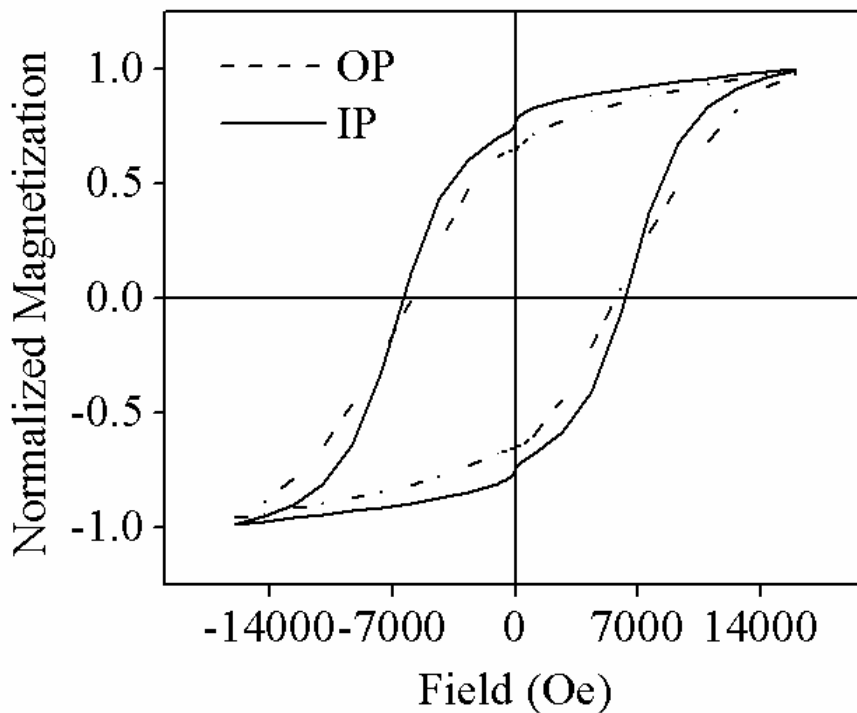


Figure 7.11. Magnetic hysteresis loop for sample C_{NW} (Co:Pt = 50:50) after heat treatment. Magnetization values are normalized here.

The enhanced coercivities of equiatomic nanostructures are expected mainly due to the creation of large magnetocrystalline fct phase $L1_0$ after the heat treatment of the NWs. The effect is similar as observed for NPs (nanoparticles). Interestingly, the coercivity enhancement is higher here compared to NPs. The NWs becomes nearly anisotropic in nature after the heat treatment. Most interesting observation is that, the phase change from fcc to $L1_0$ occurred for the NWs at much lower temperature at 650^0 C compared to the NPs occurred at 850^0 C. In case of NPs we have also seen an increment in particle size of ~ 1 nm after the heat treatment of the NPs. These observations intend us to believe that, the phase change is not only due to the intra-atomic diffusion of Co and Pt atoms controlled by thermal agitation. All of these indicate an incorporation of stress developed by the alumina matrix in the membrane that surrounds the NWs.

During the thermal annealing, the CoPt NW expands its volume and simultaneously the Co and Pt atoms go to a rearrange themselves. On cooling, the volume of NWs tries reduce to its original volume as it has before the heating. But at the same time, the crystal rearrangements change the crystallinity of it to elongated fct phase calls $L1_0$ phase as observed in NPs. This phase change is basically a transformation of disordered fcc phase to ordered $L1_0$ phase. Thus it is obvious that, the unit cell volume of the fct crystalline NWs after annealing is lower than the fcc crystalline NWs before annealing.

The surface defects of alumina nanochannels in the membranes may enhance due to thermal annealing. These can create more prominent nucleation points for the annealed NWs and hence the coercivity can enhance.

During heating, NWs will try to expand themselves along the length as well as in diameter. But as they are surrounded by alumina (have thermal expansion coefficient nearly half to that of CoPt alloy), they cannot do that. The NWs will give a force on the inner walls of the pores and in reaction the membranes also exert an opposite force on the NWs. During cooling, the stress will decay with time. But, as the thermal conductivity of CoPt metal is higher than alumina, the cooling of NWs will be slower compared to the case of NPs coated with carbon. During the structural transformation, the atoms changed their original location and move to another position

within the crystal maintaining a relative distance with respect to other. The displacement of the atoms may be few angstroms at best. Here, the transformation leads to a change in fct phase to $L1_0$ phase.

The innerward stress exerted by the alumina pores on the NWs is in perpendicular to the axis of the NWs. Hence, the isotropic nature of the NWs after the heat treatment is may be due to the negative magnetostriction which is directed towards the perpendicular direction of the NWs. The shape anisotropy and magnetostrictive anisotropies competes with each other and makes the system nearly isotropic.

7.4 Conclusions

We have successfully prepared CoPt alloy nanoparticles with different compositions in micellar media and nanowires in the pores of alumina membranes. Both the preparation techniques are easier compared to the conventional methods of preparing those nanostructures. Electron microscope characterization shows, the nanoparticles are uniform in size with an average diameter of ~ 6 nm. The nanowires have an average diameter of ~ 200 nm and the lengths are within the range of $\sim 7 - 15$ μm . For a particular sample, the NWs are found to be uniform in length throughout the membranes.

Diffraction patterns of the as prepared nanostructures show they have fcc polycrystalline phase. Magnetization measurements show the as prepared NPs are isotropic but the as prepared NWs are anisotropic with an easy axis of magnetization along their length. Heat treatment of the nanostructures with equiatomic compositions changed their phase to fct $L1_0$ phase. We see the NWs (annealed at 650 $^{\circ}\text{C}$) are more prone to change their crystal phase than the NPs (annealed at 850 $^{\circ}\text{C}$).

Formation of sodium oleate on the surface of NPs prevents the coalescence of particles restricting from much bigger particle formation during annealing. Moreover, the TEM study of heat annealed NPs indicate a slight increase in average size of the

NPs after the annealing. We believe, it is due to the Oswald ripening of the NPs that occurred during the thermal annealing. Observed experimental facts also indicate that, it is the stress given by alumina on the NWs that accelerate the crystalline phase change in case of NWs at relatively lower annealing temperature compared to NPs. This is also supported by the magnetization measurements of the NWs and NPs which show that, after the heat annealing, the NWs exhibit higher coercive field of 6.4 kOe than the NPs (4.4 kOe) for equiatomic composition of the alloy. This change is mainly due to the large magnetocrystalline anisotropy of fct $L1_0$ phase of the nanostructures. But, the higher coercive field value in NWs pointing towards an stress induced anisotropy in annealed NWs, where the stress on NWs is generated by the alumina matrix of the membrane.

Bibliography

- [1] Huang, Y. H., Okumura, H., Hadjipanayis, G. C. and Weller, D., *J. Appl. Phys.* **91**, 6869 (2002).
- [2] Yasui, N., Imada, A. and Den, T., *Appl. Phys. Lett.* **83**, 3347 (2003).
- [3] Weller, D., Moser, A., Folks, L., Best, M. E., Lee, W., Toney, M. F., Schwickert, M., Thiele, J. U. and Doerner, M. F., *IEEE Trans. Magn.* **36**, 10 (2000).
- [4] Shimatsu, T., Lodder, J. C., Sugita, Y. and Nakamura, Y., *IEEE Trans. Magn.* **35**, 2697 (1999).
- [5] Sun, S., Murray, C. B., Weller, D., Folks, L. and Moser, A., *Science* **287**, 1989 (2000).
- [6] Yamada, Y., Drent, W. P. V., Abarra, E. N. and Suzuki, T., *J. Appl. Phys.* **83**, 6527 (1998).
- [7] Mallet, J., Yu-Zhang, K., Chien, C-L., Eagleton, T. S. and Searson, P. T. *Appl. Phys. Lett.* **84**, 3900 (2004).
- [8] Mandal, M., Das, B. and Mandal, K., *J. Colloid & Interface Science* **335**, 40–43 (2009).
- [9] Whatman Pvt. Ltd. UK.
- [10] Mandal, M., Ghosh, S.K., Kundu, S., Esumi, K., Pal, T., *Langmuir* **18**, 7792 (2002).
- [11] Darling, A.S., *Platinum Met. Rev.* **7**, **96** (1963).
- [12] Farjami, S., Yasui, M., Fukuda, T., Kakeshita, T., *Scripta Mater.* **58**, 811 (2008).
- [13] Rozman, K. Z., Krause, A., Leistner, K., Fahler, S., Schultz, L., Schlorb, H., *J. Magn. Magn. Mater.* **314**, 116 (2007).

[14] Tzitzios, V., Niarchos, D., Margariti, G., Fidler, J., Petridis, D., Nanotechnology **16**, 287 (2005).

[15] Aharoni, A., Introduction to the theory of ferromagnetism, Oxford Science Publications, second edition (2000).

[16] Bogdanov, A. N., Rößler, U. K., Müller, K. -H., J. Magn. Magn. Mater. **242-245**, 594-596 (2002).

Chapter 8

Electrochemical synthesis of NiFe alloy nanowires and Ni nanotubes

8.1 Preamble

With the advent of magnetic nanowires of dimensions comparable to domain wall (DW) width, it becomes possible to move the DWs along the NWs by sending spin polarized current through the NWs or by applying a magnetic field.¹⁻⁸ The DWs exhibit a well defined precessional mode due to confinement which is fundamentally important for spintronics devices.⁹ Other modes are also possible in other structures e.g. magnetic bubble, thin films, platelets etc.¹⁰ Generally the permalloy refers to an alloy of Ni and Fe with 80% and 20% composition respectively.¹¹ Permalloy NWs are particularly attractive because of their large anisotropic magnetoresistance (AMR) so that transverse and vortex walls can be detected and identified by resistance measurements.¹² The alloy exhibit a low magnetostriction which is critical for industrial applications, where variable stresses in thin films would otherwise cause a large variation in magnetic properties. It used in recording head sensors, transformers laminations, telecommunication cables etc. Here in this chapter we briefly describe the synthesis and structural properties of NiFe permalloy NWs.

Nanotubes have some advantages over the nanowires as the magnetic property of NTs can be controlled by changing the length, outer diameter as well as by changing the inner diameter of the NTs. Nanotubes exhibit a core-free magnetic configuration leading to uniform switching fields, guaranteeing reproducibility^{13, 14} and due to their low density they can float in solutions making them suitable for

applications in biotechnology.¹⁵ In addition to the permalloy NWs, we also demonstrate here the synthesis of Ni NTs.

8.2 Synthesis of NiFe alloy NWs

Permalloy NWs are synthesized by electrodeposition technique in a three electrode electrochemical cell. The detail of the experimental set-up for electrochemical deposition is described in *chapter 2*. We deposit the Ni as well as Fe in the form of alloy within the pores of alumina membrane by using the later as working electrode in the cell. The membranes are commercially purchased from Whatman.¹⁶ Average diameter of the pores is ~ 250 nm with an average membrane thickness of ~ 60 μm (*see Chapter 2*). Back side of the membranes is coated with gold film having thickness of ~ 100 nm to make it conducting so that it can be used as an electrode in the electrochemical cell.

Electrolyte solution used for the permalloy NW deposition consists of NiSO_4 and FeSO_4 with the concentration of 1.3 and 0.151 M respectively. The pH of the solution is maintained at 3.5. Linear sweep voltametry (LSV) scan is performed before the deposition for the particular electrolyte solution and electrodes that are selected for the deposition and is shown in Fig. 8.1. The deposition voltage of ~ 1.03 V is selected from the voltage versus current plot in LSV graph where the sudden jump in current is observed (see Fig. 8.1). The first peak in the pH curve in Fig. 8.1 corresponds to Ni deposition (at ~ 0.7 V) whereas the second peak corresponds to Fe deposition (at ~ 0.93 V).

The Ni^{2+} and Fe^{3+} ions simultaneously move inside the nanopores of the membranes under the potential of 1.03 V. The positive ions get deposited at the bottom of the nanopores as they come to the contact of negatively charged gold film at the base of the pores. The simultaneous deposition of the ions at a particular rate results in the formation of alloy composed of Ni and Fe. A particular concentration of the electrolyte solution leads to a particular composition of the alloy. By changing the

concentration of Ni and Fe salts in the electrolyte solution, different compositions of the alloys are obtained.

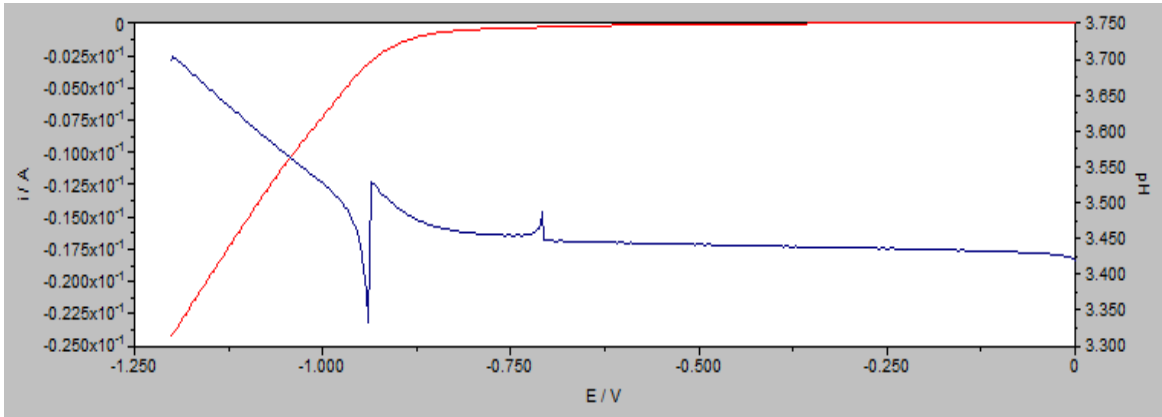


Figure 8.1. Linear sweep voltammetry scan for NiFe NTs deposition in alumina membrane having pore size of ~ 250 nm. Red line indicates the current profile and blue line indicates the pH profile of the solution during the scan.

8.3 Synthesis of Ni NTs

Ni nanotubes (NTs) are synthesized employing similar electrodeposition technique but with the use of NiSO_4 solution only. The concentration of NiSO_4 solution is of 0.7 M. 0.5 M of H_3BO_3 is added to maintain the pH at 3.6 obtained by adding ammonium solution to the NiSO_4 solution. Alumina membranes¹⁶ with gold coated at one side with pore diameter 200 nm are used to deposit the NTs. LSV scan is performed prior to Ni NTs deposition inside the pores of the membrane. Fig. 8.2 shows a typical LSV scan for Ni NTs deposition. Change in pH value is also measured simultaneously. We choose a potential of ~ 0.78 V for the NTs deposition.

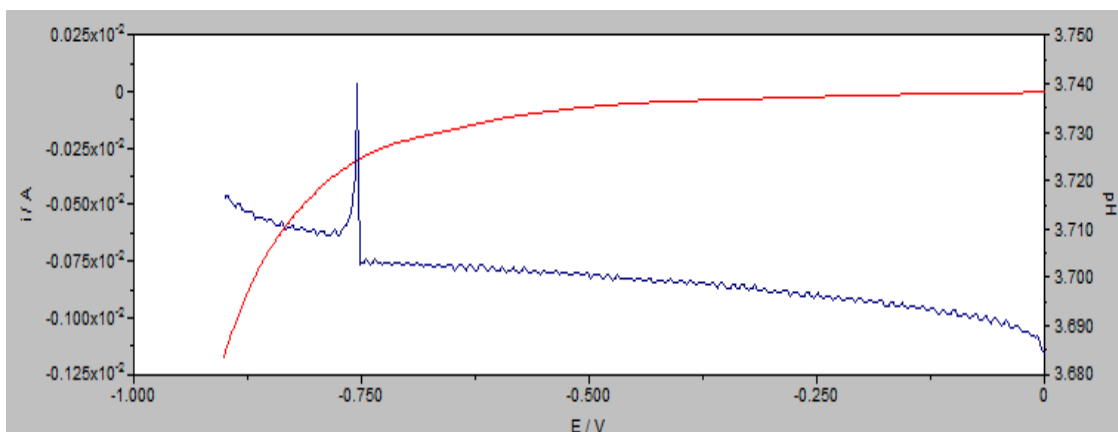


Figure 8.2. Typical LSV scan for Ni NTs deposition in pores of alumina membrane.

It is noted that a potential of ~ 0.85 V was applied to deposit the Ni NWs within the pores of alumina membrane of same pore diameter (see *chapter 2* and *4*). Under such negative potentials of the working electrode, the positively charged Ni^{2+} ions moves inside the cylindrical nanopores and become electrically neutral as soon as they come in contact with the gold film at the base of nanopores. A comparatively lower potential basically promotes the deposition of the ions along the cylindrical wall of pores instead of base of the nanopore as in the case of higher potential. The positively charged ions deposition inside a cylindrical nanochannel (nanopore) is shown schematically in Fig. 8.3. The deposition under a lower potential thus leads to the formation of NT whereas that under relatively a higher potential leads to the formation of NW inside the cylindrical nanopores.

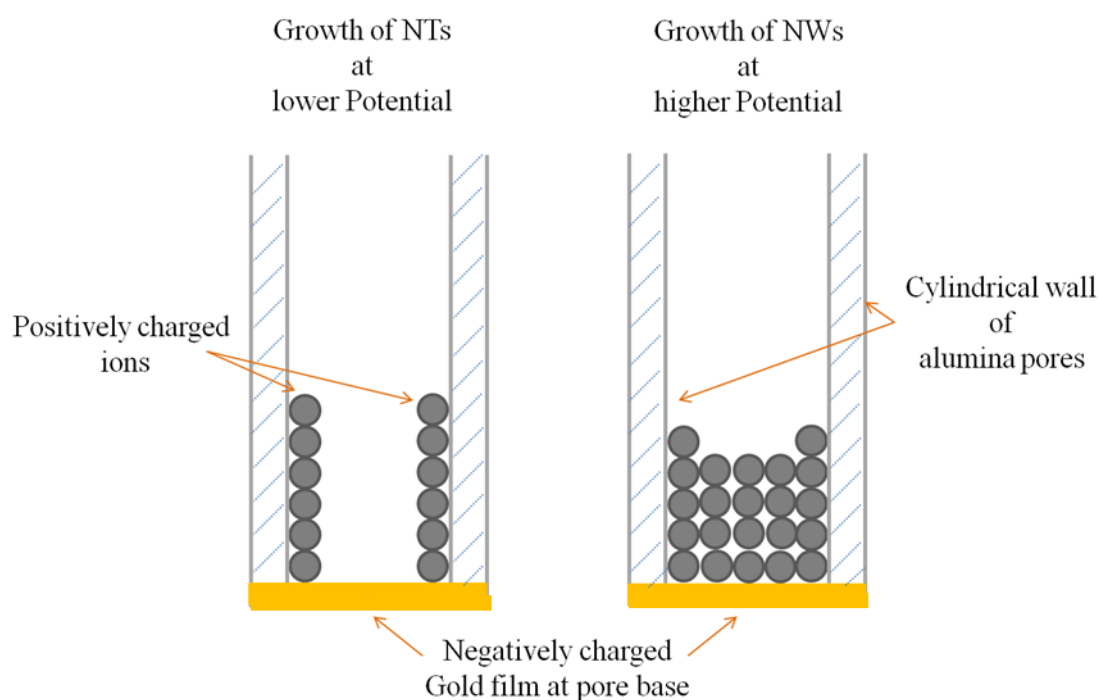


Figure 8.3. Two dimensional schematic diagram of growth of Ni NT at lower potential and of Ni NW at higher potential.

8.4 Results and discussions

8.4.1 Microstructural and elemental characterization of NiFe NWs

NiFe permalloy NWs are made free from the alumina membranes after dissolving the membrane using 2M NaOH solution. The SEM micrographs are taken in order to investigate the shape of the NWs. EDAX study is performed to confirm the composition of the NWs. Fig. 8.4 shows SEM micrographs of NiFe permalloy NWs. Corresponding EDAX spectrum of the NWs confirms the composition of the alloy as Ni:Fe = 80:20 (atomic %) and is shown in Fig. 8.5.

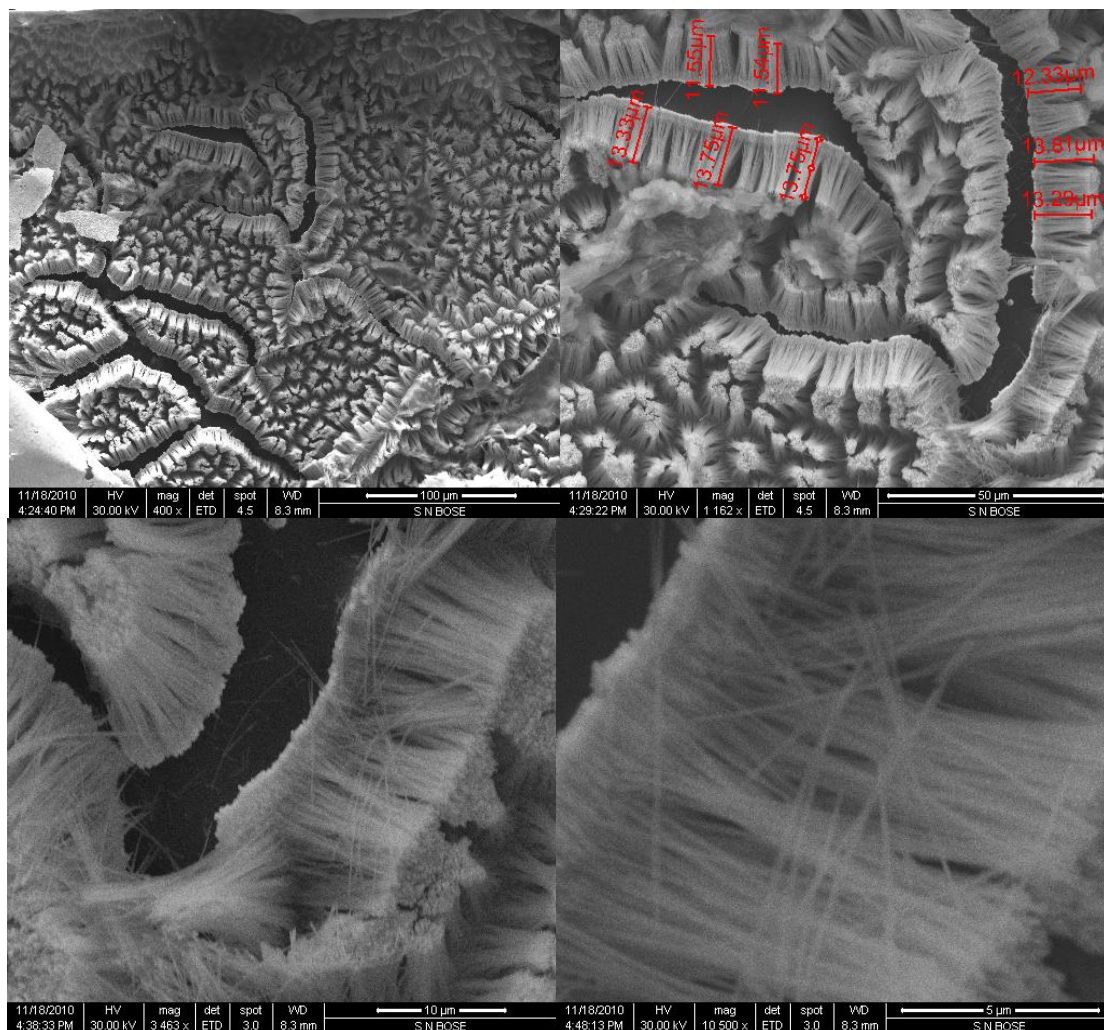


Figure 8.4. SEM micrographs of NiFe NWs with the composition of Ni:Fe = 80:20 (atomic %)

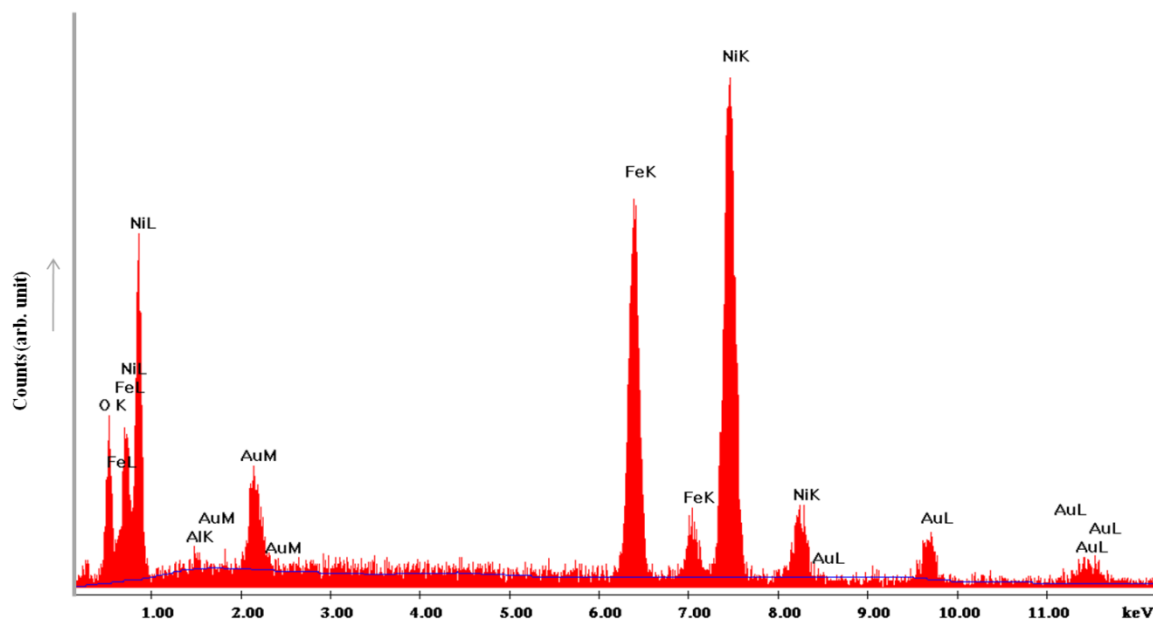


Figure 8.5. EDAX spectrum of NiFe permalloy NWs having composition as Ni:Fe = 80:20. Gold peaks correspond to the gold thin film and residual alumina is responsible for the observed peaks of aluminum and oxygen in the spectrum.

The SEM micrographs (Fig. 8.4) of the arrays of $\text{Ni}_{0.8}\text{Fe}_{0.2}$ permalloy NWs are taken after dissolving the membrane which show uniform length of the NWs throughout the sample. The NWs are formed within the alumina membrane by the electrodeposition of Ni and Fe for 20 minutes. Average length of the NWs is found to be of $\sim 13.1 \mu\text{m}$. The NWs are stable enough to stand freely on the gold film after dissolving the membranes. The composition of the alloy can be change by changing the concentration of the metal salts used in the electrolyte solution. We prepare $\text{Ni}_{0.67}\text{Fe}_{0.33}$ and the corresponding SEM micrographs and EDAX spectrum are shown in Fig. 8.6 and Fig. 8.7 respectively. Average length of the NWs is $12 \mu\text{m}$.

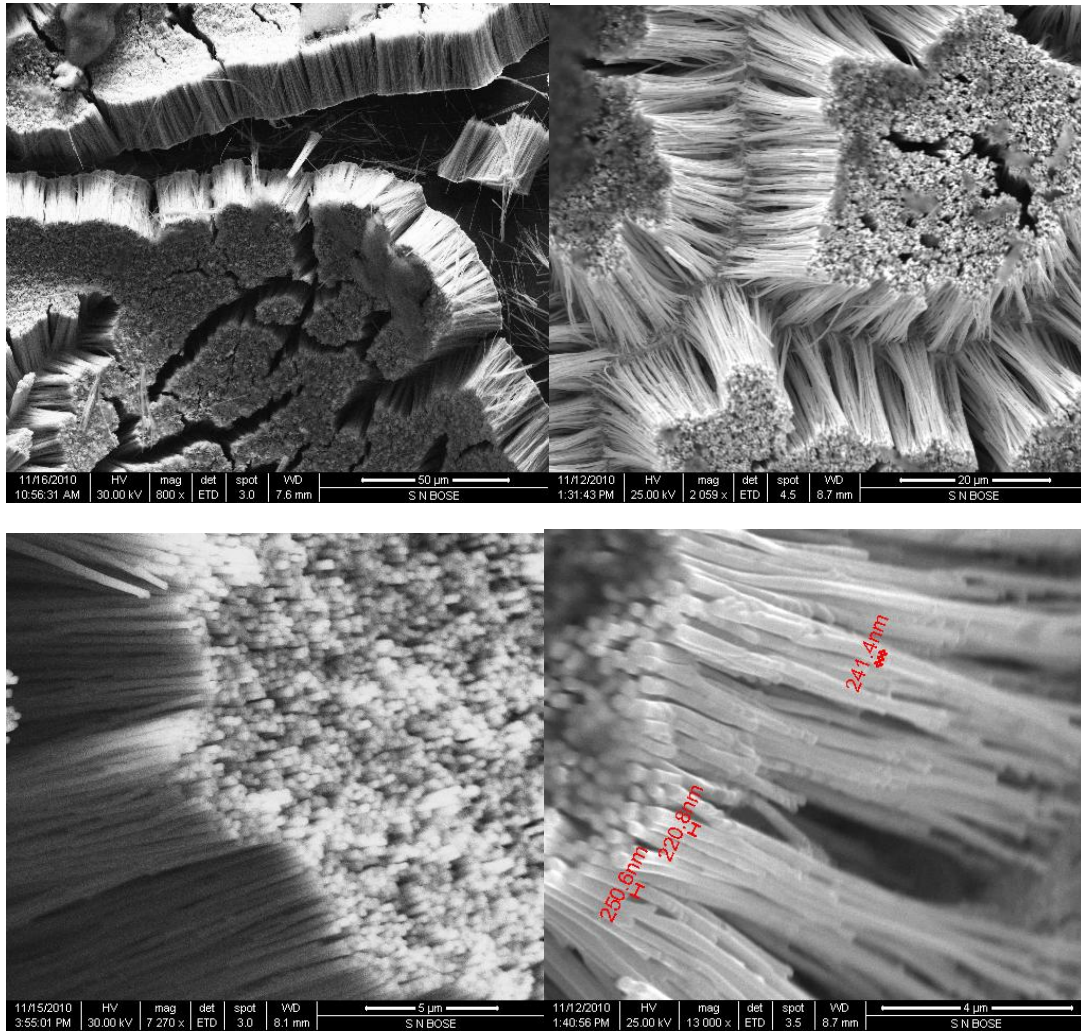


Figure 8.6. SEM micrographs of NiFe NWs with the composition of Ni:Fe = 67:33 (atomic %)

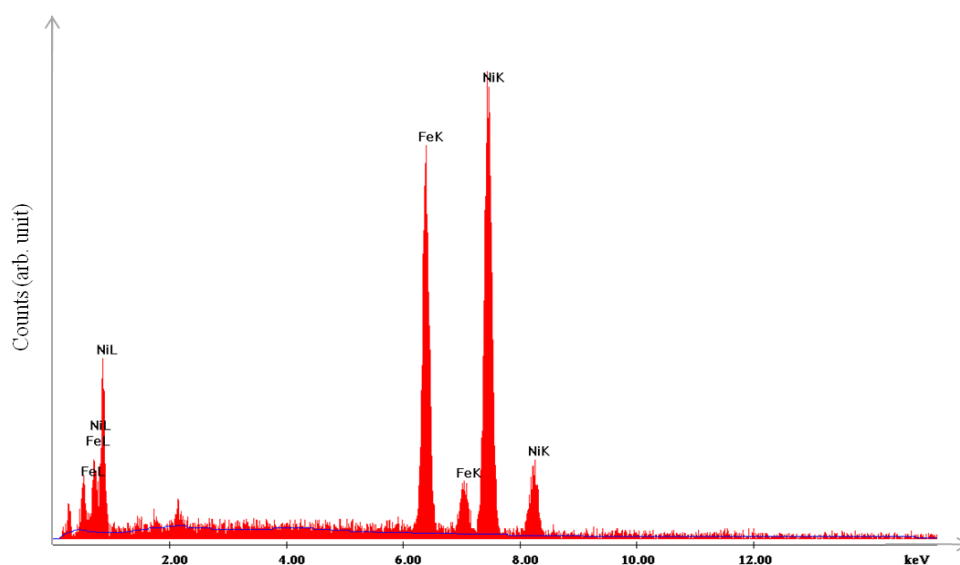


Figure 8.7. EDAX spectrum of NiFe permalloy NWs having composition as Ni:Fe = 67:33. Other peaks correspond to aluminum, oxygen and gold due to residual membrane and gold thin film.

Crystalline structure of the NWs is confirmed from the powder X-ray diffraction pattern obtained from the NWs after dissolving the membrane in NaOH solution. The XRD pattern is shown in Fig. 8.8. It indicates face centered cubic crystalline structure of the permalloy NWs.

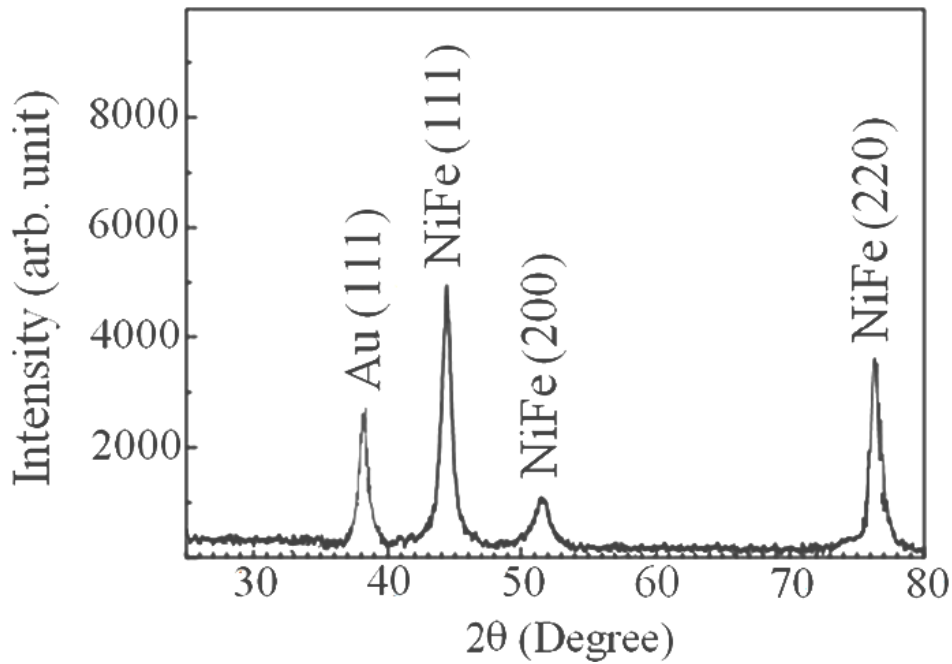


Figure 8.8. XRD pattern of NiFe NWs indicates fcc crystalline structure.

8.4.2 Microstructural characterization of Ni NTs

Surface morphology of Ni nanotubes is studied by scanning electron microscope after dissolving the membrane by NaOH solution. Fig. 8.8 shows the SEM micrograph of Ni nanotubes grown within the pores (diameter \sim 200 nm) of alumina membrane by a 500 sec deposition. It clearly shows the hollow cylindrical shape of the NTs. The inner diameter of the NTs is \sim 120 nm (approx). Average length of the NTs is about \sim 1.8 μ m.

The dissolving of alumina template and then washing of the residual alumina is crucial for SEM study of the NTs. In Fig. 8.8, all the NTs do not show hollow cylindrical shape at their top end. This may be due to the presence of residual alumina at the opening of those NTs. However in case of uprooted NTs from bottom, the bases of the NTs clearly shows hollow cylindrical patterns indicate tubular growth of the NTs from their bottom (see last two micrographs in Fig. 8.8).

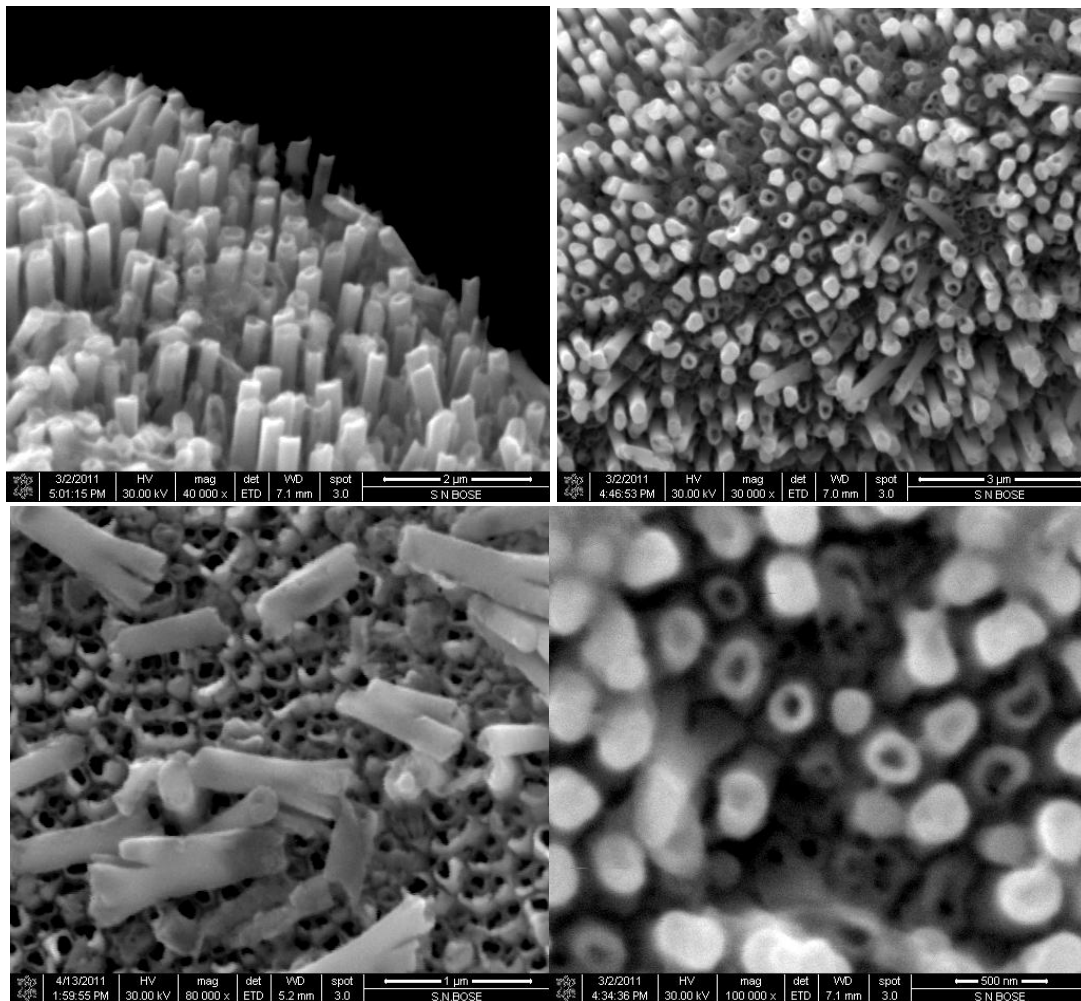


Figure 8.8. SEM micrograph of Ni NTs with an average outer diameter ~ 200 nm and inner diameter of ~ 120 nm. Average length of the NWs is of ~ 1.8 μm .

8.5 Conclusion

NiFe alloy NWs and Ni NTs are synthesized successfully by DC electrodeposition technique. Surface morphological study of the NWs carried out by scanning electron microscope clearly shows the uniform growth of the NWs throughout the membranes with an average wire diameter of ~ 200 nm. EDAX

analysis confirms two different compositions of NiFe NWs which are Ni : Fe = 80 : 20 and 67 : 33. The NWs possess fcc crystal structure. On the other, we synthesize Ni NTs within the pores of alumina membrane relatively at lower deposition potential compared to Ni NWs. SEM study shows clear formation of Ni NTs with an average outer diameter of ~ 200 nm and inner diameter of ~ 120 nm. The average length of the NWs is found to be of ~ 1.8 μm for 500 sec deposition.

Bibliography

- [1] T. Ono, H. Miyajima, K. Shigeto, K. Mibu, N. Hosoi, T. Shinjo Science 284, 468 (1999).
- [2] Atkinson, D., Allwood, D.A., Xiong, G., Cooke, M.D., Faulkner, C.C., Cowburn, R.P., Nature Mater. **2**, 85 (2003).
- [3] Beach, G. S. D., Nistor, C. Knutson, C., Tsoi, M. and Erskine, J. L., Nature Mater. **4**, 741 (2005); Phys. Rev. Lett. **97**, 057203 (2006); Yang, J., Nistor, C., Beach, G. S. D. and Erskine, J. L., Phys. Rev. B **77**, 014413 (2008).
- [4] Kläui, M., Vaz, C. A. F., Bland, J. A. C., Wernsdorfer, W., Faini, G., Cambril, E., Heyderman, L. J., Nolting, F. and Rüdiger, U., Phys. Rev. Lett. **94**, 106601 (2005).
- [5] M. Hayashi, L. Thomas, Ya. B. Bazaliy, C. Rettner, R. Moriya, X. Jiang and S. S. P. Parkin, Phys. Rev. Lett. **96**, 197207 (2006); Thomas, L., Hayashi, M., Jiang, X., Moriya, R., Rettner, C. and Parkin, S. S. P., Nature (London) **443**, 197 (2006); Hayashi, M., Thomas, L., Rettner, C., Moriya, R., Bazaliy, Y. B. and Parkin, S. S. P., Phys. Rev. Lett. **98**, 037204 (2007).
- [6] Zhang, S. and Li, Z., Phys. Rev. Lett. **93**, 127204 (2004).
- [7] Tatara, G. and Kohno, H., Phys. Rev. Lett. **92**, 086601 (2004).
- [8] Thiaville, A., Nakatani, Y., Miltat, J. and Suzuki, Y., Europhys. Lett. **69**, 990 (2005).
- [9] Hayashi, M., Thomas, L., Rettner, C., Moriya, R. and Perkin, S. S. P., Nature Physics **3**, 21 (2007).
- [10] Malozemo, A. P. and Slonczewski, J. C. Magnetic Domain Walls in Bubble Material, Academic Press, New York (1979).
- [11] Slonczewski, J. C., Theory of domain-wall motion in magnetic-films and platelets. J. Appl. Phys. **44**, 1759–1770 (1973).
- [12] Hayashi, M., Thomas, L., Rettner, C., Moriya, R., and Parkin, S. S. P. Nature Physics **3**, 21 (2007).
- [13] Wang, Z. K., Lim, H. S., Liu, H. Y., Ng, S. C., Kuok, M. H., Tay, L. L., Lockwood, D. J., Cottam, M. G., Hobbs, K. L., Larson, P. R., Keay, J. C., Lian, G. D. and Johnson, M. B., Phys. Rev. Lett. **94**, 137208 (2005).
- [14] Escrig, J., Landeros, P., Altbir, D., Vogel, E. E. and Vargas, P., J. Magn. Magn.

Mater. **308**, 233 (2007).

[15] Nielsch, K., Castaño, F. J., Ross, C. A. and Krishnan, R., J. Appl. Phys. **98**, 034318 (2005).

[16] Whatman Ltd. UK.